UNIVERSITY OF SOUTHAMPTON

Heat Budgets and Diurnal Mixing in the Western Equatorial Pacific Ocean

Mark Edward Inall

Submitted for the degree of Doctor of Philosophy

Department of Oceanography

May 1995

UNIVERSITY OF SOUTHAMPTON

ABSTRACT

FACULTY OF SCIENCE
OCEANOGRAPHY
Doctor of Philosophy

HEAT BUDGETS AND DIURNAL MIXING IN THE WESTERN EQUATORIAL PACIFIC OCEAN

by

Mark Edward Inall

This thesis presents a study of upper ocean processes effecting the heat content and sea surface temperature of the western equatorial Pacific Ocean. The study uses high resolution ship-borne measurements of upper ocean hydrography and current structure, and simultaneous measurements of air/sea fluxes of heat, moisture and momentum. Two periods are investigated, (1) April 1988 and, (2) December 1992–February 1993. Methods of analysis are heat budget estimation of the two data sets and one dimensional numerical mixing model experiments.

The second heat budget shows that over the period December 1992–February 1993 the heat balance is between the net surface heat flux and the local change in heat content of the upper 40 m to within 10 W m^{-2}. Exceptions to this local balance are of short duration, order(days), and of large amplitude, order(100 W m^{-2}). During April 1988 the local change in heat content is found to be dominated by horizontal advection down to 200 m. The net surface heat flux is found to be balanced by an estimate of vertical turbulent diffusion of heat to within 10%. Evidence is presented, using a combination of observations and numerical simulations, showing sub-surface density structure to interact with the mixed layer in such a way as to effect the sea surface temperature.

One dimensional mixing models are shown to be able to simulate the observed diurnal cycle of mixing in the upper ocean. Sensitivity studies show the diurnal momentum cycle to be sensitive to vertical velocity shear and the value of the Coriolis parameter, f, and relatively insensitive to the zonal pressure gradient. The diurnal thermal cycle is shown to be sensitive to short wave radiation, and to a lesser extent latent heat loss.

Mixing models are used to investigate the effects of precipitation on the sea surface temperature. Rain is shown to depress the sea surface temperature by up to 0.3 degree C immediately following a rain event, but after a period of weeks there is an increase in sea surface temperature, caused by local barrier layer formation. For a simulation of the period December 1992–February 1993 the increase is small (0.05 degree C). Implications of the work for general circulation modelling are discussed.

dedicated to the memory of my father, John Albert Inall

Acknowledgements

I would like to thank Dr. Kelvin Richards for his supervision, scientific guidance and friendship during my years in Southampton. Much valuable scientific discussion was had with Dr Wolfgang Barkmann, Dr Neil Wells and Dr Tom Haine. Staff of the James Rennel Centre helped greatly improve my knowledge of Pstar programming and Unix administration, I particularly thank Vic Cornell, Mike Griffths, Stuart Cunningham and Steve Alderson. The officers and crew of *Le Noroit* deserve thanks for making 8 weeks in the equatorial Pacific bearable.

Thanks to my mother, my sister and my brother in law for keeping me in clothes, food and good humour.

Thanks to my friends for putting up with the highs and lows of my PhD studentship: Crawford, Tom, Louisa, Helene.

Contents

Chapter 1

Introduction and Review

1.1 Relevance of Thesis to Climate Fluctuations

The "warm pools" of the world ocean are defined as the regions with temperature in excess of 28°C. The largest of these warm regions lies in the western Pacific and eastern Indian Oceans. Predominantly in the western equatorial Pacific (WEP) this region, occupying about 20% of the surface of the World ocean, is recognised as being crucial in the initiation and evolution of global scale climate fluctuation phenomena. The phenomena are collectively referred to as El Niño and the Southern Oscillation or ENSO. Inter-annual variations in the extent and sea surface temperature (SST) of the warm pool are clearly related to ENSO events. Positive SST anomalies in the WEP of 0.5°C have been observed prior to the onset of an El Niño . Prediction of ENSO phenomena is highly desirable from a purely scientific and from an economic point of view. If the aim is to be able to predict ENSO phenomena, something not possible at present, then factors which effect the evolution of SST within the Indo/Pacific warm pool must be understood. Atmosphere/ocean coupling in strong in the tropics and known to be vital to ENSO. Fluxes of heat and moisture are generally modulated by mesoscale atmospheric convective events. However the heat flux depends on the SST, and changes in SST depend strongly on mixed layer thermodynamics. Momentum and buoyancy fluxes at the sea surface, combined with initial vertical thermal and haline structure determine the evolution of the upper ocean and it's heat content. Thus both heat and moisture fluxes may exert a control on the upper ocean heat budget, and consequently on changes in SST and on the heat flux to the atmosphere.

Incoming solar radiation is primarily modulated by the diurnal cycle. When winds are light there are large diurnal variations in SST and upper ocean mixing. Diurnal variations in SST of more than a degree celsius have been observed. These diurnal peaks in SST may

be important in ocean/atmosphere feedback mechanisms.

In this thesis changes in heat content and SST in the western equatorial Pacific are examined. Processes which effect changes in both are identified, described and quantified using a combination of observations and numerical modelling.

This chapter describes the large scale structure of the western equatorial Pacific (Section 1.2) including momentum, heat and salt balances. The variability of the region from seasonal to interannual times scales is described in Section 1.3. The La Niña of 1988-1989 and the El Niño of 1991-1994 are examined in more detail (the data analysed in this thesis were collected during these two periods). Experimental efforts in the western equatorial Pacific are reviewed in Section 1.4. The chapter concludes with a statement of the objectives of the project, the methodology employed to achieve these goals and an outline of the contents of the thesis.

1.2 Large Scale Structure of the Central and Western Equatorial Pacific

1.2.1 Upper Ocean Circulation and Hydrology

Although there are large seasonal (Monsoonal) and inter-annual variations, the typical equatorial surface ocean currents driven by the trade wind system are as follows: the North Equatorial Current (NEC) flows westward between 10°N and 20°N with a mean velocity of 20-30 cm s^{-1} ; the North Equatorial Counter Current (NECC) flows eastward between 3°N and 10°N with maximum velocity in August of up to 60 cm s^{-1} ; the South Equatorial Current (SEC) flows westward between 15°S and 3°N, velocities here can exceed 100 cm s^{-1} . Figure 1.1, taken from Delcroix et al (1992), shows the 1984–1986 mean zonal flow at 164°E.

In addition to these three elements there is an equatorial undercurrent (EUC), which flows eastward below the SEC with its core at 150–200 m, attaining velocities of up to 60 cm s^{-1} in August, but which has been observed to disappear during an El Niño (McPhaden et al. 1990). Weak westward flow beneath the EUC is often referred to as the Equatorial Intermediate Current (EIC) and may or may not be separated from the SEC by two weak eastward flowing jets called the Sub-Surface Counter Currents (SSCC), which are found typically at around 250 m, 3°north and south of the equator.

Temperature and salinity sections on 156°E averaged from December 1992 to February

1993 are shown in Figures 2.1 [a] and [b]. The 28° C isotherm is fairly flat, varying from 60 m at 3°N to a maximum of 75 m on the equator. This is a cooler and shallower warm pool than 1984–1986 mean temperature (Delcroix et al. 1992), and is consistent with the continued El Niño conditions at that time. The bulging of the isotherms on the equator between 100 m and 250 m shows the position of the EUC.

The surface salinity field is characterised by a fresh layer with a minimum of 34.0 psu at 2.5°N, increasing more to the south (34.4 psu at 5°S) than the north (34.1 psu at 5°N). The layer is fairly homogeneous down to 40 m northward of 1°N, with horizontal and vertical stratification increasing southward. The fresher surface waters have their origins in the northern hemisphere, freshened in the ITCZ. The prominent sub-surface feature is the intrusion of the high salinity southern hemisphere subtropical salinity maximum waters (SSMW) centred within the thermocline at 150 m. Between 90 m and 150 m the SSMW appears to cross the equator, the 35.0 psu contour vertical at 3.5°N. The processes by which this apparent cross equatorial mixing occurs are thought to be due to lateral double diffusive salt fingering (Richards 1991) in addition to horizontal shear instabilities. The latter is likely to be the dominant mechanism. The sub-surface temperature structure in Figure /reff:iopmeants [a] is similar to the 1984–1986 mean (Delcroix et al. 1992). The 1993 surface salinity is about 0.5 psu fresher, again characteristic of the on going El Niño conditions.

1.2.2 Momentum Balance: Meridional and Zonal

The Intertropical Convergence Zone (ITCZ), which lies between the NE trade winds of the northern gyre and the SE trades of the southern gyre, is found almost always north of the equator. The surface currents described are essentially wind driven by prevailing NE and SE trade winds. Munk's basin scale, upper ocean circulation using averaged annual zonal windstress illustrates the general features of the NEC, NECC and SEC as described above (Bearman 1989). The change in sign of f, the Coriolis parameter and the cross equatorial SE trade winds gives rise to meridionally divergent Ekman flow at the equator and hence upwelling. The convergence of NE and SE trades at the ITCZ gives rise to upper ocean Ekman convergence at the southern edge of the ITCZ (due to non-zero windstress curl). Whilst at the northern edge of the ITCZ the NE trades accompanied by rapid latitudinal change in f gives rise to oceanic Ekman divergence. The mean meridional surface height field therefore has a minimum at the equator and approximately 10°N (south of the NEC),

with a maximum at approximately 3°N. The NECC is thus a combination of a return flow down the upper ocean zonal pressure gradient set up by the westward windstress and geostrophic flow due to the sea surface sloping down from 3°N to 10°N.

The EUC too is conventionally viewed as driven in the main by the negative zonal pressure gradient along the equator. However a more enlightening approach which links equatorial dynamics to the sub-tropical regime is proposed by Pedlosky (Pedlosky 1987; Pedlosky 1991). In these two papers he links the initial strength of the undercurrent to the bifurcation latitude of the western boundary currents which feed the undercurrent, and the subsequent eastward intensification of the current to meridional advection of waters ventilated in the subtropical gyres. From this point of view, it is less the wind stress right at the equator which drives the undercurrent so much as the stress distribution across the neighbouring subtropical zones.

All the mean zonal surface flows at and near the equator (NECC,SEC and NEC) have been shown to be in approximate geostrophic balance with meridional pressure field, where the meridionally differentiated form of the geostrophic equation is used (Picaut et al. 1989).

$$\rho\beta u = -\partial^2 p/\partial y^2 \tag{1.1}$$

where, the equatorial beta $\beta = 2\Omega/r$ (Ω and r are Earth's angular rotation rate and radius respectively).

This is in agreement with the meridional surface height field described above. The EUC and SSCCs are also in geostrophic balance in the mean with the meridional density gradients. This is evident in the mean density structure taken from observations in December 1992 to February 1993 described in Section 2.1 (Eldin et al. 1994). The EUC is evident in the bulging of the isopycnals on the equator at 150 to 200 m and the SSCCs in the upward slope of the isopycnals at 280 m at the poleward edges of the equatorial pycnostad. These observations have been quantified in earlier studies (McPhaden 1984) as well as in the present case (Eldin, personal communication).

Thus the mean zonal flows are in geostrophic balance, although the time dependent flows are found not to be (Moum et al. 1987; Johnson et al. 1988). But what of the zonal momentum balance? Specifically what balances the zonal wind stress, given that a balance with the Coriolis force is not possible on the equator.

The conventional view holds that the zonal equatorial windstress is balanced, in the mean, by the vertical integral of; (i) the zonal pressure gradient, (ii) horizontal (merid-

ional) and vertical advection of eastward momentum, and (iii) mesoscale eddy mixing. It is thought that in the mean about eighty percent of the windstress is balanced by the zonal pressure gradient (Bryden and Brady 1985). The addition of advection of eastward momentum over compensates the windstress, implying the important role of eddy mixing in decelerating the eastward undercurrent. The important role of eddy mixing is also stressed by Kraus (1987) using the same balance argument. However a key issue not yet fully understood is how the wind stress is communicated into the interior. Bryden and Brady (1985) show implied stress penetration to at least 200 m, while Dillon and co-workers (Dillon et al. 1989) find, with use of microstructure measurements that the vertical stress divergence has a length scale inconsistent with such a depth. They conclude that; (i) processes other than simple shear instabilities are transporting momentum vertically, and/or (ii) the assumption of a production-dissipation balance in the turbulent kinetic energy budget (an assumption made in the turbulent kinetic energy (TKE) estimates) is incorrect. More recent work has shown (Herbert et al. 1991) that the large scale terms in the momentum equation, specifically the zonal pressure gradient, zonal advection of momentum and vertical advection of momentum can change over short time and space scales and that variability in the turbulent stress divergence term is also large. They conclude that insufficient micro-structure measurements exist over a year to compare a turbulence stress divergence term with the residual of Bryden and Brady. Thus any balance between windstress and zonal pressure gradient exists on longer than seasonal time scales. They also conclude that during periods of moderate to high wind conditions some other process than locally generated turbulence must be responsible for transporting momentum at intermediate depths and so the conclusion of Dillon (1989) is still relevant despite their paucity of turbulence measurements.

The most likely candidate for this transport mechanism is vertically propagating internal waves. The diurnal modulation of internal waves and their possible role in vertical momentum transport have been considered in a number of papers (Moum et al. 1992; Herbert et al. 1992; McPhaden and Peters 1992; Moum et al. 1992). These articles demonstrate a correlation between fine-scale velocity and temperature variance attributed to internal waves and turbulent dissipation rates. The most recent paper on the subject (Peters et al. 1994) goes further, showing that enhanced internal wave activity is accompanied by enhanced fine scale shear and that variations in large scale, low frequency shear and stratification within the pycnocline are also part of the enhanced internal wave signature.

It is clear then that the processes which effect the communication of surface stress into the interior have both local and regional significance, and that these processes are still relatively poorly described.

1.2.3 Heat Balance

One of the largest gaps in our knowledge of the coupled ocean-atmosphere system in the warm pool areas of the tropics is of the upper ocean heat balance of the region and the processes which regulate the SST. The importance of this is that the response of the atmosphere is extremely sensitive to SST (Palmer and Mansfield 1986), and that heat fluxes within the ocean can modify the mean circulation (Bryden and Brady 1989). Evidence of our lack of knowledge can be found in the widely varying estimates of the surface heat flux. Estimates of the annual mean net surface heating in climatic atlases vary from about 30 W m^{-2} (Esbensen and Kushnir 1981; Hsiung 1985) to 50 W m^{-2} (Weare et al. 1980) to 70 W m^{-2} (Reed 1985). More recent estimates from both numerical models (Gordon and Corry 1991; Gent 1991) and direct measurements (Godfrey and Lindstrom 1989) suggest that the mean heating may be closer to zero, although on time scales of weeks the fluxes may be far from zero, as will be seen in Chapter 3.

What can be said about the balance between surface flux, advective fluxes, eddy diffusive fluxes and turbulent diffusive fluxes? Considering the warm pool region, both modelling studies (Gent 1991) and climatological studies (Niiler 1982; Enfield 1986) suggest the predominant balance is between net surface heating and vertical diffusive processes. On the basis of this, Godfrey and Lindstrom (1989) infer from vertical turbulent flux measurements that the net heating must indeed be small. However, as they point out, their measurements were taken over a period of a few days of generally quiescent conditions. Additionally, as shall be shown, the assumption of negligible heat advection on these time scales in not necessarily good.

1.2.4 Salt Balance

The details of the surface freshwater flux are even more uncertain. No long term measurements of open ocean rainfall exist. Climatologies of net evaporation minus precipitation suggest net precipitation over the whole of the warm pool region, from the Indonesian coast to 165°E and between 5°N and 5°S. Highest values of 140 cm yr^{-1} net precipitation are found in the east of the region and north of the equator associated with the ITCZ, lower

values of 70 cm yr^{-1} are quoted at 165°E (Baumgartner and Reichel 1975). Estimates of rainfall over the ocean are controversial, with a discrepancy of over 60 cm yr^{-1} for the equatorial Pacific between two more recent estimates (Dorman and Bourke 1979; Elliot and Reed 1984).

The salinity transport by ocean currents is also ambiguous. A qualitative description is of wind driven poleward flows of relatively fresh surface waters, equatorward flows of salinity-maximum waters between 60 and 180 m, an increase in salinity of the SEC as it flows westward and a freshening of the EUC as it flows eastward. Compared with these terms the net surface flux is small and even it's sign could not be reliably inferred as a residual from a salt budget performed between 150°W and 110°W (Bryden and Brady 1985).

However it is generally agreed that there is a positive net freshwater flux into the warm pool region, and that precipitation can be locally intense and have a diurnal or possibly a semi-diurnal signature (Berg 1993; Albright et al. 1985). Individual atmospheric convective events typically have a scale of tens of kilometres and precipitate relatively cool water at a rate of a few cm hr^{-1} for an hour or more. Although the integrated affect of such events may be negligible, with the net heat and evaporation minus precipitation small, the local response of the upper ocean is expected to be substantial. In Chapter 5 the magnitude of this local response is investigated.

1.3 Variability

1.3.1 Monsoonal Circulation

The word monsoon is derived from an Arabic word meaning "winds that change seasonally". This seasonal change, most pronounced in the reversal of wind direction over the Indian sub-continent, is a direct consequence of the seasonal changes in the areas of surface level atmospheric convergence, which themselves correspond to regions of warmest SST.

In the Pacific the ITCZ is furthest south (close to, but typically still north of the equator) in March/April. The north east trades are at their strongest over the WEP and flow has a southerly component across the equator west of the date line. By September/October the ITCZ is at its northernmost position of around 14°N, the south east trade winds are now at their strongest and penetrate into the northern hemisphere all across the Pacific basin. Typical rainfall patterns from tropical Pacific islands show maxima corresponding to the

position of the ITCZ.

The atmospheric circulations described in the following section also show seasonal variability. The more intense of the meridional Hadley circulation cells has subsiding motion in the winter hemisphere, due to larger latitudinal thermal gradients. The zonal Walker circulation is weakest in March and April when zonal sea level pressure differences are small.

1.3.2 The Southern Oscillation

Much has been written on El Niño and the Southern Oscillation, such that the wide range of atmospheric and oceanic manifestations of the phenomenon are referred to generically as ENSO phenomena. Interannual variability in the atmosphere centred over the Pacific basin was first commented on by Lockyer and Lockyer (1904), following the observation of Hildebrandsson that surface pressure fluctuations in Sydney were 180° out of phase with those in Buenos Aires. By correlating pressure fluctuations at stations around the globe Lockyer and Lockyer showed that the tropical Pacific atmosphere exhibits an oscillation with an approximate period of 3.8 years, manifest most clearly in the anti-phase correlation of surface pressure between two areas, one over the western equatorial Pacific/eastern equatorial Indian oceans and the other centred over the southeastern tropical Pacific. The term "Southern Oscillation" (SO) was coined by Walker (Walker and Bliss 1930) who showed that many other atmospheric phenomena are correlated with the SO Index (SOI, now defined as the difference in surface pressure between Darwin and Tahiti), most importantly major changes in windfield and rainfall patterns. The SOI from 1975 until present is shown in Figure 1.2. It was not until 1969 that a plausible physical mechanism which shed some light on the observed correlations was put forward. Incorporating the observed correlation of SST fluctuations in the tropical Pacific with the SOI, Bjerknes' (Bjerknes 1969) principal result was that large scale atmospheric circulations on time scales of months or greater, correspond to direct thermal circulations. In these circulations moist air converges on regions of warmest SST (>27.5°C) where the air rises, condenses (therefore warming and rising further). These areas therefore typically have high cloudiness and precipitation. Elsewhere subsiding cold, dry air from the upper troposphere suppresses the formation of cumulus clouds in the atmospheric boundary layer.

Two examples of direct thermally driven circulations are of interest here. (1) The meridional or 'Hadley' circulation, in which warm air rises close to the equator and subsides

in the sub-tropics (at around 23°). In broad terms this circulation is responsible for the trade winds, with air at rest relative to the Earth at a latitude of 23° acquiring a westward velocity as it is advected to the equator. (2) The zonal or 'Walker' circulation, in which the east to west SST gradient along the equator, particularly in the Pacific, gives rise to a direct thermally driven zonal circulation, with air rising over the warmer western equatorial Pacific and subsiding over the eastern side. The SO is a perturbation to these direct thermal circulations, associated with the intensity and positions of the regions of rising air.

The two phases of the SO, which correspond to the oceanic states termed El Niño and La Niña , correspond broadly to periods of, respectively, weakened and intensified Walker and Hadley circulations. The forcing region for these buoyancy driven circulations, namely the warm water of the western equatorial Pacific, is thus of key interest when studying the SO phenomenon. Of particular importance are the factors which influence the SST and extent and location of the warm pool, as these directly effect the intensity and location of the circulations.

1.3.3 Oceanic Signature

A very important aspect of the ENSO phenomenon is the quasi-periodic nature of the oscillation. It is perhaps differences between particular ENSO events which give us most insight into the complex coupled physical processes involved. Rasmusson and Carpenter (1982) give a much cited description of a composite ENSO event in terms of surface meteorology and SST anomalies. Their composite El Niño is summarised here, additional upper ocean manifestations subsequently described are included.

Conditions in the western equatorial Pacific during the La Niña which followed the El Niño of 1986–87 and the extended El Niño conditions of 1991–93 are then examined in more detail. These two periods correspond to the two data sets analysed in this thesis.

The description of the equatorial Pacific given in Section 1.2 broadly corresponds to the La Niña phase of the SO. The description of a composite El Niño is of an evolution of the atmosphere/ocean system away from the La Niña conditions. More thorough descriptions can be found in a number of publications (McPhaden et al. 1990; Delcroix et al. 1992; Gill and Rasmusson 1983).

The composite El Niño has a duration of 18 months, beginning in year (-1), ending in year $(+1)$. Towards the end of year (-1) the SOI decreases, mainly due to low sea level pressure in the central and south eastern Pacific. Consequently there is a weakening

of the easterly trade winds west of the date line. In the early part of year (0) SST and rainfall are anomalously high in the eastern equatorial pacific. These conditions persist beyond their usual seasonal maximum. The ITCZ fails to migrate northward, weakened trade winds on and east of the date line means the cold tongue (the signature of equatorial upwelling) fails to intensify and propagate eastward, resulting in positive SST anomalies for the season in the central Pacific. By April of year (0) the convective region over the western equatorial Pacific begins to move eastward following the eastward movement of the western Pacific warm waters, which relax eastward due to the reduced westward wind stress. By September year (0) the collapse of the easterly trade wind system is emphasised by westerly wind bursts (WWBs) of up to 10 m s^{-1} and 10-15 days duration in the western equatorial Pacific. WWBs appear to be clustered at a certain phase of the 30 to 60 day Madden–Julian oscillation (MJO) (Weickmann 1991). Negative rainfall anomalies exist over New Guinea and Indonesia. The WWBs in the west reach their maximum intensity at the end of year (0) and the beginning of year (+1). The upper ocean responds rapidly (O(days)) in two ways. An eastward surface jet is directly excited, observed to flow at over 100 cm s^{-1} within a week of the onset of the westerly winds (McPhaden et al. 1992) in mid to late year (0). Strong surface Ekman convergence occurs west of the date line, resulting in a depression of the thermocline by tens of metres and a rise in sea level of approximately 10 dyn cm. The EUC is also observed to slow and even reverse direction. These responses of the upper ocean result in an increased eastward advection of the warm pool surface waters, the jet directly and the convergence by eastward geostrophic flow associated with the surface height field anomaly, which itself is postulated to travel eastward at a speed of approximately 50 cm s^{-1} as an equatorial Kelvin wave.

The eastward advection of warm pool waters at speed of up to 1 m s^{-1} has the affect of moving the forcing location for the atmospheric Hadley and Walker circulations. The advected water reaches the eastern Pacific in a time period of about nine months, with devastating affect on the Peruvian fishing industry (Barber and Chavez 1993). The SOI increases towards the middle of year (+1), trade winds begin to re-establish in the central and eastern Pacific inducing equatorial upwelling resulting in the appearance of colder surface waters. These low SSTs spread westward by which time the trade wind system intensifies and the ocean/atmosphere system enters to the La Niña phase of the SO by mid to end year (+1).

1.3.4 La Niña 1988

In February 1988 the SOI and eastern Pacific SST anomaly crossed zero (SOI from negative to positive, SST anomaly from positive to negative) suggesting a return to "normal" conditions, Figure 1.2. West of the date line the wind remained anomalously eastward, but reduced from the previous year. The surface dynamic height at 165°E rose abruptly off the equator in March 1988. By March the easterly trade winds had expanded across the breadth of the Pacific, a pronounced dip in the surface dynamic height field on the equator at 165°E was associated with Ekman divergence and strong equatorial upwelling. The SEC flowed westward between the equator and 6°S at speeds of up to 60 cm s^{-1} . The EUC, absent only 6 months earlier was likewise strong. Undercurrent core speeds in excess of 70 cm s^{-1} were centred on the equator at 150 m, commensurate with an anomalously large eastward pressure gradient in the thermocline observed at this time (McPhaden et al. 1990). The NECC at 7°N was weak (maximum 10 cm s^{-1}). Despite the strong EUC and SCCs the net transport was to the west, restoring warm surface waters to the western Pacific, until November 1988 when dynamic heights at the equator were comparable to reference values and exceeded them away from the equator.

1.3.5 El Niño 1991 to 1993

Throughout much of 1990 and early 1991, conditions in the equatorial Pacific suggested that an El Niño was beginning to develop. SOI values of between 0 and -1 at this time were mainly a result of higher than normal surface pressures at Darwin, and were associated with positive SST anomalies in the western Pacific. West of the date line the trade winds were characterised by frequent WWBs of several days duration. Positive SST anomalies first began to appear in the central and eastern equatorial Pacific in June (McPhaden 1993). Three pronounced WWBs penetrated successively further east in August 1991, November 1991 and January 1992, with the January WWB producing westerly winds as far east as 140°W for a few days. SST anomalies east of the date line reached a maximum of 2°C at 155°E in March 1992. The lowest values of the SOI was -2.4 in October 1991. The SEC reversed direction flowing eastward with speeds of up to 100 cm s^{-1} in January 1992. This eastward expansion of the warm pool waters, modulated by the passage of wind forced Kelvin waves, flattened the east west slope of the thermocline, even reversing the slope between 140°W and 170°W in February. Consequent weakening of the baroclinic zonal

pressure gradient, the driving force for the EUC, caused a weakening, but not a reversal, of the EUC to around 30 cm s^{-1} from December 1991 to March 1992. Westerly wind anomalies became less frequent during March 1992, at the same time a westward flowing SEC returned. By April the positive SST anomaly began to retreat west of the date line, the thermocline began to rise in the eastern Pacific and the SOI was rising. By June 1992 the cold tongue was developing in the eastern and central Pacific, by August 1992 the SOI was again near zero. It appeared as if the El Niño had terminated.

However west of the date line positive SST anomalies remained, the thermocline remained some 25 m shallower than climatology and westerly wind anomalies persisted. WWBs intensified in November and December, equatorial Kelvin waves were forced and positive SST anomalies were seen in the cold tongue in the central Pacific. By April the SOI was -1.2 and El Niño conditions clearly existed in the tropical Pacific. By July 1993 the ENSO anomalies had diminished.

The departure of the 1991–1993 El Niño from the composite El Niño is not without precedent, El Niño events spanning three calender years have occurred before (eg. 1957–1959). The second re-intensification in November 1992 and again in 1994 do appear to be without analogue in the recent past (McPhaden 1993). It is rather striking that the last three El Niño events have all appeared to develop in different manners to those in the preceding 40 years and that this coincides with our concerted observational efforts in the equatorial Pacific. Our understanding of ENSO is clearly far from complete.

1.4 Observing Programmes Pre–1992

The first intensive studies in the Equatorial Pacific were carried out east of the date line in 1979. The Equatorial Pacific Ocean Climate Studies (EPOCS), with current meter moorings at 110°W and 140°W from 1979 until 1981, were designed to look at transport variations in the equatorial currents (Knox and Halpern 1982). The Hawii–to–Tahiti Shuttle experiment (Wyrtki et al. 1981) consisted of 15 quasi–meridional hydrographic sections between 158°W and 150°W from Hawii (21°N) and Tahiti (17°S) during which bulk estimates of surface fluxes were made, and of current meter moorings at 152°W. Also in 1979 the North Pacific Experiment (NORPAX) was extended south to the equator with 3 current meter moorings deployed at approximately 152°W. The data from these sets of moorings were used in a series of papers addressing three dimensional heat and momentum budgets in the region

(Bryden and Brady 1985; Brady and Bryden 1987; Bryden and Brady 1989). Analyses of mixed layer depth properties arose from the shuttle hydrographic sections, (Schneider and Müller 1990).

It was 1984 that saw the beginning of concerted observational effort in the equatorial pacific, our lack of understanding of the region having been emphasised by the unexpectedly severe El Niño of 1982–1983. The first ATLAS (Autonomous Temperature Line Acquisition System) moorings were deployed at 110°W as prototypes for the TOGA–TAO array to be initiated the following year. The need for these *in situ* observations was motivated by Stanely Hayes of the National Oceanic and Atmospheric Administration's Pacific Marine Environmental Laboratory (NOAA PMEL). The array now covers the equatorial waveguide with 70 moorings giving approximately 10°longitudinal by 2°latitudinal resolution, transmitting data to shore in real time, (McPhaden 1993).

In 1984 two meridional hydrographic sections along 165 °E were made by the Institut Francais de Recherche Scientifique Pour le Développement en Coopération (ORSTOM) as part of their SURTROPAC programme (Surveillance Trans–Océanique du Pacifique). These were the first of many such sections occupied by ORSTOM between 1984 and 1988, which yielded a good description of the upper ocean temperature, salinity and current variability over a period spanning an El Niño and La Niña (Delcroix et al. 1992).

The other significant field program of 1984 was Tropic Heat 1. Motivated by previous findings of a meridional peak in turbulent dissipation in a narrow belt around the equator (Crawford and Osborn 1981), Tropic Heat 1 carried out systematic microstructure turbulence measurements at 140°W. The program was designed to study "the tropical Pacific upper ocean heat, mass and momentum budgets" (Eriksen 1985), recognising the essential role of small-scale turbulent mixing therein. As discussed already, to lowest order the momentum balance of the undercurrent is between driving zonal pressure gradient and retarding vertical turbulent friction. The most significant finding of Tropic Heat 1, confirmed by Tropic Heat 2 in 1987, was the strength of the diurnal cycle in turbulent dissipation rates. Not only were there much larger dissipation rates at night, but the high dissipation rates penetrated well into the stratified region below the well mixed surface layer. The deep diurnal variation was first linked to high frequency internal gravity waves by Gregg et al. (1985). The most thorough disposition of the Tropic Heat findings is given by Peters et al. (1994), who go further than previous papers by showing that variations in large-scale, low-frequency shear and stratification within the pycnocline were also part of the overall

diurnal cycle of the upper ocean.

In 1985 and 1986 the Australians began work in the equatorial Pacific with their new ship *RV Franklin*. The Western Equatorial Pacific Ocean Circulation Studies (WEPOCS 1 and 2) were joint ventures with the US timed to coincide with the height of the SE and NW monsoons. The main observational components were a grid of CTD stations extending from 143°E to 155°W and from 8°S to 5°N, continuous ADCP and current meter moorings in the straits between Papua New Guinea, New Britain and the Solomon Islands. The focus was on the western boundary currents along the north east coast of Papua New Guinea. They showed that the high salinity waters in the EUC do indeed originate from the Coral and Solomon Seas via the western boundary current (Lindstrom et al. 1987). As the first intensive set of CTD measurements west of 165°E, WEPOCS also provided a statistical description of mixed layer structures of the WEP and an opportunity to estimate a one dimensional heat budget of the surface layer. In particular the idea stemming from a trans–Pacific equatorial temperature section observed in 1964 (Lemasson and Piton 1968) that the mixed layer in the WEP is very deep (100 m or more) was shown to be anomalous. The average mixed layer depth was 29 m from the WEPOCS cruises. On average during the WEPOCS cruises the thermocline was 20 m deeper than the base of the mixed layer. This isothermal layer beneath the mixed layer was termed the "barrier layer", since entrainment into such a layer would not cause cooling. The WEPOCS investigators defined their "barrier layer" to be the thermocline depth minus the pycnocline depth (Lukas and Lindstrom 1991). The same definition has been used subsequently by others (Sprintall and McPhaden 1994). The usefulness of this definition and an alternative definition are discussed in Section 2.5.

Heat budget calculations from the WEPOCs data showed a near zero net heat flux into the surface layer (Godfrey and Lindstrom 1989), casting some doubt on previous estimates of heating of 10s of W m^{-2} .

The first of 6 USA–PRC (Peoples Republic of China) TOGA cruises took place in 1986, the last one in 1989. The cruises consisted of CTD and ADCP (frequently malfunctioning) sections between 123°E and 165°E. From such data it was possible to compute the zonal pressure gradient (ZPG) on the equator and show that the ZPG changes sign seasonally in the WEP, indicating a rapid (O(weeks)) adjustment of the surface waters to seasonally changing wind patterns, (Mangum et al. 1990).

In 1987 Tropic Heat 2 was undertaken as discussed above. In 1988 the British research vessel *RRS Charles Darwin* was in the western equatorial Pacific. A seven day survey was

carried out centred on a drifting buoy at 165°E on the equator. Analysis of the results from this cruise are presented in Chapter 3.

A drifter data assembly centre was established in 1988 at the NOAA Atlantic Oceanographic and Meteorological Laboratory in Miami in support of the TOGA program, (Hansen et al. 1994). They acquire data from the operators of WOCE/TOGA-Standard drogued surface drifters for uniform processing and publish monthly activity maps of all drifters in the tropical Pacific. Approximately 1000 drifters have been deployed in the tropical pacific by American, Japanese, French and Chinese vessels between 1988 and 1993.

In 1990 Australian investigators on board *RV Franklin* performed a 10 day lagrangian experiment following a drifting buoy drogued at 20 m, making 4 CTD casts per day and continuously measuring air/sea heat, moisture and momentum fluxes by bulk methods and additionally sensible and latent fluxes by eddy covariance methods, (Bradley et al. 1993). They found it possible in this region, 4°S 149°E, to close the upper ocean heat budget to within 25 W m^{-2} .

1.5 TOGA Programme

The ten year TOGA (Tropical Ocean Global Atmosphere) programme (1985–1994) was a major component of the World Climate Research Program (WCRP) aimed specifically at the prediction of climate phenomena on time scales of months to years. The underlying premise of TOGA was that dynamic adjustment of the ocean in the tropics is more rapid than at higher latitudes where rotation is a constraint on the flow. Thus a disturbance originating from the western equatorial Pacific may propagate across the basin on time scales of months compared to years at higher latitudes due to the $1/f^2$ dependence of mid-latitude planetary wave speed. The tendency of f to zero at the equator means steady forcing will lead to a greater Ekman mass transport, in addition to a faster response to unsteady forcing. The significance of shorter time scales near the equator is that they are similar to those of highly energetic atmospheric modes such as 10 to 20 day westerly wind bursts and the 30 to 60 day MJO (Madden and Julian 1972). This similarity would lead one to expect the formation of coupled modes between the atmosphere and tropical atmosphere.

Thus the scientific objectives of the TOGA program were laid down as follows (WCRP 1990).

1) To gain a description of the tropical oceans and global atmosphere as a time dependent system in order to determine the extent to which the system is predictable.

2) To study the feasibility of modelling the coupled ocean-atmosphere system.

3) To provide the scientific background for designing an observing and data transmission system for operational prediction, if this capability is demonstrated, by coupled models.

The particular importance of the western Pacific warm pool area was recognised early in the planning stages of TOGA. Thus a regional process study of this area was conceived, the Coupled Ocean Atmosphere Response Experiment or COARE.

1.5.1 TOGA COARE

The overall goal of COARE was to provide an understanding of the role of the warm pool regions of the tropics in the mean and transient state of the tropical ocean-atmosphere system. The specific scientific objectives were to describe:

1) The principle processes responsible for the coupling of the ocean and the atmosphere in the western Pacific warm pool system;

2) The principle atmospheric processes that organise convection in the warm pool region;

3) The oceanic response to combined buoyancy and wind stress forcing in the western Pacific warm pool region; and

4) The multiple scale interactions that extend the atmospheric and oceanic influence of the western Pacific warm pool system to other region and vice versa.

1.5.2 Intensive Observing Period (IOP)

The main focus of TOGA COARE was the Intensive Observing Period (IOP). The IOP was a 120 day long observing program which took place from 1 November 1992 to 28 February 1993. Twelve hundred people from 20 nations conducted 700 days of ship operations, launched 12000 rawindsondes, completed 125 aircraft flights, and maintained continuous operation of 30 moorings. The operations were centred at 2°S 155°W around the so–called Intensive Flux Array (IFA), see Figure 1.3. Ship operations occurred entirely within the IFA with the exception of the large scale survey of *RV Le Noroit*. In total 14 research ships took part. Details of their instrumentation can be found in the working version of the Operations Plan, (TCIPO 1992). Ship borne measurements made include: Rain radar covering most of

the IFA (*RV John Vickers* and *RV Xiangyangong 5*), ocean optics *RV John Vickers*, atmospheric profile soundings (ISS stations) (*RV Kexue 1, RV Shiyan 3, RV Moana Wave*), hydrographic and current surveys (*RV Wecoma, RV Le Noroit, RV Franklin*), microstructure measurements and air/sea fluxes (*RV Moana Wave, RV Natsushima*) and, nutrient measurements (*RV Alis*). The large scale (5°N to 5°S) survey of *Le Noroit*, which will be essential in putting the IFA work into a regional context, is reported in Chapter 2 and Appendix A.

The TOGA COARE International Project Office has published an Operations Summary (TCIPO 1993). This provides a day by day account of all operations. It includes surface wind analysis, IR satellite images, atmospheric soundings, rain radar maps (uncalibrated) and upper ocean temperatures for each of the 120 days. The majority of the data are made available to participants on the internet via World Wide Web as they are processed. The TOGA COARE Data Management Plan, (TCIPO 1994), is updated frequently and lists currently available data sets.

1.6 Thesis Objectives

This research project began at a time when the response and coupling between atmosphere and ocean in the western equatorial Pacific were recognised as crucial elements of the ENSO phenomenon. No oceanic heat budget of the region had been attempted, the net heat and moisture flux of the region was poorly known and the oceanic response to extreme wind and rain events was just beginning to be described: thus objective (3) of TOGA COARE (Section 1.5). The research reported in this dissertation addresses some specific aspects of the oceanic response to buoyancy and momentum forcing.

The objectives were to identify and quantify the factors effecting the heat content and SST of the warm pool region. The methodology was to use two distinct observational data sets of the hydrographic and current structure of the upper 300 m of the ocean to calculate heat and salt budgets. The second thrust of the research was to use simple mixing models to investigate the sensitivity of the SST to atmospheric processes, specifically precipitation. The two data sets turned out to cover a rich variety of atmospheric conditions, allowing a broad range of oceanic responses to be described.

1.7 Description of Chapter Contents

Chapter 2 presents the results and analysis of a large scale experiment (10°latitude, 50 days) carried out in December 1992 to February 1993 as part of the TOGA COARE IOP. The data collection, processing and calibration techniques are described in Appendix A. The mean temperature, salinity and velocity structures of the 18 sections are presented. Features are identified and comparisons made with climatology and previous measurements. The rapid response of the upper ocean to the changing wind field is described and striking effect of heavy precipitation illustrated. A statistical description of mixed layer cycling (diurnal variability) and the effect of rainfall and barrier layer formation are given. Changes in heat and salt content are compared with surface flux measurements.

Chapter 3 concentrates on smaller time and space scales. Results of an experiment carried out in April 1988 centred around a drifting spar buoy on the equator at 165°E are analysed. The diurnal thermal cycle of the upper ocean is discussed. Three dimensional heat and salt budget calculations of the upper ocean are presented, including an analysis of errors incurred by the observational technique. Vertical velocities are estimated by two methods. The relevance of this experiment to a similar one carried out during TOGA COARE is discussed.

Chapter 4 presents a number of one dimensional numerical mixing models. Work to date using such models in the WEP is reviewed. Two mixing models are placed in an idealised western equatorial setting. Sensitivity studies of the diurnal thermal cycle to boundary and initial conditions are presented.

Chapter 5 describes a series of one dimensional numerical studies stimulated by the observations; in particular effects of rainfall on upper ocean processes are considered. Two models are utilised in both direct simulations and in process studies of precipitation.

Chapter 6 discusses the relevance of the present work, conclusions to be drawn from the research and the directions future data analysis and numerical experimentation should take.

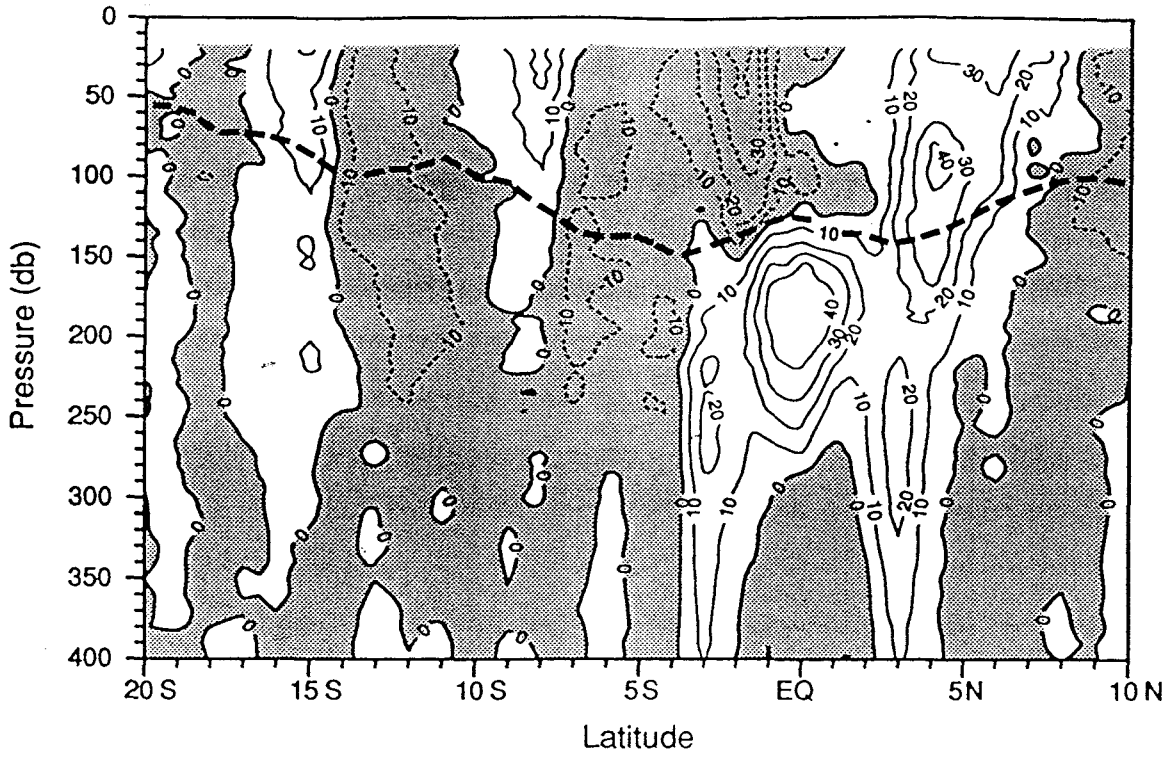

Figure 1.1: Mean zonal currents at 165°E 1984–1986 taken from Delcroix et al. (1992). The contour interval is 10cm s^{-1} ; shaded areas denote westward flow. Currents are relative to 600 db. The heavy dashed line is the mean 23.5 isopycnal.

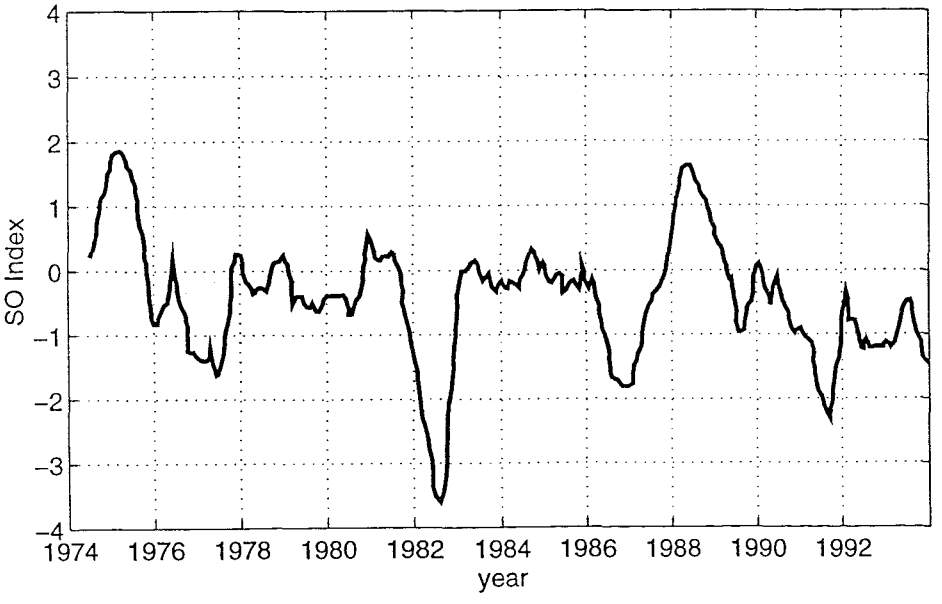

Figure 1.2: Southern Oscillation Index 1974–1994

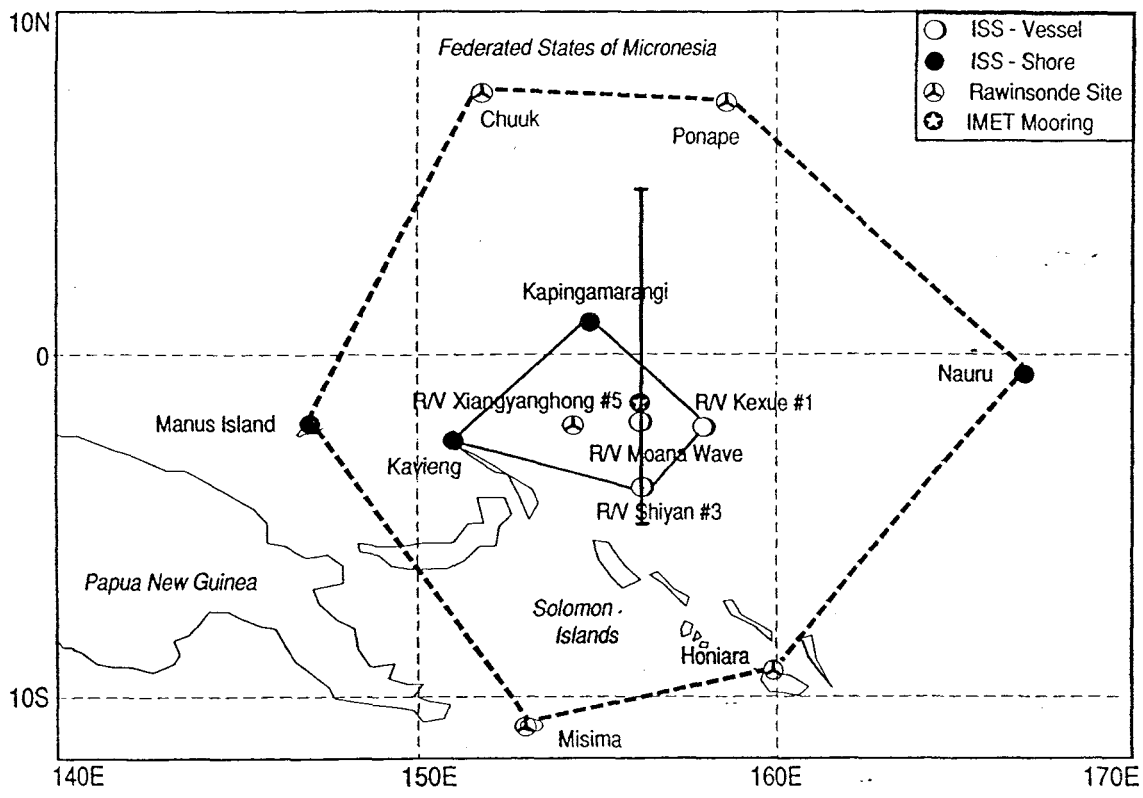

Figure 1.3: TOGA COARE Intensive Flux Array (IFA) region (solid quadrilateral). Continuous vertical heavy line marks cruise track of *Le Noroit* . Kavieng and Kapingamarangi are island observation sites.

Chapter 2

TOGA COARE

As described in Chapter 1, the Intensive Observation Period (IOP) represented the culmination of the observational efforts of the TOGA programme. The POI cruise (Période d'Observations Intensives) of the French research vessel *Le Noroit* was designed to obtain a series of 18 hydrographic sections between 5°N and 5°S along 156°E in a series of three legs (Richards et al. 1993; Delcriox et al. 1993) between 1 December 1992 and 1 March 1993. Throughout the whole cruise continuous measurements were made with a Seabird thermosalinograph (TSG) and a hull mounted Acoustic Doppler Current Profiler (ADCP). On leg 1 (1 December to 28 December 1992) five sections were completed with full depth CTD casts every 0.5° of latitude. On leg 2 and half of leg 3 (30 December 1992 to 17 February 1993) twelve sections were completed using a towed, undulating CTD (Seasoar), to a nominal depth of 300 m. The Seasoar was operated by a three man team from the UK; K. J. Richards, M. E. Inall and S. Keene. On the second half of leg 3, 19 February to 1 March 1993, one further section was made with full depth CTD casts at 1° latitude intervals. Additionally throughout the cruise 54 WOCE-Standard drifting buoys were deployed and 4 TOGA-TAO moorings repaired. An account of the cruise operations can be found in Delcroix et al. (1993), that of the Seasoar operations alone, data collection, calibration and processing can be found in Richards et al. (1993). A summary of the data collection, calibration and processing is presented in Sections A.1 to A.3, with emphasis on the novel approach developed to enable Seasoar processing to be carried out on a non-UK research vessel.

Much of the on-board processing was carried out using Pstar data processing programs. Pstar is a software system, written in Fortran 77, designed for interactively processing large data sets which are stored in a common binary format. A large number of general routines

exist, with the modular structure of the system making it straightforward for users to build their own programs. The programming system was originally developed at the Institute of Oceanographic Sciences, Deacon Laboratory (IOSDL) (Read et al. 1989) and is now maintained jointly between IOSDL and James Rennel Centre for Ocean Circulation (JRC). Subsequent data analysis was carried out with programmes written by the author in Fortran 77 and Unix C-shell scripts.

Throughout this and subsequent chapters sea surface temperature (SST) is taken to be the sea temperature at a depth of 1 m. Often in equatorial regions there can considerable temperature stratification in the upper 1 m of the ocean. No measure of temperature shallower than 1 m is used or talked about in this thesis, therefore SST has been used to mean 1 m temperature for the sake of brevity.

2.1 Mean Structures on 156°E

Before examining the variability of the 10°region over the 70 days of TOGA COARE, upper ocean properties averaged over the 18 sections taken by *Le Noroit* are presented. Comparisons with climatology and with previous measurements are made. These time averaged sections from 5°N to 5°S, 0 to 300 m have been reported in less detail by Eldin et al. (1994).

2.1.1 Temperature and Salinity

The mean temperature and salinity sections are shown in Figures 2.1[a] and [b]. SST is in excess of 29°C everywhere south of 3°N. The depth of the 28°C isotherm is fairly uniform, varying from 60 m at 3°N to a maximum of 75 m on the equator. This is a cooler and shallower warm pool than observed in 1984-1986 (Delcroix et al. 1992), and is consistent with the continued El Niño conditions at the time of COARE. The surface salinity field is characterised by a fresh layer with a minimum of 34.0 psu at 2.5°N, increasing more to the south (34.4 psu at 5°S) than the north (34.1 psu at 5°N). The layer is fairly homogeneous down to 40 m northward of 1°N, with horizontal and vertical stratification increasing southward. The fresher surface waters have their origins in the northern hemisphere, freshened in the ITCZ. The prominent sub-surface feature is the intrusion of the high salinity southern hemisphere subtropical salinity maximum waters (SSMW) centred within the thermocline at 150 m. The highest salinity is 35.7 psu at 5°S, the 35.15 isohaline penetrates

to the equator and is vertical from 120 to 200 m. Between 90 m and 150 m the SSMW appears to cross the equator, with the 35.0 psu contour vertical at 3.5°N. Processes by which cross equatorial mixing occurs are thought to be due to both lateral double diffusive salt fingering (Richards 1991) and horizontal shear instabilities. It is likely that the latter process is predominantly responsible for the cross-equatorial intrusion of the 35.0 psu contour. The subsurface structure is similar to the 1984–1986 mean (Delcroix et al. 1992). The 1993 surface salinity is around 0.5 psu fresher, again characteristic of the on going El Niño conditions.

2.1.2 Stratification

The influence of vertical stratification on vertical mixing is a principal interest. The buoyancy frequency squared, N^2 Figure 2.2[b] shows maximum density gradients between 80 m and 100 m from 3°S to 4°N. North of this the maximum is slightly deeper at 140 m, south of 3°S there is a broad maximum in N^2 from 60 m to 180 m. Beneath about 220 m the stratification generally decreases across the whole section. Meridionally there is a maximum in stratification on the equator associated with pinching of the isopycnals above the EUC. In the upper 50 m the reduced stratification in the northern part of the section is also apparent. It is of great interest to know how the density stratification is partitioned between salinity and temperature stratification, given the role salinity may play in limiting vertical mixing in the region. Using a linearised equation of state, N^2 may be written,

$$N^2 = -\alpha g \frac{\partial T}{\partial z} + \beta g \frac{\partial S}{\partial z} \tag{2.1}$$

where α and β are the thermal and haline expansion coefficients. From this R_ρ can be calculated,

$$R_\rho = \frac{\alpha \frac{\partial T}{\partial z}}{\beta \frac{\partial S}{\partial z}} \tag{2.2}$$

Figure 2.2[a] shows a contour plot of R_ρ for the upper 80 m. Everywhere beneath 80 m $R_\rho \geq 2.0$ indicating that temperature stratification dominates over salinity stratification by a ratio of 2:1 or more. This has implications for water mass interleaving across the equator. Laboratory experiments, (Holyer et al. 1987), have suggested that the saltier water should rise in the regime of $R_\rho > 0.62$, which may help explain the shallower depth of the high salinity north of the equator, although increased horizontal shear at the shallower depth could also contribute to this.

South of the equator there are almost no areas where $R_\rho < 1$, showing thermal stratification to dominate and thus little evidence of a "barrier layer" in the mean. North of the equator the situation is quite different. A great deal of the region between 0-60 m north of the equator has $R_\rho < 0.6$, illustrating the significance of the salinity stratification. How this relates to the presence of a barrier layer and precipitation is discussed in Section 2.3.

2.1.3 Velocity Field

The mean zonal and meridional velocity fields from the ADCP are shown in Figures 2.3[a] and [b]. They are averages over the whole cruise. Both zonal and meridional currents were highly variable during the observation period; the apparently low values are a result of averaging. The subsurface currents are consistent with the description in Section 1.2. The EUC, centred at 0.5°S with the core at 180 m, is relatively weak at 35 cm s^{-1} . A weak westward flowing EIC is present beneath the EUC. The sub-surface counter currents, SSCC and NSCC, symmetric about the equator at 3°and 270 m have quite strong eastward flows of 35 cm s^{-1} . The surface currents appear less "typical". The NECC is mostly subsurface, with a core of 35 cm s^{-1} at 130 m 3.5°N, with eastward flow on the surface north of 4°N and only 5 cm s^{-1} . The NECC appears to be driven subsurface by a 25 cm s^{-1} westward flowing current centred at 100m between 2°N and 2°S. This current is described as the SEC by Eldin et al (1994). An alternative proposition has been put forward that this current is the remnant of a subsurface counter current set up in response to an eastward surface flow driven by the prevailing westerlies of the preceding 6 months (McPhaden, personal communication). If this current is driven by a positive east-west zonal pressure gradient (ZPG) it may help explain the weakness of the EUC in that the negative east-west ZPG, one of the driving mechanisms of the EUC, may have been reduced.

The $\frac{\partial V}{\partial y}$ field, not shown, exhibits weak convergence associated with the EUC. It also shows weak convergence associated with the SEC. The values are of the order $\frac{\partial V}{\partial y} = 20 \times 10^{-8}$ s^{-1}. Assuming zero horizontal divergence this would give rise to a zonal acceleration of approximately 10cm s^{-1} over 10°of longitude. The convergence of the westward flow is counter-intuitive, as one would expect a westward flowing equatorial current to diverge. The average meridional convergence over the whole area is probably a reflection of the mean Ekman transport over the period of intermittently strong westerlies.

2.2 Regional Scale Variability

Before looking in detail at the oceanic response on 156° E, a picture of the mesoscale situation in the lower atmosphere over the warm pool is presented. Surface wind analyses are shown for 22 December, 8 January, 23 January and 1 February in Figures 2.4[a] to [d] respectively. The IFA region is marked by a dashed line. Data from the TAO Array are also presented which show some features of the basin wide variability during TOGA COARE. The 5 day mean zonal wind and 20°C isotherm depth anomaly are shown in Figures 2.5[a] and [b] for the period December 1992 to November 1993. Data are averaged over 2°S to 2°N.

The general situation was of westerly winds from 10 December to 5 January, illustrated in Figure 2.4[a], with winds generally around 8 to 10 m s^{-1} but with peaks of 23 m s^{-1} observed in the IFA. From 8 to 12 January winds were light or zero in the IFA, Figure 2.4[b]. A period of easterly wind flow with speeds of around 3 to 4 m s^{-1} followed until 27 January, Figure 2.4[c]. Westerlies returned over the southern part of the IFA from the 27 January onwards, Figure 2.4[d], with speeds of around 5 m s^{-1} .

This pattern of westerlies followed by easterlies followed by westerlies can be seen also in the 5 day mean zonal winds from the TAO Array, Figure 2.5[a]. The winds are averaged from 2° N to 2° S. It can also be seen that the first period of westerlies are more intense further east, at about 165°E. The persistence of westerly events throughout 1993 is indicative of the continuation of El Niño conditions. The 20°C isotherm depth is a good indicator of vertical displacement of the thermocline. Figure 2.5[b] shows the eastward propagation of a positive anomaly in January/February between the date line and 140°W. A similar feature can be seen in September. These anomalies can be traced back to the strong westerlies of December/January and July/August respectively. They are likely to be the signatures of a downwelling Kelvin wave front, which is non-dispersive, excited by the equatorial Ekman convergence associated with westerly winds. What is interesting is that the intervening westerly episodes did not excite such a response in the upper ocean.

2.3 Ocean Response on 156° E

In order to focus on the IFA and the extended region of *Le Noroit's* survey, the upper panel of Figure 2.6 shows a time latitude plot of wind pseudo-stress vectors from the TAO moorings on 156°E. The wind pseudo-stress is simply the 10 m wind speed squared. TAO Array anemometers are situated at 3.8 m above sea level. Winds speeds were extrapolated to 10 m

assuming neutral conditions (constant stress atmospheric boundary layer) and a roughness length of 3×10^{-4} m. These assumptions would make it unwise to use the derived wind pseudo-stress estimates in any quantitative studies, but they serve the purpose here of showing the pattern of momentum flux into the ocean. The wind pseudo-stress figure shows clearly the latitudinal asymmetries. Both westerly events are almost confined to the southern hemisphere. Indeed the wind has a eastward component at 5°N throughout the entire IOP. It is also the case that the easterly event is stronger north of the equator.

In this section the variability of the upper ocean structure along 156°E is presented and discussed with reference to the wind stress field from the TAO array at 156°, and precipitation measurements made on board *Le Noroit*. ECMWF (European Centre for Medium Range Weather Forecast) model surface flux forecasts are now available for the TOGA–COARE domain, however they became available too late to be included in this thesis. Figures of latitude versus Julian day, with 1992 negative, are presented. Data for the contoured plots are gridded on 1 day and 0.5°latitude, with "search radii" for griding of 4 days and 0.5°respectively. Absent data are filled by linear interpolation or left as blank.

2.3.1 Surface Current Variability

The remarkably rapid response of the surface currents to varying wind forcing can be seen in Figure 2.6. Figure 2.6[a] shows the wind pseudo-stress and Figure 2.6[b] the ADCP velocity vectors averaged over the top 60 m. The upper 60 m can be seen to respond to the onset of strong easterlies within days, with flow reversal and mean wind driven velocities of up to 1 m s^{-1} . The north/south asymmetry of the wind stress field is reflected in the upper 60 m currents. The eastward flows associated with westerlies are stronger south of the equator and the westward flow stronger north of the equator. The second westerly event did not accelerate the upper ocean as much as the first, despite the similar duration of the events. However the second westerly burst was weaker than the first. The turning of the surface currents relative to the wind due to Ekman dynamics is also evident poleward of about 2°latitude.

2.3.2 Upper Ocean Variability: T, S, and Derived Fields

Figures 2.7[a] and [b] show the SST and surface salinity respectively from the CTD and Seasoar data. The SST varies by 1.5°C over the domain. The SST shows broadly the same patterns to the wind, with SST inversely related to wind speed. However there

are exceptions to this. In the first few days of January when the wind speed is large at all latitudes, the SST near the equator remains above 29°C whilst poleward SST drops to below 28.5°C. Equatorial convergence as a result of the westerly component of the wind could help maintain the relatively high equatorial SST. Without surface flux information it is impossible to verify this. The surface salinity field shows the general trend of fresher water to the north. There is no obvious relationship surface salinity and SST or wind stress. Surface flux information would allow the relative influence of evaporation and precipitation to be assessed.

Figure 2.8 shows, [b] the depth of the 20°C isotherm and, [a] the "mixed layer depth" (MLD) based on a temperature gradient criterion of 0.0134°C m^{-1}. The MLD was deepest during strongest winds. Values in excess of 90 m occurred during the January westerlies, persisting for 5 days after the end of the wind burst. Similarly from 8 to 15 January, light winds coincided with MLDs as shallow as 10 m. There are periods when this simple wind mixing explanation is less convincing, particularly with regard to the strong easterlies around 4°N throughout the survey. The general pattern, however, is of locally wind stress determined MLDs.

The depth of the 20°C isotherm, Figure 2.8[b], gives an indication of the vertical displacement of the thermocline. There is greater equatorial symmetry in this figure than in the MLD figure illustrating the reduced direct action of local forcing at this depth. The shallowing of the 20°C isotherm after 10 January from 150 m to 110 m is likely to be a result of Ekman dynamics. Both easterlies on the equator and stronger winds north of the equator (positive $\frac{\partial u}{\partial y}$) would induce equatorial upwelling, skewed north of the equator. The reduction in the 20°C isotherm depth at 3°N and S is also indicative of a change in meridional circulation as the surface equatorial flow becomes horizontally divergent.

There is less evidence for equatorial downwelling as a result of the preceding westerlies. This is somewhat surprising given that the December/January windburst was observed to excite a downwelling equatorial Kelvin wave front. However this particular westerly burst was centred further east. Additionally the depth of the 20 °C isotherm prior to the wind burst in unknown.

Figure 2.9 shows, [a] rain rate ,[b] surface salinity anomaly and, [c] barrier layer thickness. The rain rate is from the optical rain gauge on board *Le Noroit*. Surface salinity anomaly is calculated as the measured value minus the salinity averaged in one degree latitude bins The barrier layer thickness is calculated as thermocline depth minus halocline

depth. These depths were calculated in two ways giving similar results; (i) a step criterion of 0.5°C (or density equivalent salinity step) from the surface value and, (ii) depth at which a temperature gradient of 0.01 kg m^{-3} m^{-1} (temperature and salinity equivalents) are exceeded. The results shown are for gradient criteria.

There can be little doubt that the low salinity anomalies (O(0.2 psu)) are associated with precipitation. The heterogeneous nature of rainfall makes this hard to show, but the frequent and heavy precipitation measured at the end of December 1992 correspond to the extensive negative surface salinity anomaly between 5°S and 3 °N from 10 to 30 December. The extensive precipitation observed around jday 15 at 3–5°S has little, if any, surface salinity signature. It can only be assumed that the strong surface currents, forced by the strong westerlies and veered to the right of the wind stress at these latitudes, advected surface salinity anomalies away from the ship and out of the survey area without them being observed.

Negative barrier layer thickness south of the equator between 10 and 30 January correspond well with the period of light winds, high SST and near zero precipitation. The shallow (10 m) MLD at this time is a consequence of strong diabatic solar heating and little wind mixing. The thermocline is thus up to 40 m shallower than the halocline. Over much of the domain the barrier layer thickness is negative, indicating thermal stratification to be limiting vertical mixing processes.

Over approximately 30% of the domain the barrier layer thickness is positive. These regions correspond closely with the negative surface salinity anomalies. In these regions salinity stratification plays a role in inhibiting vertical mixing and thus entrainment cooling of the mixed layer is reduced. These observations suggest that the barrier layers observed here are locally formed by precipitation. The observations also show that during TOGA COARE, precipitation had a greater role to play in terms of creating near surface salinity stratification north of the equator. This is seen in the mean R_ρ section, Figure 2.2, demonstrating that in the mean the IFA Interrupt north of the equator.

2.3.3 Variation in Vertical Structure

Figure 2.10 shows three vertical temperature sections down to 80 m. The first section (Figure 2.10[a]) was taken in the first 3 days of January during the height of the westerly winds. This section is characterised by a vertically homogeneous upper ocean across the 10° section width, mixed down to 80 m on the equator. By 6 to 9 January (Figure 2.10[b])

the section has become weakly temperature stratified from 5°S to 3°N, commensurate with the prevailing light winds over these latitudes at this time. North of this, the temperature is still homogeneous to approximately 40 m. This restratification of the upper ocean is remarkably rapid. The SST field between these two sections does not change greatly nor does the MLD field based either on a step or gradient criterium. The most interesting feature of this section is the sharp horizontal temperature gradients at around 2°South. Such frontal structure is suggestive of an eddy-like feature. This feature has been noted by others (Lukas, personal communication) and will have implications for the ocean heat budget work being performed around 2°S. By 23–27 January (Figure 2.10[c]) the thermocline has risen dramatically on the equator in response to the easterly winds and deepened particularly in the north. An experiment to determine how much of these observed changes is due to direct vertical wind mixing and how much due to Ekman dynamics is proposed in Section 6.6.

2.3.4 Diurnal Variability

The figures and discussion in the previous section did not resolve the diurnal cycle. All data were effectively averaged over 8 days (equivalent to two consecutive N–S sections) and 1° of latitude in the griding and contouring process. Using the raw 1 second averaged SeaSoar data the extent of the diurnal cycle over the period can be examined. The periods corresponding to the CTD sections (1-28 December and 19-28 February) have been included in the statistics but not the time series analysis. Averages over the whole survey of SST, surface salinity, mixed layer depth and barrier layer thickness are given in Table 2.1. Standard deviation and minimum and maximum values are also given.

Property	mean	std. dev.	min	max
SST (°C)	29.1	0.4	28.1	30.8
Salinity (psu)	34.1	0.2	32.38	34.7
Gradient Thermocline (m)	36	27	1	106
Gradient Halocline (m)	51	24	1	110
Barrier Thickness (m)	−14	19	−91	30

Table 2.1: Averages over the survey of SST, surface salinity, mixed layer depth based on temperature and salinity gradient criteria and barrier layer thickness (thermocline depth minus halocline depth)

These figures show a shallow (36 m on average) but highly variable mixed layer depth,

deeper than observed during the 1991 TOGA-Pilot study but similar to that found by Lukas and Lindstrom (1991). In the mean the thermocline is shallower than the halocline (negative barrier layer thickness), however the standard deviation is greater than the mean, and as has been shown positive barrier layers are observed in up to 30% of observations. Standard deviations of SST and surface salinity were 0.4°C and 0.2 psu. Their variation with latitude is discussed in the next section.

Power spectra of the time series of SST, thermocline depth, surface salinity, and halocline depth are shown in Figure 2.11[a] to [d]. The time series were de-trended, and the spectra normalised by the variance. The SST and thermocline spectra (Figure 2.11[a] and [b]) show a clear peak at 1 cpd, indicative of the diurnal thermal cycle. There are very small 1 day peaks in the surface salinity and halocline spectra. All spectra show a broader peak at 6.8 days. This is likely to be from the sampling strategy (each section took approximately 3.4 days). The peak at 3.4 days in the SST spectrum is also likely to be due to spatial aliasing. The 10 day peak in the SST and surface salinity spectra is of atmospheric origin, anticipating the results of the next section, rather than of oceanic wave origin. This is confirmed by the absence of the 10 day peak in either mixed layer depth spectrum. There is a peak at 20 days in both thermocline and halocline depth spectra. This could be the signature of a mixed Rossby-gravity wave. Observations in the central and eastern Pacific during EPOCS have shown mixed Rossby-gravity waves with periods of 20 days, (Halpern et al. 1988). The time series here are too short (50 days) to provide more than a suggestion of 20 day waves.

Focusing more closely on the diurnal cycle, Figures 2.12[a] to [d] show SST, surface salinity, thermocline depth, and halocline depth averaged by local hour of day for the whole time series. Amplitudes of the diurnal SST and mixed layer depth variation are 0.4°C and 30 m. Thus despite the periods of strong westerlies and easterlies the mean diurnal signature of the mixed layer is large. There is a diurnal range in the halocline depth of about 10 m. Some of the diurnal signal in the mixed layer depth records may be due to tidal motions, of which no consideration has yet been taken. However at least part of the diurnal signal in the halocline depth is a reflection of the role of salinity stratification in limiting the depth of night time mixing during certain periods, particularly during times of positive barrier layer thickness.

There is some suggestion in the surface salinity diagram (Figure 2.12) of two minima, one around local midnight the other around 3 pm. The rainfall data do exhibit maxima at these times (see Section 5.4).

2.3.5 Low Surface Salinity

Associated with precipitation events were surface salinities as low as 32.3 psu and temperature differences over the top 10 m greater than $\pm 0.5°C$.

Figures 2.14[a] and [b] show contour plots of temperature and salinity. The upper 30 m is shown, the horizontal axis is distance in km, the full scale of 200 km represents 13 hours of steaming, starting at 20:00, ending 08:00 local solar time at 1–2°N on jday 39 (UT). The figures show SST reduced by up to 0.5°C and surface salinity reduced by more than 1 psu for several hours. The upper 10–15 m are salt stratified throughout the night. There is evidence of localised convective plumes penetrating to 15–20 m intermittent in either space or time. The length scale of these plumes is of order 2 km. The precipitation measured from *Le Noroit* was not particularly heavy at this time (see Figure 2.9), but given the observed salinity anomaly, and anticipating the results of the modelling experiments (Section 5.3), it is clear that the ship missed most of the precipitation.

Figure 2.13 shows a scatter plot of the 1 m temperature minus the 11 m temperature (ΔT) versus surface salinity. The dark band along 0°C shows the upper 11 m to be well mixed for about 70% of the observations. In 25% of observations $\Delta T \geq 0.1°C$, indicating stable thermal stratification from short wave warming. Unstable thermal stratification, $\Delta T \leq -0.1°C$, was observed in 6% of the observations. This 6% represents fresh surface pools which have not been mixed to a depth greater than 11 m. From the modelling experiments this is indicative of pools which are at most 48 hours old, and more likely to be less than 24 hours old. This is because only the heaviest rainfall will produce a pool whose signature, as defined here, will survive more than one cycle of diurnal mixing. It is impossible to say what percentage of observations exhibit enhanced surface warming due to buoyant surface layers since the latitudinal range of "ambient" surface salinity allows fresh, warm pools to be detected only at the low salinity end of the ambient range, ie. in the northern-most observations. However, below 33.8 psu there was an order of magnitude fewer observations with $\Delta T \geq 0.1°C$ than with $\Delta T \leq -0.1°C$. Anticipating the results of Section 5.3 the preponderance of cool fresh pools over warm fresh pools is a reflection of the rain temperature being consistently 5°C lower than the SST.

2.4 Heat Content on 156°E

Using the 12 Seasoar sections and the 6 CTD sections the change in heat content along 156°E has been calculated. The net surface heat flux at 2°S is known from measurements made by the Woods Hole Oceanographic Institution (WHOI) IMET Buoy. The fluxes used here are courtesy of Bob Weller of WHOI. From this information it is possible to examine the balance between the surface heat flux term and the change in heat content term in the heat budget.

It is possible to estimate the turbulent heat flux divergence using the hydrographic and ADCP data and a turbulent diffusion parameterisation based on the gradient Richardson number. This method is used in Chapter 3, but has not yet been applied to the TOGA data set. In principle it would also be possible to estimate the meridional heat advection, $V\frac{\partial T}{\partial y}$, from the data after the extraction of tides. The zonal advection cannot be estimated from the data as no measure of $\frac{\partial T}{\partial x}$ exists, although it may be possible in the future to use data from the TAO array to estimate this term although on very coarse resolution (10°). A better method to estimate the zonal heat advection would be to use the SST maps of Reynolds and Smith (1994) which have a spatial resolution of 1°x 1°. This is currently being investigated.

Without the advective terms there is little point in calculating deep budgets so a one dimensional budget for only the surface layer is calculated. There is some reason to anticipate that the surface layer heat balance will be predominantly local and the advective terms small on the long term in this region. Niiler and Stevenson (1982) in considering the annual mean heat budget of the region defined by the 28°C isotherm found that fluxes of heat across lateral boundaries to be negligible. However on shorter time scales advective terms are likely to be important, as was found in a 7 day experiment at 165°E (Richards et al 1995, ibid Chapter 3), where the advective terms dominated the local rate of change of temperature. Preliminary results from TOGA COARE also find advective terms of up to 100W m^{-2} on daily time scales (Godfrey et al, 1994).

2.4.1 Heat Content Change

In estimating the upper ocean heat content it is necessary to choose a depth over which to integrate the temperature profiles. A number of depths ranging from 30 m to 100 m were used in the analysis. A depth of 40 m was found to give the highest correlation between net surface heat flux and heat content change. This is close to the average maximum depth

of the diurnal thermocline. Little short wave radiation penetrates beyond 40 m, although even a figure of a few W m^{-2} could be significant in the long term.

In order to compare with the surface heat flux at 2°S the heat content was averaged between 0.4°S and 3.6°S and differenced between consecutive sections. To compensate for the effect of vertical advection, the temperature profiles were "squashed" or "stretched" according to the vertical displacement of the 23.1 sigma surface between sections by assuming a linear decrease in vertical displacement to zero at the surface. This is consistent with low mode number internal motions. The transformed profiles, $T'(z)$ were first integrated over a range of depths z_h from 30 m to 100 m and then averaged over a specified latitude band of 3.2° width. It was necessary to average over a latitude band of 3.2° to minimise aliasing of the diurnal heating cycle (at 8 knots the ship covered 3.2°in 24 hours). Thus the change in heat content of the upper ocean was calculated as,

$$T_{z_h} = \rho C_p / \Delta t \overline{\left(\int_0^{z_h} T' dz \right)} \tag{2.3}$$

The overbar denotes the latitudinal average and Δt the time between averaging periods. The highest correlation with the net surface heat flux was found for $z_h = 40$m and this is plotted in Figure 2.15[a] along with the net surface heat flux. The correlation coefficient between the two curves is 0.68.

The figure shows that over three degrees of latitude the trend of the heat content change is to balance the net surface flux, but that periods of O(5 days) exist when this balance clearly does not hold and horizontal or vertical advection transport significant quantities of heat. Three periods of largest deviation are labelled. Periods 2 and 3 unfortunately coincide with 4 day port calls resulting in $\partial t = 7$ days and 10 days respectively. It is quite possible that fluctuations in the upper ocean heat content were missed particularly during period 3. However, any net change would be seen in the heat content. Periods 1 and 2 are of interest as they correspond to the time of strongest westerly winds at 2°S. The intermittent nature of the WWBs is reflected in the net heat flux profile, with the sharp peaks into the +ve corresponding to breaks in the strong westerlies. The coarse time resolution of the heat calculation makes it impossible to detect any correspondingly sharp changes in upper ocean heat content. Although there is no heat content data point during period 1, the subsequent data point shows no indication of the heating implied by the positive net heat flux of the period. It is possible that the heating was local to 2°S. It is interesting to note

that the averages of the two curves, -14 W m^{-2} for the net surface flux and -3 W m^{-2} for the heat content change, support the conclusion of a local heat balance. Figure 2.16[a] shows the time integral of Figure 2.15[a] (divided by $Cp \times \rho \times 40$ m, to give °C). Thus the difference of 11 W m^{-2} between the surface flux and heat content change translates into a 0.3°C integrated temperature difference. This is a small, but significant deviation from a one dimensional balance; significant in terms of atmospheric sensitivity to SST fluctuations.

A similar comparison of salt content change with surface moisture flux gave no significant correlation, suggesting that the considerable short space scale O(km) heterogeneity in the surface salinity (caused by precipitation) makes the advective term dominate the surface salt budget.

2.5 Latitudinal Variability on 156°E

The previous sections showed that in addition to the large temporal variation in upper ocean properties, latitudinal differences exist also. Describing these latitudinal variations is important to the TOGA COARE community since the majority of the oceanographic observations were carried out in the IFA centred on 2°S. It is important to know over what spatial scales these observations may be representative. To describe the latitudinal variation, the survey area was split into 3 latitude bands, (1) 5°S to 1.7°S (2) 1.7°S to 1.7°N (3) 1.7°N to 5°N. Each band thus represents 24 hours of data, reducing aliasing of the diurnal thermal cycle.

2.5.1 Surface Layer Properties

Table 2.2 shows the mean and standard deviation over each of the three latitude bands of SST, surface salinity, and gradient criteria mixed layer depth estimates. In addition estimates of thermocline and pycnocline depths and barrier layer thickness using the same criteria as Sprintall and McPhaden (1994) are given. They used the depth at which the temperature differed from the SST by more than 0.5°C as the thermocline depth, and the barrier layer thickness as the thermocline depth minus the pycnocline A corresponding quantity for the gradient criteria is thermocline depth minus pycnocline depth. This is also given in Table 2.2.

The general trend seen in the time/latitude plots of warmer water on the equator and fresher surface water to the north is apparent. There is a greater SST variability in the

Property	5°N to 1.7°N		1.7°N to 1.7°S		1.7°S to 5°S	
	mean	std	mean	std	mean	std
Wind Stress (N m^{-2})	0.03	0.016	0.02	0.016	0.02	0.02
SST (°C)	28.9	0.26	29.3	0.27	29.0	0.51
Surface Salinity (psu)	33.9	0.17	34.1	0.08	34.3	0.16
Gradient Thermocline (m)	38	28	40	29	30	25
Barrier Thickness (A) (m)	0	27	-11	29	-6	20
Barrier Thickness (B) (m)	8	14	2	13	4	11
MLDs using step criteria of 0.5°C or equivalent						
Step Thermocline (m)	58	22	59	24	48	25
Step Pycnocline (m)	49	22	55	24	42	24
Barrier Thickness (B) (m)	9	14	3	8	6	11

Table 2.2: Means and standard deviations of upper ocean properties averaged over three latitude bands as indicated.

southern band, which is perhaps a reflection of the greater range of the wind stress in the southern latitudes. It is interesting that surface salinity variability was not greater in the northern band, given the apparent greater rainfall there. The *Le Noroit* rain measurements do represent poor sampling of such a heterogeneous field. Rain radar data will provide a more complete description of the rainfall pattern in the near future.

Barrier Layers

The various mixed layer depth estimates generally show deeper layers in the northern latitudes, although the variance is large on all estimates. The latitudinal variation of the diurnal cycle will be discussed in the next Section. The two definitions of the barrier layer thickness require some comment: definition (B) is thermocline depth minus pycnocline depth, definition (A) is thermocline depth minus halocline depth. Definition (A) is used here because the "barrier layer" as defined by Lukas and Lindstrom (1991) and used by Sprintall and McPhaden (1994) (definition (B)) gives no indication of the *strength* of salinity stratification. It is thus an unquantitative and rather vague term. It gives no indication of how much turbulent kinetic energy is required to do work against temperature stratification versus salinity stratification. Therefore it is not clear to what degree entrainment cooling is affected (reduced) by the thickness or even the presence of a barrier layer so defined. The difference between thermocline and halocline depths on the other hand does make a statement about the relative depths of equivalent stratification. However *it* fails

to identify weak salinity stratification which may significantly influence vertical mixing. The conventionally defined barrier layer (B) does identify such situations, albeit in an unquantitative manner. Vertical profiles of R_ρ show the relative strength of temperature and salinity stratification at all depths and thus provide more information than either barrier layer definition.

Returning to Table 2.2. Barrier layer A is zero or positive over most of the domain (shown in Figure 2.9), while Barrier layer B is positive over most of the domain. Thus there was salinity stratification at the base of the mixed layer at all latitudes throughout TOGA COARE. What Barrier layer A shows is that there were occasions when salinity stratification limited the depth of vertical mixing, and that these occasions occurred more extensively in the northern latitude band.

2.5.2 Diurnal Cycle

Rather than presenting three sets of figures similar to those in Figure 2.12, the latitudinal variability of the diurnal cycle is summarised in Table 2.3. The table shows the maximum value and the diurnal range of the SST, thermocline depth and halocline depth for the three latitude bands.

Property	5°N to 1.7°N		1.7°N to 1.7°S		1.7°S to 5°S	
	max	range	max	range	max	range
SST (°C)	29.05	0.26	29.5	0.4	29.3	0.4
Thermocline (m)	56	34	58	36	43	30
Halocline (m)	61	20	67	17	52	15

Table 2.3: Latitudinal variation of diurnal cycling

The numbers show a clear thermal diurnal signal at all latitudes, with a SST range of a few tenths of a degree C and a thermocline depth range of approximately 30 m. The diurnal thermocline was shallower in the southern band, probably a reflection of the lower mean wind stress there. The diurnal signal in the halocline depth at all latitudes is worthy of note. There is no clear diurnal signal in the surface salinity, other than the suggestion of two minima corresponding to precipitation maxima (see Figure 2.12). As mentioned previously, both night time convection penetrating to the halocline and diurnal internal tidal motions could be responsible for the diurnal signal in the halocline record. Given the non-zero barrier layer thickness observed in the mean at all latitudes it seems likely that

part of the diurnal halocline signal is attributable to salt stratification arresting night time convection.

2.5.3 Heat Content

Figure 2.15[a] shows the heat content change averaged over the northern and southern latitude bands. Figure 2.16[b] shows the mean 0–40 m temperature curves. Both similarities and dissimilarities between the curves are noteworthy. That both curves of Figure 2.16 end up within 0.1°C of each other shows a remarkable consistency in heat content over 10° of latitude within the warm pool. The largest deviation between the curves is about 0.7°C. The periods in Figure 2.15[a] when the curves closely coincide (10 to 25 December 1992 and 20 January to 15 February 1993) shows how remarkably coherent the relatively high frequency (1/10 days) changes in heat content are over a large part of the warm pool. The wind stress (the only available surface flux information available at present) presents a possible cause for the difference in heat content change over the region. Particularly important is the phase difference between the timing between north and south of the peak in wind stress. In both northern and southern latitudes the similarly sized peak in wind stress coincides with heat loss. However this is far from the whole story. The correlation coefficients between wind stress and heat content change peak in the equatorial band ($r = -0.62$) and drop significantly north ($r = -0.44$) and south ($r = -0.38$). Combining this information with the knowledge that barrier layers were observed throughout the 10° of latitude leads one to speculate that lateral advection and mixing processes may be important in changing the heat content in the warm pool away from the equator. This idea is expanded upon in the discussion.

2.6 Discussion

This chapter has examined the western equatorial Pacific upper ocean on a space scales of hundreds of kilometres and time scales ranging from days to months.

The mean (over 70 days) picture was characteristic of the ongoing El Niño conditions which persisted into 1993. Relatively fresh surface layers, relatively cool sub-surface water and a shallow mixed layer being observed. Zonal flows were weaker in the mean than in previous observations, but the variability was high with the standard deviation greater than the mean in the top 40 m. The high variability was result of the dramatic changes in

meteorological conditions during the IOP. The SEC was generally sub-surface (60–150 m). Previous observations during El Niño conditions (WEPOCS 2 1986 (Tsuchiya et al. 1989) showed a westward flowing SEC from the surface down to the EUC (150 m). It is possible that the westward flowing current between 60 m and 150 m was the remnant of a return flow set up by the preceding six months of anomalously westerly winds.

Stratification was dominated by temperature south of the equator in the mean (70 days). North of the equator, the mean section showed regions where salinity stratification dominated. This situation is a result of greater rainfall and closer proximity to the ITCZ.

In many ways the TOGA community was fortunate in the timing of the COARE IOP. Meteorological conditions varied dramatically, giving a wide range of conditions in which to observe the atmosphere and oceanic response. Strong westerlies, strong easterlies and periods of little wind were observed. Throughout these conditions and at all latitudes a strong diurnal thermal cycle was seen. The diurnal thermocline, 10 m shallower in the latitude band south of 2.7°S, varied by 30 to 35 m at all latitudes, the 1 m temperature showed a mean diurnal signal of 0.3 to 0.4 °C. The halocline depth also exhibited a diurnal signal of around 17 m. This suggests salinity stratification has a role to play in limiting vertical mixing at all latitudes, although as discussed in the main text it is necessary but not sufficient evidence.

One of the important results from this chapter is how remarkably rapidly the ocean responded to the change in wind forcing. The upper layer (16–60 m) currents reversed direction within days during the transition from westerlies to easterlies. The thermocline was seen to rise as a result of Ekman dynamics, again over a period of days. A dramatic reflection of the rapid response is the close correspondence between the change in heat content of the upper 40 m and the net heat flux at 2°S. The ocean is seen to respond to the high frequency (O(1/10 days)) changes in surface flux, and these oceanic heat fluctuations are just resolved by the sampling strategy. The implied temperature change from the surface heat flux shows a net decrease of 0.1°C, which is some 0.4°C less than the observed decrease. This difference is brought about primarily by a short period (5 days) of warming which was not reflected in the oceanic heat content. The possibility exists that this warming was very local to 2°S. ECMWF fluxes may help to address this in the future. The heat content change in the northern and southern latitude bands show the same O(10 day) fluctuations. There is a phase shift of about 7 days between the strong heating peaks around 10 January. A similar shift in the TAO Array wind stress is likely to account for this. It is a significant

result that the ocean response, in terms of heat flux, is so coherent across 10° of latitude. It will be interesting to see how coherent the surface fluxes turn out to be in future analysis.

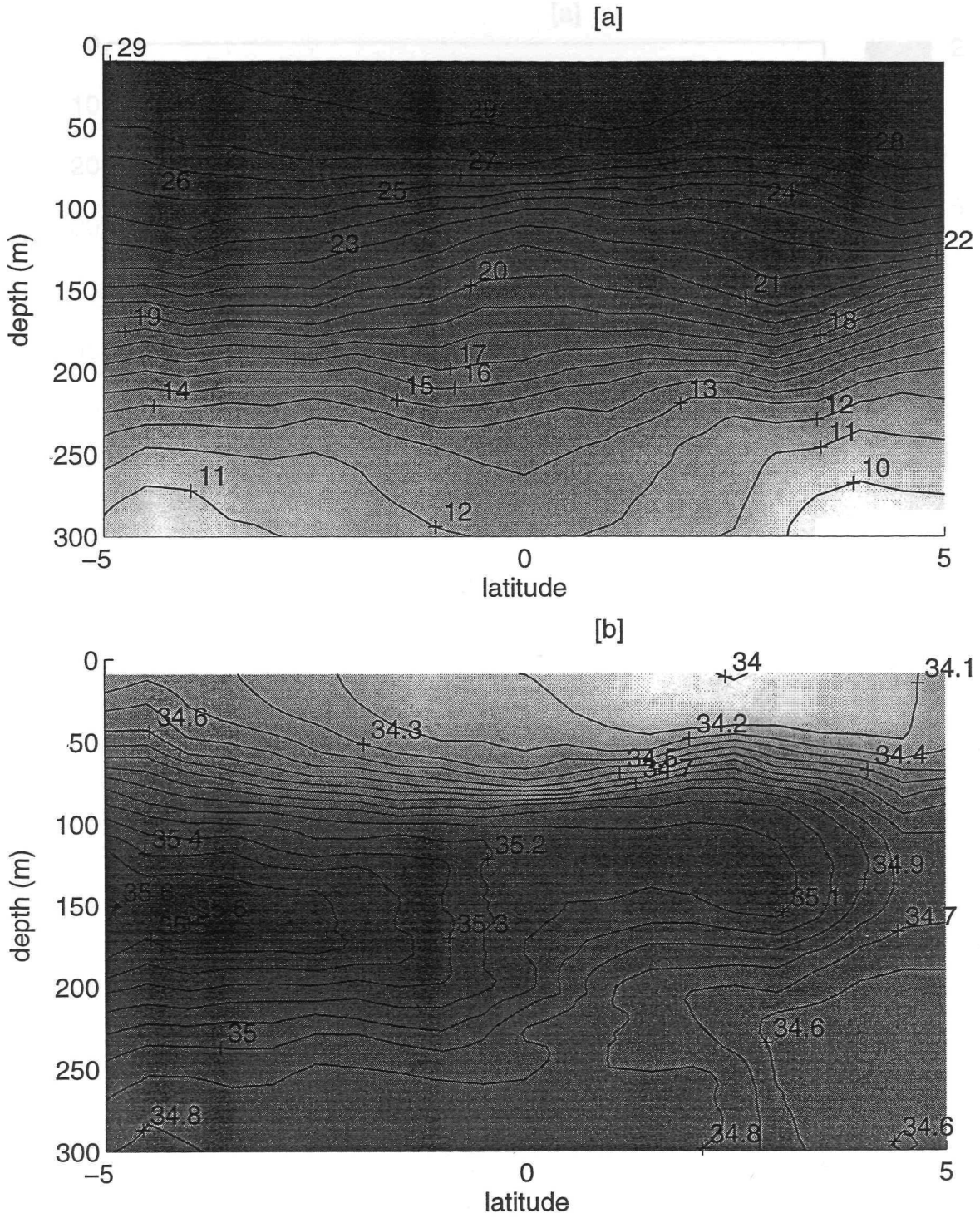

Figure 2.1: [a] Mean temperature (upper panel) and [b] salinity (lower panel) December 1992-February 1993. Contour intervals are 1°C and 0.1 psu.

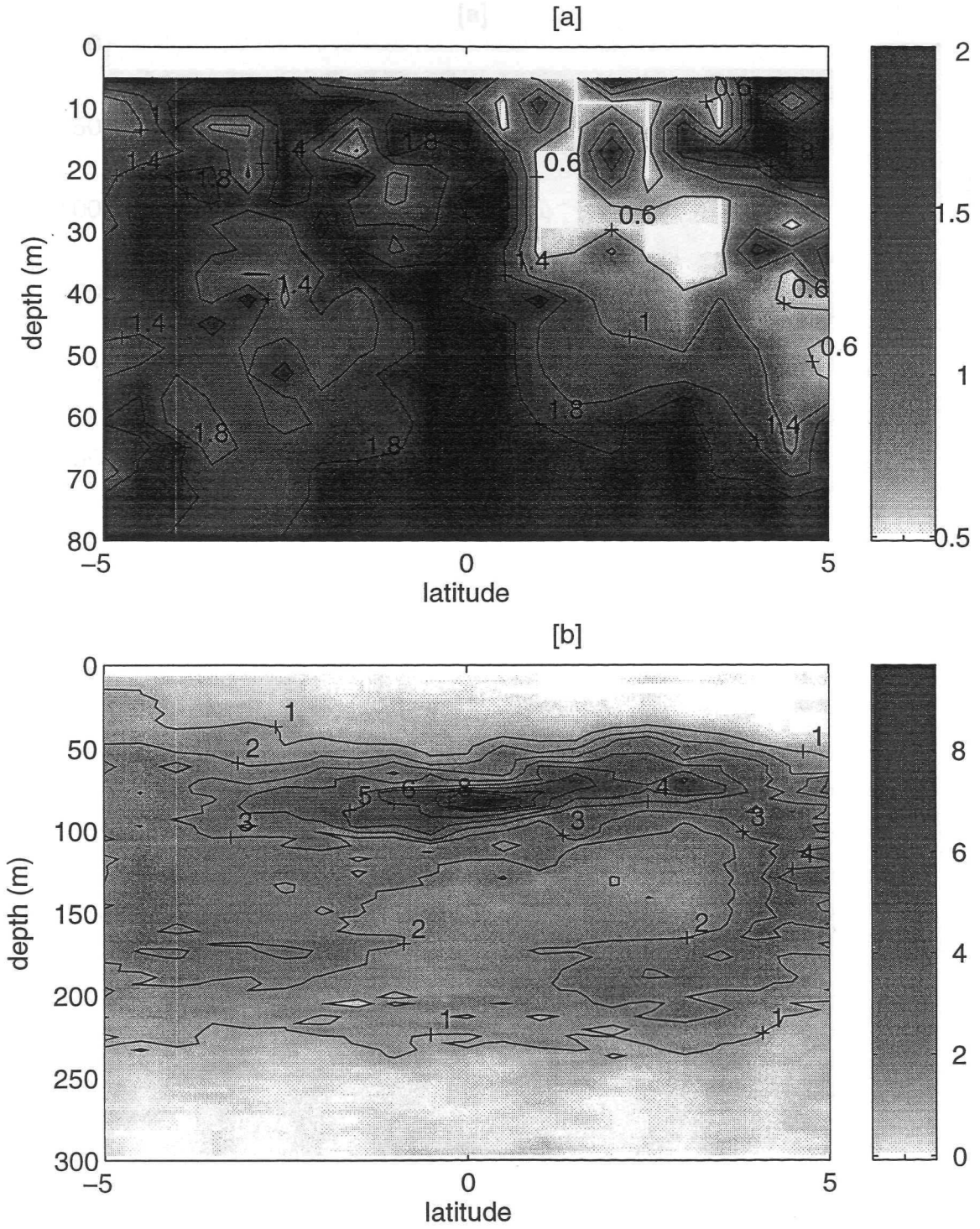

Figure 2.2: [a] Mean R_ρ [a] (upper panel, see text for definition) Contour intervals are 0.4. [b] buoyancy frequency squared (lower panel). Units are 1×10^{-4} s^{-2}, contour intervals are 1×10^{-4} s^{-2}.

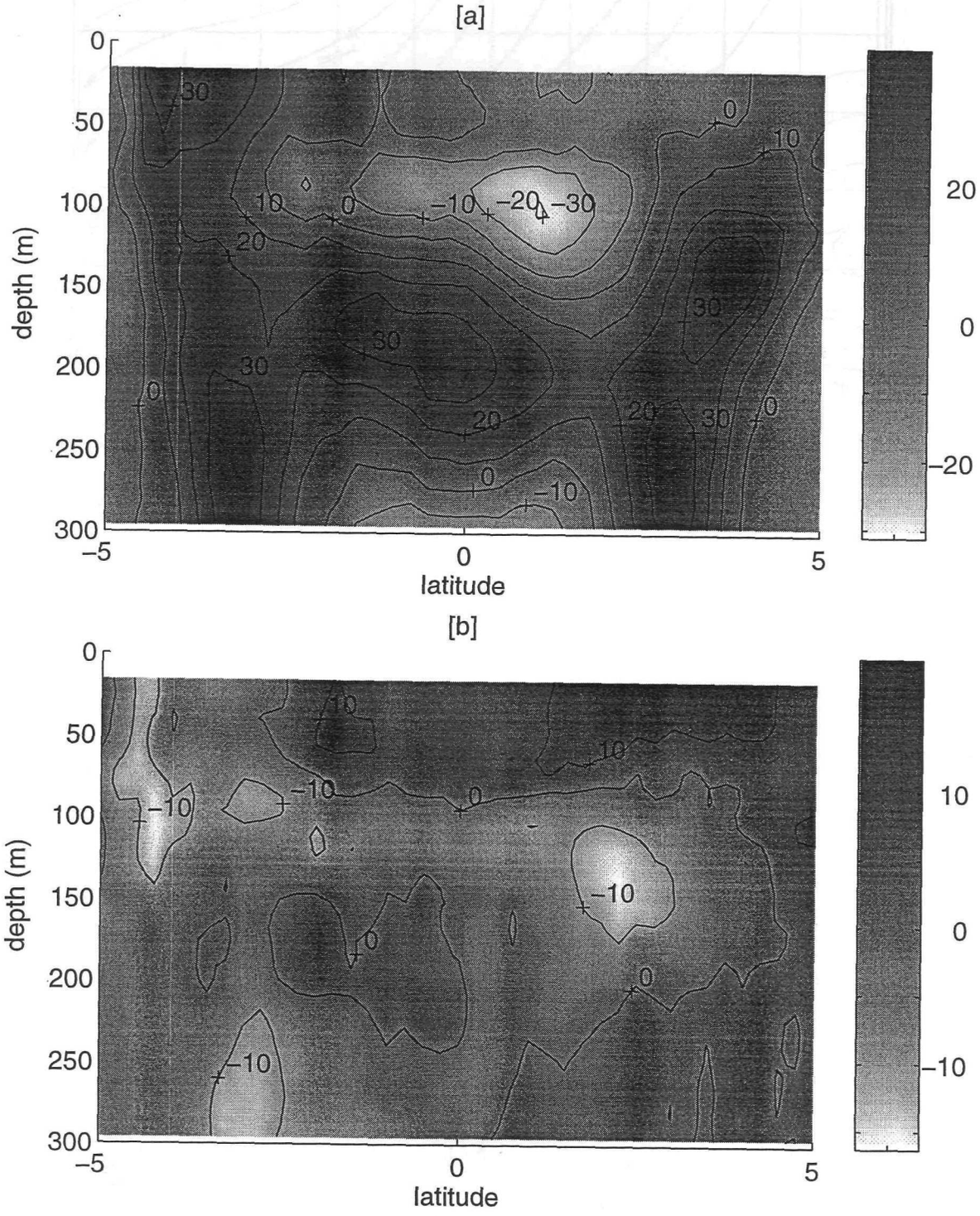

Figure 2.3: [a] Mean zonal velocities (upper panel) and [b] meridional velocities (lower panel) December 1992-February 1993. Contour intervals are 10cm s^{-1} .

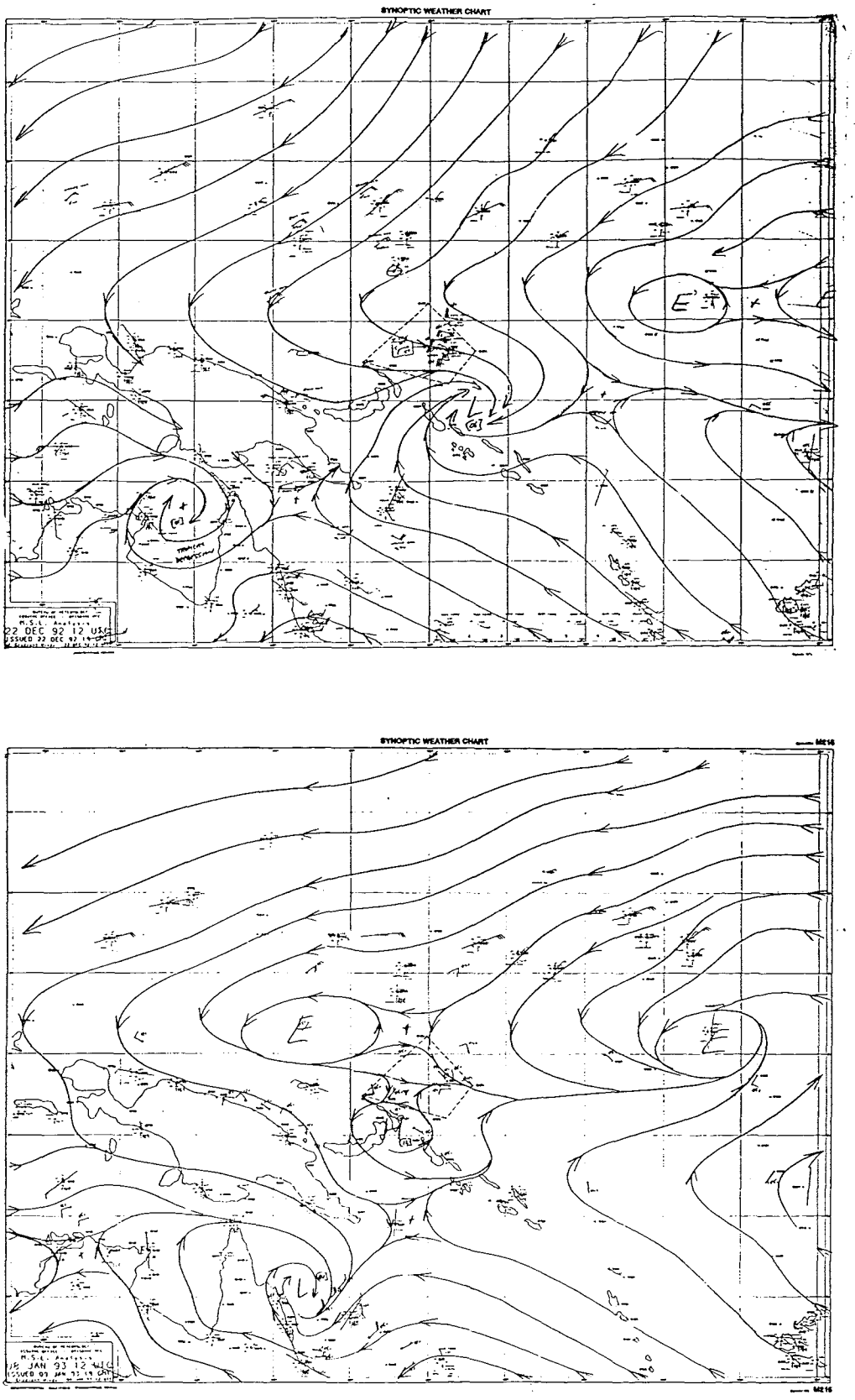

Figure 2.4: Surface wind analysis: [a] 22 December 1992 (upper panel), [b] 8 January 1993 (lower panel). IFA region marked by dashed quadlilateral. Figures taken from TOGA COARE Meteorological Atlas (Bond and Alexander 1994).

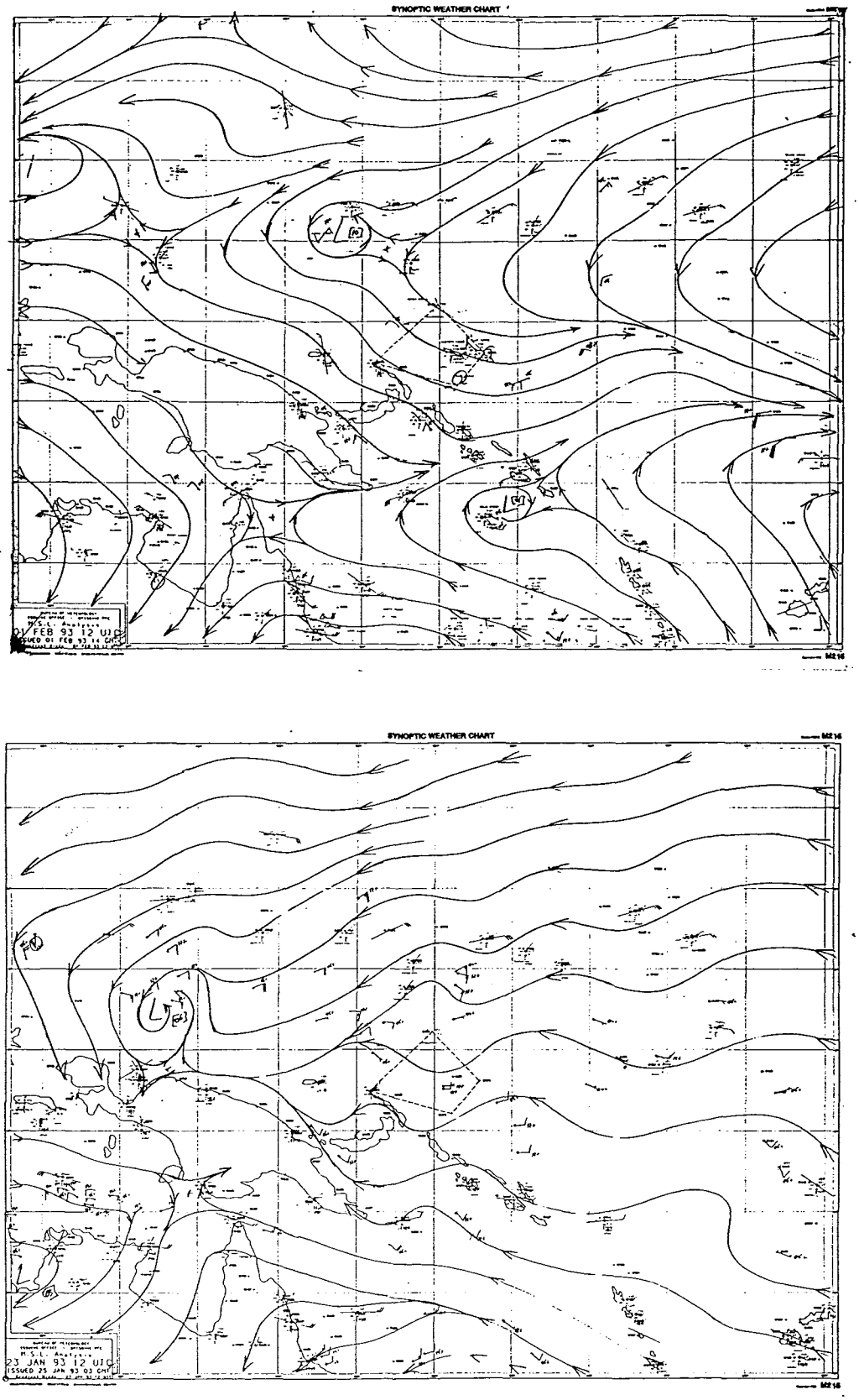

Figure 2.4: Surface wind analysis: [c] 20 January 1993 upper panel), [d] 1 February 1993 (lower panel). IFA region marked by dashed quadlilateral. Figures taken from TOGA COARE Meteorological Atlas (Bond and Alexander 1994).

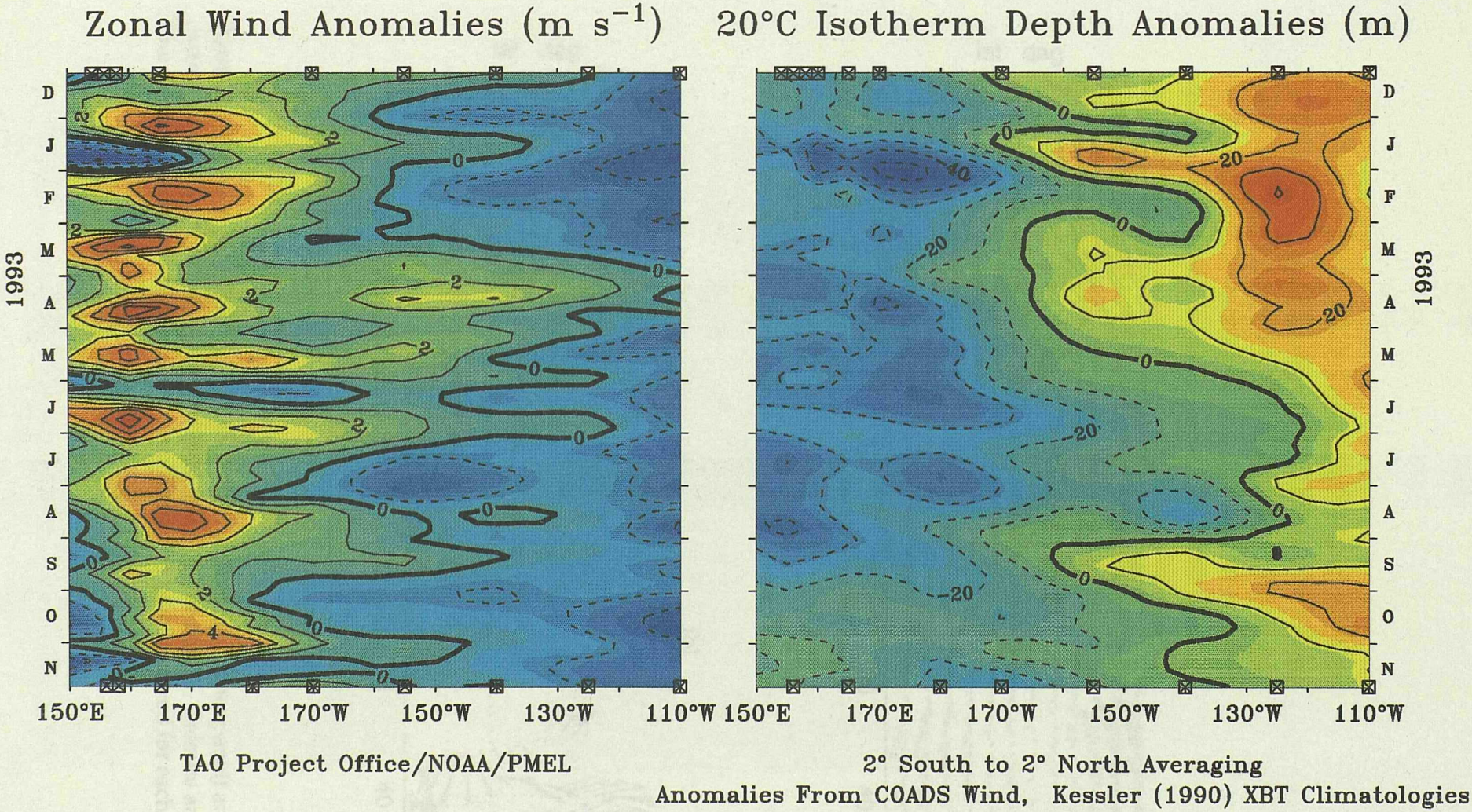

Figure 2.5: [a] Mean zonal wind (left panel) and, [b] 20°C isotherm depth anomalies (right panel) from TAO Array.

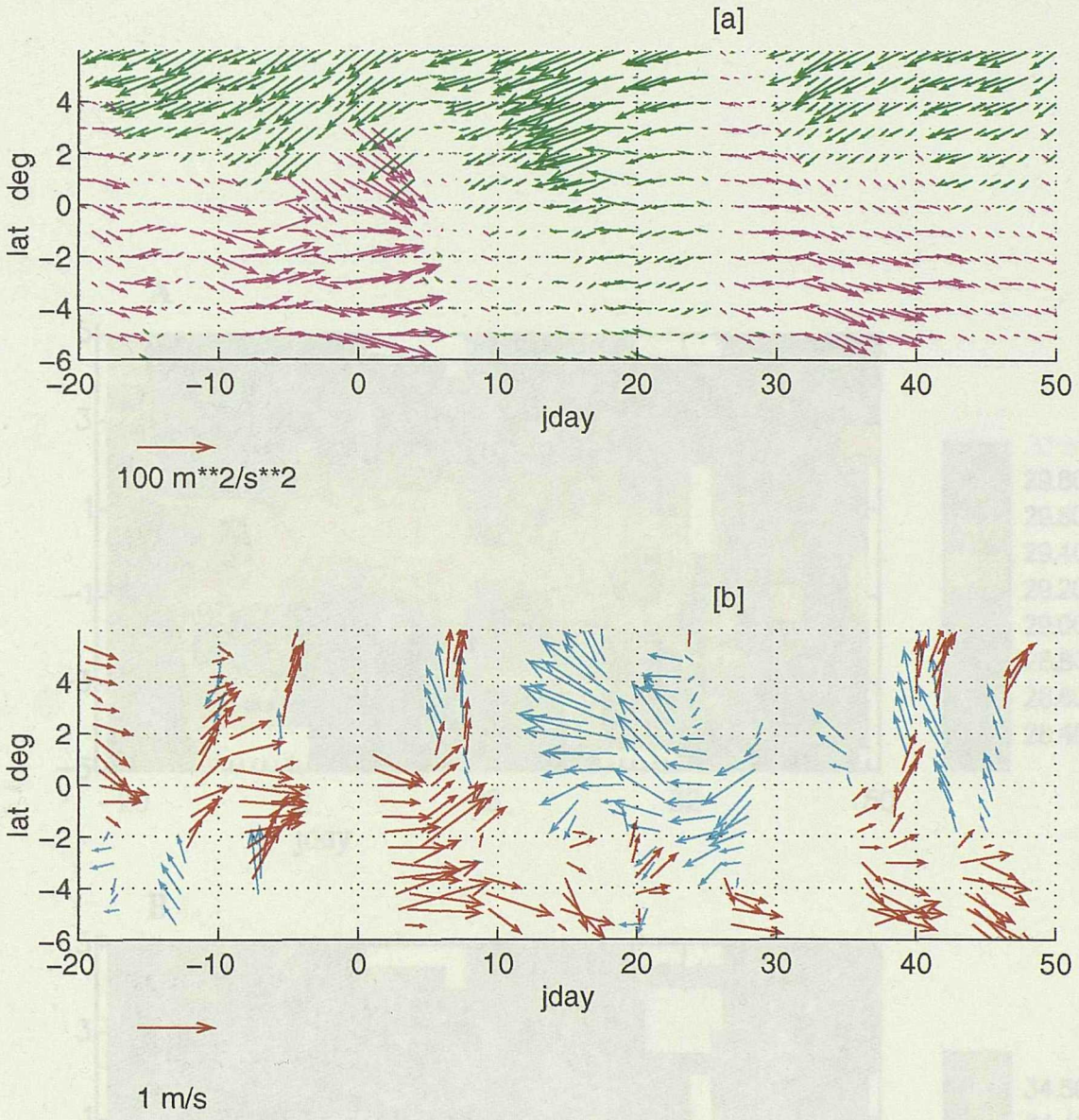

Figure 2.6: [a] Wind pseudo-stress on 156°E from TAO Array (upper panel) and [b] ADCP current velocity vectors averaged from 16 to 56 m (lower panel). Colours are green and blue westward and red and pink eastward. The scale is shown in red for each panel.

Figure 2.7: [a] SST (upper panel) and [b] surface salinity (lower panel). Contour intervals are 0.2°C for temperature and 0.1 psu for salinity.

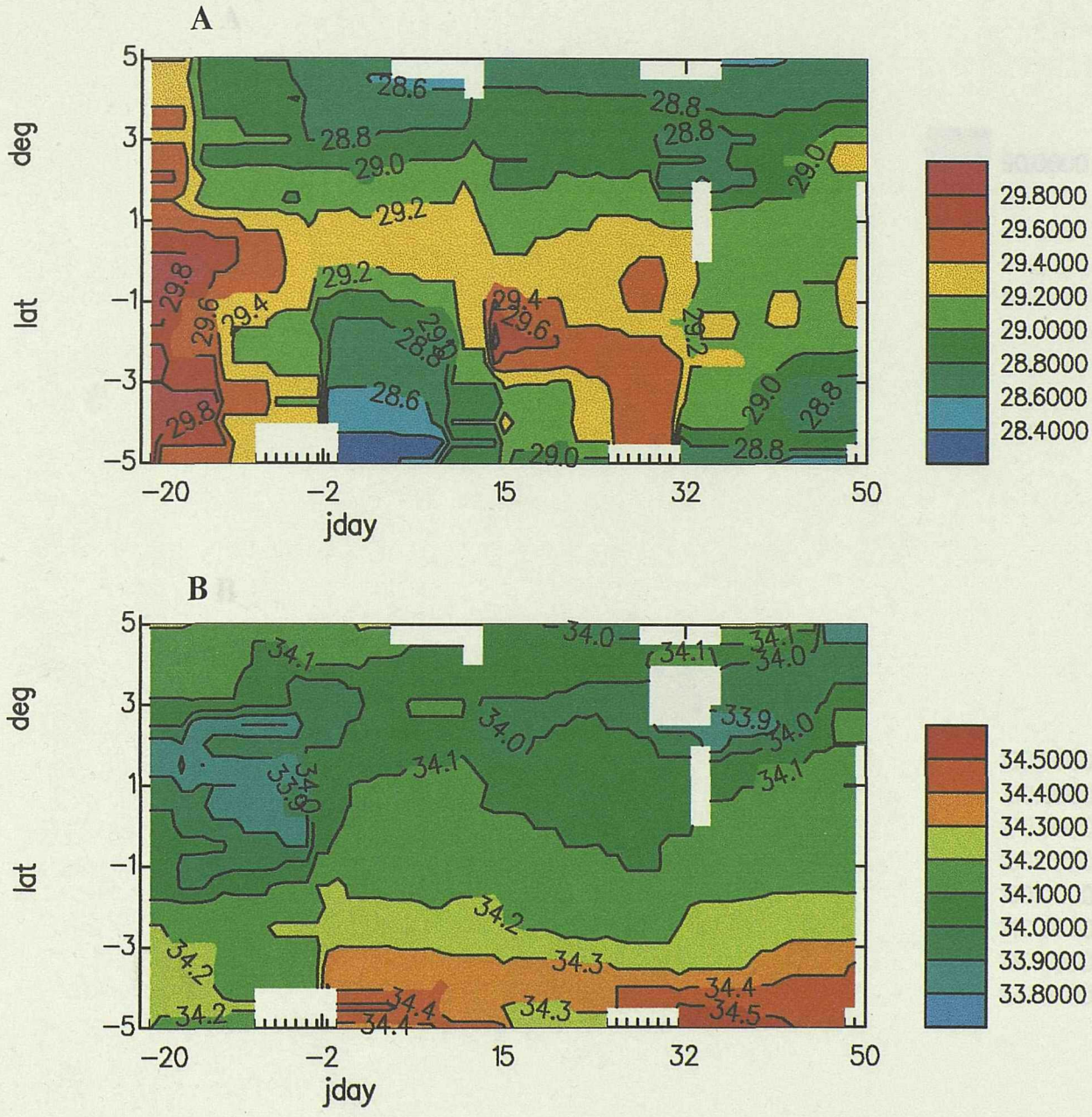

Figure 2.8: [a] mixed layer depth based on temperature gradient criterion (upper panel, see text for details). [b] depth of the 20°isotherm (lower panel). Contour interval is 10 m for both [a] and [b].

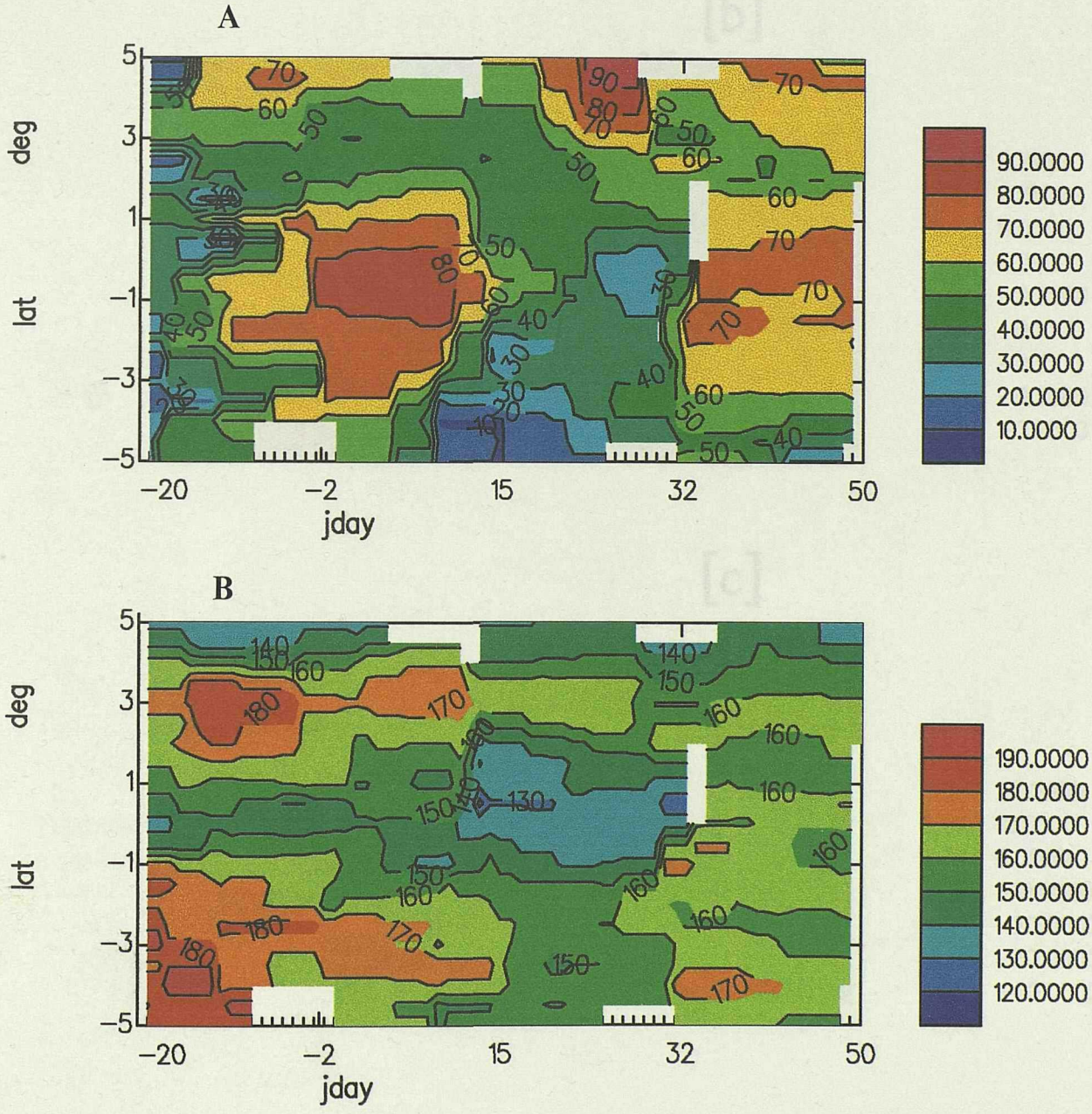

Figure 2.9: [b] zonal surface salinity anomaly, defined in text (upper panel). [c] barrier layer thickness defined as thermocline minus halocline depth (lower panel). Contour intervals are 0.05 psu and 10 m.

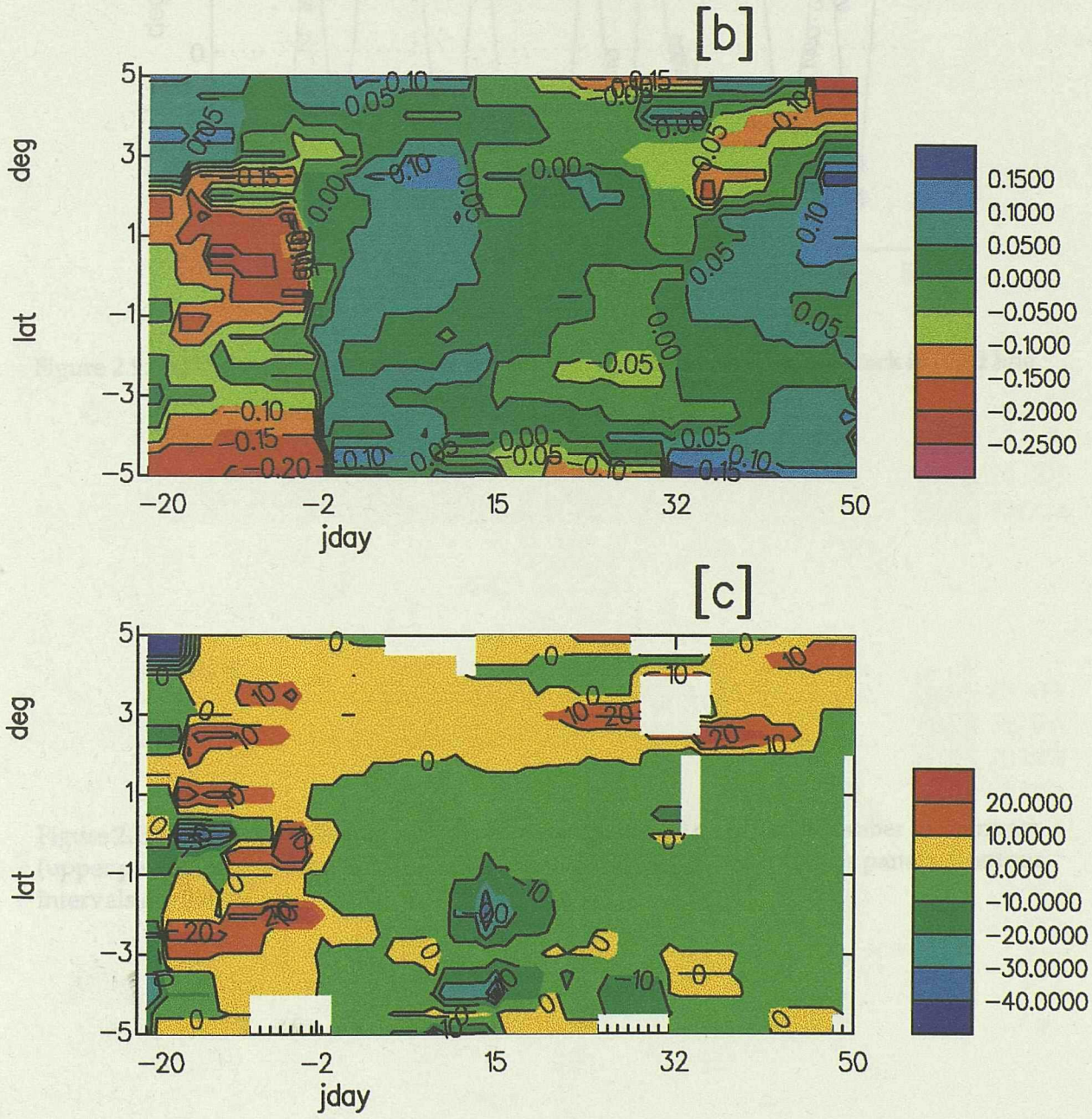

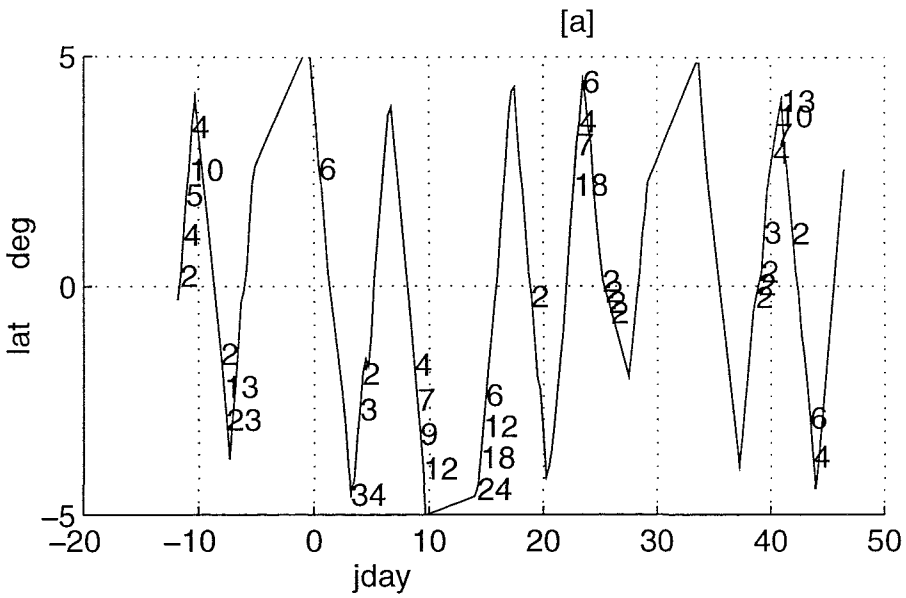

Figure 2.9: [a] Rain rate in mm/hr averaged over 8 hour periods. Cruise track is solid line.

Figure 2.10: (next page) Vertical temperature structure 0-80 m: [a] 31 December to 3 January (upper panel), [b] 6 to 9 January (middle panel), [c] 23 to 27 January (lower panel). Contour intervals are 0.05°C.

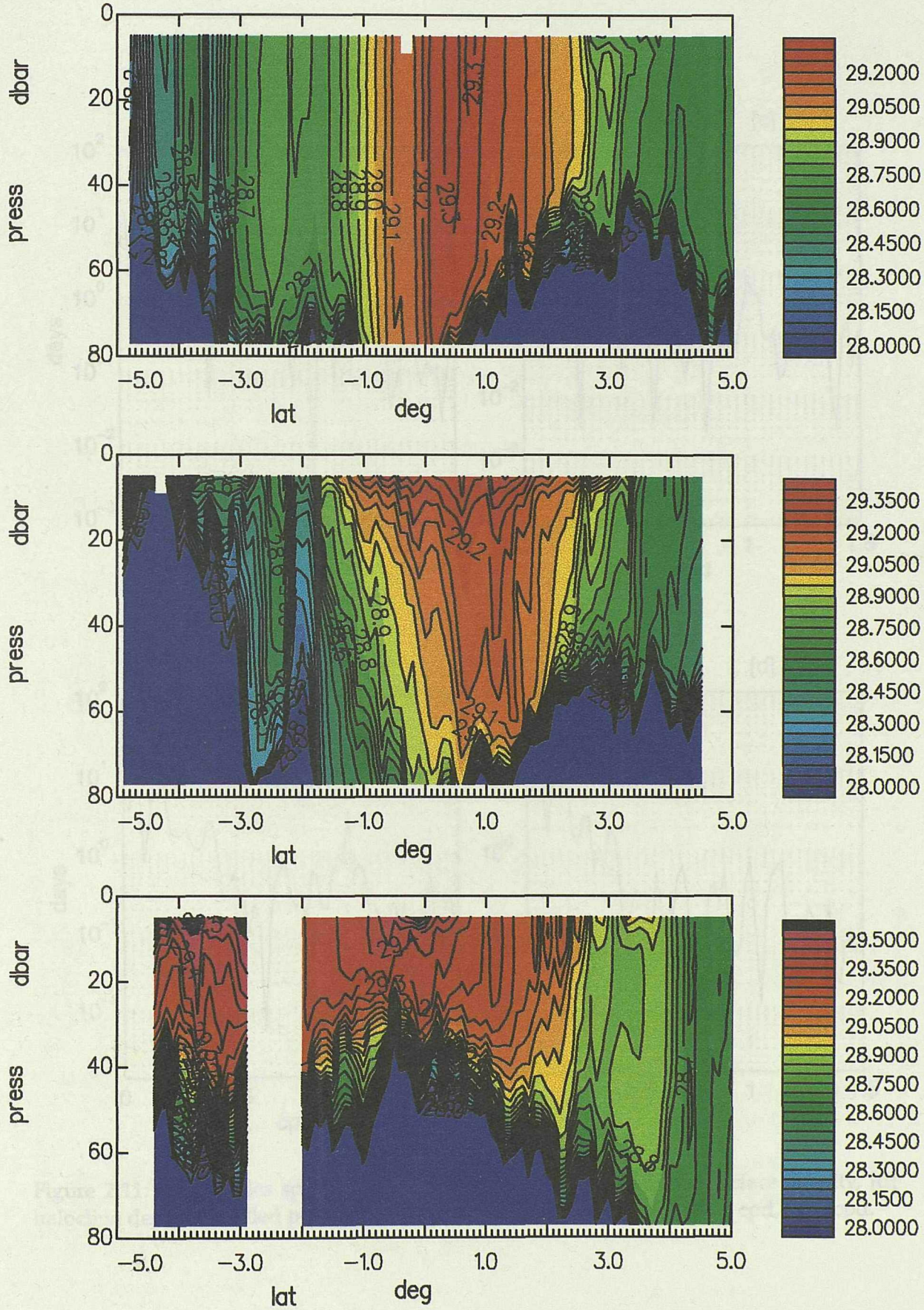
press dbar
0
20
40
60
80
−5.0
−3.0
−1.0
1.0
3.0
5.0
lat deg
29.2000
29.0500
28.9000
28.7500
28.6000
28.4500
28.3000
28.1500
28.0000
press dbar
0
20
40
60
80
−5.0
−3.0
−1.0
1.0
3.0
5.0
lat deg
29.3500
29.2000
29.0500
28.9000
28.7500
28.6000
28.4500
28.3000
28.1500
28.0000
press dbar
0
20
40
60
80
−5.0
−3.0
−1.0
1.0
3.0
5.0
lat deg
29.5000
29.3500
29.2000
29.0500
28.9000
28.7500
28.6000
28.4500
28.3000
28.1500
28.0000

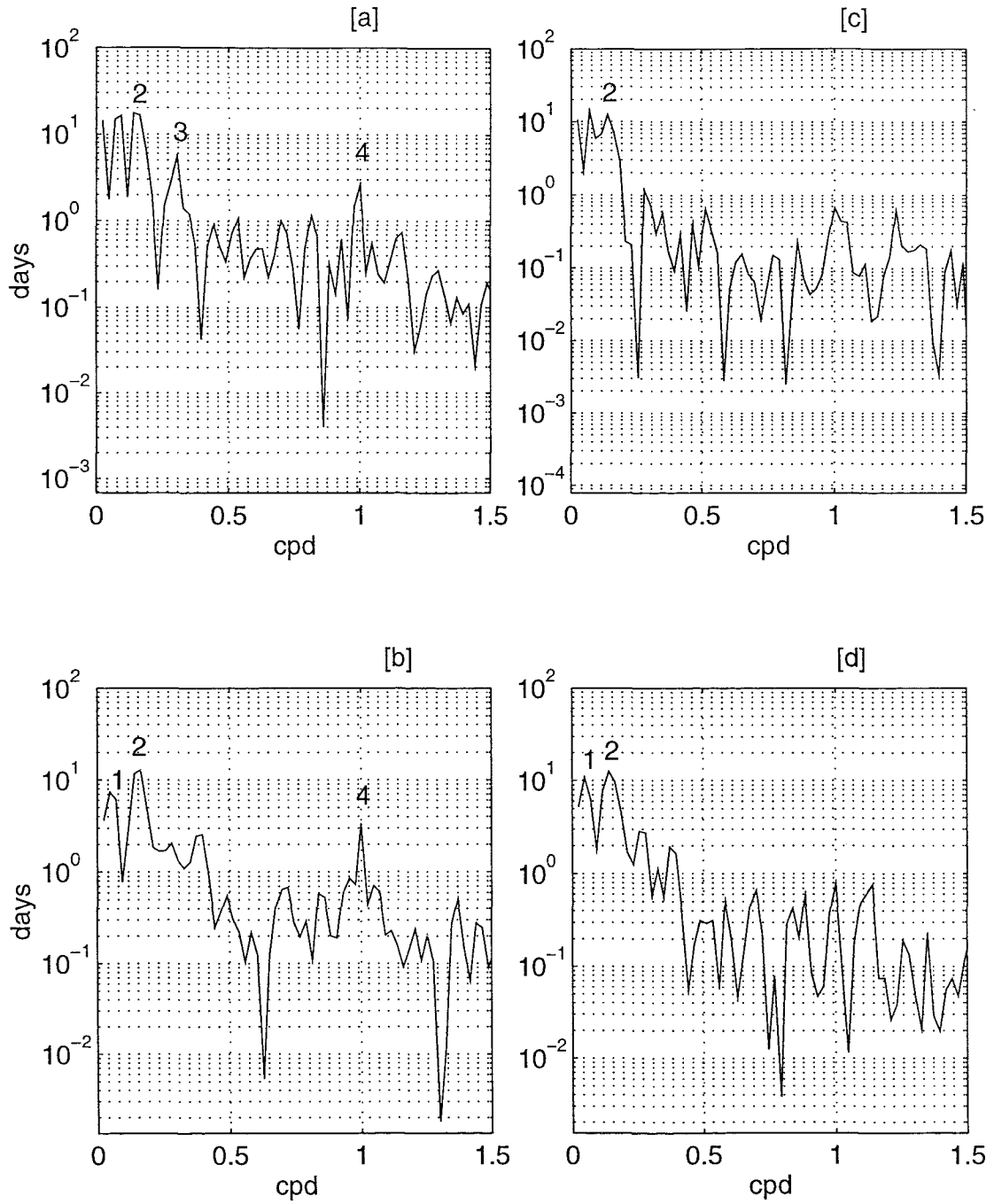

Figure 2.11: Time series spectra: [a] SST, [b] thermocline depth, [c] surface salinity, [d] halocline depth. Labelled peaks are; [1] 1/20 cpd, [2] 1/6.8 cpd, [3] 1/3.4 cpd, [4] 1 cpd.

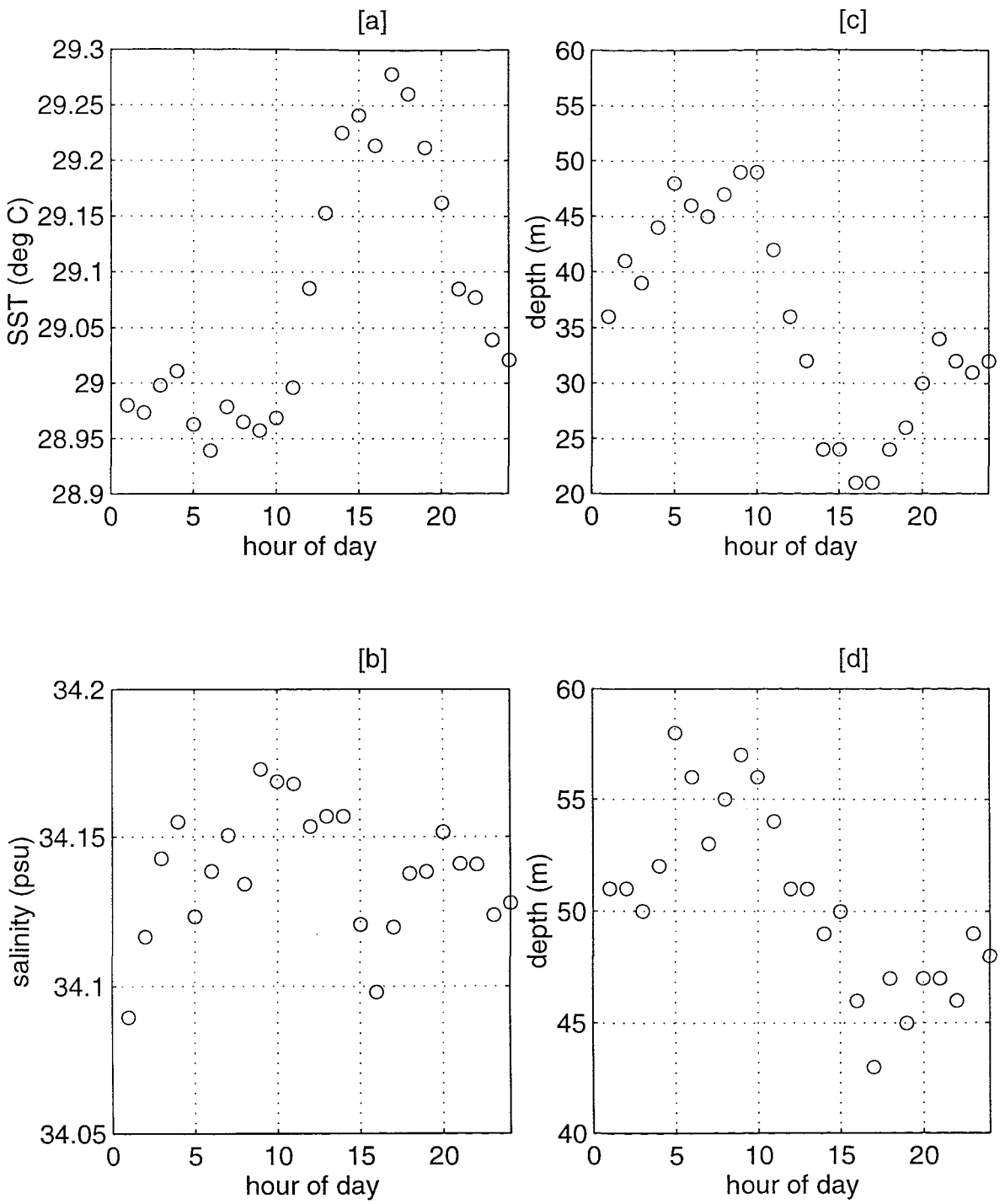

Figure 2.12: Mixed layer properties averaged by hour of day. [a] SST, [b] sea surface salinity, [c] thermocline depth, [d] halocline depth. Mixed layer depth estimates are based on gradient criteria, see text for definitions.

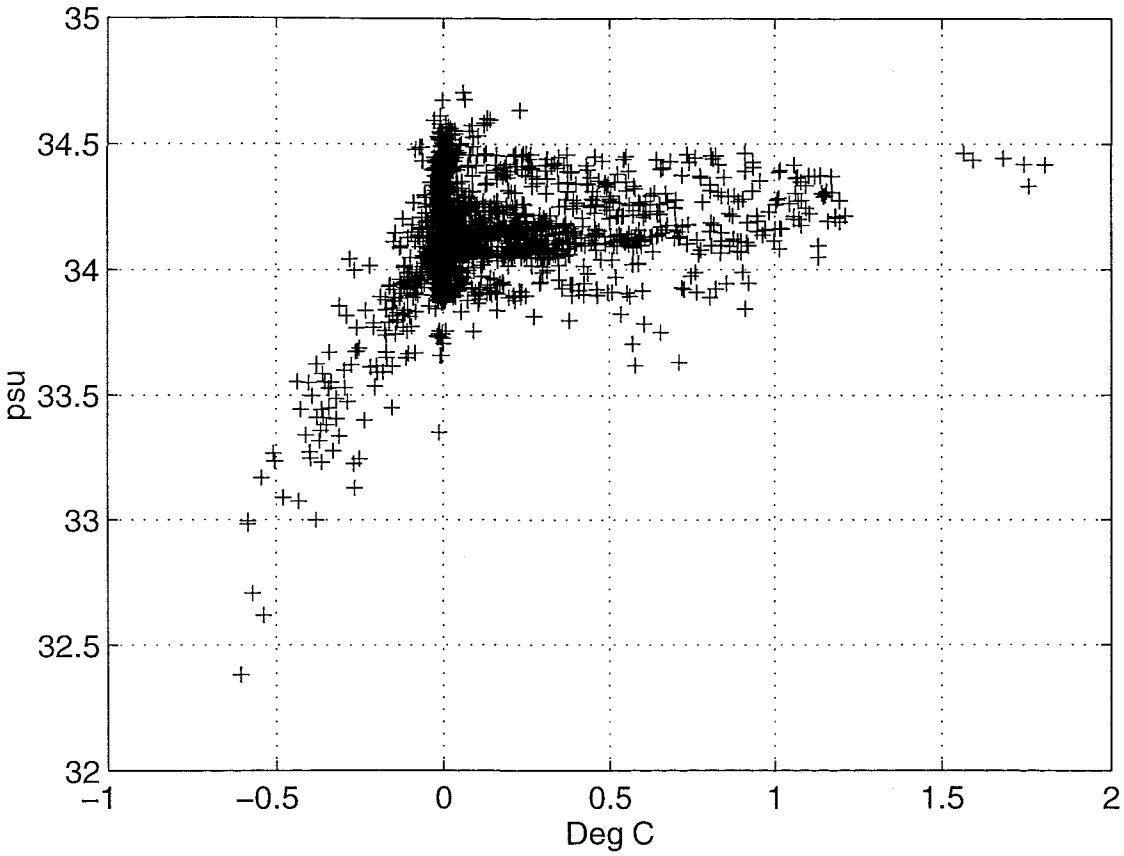

Figure 2.13: Scatter plot of surface (1 m) salinity and T(11 m)-T(1 m). 25% of observations have $\Delta T \geq 0.1$°C, 6% have $\Delta T \leq 0.1$°C.

Figure 2.14: [a] Temperature upper panel) and [b] Salinity (lower panel) of upper 30 m during rain event. Contour intervals are 0.1°C and 0.1 psu. The horizontal scale is distance in km. The section runs from 20:00 to 08:00 local solar time, a period of 13 hours.

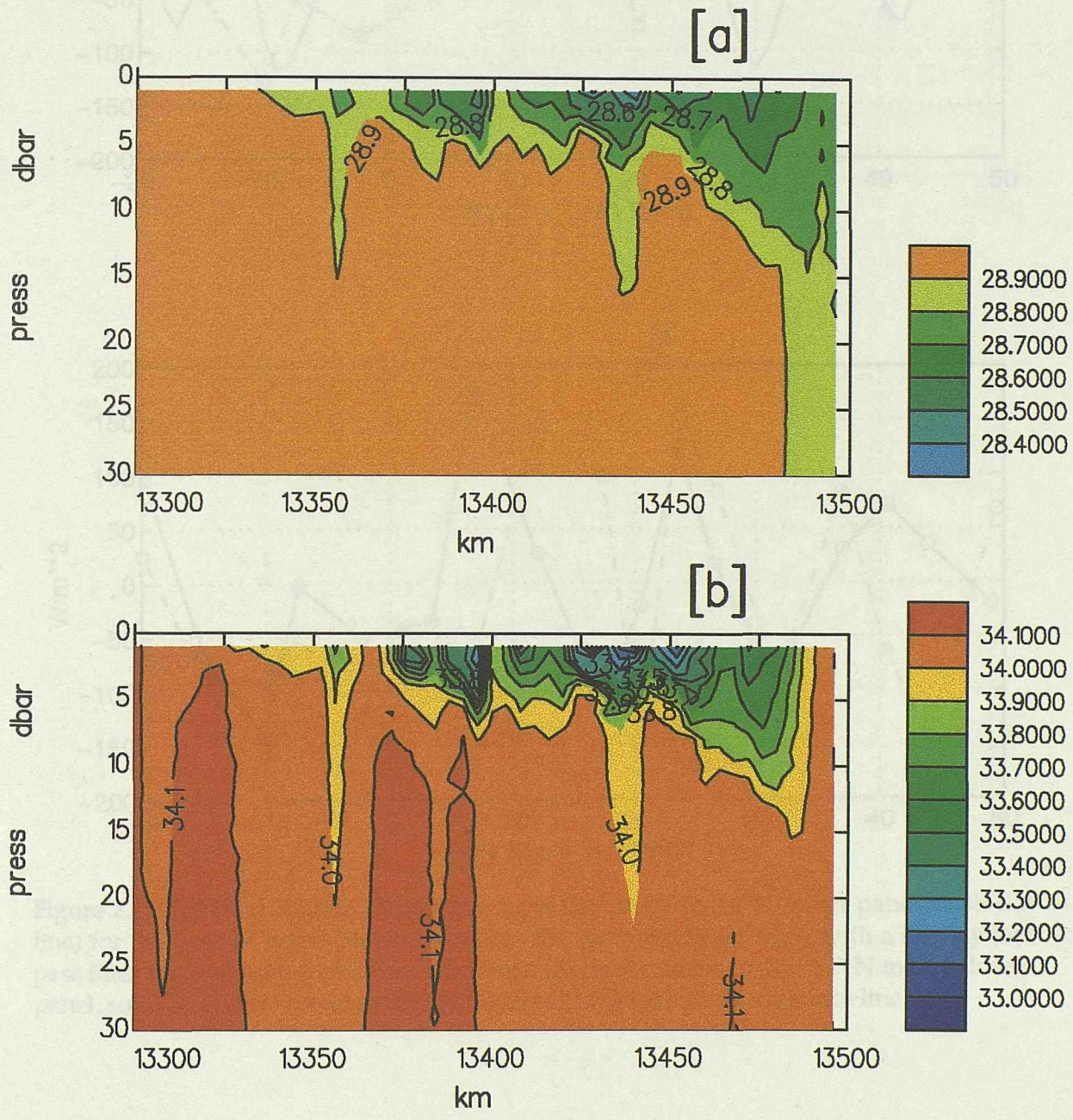

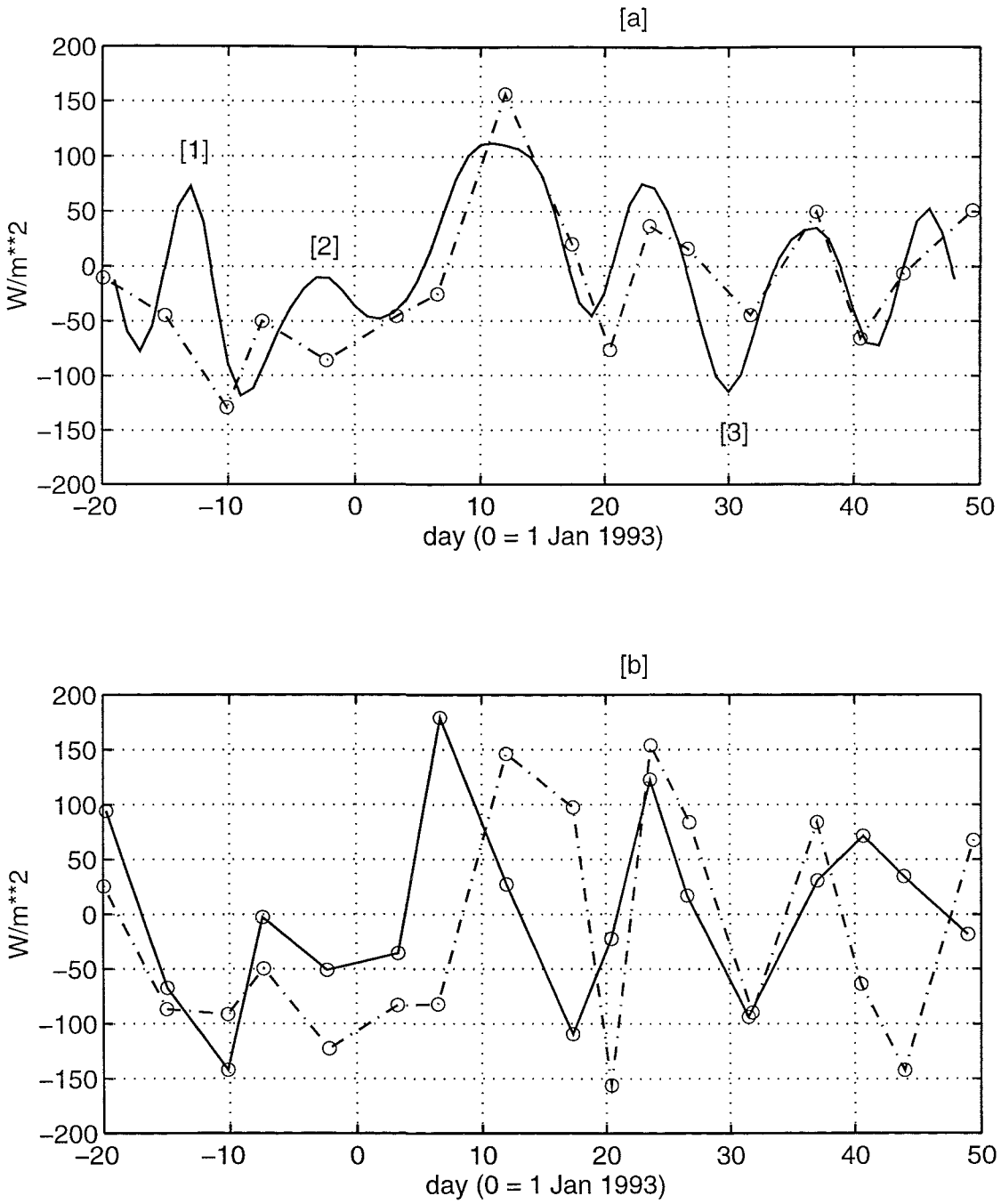

Figure 2.15: [a] Heat content change averaged from 0.4°S to 3.6°S (upper panel, dash-dot line) for the 0–40 m layer. Net surface heat flux from the IMET Buoy with a six day low pass filter applied (upper panel, solid curve). [b] Heat content change 1.7°N to 5°N (lower panel, solid line). Heat content change 1.7°S to 5°S (lower panel, dash-dot line).

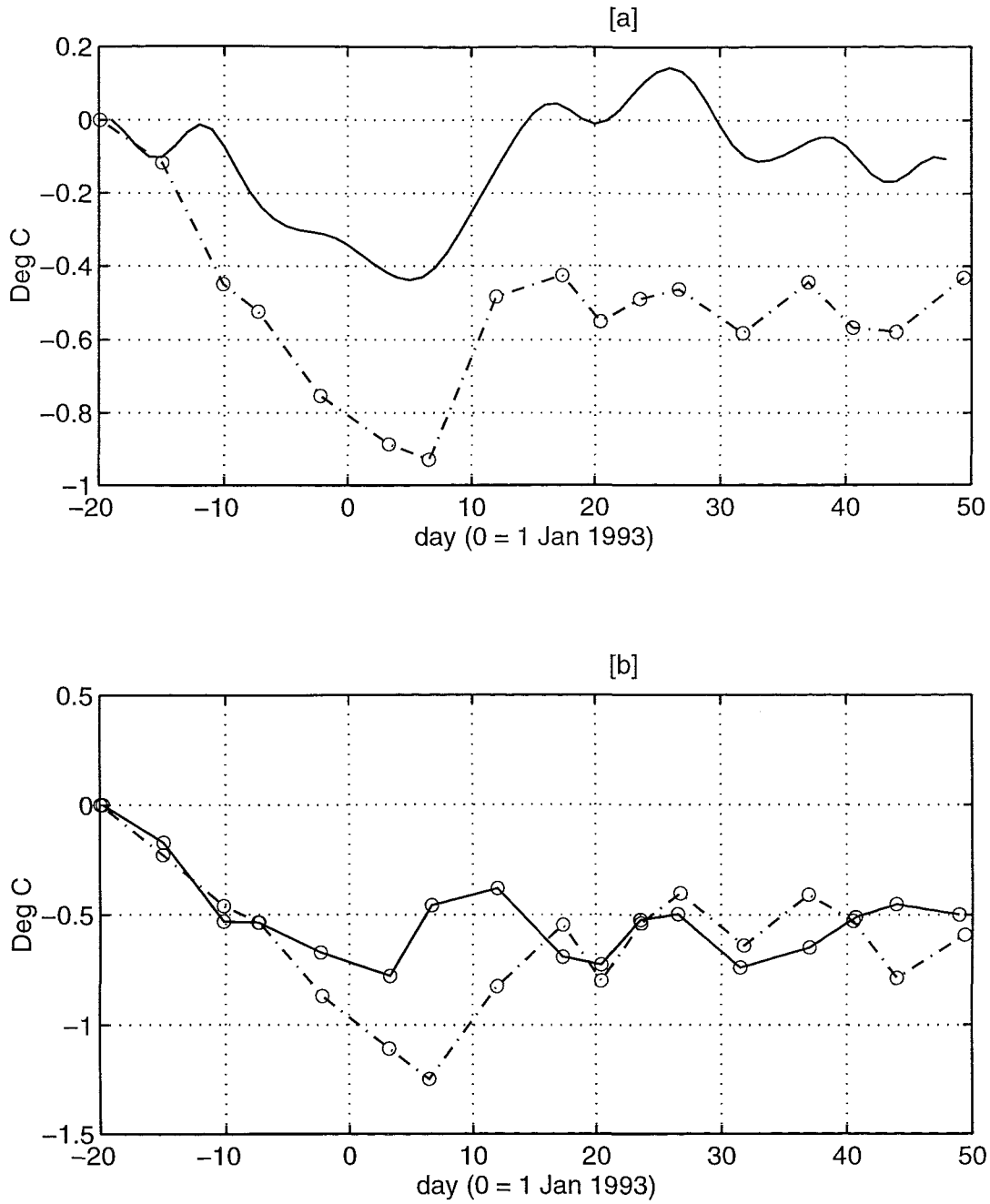

Figure 2.16: [a] Average temperature change 0–40 m averaged from 0.4°S to 3.6°S (upper panel, dash-dot line). Time integral (divided by $(C_p \times \rho \times 40$ m) of IMET net heat flux at 2°S (upper panel, solid line). [b] Average temperature change 1.7°N to 5°N (lower panel, solid line) and 1.7°S to 5°S (lower panel, dash-dot line).

Chapter 3

Heat and Salt Budget of CD32

Chapter 2 described changes in the upper ocean structure on a horizontal scale of 10°of latitude and time scales of days to weeks during the El Niño conditions which persisted into 1993. It was shown that under these conditions and at that longitude, 156°E, the heat budget of the area is predominantly one dimensional, with notable exceptions of duration 5 to 10 days. The salt budget did not show a one dimensional balance, which was attributed to the small scale (O(km)) heterogeneity in the surface salinity field due to precipitation.

In this chapter analysis of a "mini-COARE" experiment which took place during the 1988 La Niña and at 165°E is presented. The experimental strategy was such as to allow estimates of net surface heat flux, horizontal advection and turbulent mixing to be made. The confinement of the experiment to within 80 km of the equator allows for a less spatially disrupted description of the diurnal cycle of heat in the upper ocean to be made. Recall that the statistical approach used in describing the diurnal cycle in the previous chapter was taken of necessity since the ship travelled 3.5°of latitude in 24 hours.

The variable "time" in this chapter is in UT (formerly GMT), except where local solar time is indicated.

The work presented in this chapter has been accepted for publication in the Journal of Geophysical Research (Richards et al. 1995). Work of those other than the author is presented briefly when essential and acknowledged.

3.1 Upper Ocean Structure

The experimental design was similar to that of Pollard and Thomas (1989). An instrumented spar buoy was deployed from Julian day (jday) 106 to 115. Two vector averaging current meters (VACMs) were set at 15 m and 50 m depth. The position of the spar buoy was fixed

every 12 hours as the ship passed close by. The motion was predominantly north/south with little east/west movement. The average speed of the spar buoy was 2.6 cms^{-1} with instantaneous values of up to 10 cms^{-1}.

During the deployment the ship surveyed around the buoy. The ship's track during this survey is shown in Figure 3.1. The survey pattern consisted of a double figure of eight centred on the buoy, producing a large box of side 80 km and 4 sub-boxes of side 40 km. At 8 knots it took 12 hours to complete each sub-box and 2 days to complete the whole pattern. The pattern was repeated 3 times. Satellite navigation was available for approximately 8 hours per day. The timing of the survey was chosen so that the period of satellite coverage coincided with the north/south sections through the centre of the box.

As with the COARE IOP experiment, the principal means of measurement was a combination of Seasoar and ADCP. Both CTD and ADCP data were gridded onto 4 m depth intervals with a 4 km horizontal spacing. Details of calibration techniques can be found in the cruise report (Richards et al. 1988).

The cruise took place during La Niña conditions which followed the 1986/87 El Niño event (the SOI was positive for the period February 1988 to November 1989, reaching a maximum in November 1988, see Figure 1.2). The meridional structure of temperature, salinity and zonal current are very similar to the average conditions reported by Sprintall and McPhaden (1994) for the period November 1988 to November 1989 as described in Richards and Pollard (1991).

Typical vertical profiles of the horizontal components of velocity, U, V, temperature, T, and salinity, S, are shown in Figures 3.2 [a] to [d]. The profiles were taken on day 108.0, close to the beginning of the survey, at 11:00 local solar time. A strong undercurrent centred around 175 m is present. The westward flowing surface current is the South Equatorial Current (SEC) the core of which was at approximately 2°S. There is a significant north/south component to the flow which varies with depth.

The horizontal structures of the currents averaged from 0 to 50 m are shown in Figure 3.3 and Figure 3.4 for jday 107.5–108.5 and 113.5–114.5. The current changed from a predominantly NW direction to a SW direction over this time. There are significant spatial variations in the current over the survey area.

The temperature profile in Figure 3.2 shows the main thermocline beginning at approximately 120 m depth with a large gradient in temperature. Below this depth there is layering in both temperature and salinity caused by the interleaving of water masses, as reported by

Richards and Pollard (1991). Above 120 m the temperature gradient is much reduced but still with structure. The structure in salinity above 140 m, Figure 3.2, is more pronounced than that of temperature with a strong halocline at approximately 40 m depth. Fresh water surface layers with salinity values down to 34 psu were observed both north and south of the equator (Richards and Pollard 1991). Close to the equator, however, in the vicinity of the survey, the surface waters were relatively saline. The increased surface salinity (relative to values north and south) is suggestive of upwelling occurring at the equator (consistent with an easterly wind stress, (Sprintall and McPhaden 1994)). The salinity structure above 120 m is due primarily to a tongue of high salinity connected to the southern hemisphere subtropical salinity maximum water (SSMW). This tongue is shown for CD32 in the colour picture of Richards and Pollard (1991). This apparently permanent feature of the WEP has already been shown for the TOGA COARE period in Figure 2.1[b]. It is found that salinity gradients close to the surface play an important role in limiting the depth to which surface mixing penetrates. This is investigated in Section 5.1.

The temperature field in the upper 120 m on 6 of the north/south sections of the survey is shown in Figure 3.5. The sections were taken at daily intervals with the ship crossing the equator at approximately midday, local time. The structure is seen to change significantly over the survey period. At the beginning of the survey there is a marked temperature gradient at approximately 50 m with less stratified waters above and below. This region will be called the intermediate thermocline; the main thermocline begins at around 120 m. The intermediate thermocline weakens with time, with isotherms moving upwards and downwards, above and below the thermocline, respectively. A lens of almost homogeneous temperature water, 50 m thick, emerges from the north, centred around 70 m depth.

The salinity field is shown in Figure 3.6. Again large changes to the structure occur. At the beginning of the survey the surface waters are relatively fresh. The tongue of high salinity water can be seen centred around 80 m depth. There appears to be a northward displacement of the surface fresh water with time, leaving behind a sub-surface minimum in salinity. Towards the end of the survey the variation in salinity is much reduced with the maximum in salinity now occurring at the surface. The lens emerging from the north is somewhat fresher than the surrounding water.

It is clear that horizontal advection is playing a large role in the changes to both the heat and salt content of the upper ocean and therefore needs to taken into account in heat budget calculations.

3.2 Surface Fluxes

Surface heat fluxes were determined from ship-borne meteorological observations during the duration of the cruise (22 days in all). The meteorological observations were obtained from a suite of sensors on the forward mast of the ship which were controlled and integrated using the Multi-met system developed by Birch et al. (1992). Heat flux calculations were carried out by N.C. Wells. Details of the sensors together with their positioning and accuracies are given in Table 1 of Richards et al. (1995).

The SST was taken from the thermosalinograph (TSG) of a non–toxic water supply from 4 m. This record was calibrated against the calibrated Seasoar temperature at times when the upper 5 m were well mixed. The calibration drifted by less than two hundredths of a degree over the whole cruise. During three periods on days 107, 108 and 109 when the TSG malfunctioned, a linear interpolation was used to estimate the SST. These periods are seen as the straight line sections on days 107, 108 and 109 in Figure 3.11. Comparison with the 5 m seasoar temperature shows that the errors associated with this procedure are less than 0.2°C.

The components of the heat and water vapour fluxes were obtained from the bulk aerodynamic formulation using the coefficients determined by Large and Pond (1981). Hourly averaged heat fluxes for the period of the spar deployment are shown in Figure 3.7. The average over the whole 22 days and the duration of the spar deployment are given in Tables 3.2 and 3.2, respectively. Rainfall was measured at 3 hourly intervals with Champagne rain gauges. The total rainfall over the 22 day period was 0.27 m, which is in accord with the climatology of Dorman and Bourke (1979). The heat flux due to precipitation during this period was estimated to be approximately 4W m^{-2} by assuming a rain temperature equal to the wet bulb temperature. During the 7 day spar buoy deployment, the average rainfall rate was somewhat lower being only 4% of that over the whole period of the cruise (22 days).

The error in each flux has been estimated by considering the accuracy of the instruments and the inherent accuracy of the transfer coefficients used. A large source of error comes from the estimation of the latent heat flux. This error is due to uncertainties in the difference in mixing ratio between the sea surface and 10 m height, and in the value of the transfer coefficients. The error in the mixing ratio difference was estimated from the difference between the measurements taken on the forward mast and on the bridge, whilst the error

Flux	Average, 22 days (Wm^{-2})	Error (Wm^{-2})
Short wave $Q_s(1-\alpha)$	-197	$\pm$ 2
Sensible heat Q_H	+12	$\pm$ 1
Latent heat Q_L	+155	$\pm$ 17
Net long wave Q_{LW}	+19	$\pm$ 20
Net heat Q_T	-11	$\pm$ 27

Table 3.1: Average heat fluxes and estimated errors over whole cruise (22 days).

Flux	Average, spar (Wm^{-2})	Error (Wm^{-2})
Short wave $Q_s(1-\alpha)$	-240	$\pm$ 2
Sensible heat Q_H	+9	$\pm$ 1
Latent heat Q_L	+144	$\pm$ 17
Net long wave Q_{LW}	+22	$\pm$ 20
Net heat Q_T	-65	$\pm$ 27

Table 3.2: Average heat fluxes and estimated errors over the period of the spar buoy deployment (7 days).

in the value of the transfer coefficient was taken from Smith (1989).

The surface wind stress for the survey period as estimated using the drag coefficient method (Large and Pond 1981) is shown in Figure 3.8. The data have been smoothed with a three hour running mean. The surface stress is dominated by a number of high frequency gusts. The amplitude and phase of the gusts are comparable with recent observations (Bradley et al. 1993), and are probably associated with diurnal convective events in the lower atmosphere. During days 112 and 113 the amplitude of the gusts is reduced. The dashed line on the windstress figure (Figure 3.8) corresponds to a wind speed of 3 ms^{-1}. The wind speed was greater than 3 ms^{-1} for more than 95% of the observations during the spar buoy deployment. Inaccuracies associated with low wind speed determination of latent heat fluxes are therefore not of concern here.

Another large source of error is in the net long wave radiation. The estimate given is based on an instrument error of 5% of the downward longwave radiation. This brings the comparatively low net longwave radiation estimate of 19 W m^{-2} in line with other such estimates in the western equatorial Pacific (Godfrey et al. 1991).

The principal components of the heat flux are the solar radiation and latent heat fluxes.

Both sensible heat and longwave radiation have, as expected, lower magnitudes and the longwave radiation shows less variability than other components. The solar radiation shows considerable variability between the two averaging periods.

The net heat flux into the ocean over the 22 day period is not significantly different from zero. Though the period is short compared with climatological estimates it is indicative that the heat fluxes have a tendency to balance in this region of the equatorial Pacific Ocean. This agrees with the hypothesis that the net heating in the region is as low as 10 W m^{-2} (Godfrey et al. 1991).

The ship was located on the equator during the spar buoy deployment for 7 days when the heat flux into the ocean of 65 W m^{-2} was significant. This result indicates that the temporal and spatial variability of heat fluxes in the western equatorial Pacific is considerable. Both the period and spatial distribution of sampling programmes to estimate fluxes have to be chosen with some care. The large variability in the net heat flux has already been seen in the TOGA COARE data set. If one assumes the net heat flux measurements to be independent on a time scale of a day, the standard error is still greater than the mean for the 70 day record, illustrating the great difficulty in specifying by direct measurement the long term mean net surface heat flux for the region.

3.3 Diurnal Mixed Layer

Figure 3.9 shows the temperature at the spar buoy at 15 m. For the first three days of the 15 m record a clear diurnal signal of amplitude 0.15°C can be seen. This is followed by a period of cooling of around three tenths of a degree from jday 111.8 to 113.8, with a subsequent general warming and return of the diurnal signal over the last day and a half of the record. The 50 m temperature record (not shown) exhibits none of these features but is dominated by high frequency, large amplitude variability (of order two tenths of a degree) associated with internal wave and tidal activity in this stratified shear zone. The implication is that nighttime convection penetrates to a depth greater than 15 m but less than 50 m.

A useful comparison can be made between the 15 m temperature from the spar and the 15 m temperature signal extracted from the Seasoar record, shown in Figure 3.9. The Seasoar track passed the spar buoy every 12 hours. The whole day number crossings were from north to south at midday whilst the half day number crossings were at midnight

alternately east to west and west to east. It can be seen that the spatial variability over the 80 km box is of the same order of magnitude as the diurnal variation at this depth. The same trends are evident: a diurnal signal during days 107 to 111, a strong cooling during the west to east passage on day 112.5, and a general warming from 113.5 onwards. The sudden increase and decrease in temperature of 0.6°C at day 114.2 is when the ship steamed into a patch of warm water at the southern extent of the survey (this warmer patch is also evident in the temperature record of the thermosalinograph, Figure 3.11). The Seasoar temperature record from 50 m (not shown) also exhibits spatial variability of the same order of magnitude as the variability at the spar buoy.

As a measure of the depth to which the surface forcing penetrates, the Seasoar time series is used to determine a mixed layer depth. The gradient criterion of Chapter 2 are used. Recall that step criteria give similar results, echoing Sprintall and Tomczak (1992) who find either method to be suitable in the western equatorial Pacific.

Thus a density gradient criterion of 0.01 kg m^{-4} was used to define the mixed layer depth. Density equivalent gradients of 0.031 psu m^{-1} and 0.0134°Cm^{-1} were used to define the depths of isohaline and isothermal layers respectively. The justification of this use is twofold. Firstly, the density gradient is proportional to the buoyancy force which must be overcome to deepen the mixed layer. Secondly, the results obtained by the use of these gradient criteria agreed well with the subjective estimates of layer depths made by eye from the original vertical profiles. Figure 3.10 shows both the isothermal and isohaline layer depths defined as the first depth at which the absolute temperature and salinity gradients exceed the critical values given above. Both records have had a 3 hour low pass filter applied. These depths will be called the thermocline and the halocline depths respectively.

The flat sections at 9 m in the diurnal thermocline record (Figure 3.10) are due to the griding of the Seasoar data on to 4 m intervals in the vertical. A depth of 9 m is given if the critical gradient was exceeded between the 5 m and 9 m levels.

The most obvious feature of the thermocline depth trace is the remarkably well defined diurnal signal. From days 107 to 112 inclusive, the timing is such that deepening commences at about 16:00, shallowing at about 07:00 local solar time. This observation is commensurate with daytime solar volume heating rapidly stratifying the upper ocean soon after sunrise, causing the very steep shallowing observed. Shallowing of the diurnal thermocline to less than 9 m is supported by the mean Monin-Obukhov length scale being 6.4 m during these periods of net oceanic heat gain. Two hours before sunset the heat flux

changes sign and surface waters start to cool. Consequent convective overturning erodes the daytime stratification, entraining cooler water into the deepening mixed layer. This process continues throughout the night completely eroding the daytime heat stratification, mixing down to the top of the halocline at a depth of 40 to 50 m. There appears to be insufficient turbulent kinetic energy to significantly mix down into the halocline.

The clean expression of the diurnal signal shows how uniformly the upper ocean responds over a scale of 100 km to atmospheric forcing. This is noteworthy when one recalls that spatial variability in temperature is as large as the diurnal variability. Only one small scale rain event was observed in both the direct rainfall measurement and near surface salinity structure during the survey period. The sparsity of rain events doubtless contributes to the observed spatial coherency.

From day 111 onwards the situation is quite different. On all four days the diurnal thermocline fails to penetrate to the top of the halocline. Indeed on day 113 the maximum nighttime penetration depth is barely 15 m. During this later period (days 111 to 114) the mean halocline depth actually increases from an earlier value of 47 m to a later mean value of 62 m. The reduced depth of mixing is consistent with the increased diurnal signal on days 112 and 113 in the temperature trace of the TSG record (Figure 3.11). The shallower mixing the previous night produces an increase in the daytime rise in temperature. The sharp cooling in SST at the end of day 113 is also qualitatively in accordance with the deeper mixing at that time into the cooler water below.

These observations suggest that salinity stratification may be limiting the depth of nighttime convection on days 107 to 110. To investigate these observations of the diurnal cycle and it's variability, one dimensional mixing models are employed. Results of direct simulation and process type experiments are presented in Chapters 4 and 5.

3.4 Heat and Salt Budgets, Estimation of Vertical Velocities

The change in the temperature of the upper ocean, corresponding to a net cooling of the top 50 m in the presence of a net warming due to the surface heat flux, suggests that non-local effects are important in determining the evolution of the temperature and salinity structure. In order to quantify the factors affecting the temperature and salinity structure of the upper ocean the heat and salt budgets have been considered. Consideration of the heat budget also provides an indirect estimate of the vertical velocity. As will be shown this estimate is

significantly more accurate than that derived from consideration of the mass balance.

3.4.1 Heat Budget

The equation for temperature integrated over a layer of depth h is

$$< \frac{\partial T}{\partial t} > + < u\frac{\partial T}{\partial x} > + < v\frac{\partial T}{\partial y} > + < w\frac{\partial T}{\partial z} >= \frac{Q_T}{C_p \rho h} + < D > \qquad (3.1)$$

where $< >$ represents a mean taken over the layer, Q_T is the surface heat flux across the air/sea interface, C_p the specific heat, ρ the density and D represents the divergence of the turbulent diffusive flux. The calculation assumes all short wave radiation is absorbed in the 50 m thick upper layer. For the deeper layers the short wave flux divergence is set to zero. Using a 3 band short wave absorption model for Jerlov water type 1A (Woods et al. 1984) 3% of surface short wave radiation flux penetrates out of the base of the 0–50 m layer and 1% penetrates into the 75–100 m layer. The error in confining all short wave heating to the surface layer is thus small in comparison to other errors.

Estimates are made of the first three terms on the left hand side of Equation 3.1, the time rate of change and the horizontal advection, from the Seasoar and ADCP data sets of the survey. Because the box survey was centred around the drifting spar buoy velocities have been taken relative to the buoy. Data were interpolated onto 4 m depth intervals and averaged over each side of the sub–boxes of the survey. The numbering convention used for sub–boxes and sides is shown in Figure 3.12. $\overline{< T >}^{i}_{j}$ is defined to be the depth averaged temperature, averaged along side i of sub–box j.

There are a number of ways the horizontal advection terms can be calculated. The method which minimises aliasing from the tides and miscalibration of the ADCP is to use the east/west and north/south sections crossing the centre of the large box to estimate x and y derivatives, respectively, and estimate each term at the centre. Each section was repeated once a day, took 6 hours to complete, with a 12 hour interval between the mid–points of north/south and east/west sections. Thus, for instance, the component $< v\frac{\partial T}{\partial y} >$ is calculated by

$$\frac{1}{2}\left(\overline{< v >}^{2}_{1} + \overline{< v >}^{2}_{3}\right)\left(\overline{< T >}^{2}_{1} - \overline{< T >}^{2}_{3}\right)/\Delta y \qquad (3.2)$$

and

$$\frac{1}{2}\left(\overline{<v>_2^4}+\overline{<v>_4^4}\right)\left(\overline{<T>_2^4}-\overline{<T>_4^4}\right)/\Delta y \tag{3.3}$$

on alternate days, where Δy is the distance between the mid-point of each side.

The u component of advection was then interpolated in time so as to be evaluated at a common time with the v component. The time derivative is calculated using a central difference in time of the average temperature along a given section. Note that this method involves alternately east/west and north/south sections and gives a value every 12 hours.

The calculation of the net diffusive flux, D, was based on a Richardson number parameterisation of the vertical turbulent diffusion coefficient, derived from measurements made in the equatorial Pacific (Peters et al. 1988).

The results for the depth interval 0–50 m are shown in Figure 3.13 for the period day 109 to 114. The time rate of change shows an initial warming of the layer with a subsequent cooling. This cooling is much reduced towards the end of the sampling period. The heating and cooling of the layer is mirrored by the horizontal advection, indicating that a substantial fraction of the change in heat content of the layer is brought about by advection.

The sign of the difference between the curves for the time rate of change and horizontal advection of temperature in Figure 3.13 is consistent with the net heating from the atmosphere over this period. However, to a substantial extent, the surface heating is balanced by the turbulent diffusive flux at the base of the layer.

All terms averaged over the sampling period are given in Table 3.3. The results have been given in buoyancy units. Results can be put in terms of Wm^{-2} by multiplying by 6.26×10^8 for a 50 m thick layer. Although the layer undergoes significant heating and cooling during the sampling period the net change to the heat content is relatively small. The heat budget is dominated by zonal advection. It is noteworthy however that the surface heat flux is equal to within 10% of our estimate of the turbulent flux at the base of the surface layer (although considerable uncertainties exist in such an estimate).

Also given in Table 3.3 are the results for 3 deeper layers. Below the surface the divergence of the turbulent flux is insignificant. The zonal flux changes sign. The rate of change of heat content increases in magnitude but is of the wrong sign to balance advection. At all levels there is a substantial residual in the budget calculated from derivable terms.

Estimating the size of the errors involved in calculating the horizontal advection term is difficult since the errors depend on how well the sampling method has captured advec-

Depth (m)	$\partial/\partial t$	$u\partial/\partial x$	$v\partial/\partial y$	$\frac{Q_T\alpha}{C_p h}$	$D\alpha\rho$	$w\partial/\partial z$	$w \pm\sigma$ (m/day)	$w_i \pm\sigma$ (m/day)
0–50	3.7	37.0	0.19	10.3	−9.1	−39.7	-11.6 ± 1.6	-9.4 ± 4.4
75–100	20.7	−5.2	−0.9	0	−0.5	−15.1	-2.6 ± 1.8	-6.0 ± 2.3
100–150	−59.9	−159.0	−11.8	0	0.38	231.1	5.7 ± 2.2	2.7 ± 1.4
150–200	−53.8	−219.0	4.1	0	0.01	268.7	8.6 ± 3.1	4.1 ± 2.8

Table 3.3: Contributions to the heat budget (Equation 3.1) averaged over the sampling period (5 days) for a number of depth intervals down to 200 m. Units: In order to be able to compare directly the contributions of changes in temperature and salinity in terms of changes in density the results have been put in terms of buoyancy units by multiplying equation 1 by $\alpha\rho$, where α is the thermal expansion coefficient. The units are then 10^{-8} kg $m^{-3}s^{-1}$. The vertical velocity, w, has been calculated as a residual and is given in m/day. w_i is the estimate of the vertical velocity calculated by assuming the flow is along isopycnic surfaces (see text for details). The standard deviation, σ, of the daily values of each of the estimates of w are also given.

tive events, which in turn depends on the structure of those events. The Courant number $u\Delta t/\Delta x \simeq 0.4$ satisfies the necessary condition for it to be less than 1. A more quantitative estimate is given by considering the same numerical technique applied to the uniform advection of a temperature structure with known horizontal variation. A sine wave superimposed on a linear gradient moving with a given velocity was chosen to represent the field. The error depends on, (i) the ratio of the amplitude of the sine wave to the linear temperature difference across the box, (ii) the speed of advection through the box, and (iii) the wavenumber and phase of the oscillation. The analysis was applied to the sampling technique outlined above. For parameter settings appropriate to the observations an upper bound on the ratio of advective to tendency terms is approximately 1.25 and stable for the technique discussed here. Thus an error of 25% on the advection term is a conservative estimate. The estimated error for the residual is dominated by this error in the advection term.

The heat budget was calculated for each of the sub–boxes. Each box was sampled every

2 days. The Courant number is then in excess of 1 and the above error analysis applied to the advection term showed considerably larger errors. The results using the sub–boxes will therefore not be presented

3.4.2 Estimate of the Vertical Velocity

The vertical velocity is estimated by dividing the residual by the mean vertical temperature gradient and given in Table 3.3. The estimated error for w given in Table 3.3 has been calculated from the variation in w calculated from the daily values of the residual. No discernable trend could be seen in these daily values suggesting the method is unable to identify temporal variations in w over the time period. The variation in w is close to that expected from the error estimates of the residual term in the heat budget which is dominated by the error in the advection term.

The vertical velocities above (0–100 m) and within (100–200 m) the main thermocline are found to have differing sign. The upward nature and magnitude of the vertical velocity within the thermocline are consistent with an easterly wind stress and the estimates made by Brady and Bryden (1985) for the central equatorial Pacific. However, the predominance of zonal advection in the heat budget suggests that the vertical motion comes principally from flow along a sloping density surface (see below).

Above the main thermocline the estimate of vertical velocity from the two depth intervals 0–50 m and 75–100 m are similar in sign and magnitude despite the differing sign of the time rate of change and advection terms in the two intervals. Below 50 m the estimated downward velocity is consistent with the observed downward displacement of isotherms. This is not so above 50 m where horizontal advection dominates. It is interesting to note that Richards and Pollard (1991) infer a downward vertical velocity of around 25 m/day at a depth of 25 m from the observation of a strong surface convergence.

A second estimate of the vertical velocity, w_i, has been made by assuming the flow is along isopycnic surfaces. Using the data from the central cross of the survey, the slope of the density level which lay at the vertical centre of each level at the spar buoy was calculated. The vertical velocity, w_i, was then calculated by assuming $w_i = D\eta/Dt$, where η is the height of the isopycnal surface. Daily estimates were made of w_i and the mean over the survey period together with the standard deviation are given in Table 3.3. The estimate w_i is dominated by the contribution from zonal advection in all but the 75–100 m layer. In the 75–100 m layer both zonal and meridional advection are equally important.

The vertical velocities agree to within one standard deviation of those estimated by the heat budget method. This agreement is due in large part to the isopycnic and isothermal surfaces being approximately coincident. Nevertheless it is encouraging as it supports our faith in the method used to calculate the heat budget and supports the expectation that diapycnal mixing has a small contribution to the vertical velocity on the equator (Bryden and Brady, 1985).

As alluded to earlier consideration of the mass budget was unrewarding. The standard error in the estimation of the horizontal velocity divergence calculated from either the sub–boxes or the central cross was approximately $1 \times 10^{-6}\mathrm{s}^{-1}$ and constant with depth. Integrating from the surface, the two methods gave vertical velocities of opposite sign. An error of $1 \times 10^{-6}\mathrm{s}^{-1}$ in divergence is equivalent to a Δu of 0.04 ms^{-1} over 40 km and a Δw of 20 m/day over 200 m depth. Absolute and systematic errors (mis–alignment) in the ADCP are of the order of a few cm s^{-1} .

3.4.3 Salt Budget

A similar analysis was applied to the salt budget. The results are given in Table 3.4. Again the results are presented in buoyancy units. Except for the surface, the change in buoyancy due to the salt flux is insignificant compared to that of heat. Zonal advection is seen to play less of a dominant role and the residual in the salt budget is much smaller compared to the heat budget. Because of this, together with the fact that vertical gradients in salinity are small and change sign, the estimate of vertical velocity is unreliable and therefore not quoted.

3.5 Discussion

The results presented in this Chapter have shown the response of the upper ocean in the western equatorial Pacific to atmospheric forcing on timescales of a few days to be sensitive to subtle changes in the vertical structure of both temperature and salinity. Chapter 4 investigates this sensitivity more fully. The short time and space scales of variation in the structure of the upper ocean require a rapid sampling. The strategy employed here has been proven to be adequate in studying the response over a few days.

It should be noted however that not all of the short time scale events were captured. In particular, a rain event lasting a few hours was observed to produce a shallow pool of fresh

Depth (m)	$\partial/\partial t$	$u\partial/\partial x$	$v\partial/\partial y$	Q_S/h	$D\alpha\rho$	$w\partial/\partial z$ (residual)
0-50	5.5	-12.0	-0.3	0.13	2.3	9.2
75-100	-0.78	-0.73	-0.12	0	-1.4	0.4
100-150	4.5	8.7	0.34	0	0.71	-12.9
150-200	17.2	0.3	-5.6	0	-0.13	-12.0

Table 3.4: Contributions to the salt budget. Units: 10^{-8} kgm^{-3}s^{-1}. Q_S is the surface buoyancy flux due to fresh water exchange, D_S the divergence of turbulent salt flux, and β the haline expansion coefficient.

water on one of the east/west sections. This pool was advected out of the survey region before it could be resampled. This is discussed in the modelling studies, Section 5.1.

The diurnal response of the near surface temperature to day time heating and nighttime cooling was found to have an amplitude of a few tenths of a degree C. This compares with a horizontal variation of temperature on scales of a few tens of kilometres of a similar magnitude. Even away from the very fresh surface layers typical of the area, salinity is found to play an important role in limiting the depth of night time mixing. In this case a sub–surface salinity maximum restricts the depth to around 40 m.

The diurnal mixing was found to be coherent over the survey area with a marked reduction in nighttime mixing during days 112–113. It is important to know whether the reduced mixing is a local response to atmospheric forcing or caused by advective influences. This issue is addressed in the modelling experiments of Chapter 4.

Gaining an understanding of the mechanisms controlling the surface mixing is important in predicting the response of the SST to atmospheric forcing events. Here it is seen that relatively small changes in the atmospheric forcing or sub–surface structure can have relatively large effects on the diurnal cycle of mixing and more importantly the SST.

The estimated net surface heat flux from the atmosphere to the ocean was found to be not significantly different from zero at 10 Wm^{-2}. This is in agreement with the hypothesis

that net oceanic heating in the region is as low as 10 Wm^{-2} (Godfrey et al. 1991). The net surface heat flux during the period of the heat budget experiment, which took place on the equator, was substantially higher at 65 Wm^{-2}. Using the parameterisation of the turbulent diffusion coefficient suggested by Peters et al (1988), the surface heat flux is found to be balanced by vertical turbulent diffusion to within 10%. However, the heat budget calculation shows the importance of horizontal advection and the need to take advection into account when studying the changes to the upper ocean structure.

The estimated vertical velocity is found to be of order 10 m/day. The sign of the vertical velocity (except in the 75–100 m layer) is consistent with a shear flow (westward above 50 m, eastward below) along density surfaces sloping up towards the east. The east/west slope of isopycnic surfaces is probably due to an equatorially trapped wave (because of the short time and space scales of the survey the type of wave cannot be identified). This leads one to speculate that the uplifting of density surfaces may cause the surface waters to become cooler and this cooler water, advected west by the surface current, may affect the diurnal response and hence SST.

It is interesting to compare these results with those of Sprintall and McPhaden (1994) who consider a period of similar prevailing conditions but over a much longer time. Averaged over the period November 1988 to November 1989 they find that the SST and sea surface salinity were influenced by both upwelling and horizontal advection. In their case the upwelling is a consequence of local Ekman divergence caused by the predominantly easterly wind. They estimate a standard deviation wind–driven upwelling of 0.4 m/day and at 125 m the rate of change of temperature due to wind induced upwelling to be 1.8×10^{-7} °C s^{-1}. Table 3.3 shows the vertical velocity induced by the flow along isopycnic surfaces to be an order of magnitude higher and the rate of temperature change due to $w\partial T/\partial z$ to be 7×10^{-6} °C s^{-1} (converting from the buoyancy units given in the table). At the surface, both the vertical velocity and rate of change of temperature are of opposite sign because of the change in direction of the zonal current with depth. With regard to lateral advection, the zonal temperature gradient averaged across the CD32 survey area was typically 4×10^{-6} °C m^{-1}, a factor of 5 greater than that reported by Sprintall and McPhaden (1994) for the large scale gradient during the prevailing La Niña conditions. On the other hand the average time rate of change of temperature in the depth range 100–150 m given in Table 3.3, which is equivalent to 1.8×10^{-6}°C s^{-1}, is comparable to Sprintall and McPhaden's value of 0.8×10^{-6} °C s^{-1} for the variability of $\partial T/\partial t$ at 125 m during

their longer sampling period. This shows that the conditions during our survey were not particularly anomalous. Therefore changes to the temperature structure of the upper ocean induced by motions with a timescale of a few days (possibly planetary waves) are found to be significantly greater than longer term wind induced upwelling or advection. Lastly it is noteworthy that the variation in near surface temperature and the magnitude of the vertical velocity are both greater than those reported by McPhaden et al (1992) for the ocean response to a westerly wind burst.

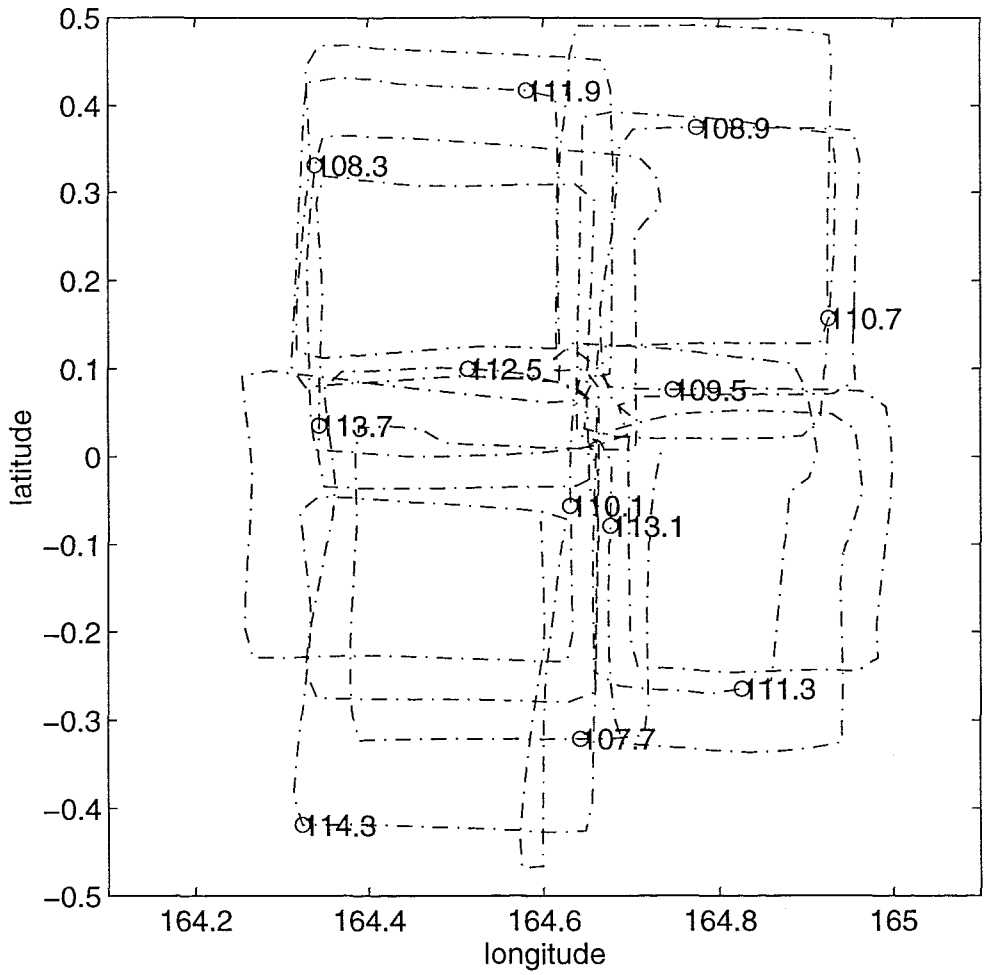

Figure 3.1: Ship's track. Numbers refer to Julian day.

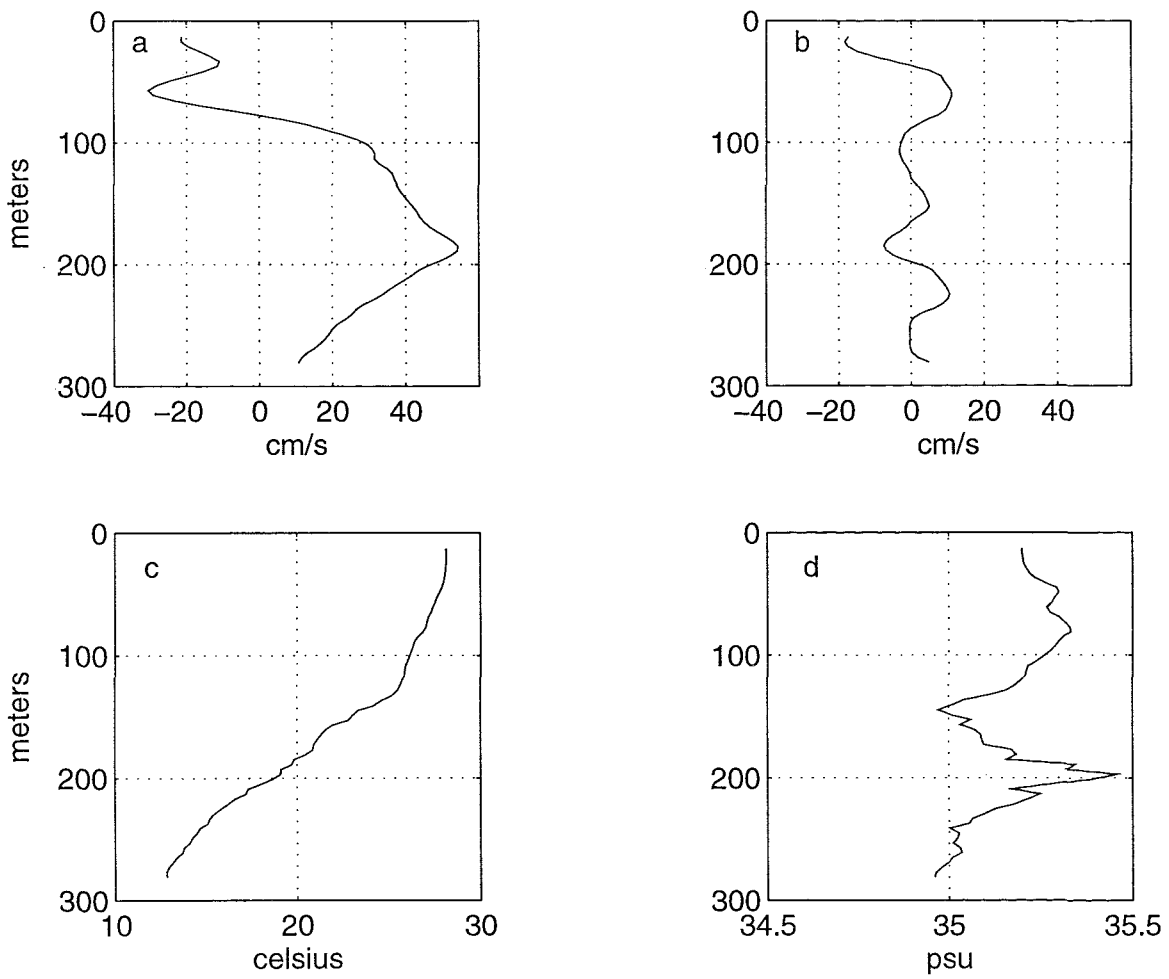

Figure 3.2: Vertical profiles of [a] eastward component of velocity, [b] northward component of velocity, [c] temperature, and [d] salinity.

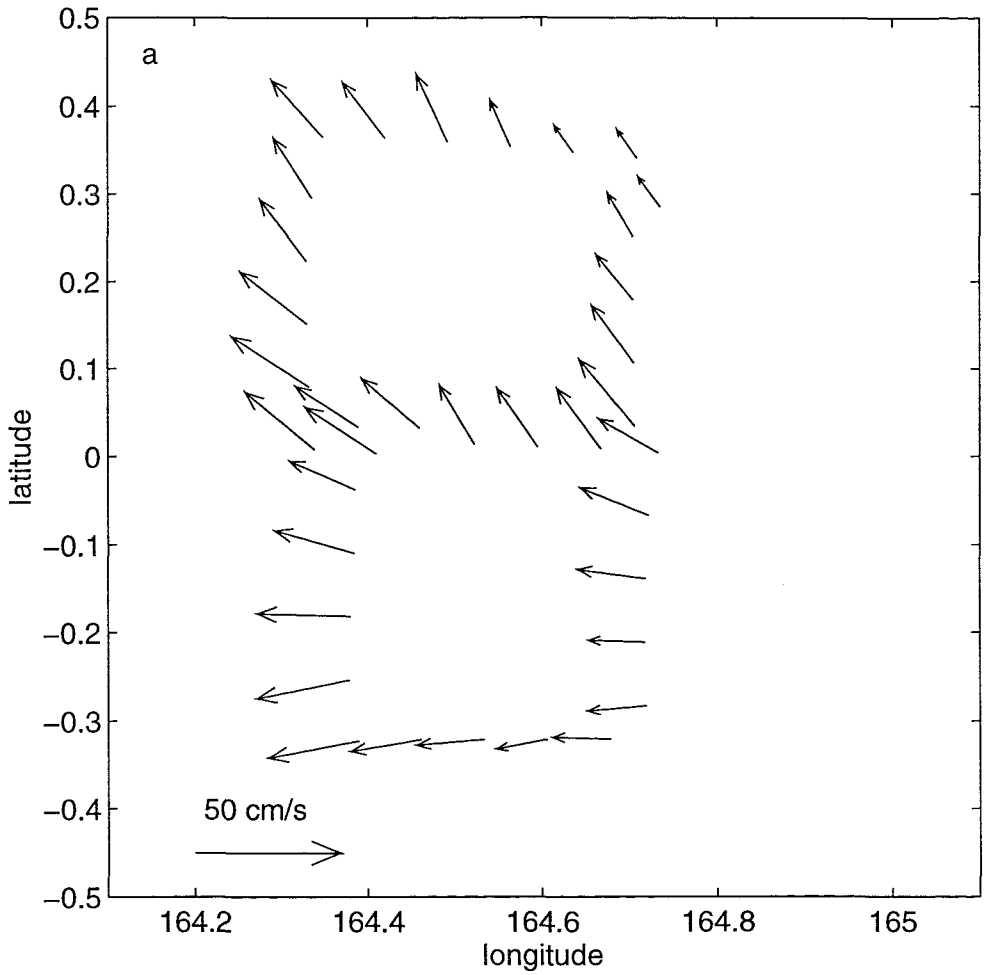

Figure 3.3: Horizontal distribution of velocity averged between 0–50 m for Julian days 107.5–108.5.

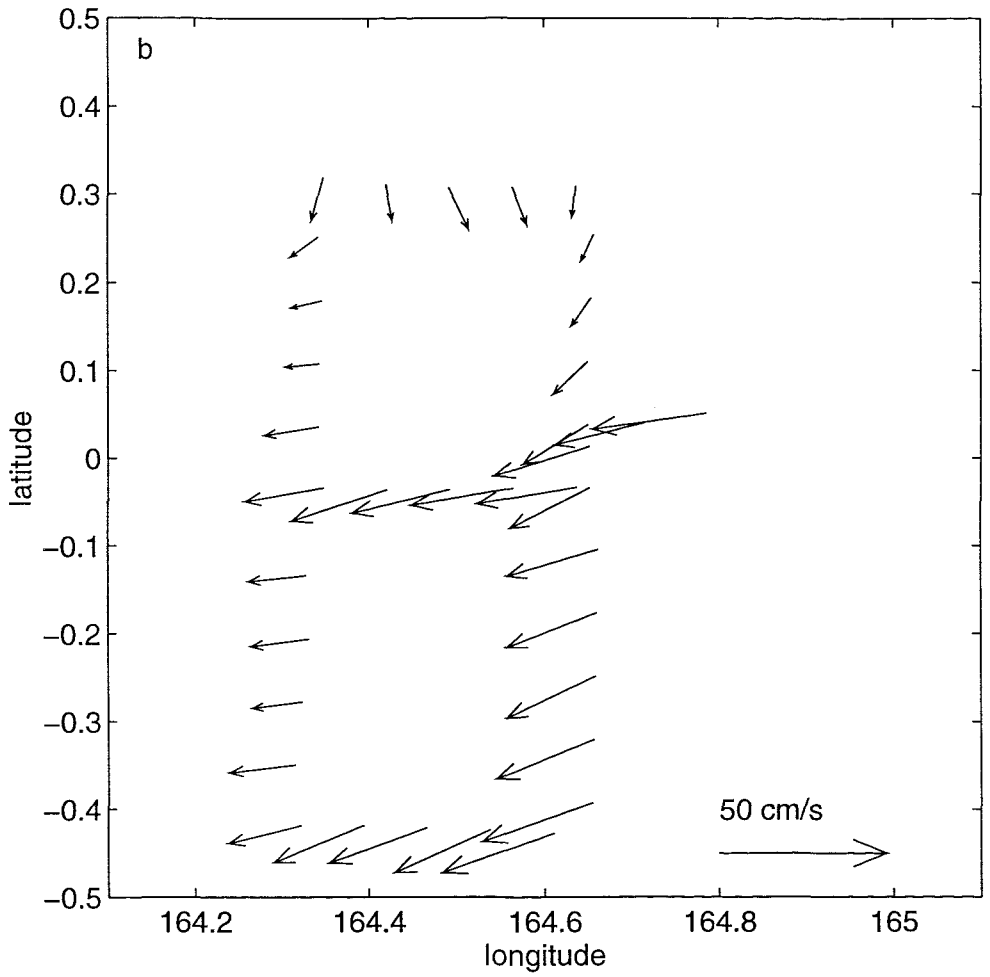

Figure 3.4: Horizontal distribution of velocity averged between 0–50 m for Julian days113.5–114.5.

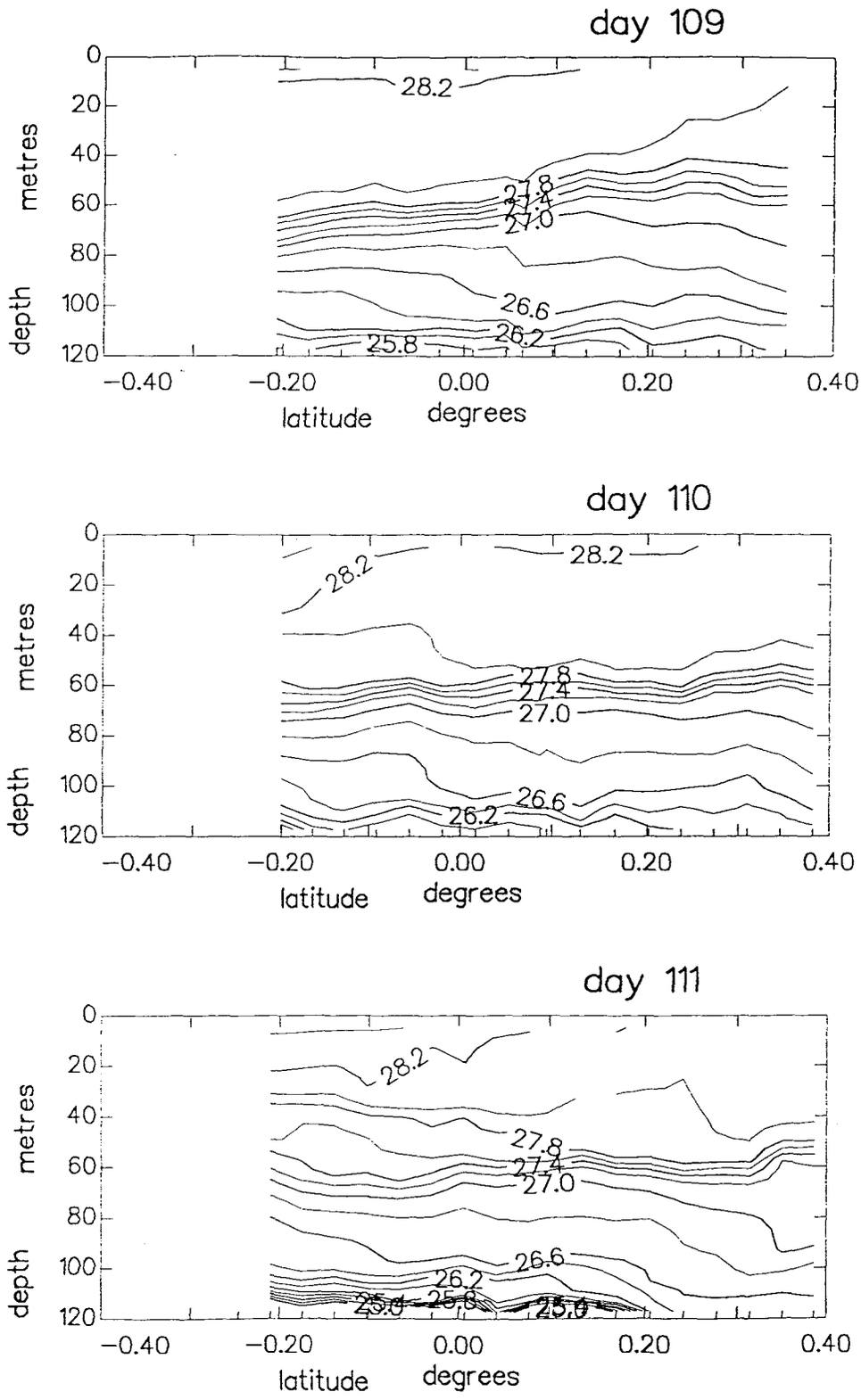

Figure 3.5: Meridional sections of temperature down to 120 m depth taken on consecutive days starting at day 109. All sections were taken north to south and took approximately 6 hours to complete. The timing of each section is such that the ship crossed the equator at approximately midday local time. Continued overleaf.

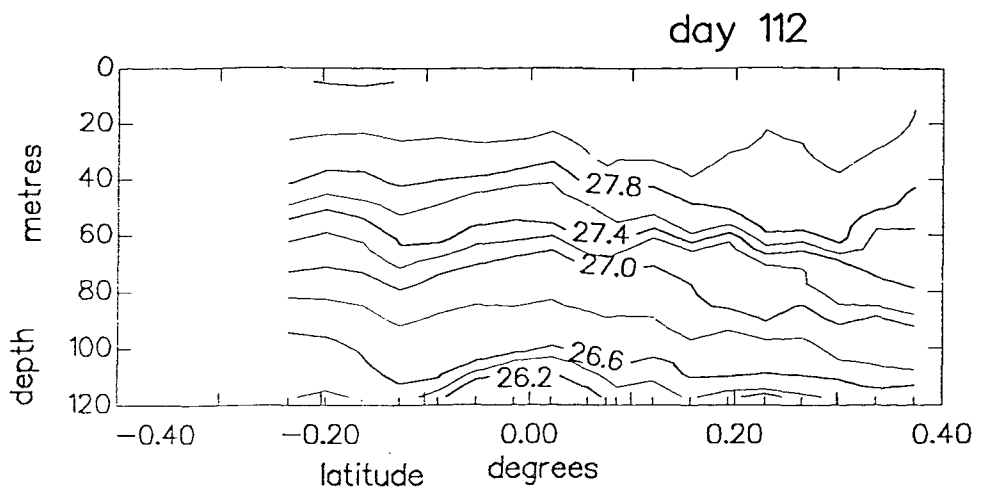
day 112
depth
metres
0
20
40
60
80
100
120
27.8
27.4
27.0
26.6
26.2
−0.40
−0.20
0.00
0.20
0.40
latitude
degrees

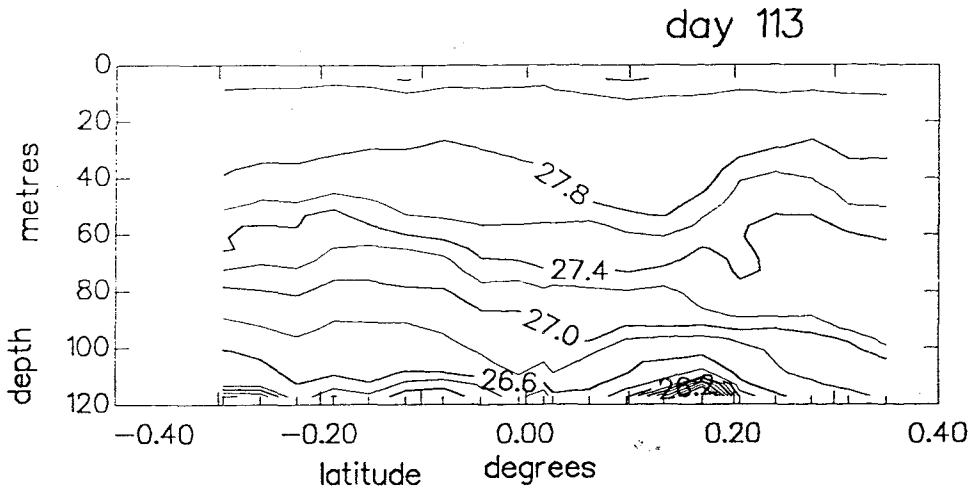
day 113
depth
metres
0
20
40
60
80
100
120
27.8
27.4
27.0
26.6
−0.40
−0.20
0.00
0.20
0.40
latitude
degrees

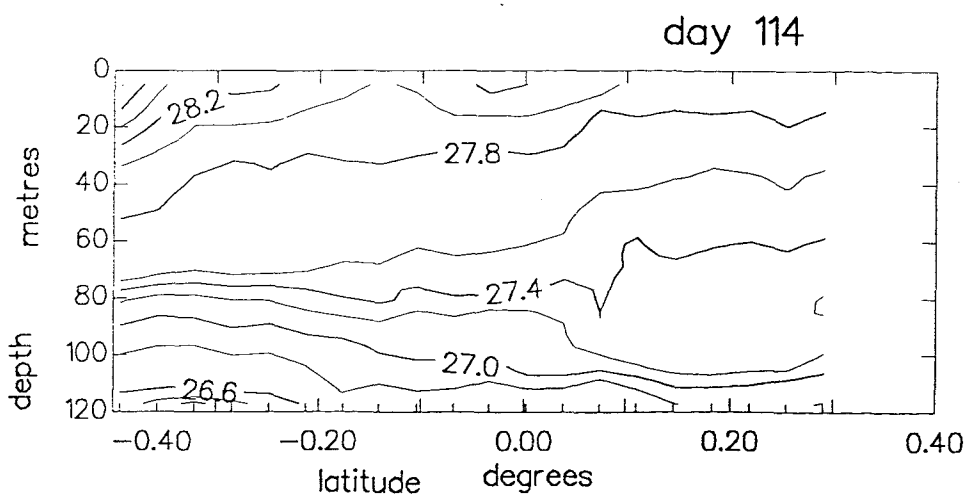
day 114
depth
metres
0
20
40
60
80
100
120
28.2
27.8
27.4
27.0
26.6
−0.40
−0.20
0.00
0.20
0.40
latitude
degrees

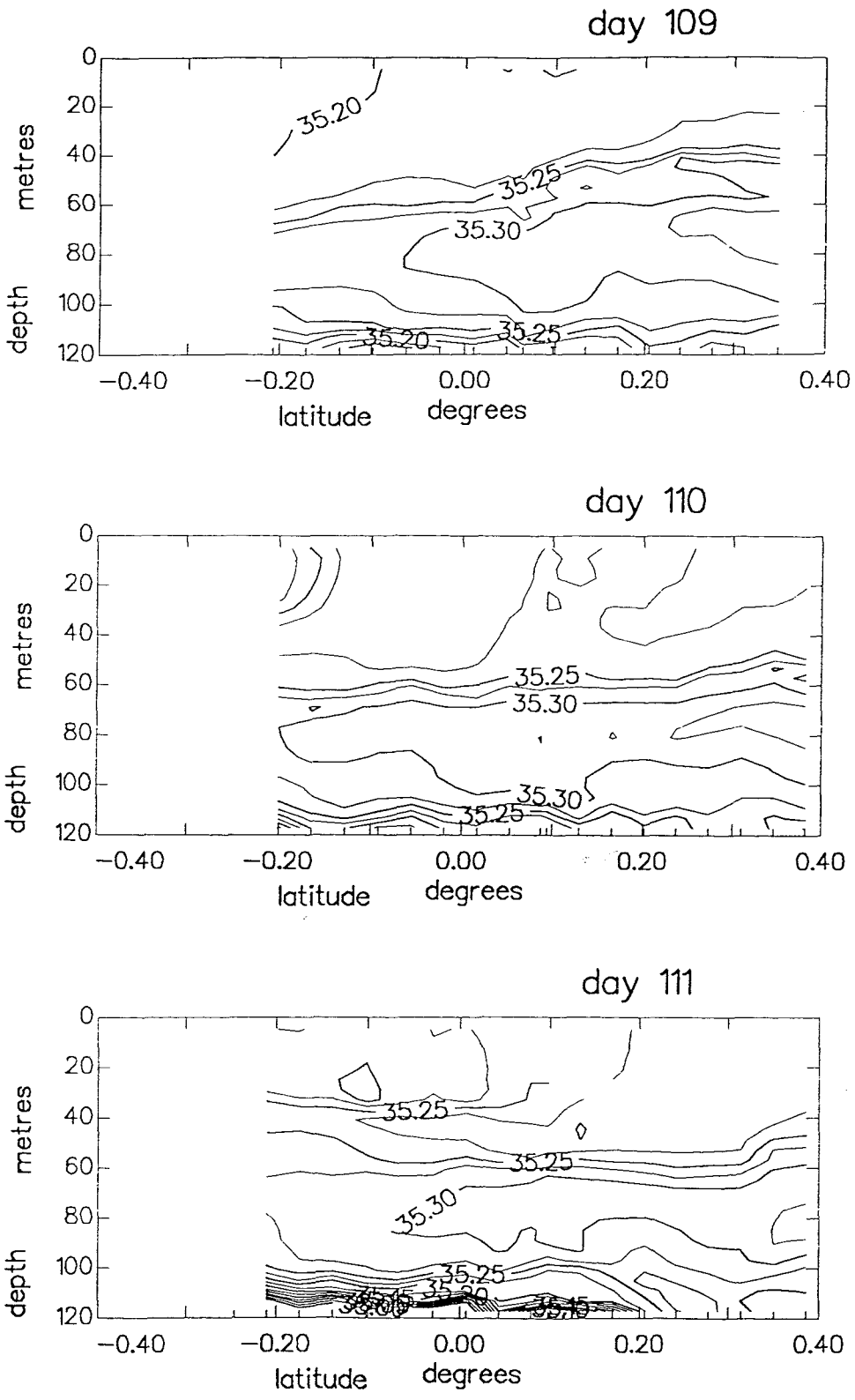

Figure 3.6: Same as Figure 5, except for meridional sections of salinity. Continued overleaf.

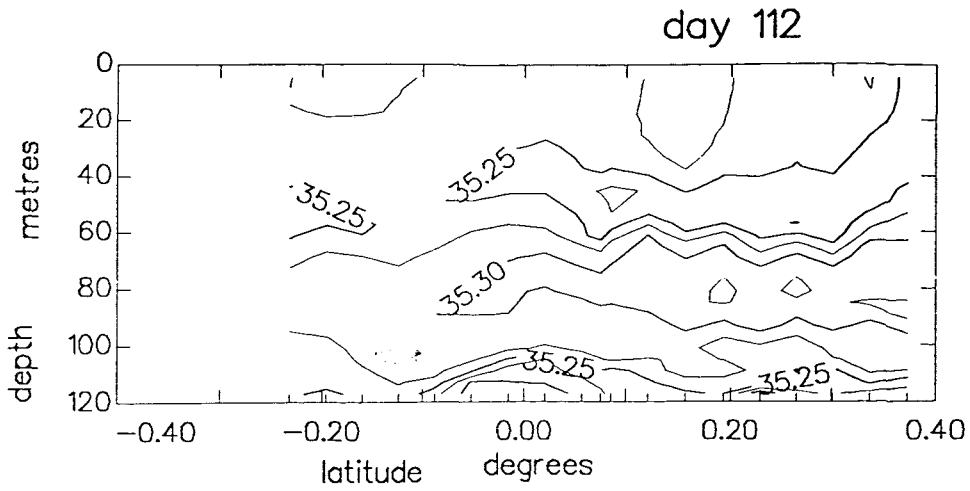
day 112
depth
metres
0
20
40
60
80
100
120
35.25
35.25
35.30
35.25
35.25
−0.40
−0.20
0.00
0.20
0.40
latitude
degrees

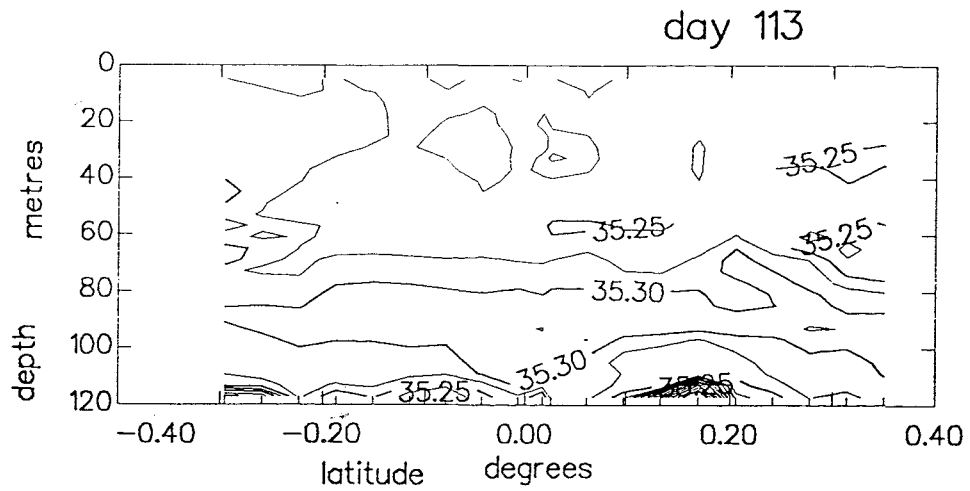
day 113
depth
metres
0
20
40
60
80
100
120
35.25
35.25
35.25
35.30
35.30
35.25
−0.40
−0.20
0.00
0.20
0.40
latitude
degrees

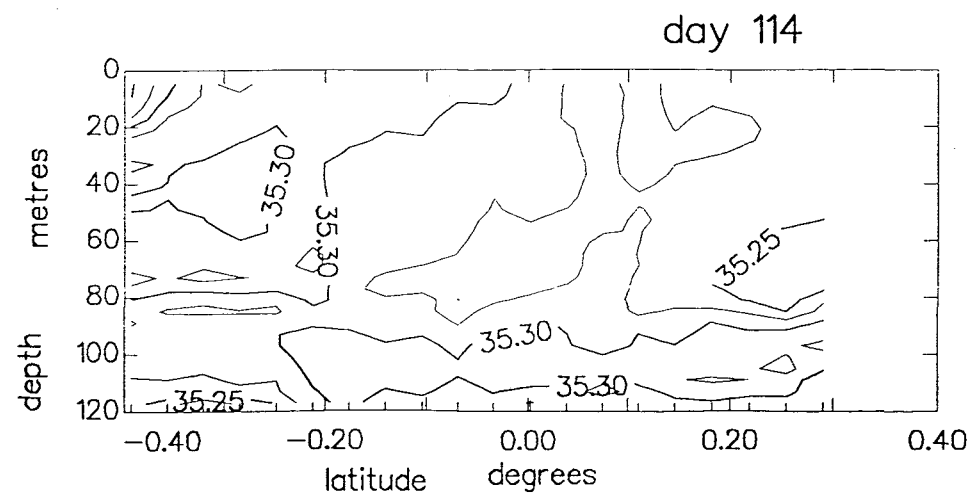
day 114
depth
metres
0
20
40
60
80
100
120
35.30
35.30
35.25
35.30
35.30
35.25
−0.40
−0.20
0.00
0.20
0.40
latitude
degrees

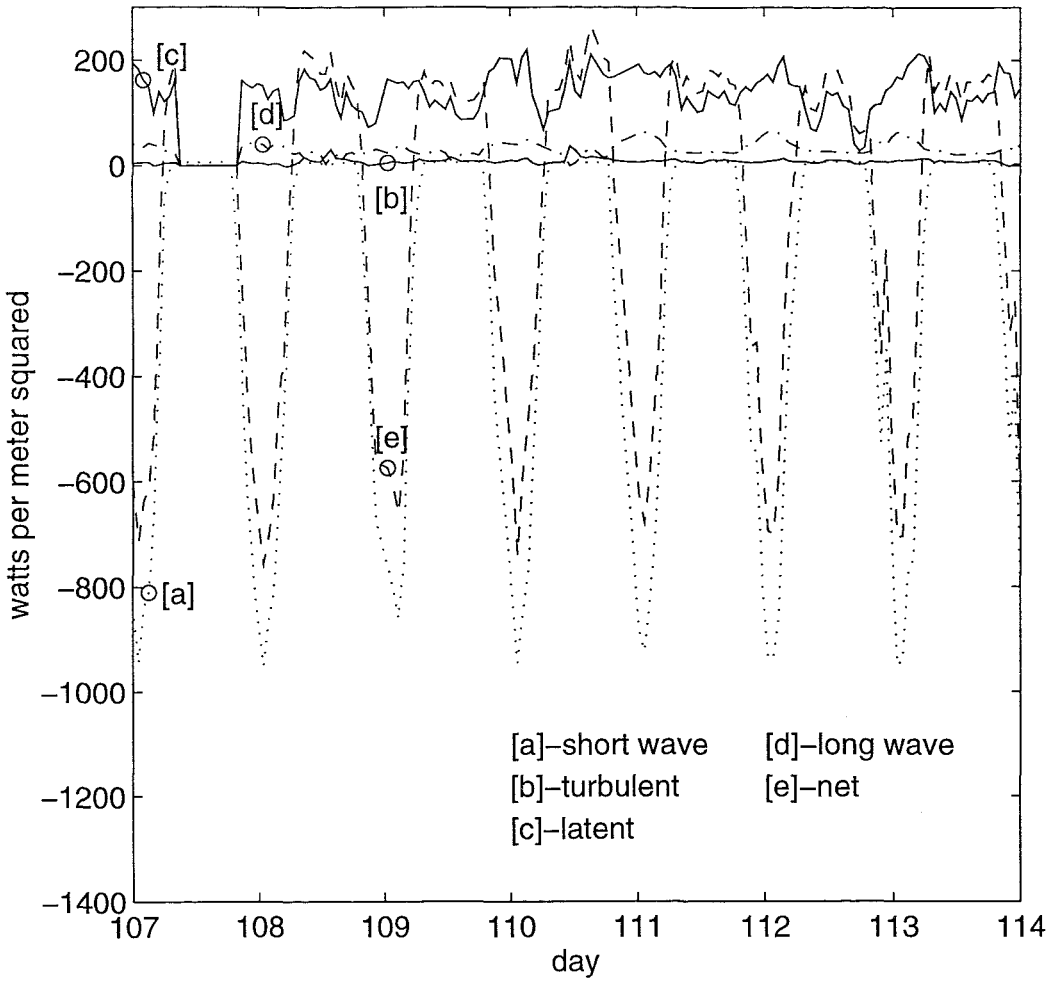

Figure 3.7: Components of the hourly averaged heat flux during the period of the spar buoy deployment. The major components contributing to the net flux (dashed line) are the short wave (dotted line) and latent heat (upper solid line) components. Positive values are taken as an upward flux.

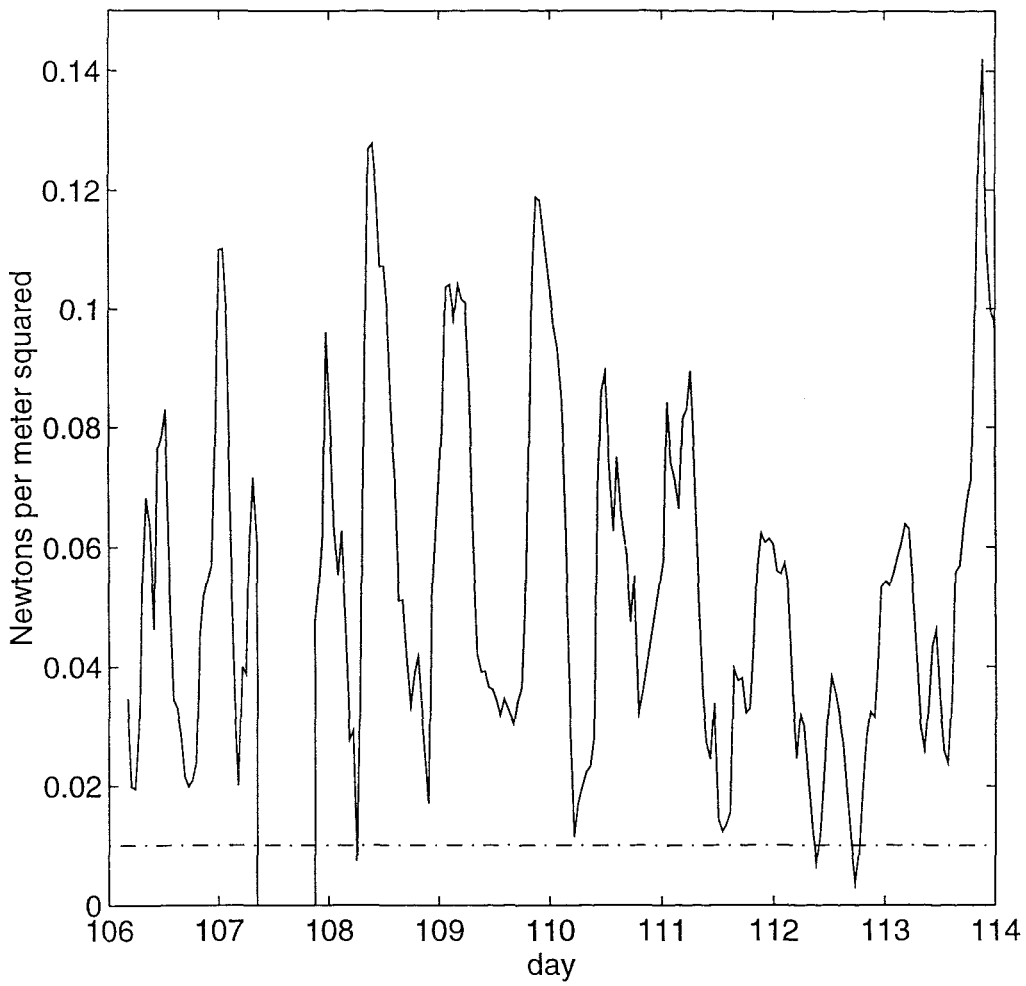

Figure 3.8: Magnitude of the surface windstress: 3 ms^{-1} windspeed marked

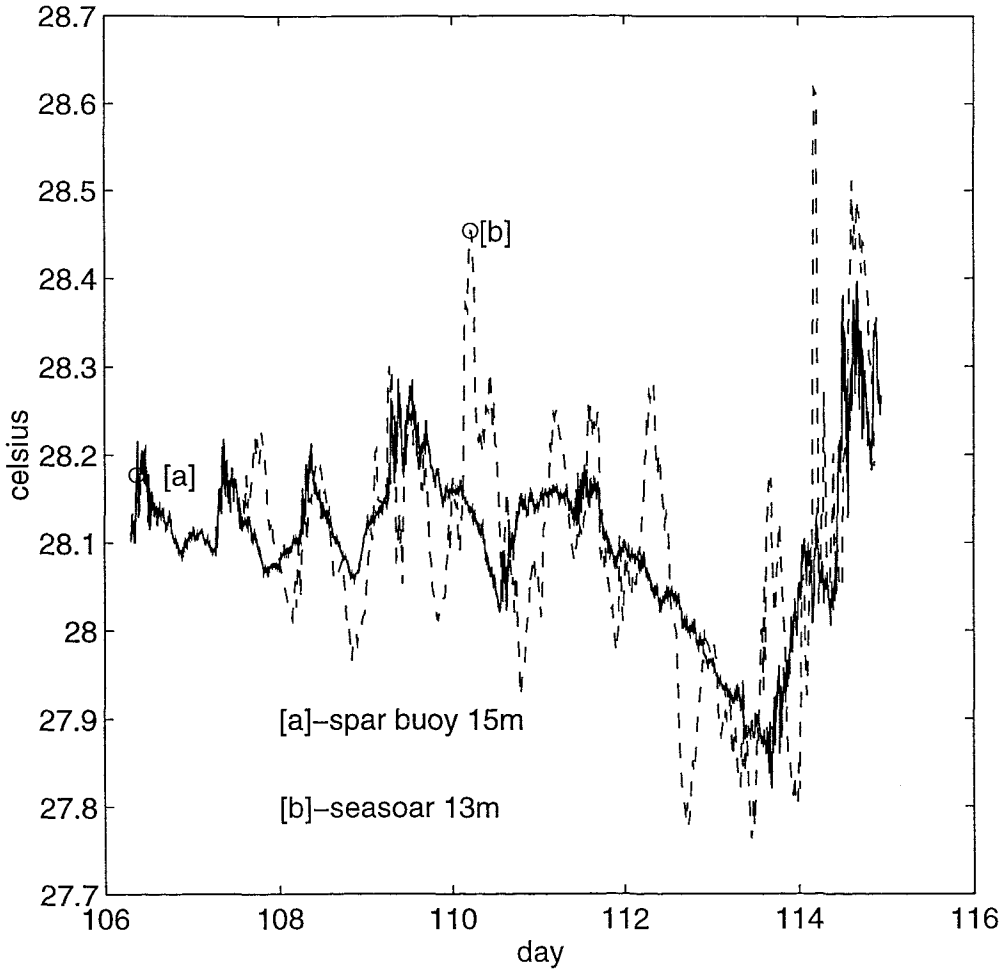

Figure 3.9: Temperature as a function of time from the spar buoy at 15 m depth (solid line labeled a) and the Seasoar at 15 m depth (dashed line labeled b). The Seasoar passed close to the spar at 12-hour intervals, corresponding to whole day and half-day values.

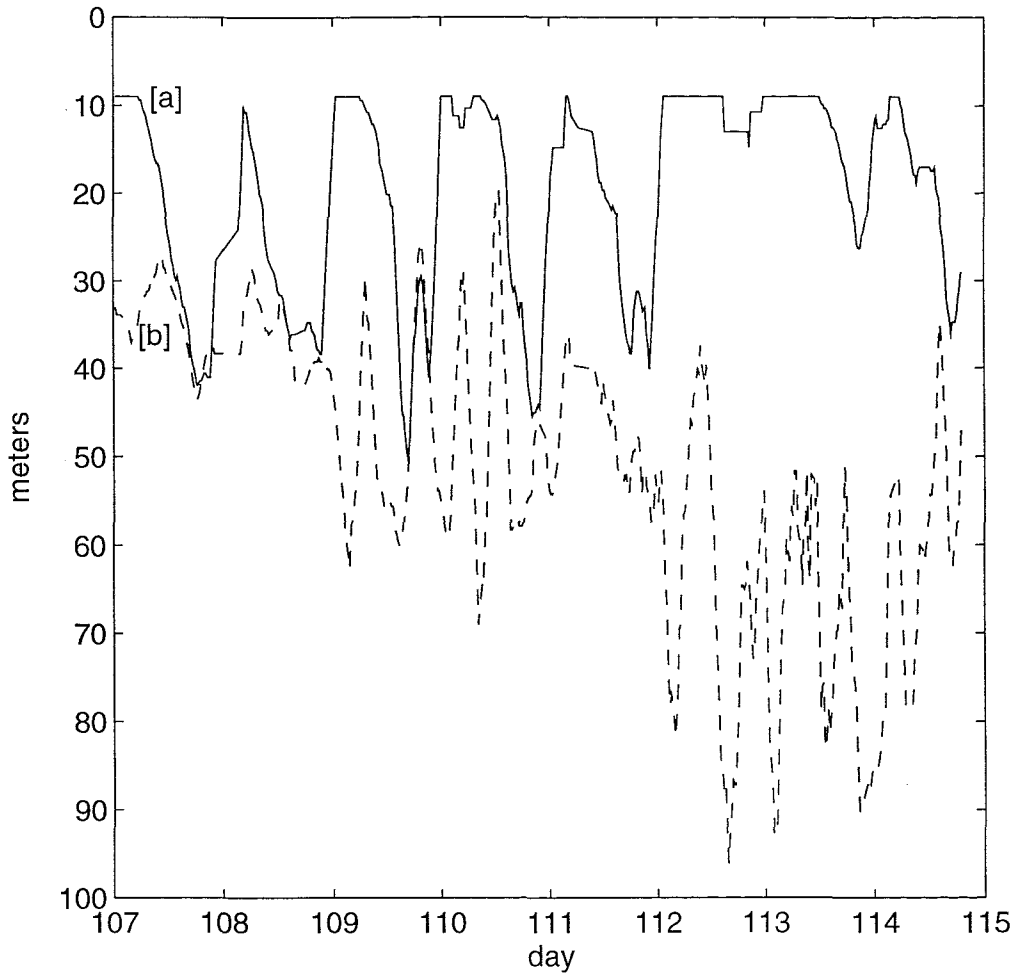

Figure 3.10: Mixed layer depth as a function of time defined in terms of vertical temperature gradient (isothermal layer depth, solid line labeled a) and vertical salinity gradient (isohaline layer depth, dashed line labeled b). See text for criterion for each depth.

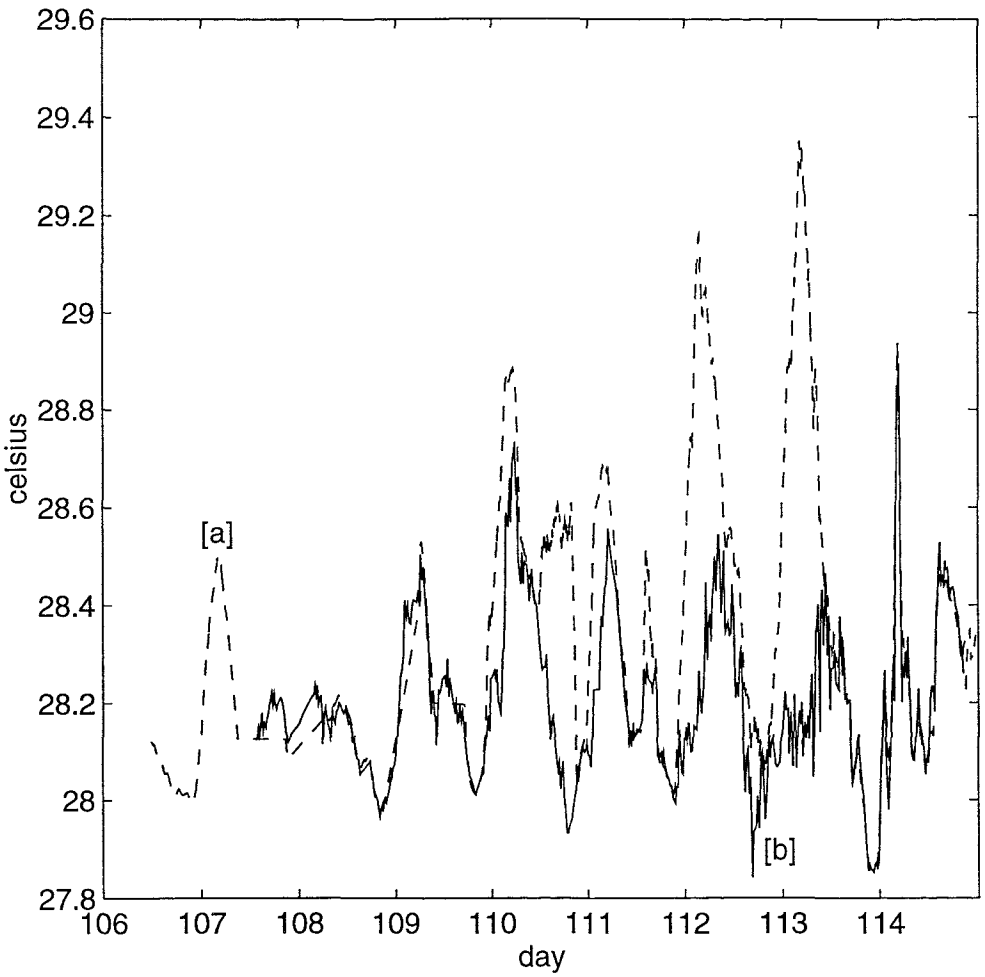

Figure 3.11: Temperature as a function of time from thermosalinograph (dashed line labeled a) and 5 m temperature record from Seasoar (labeled b).

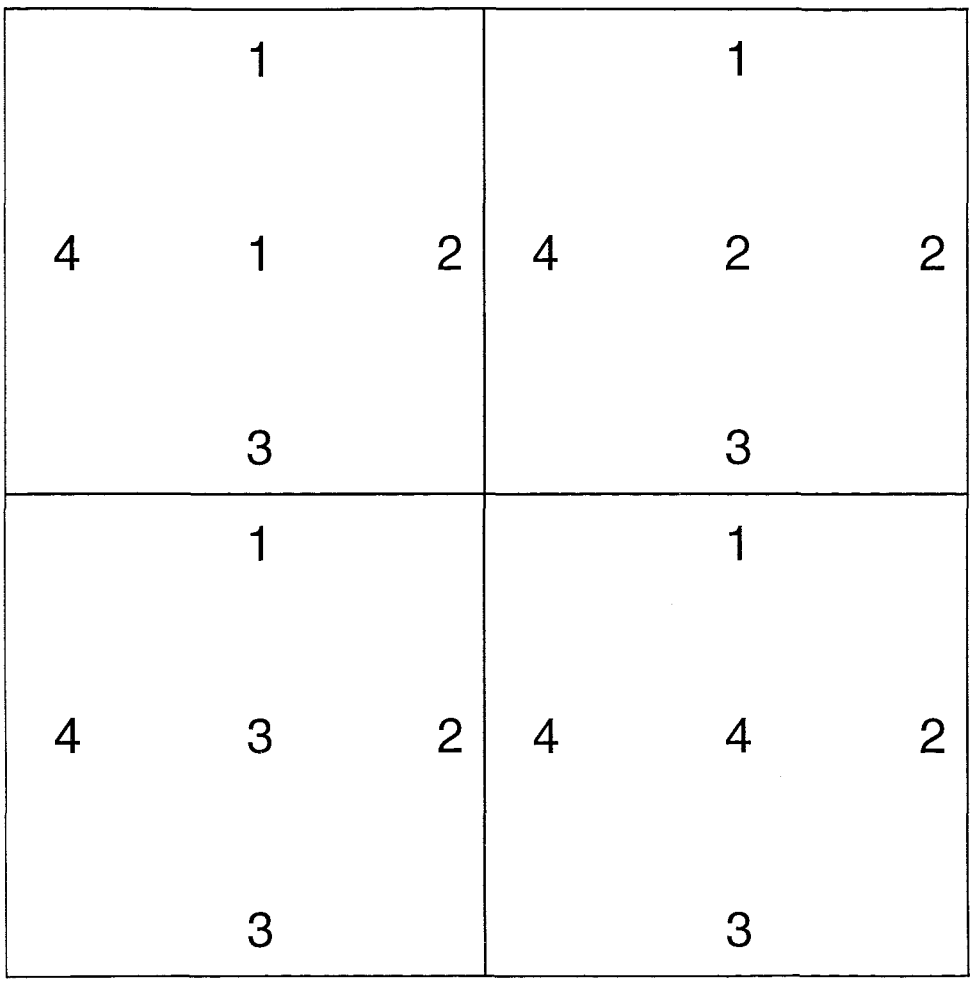

Figure 3.12: Box and side numbering scheme. Box numbers are central (index j), side numbers are peripheral (index i).

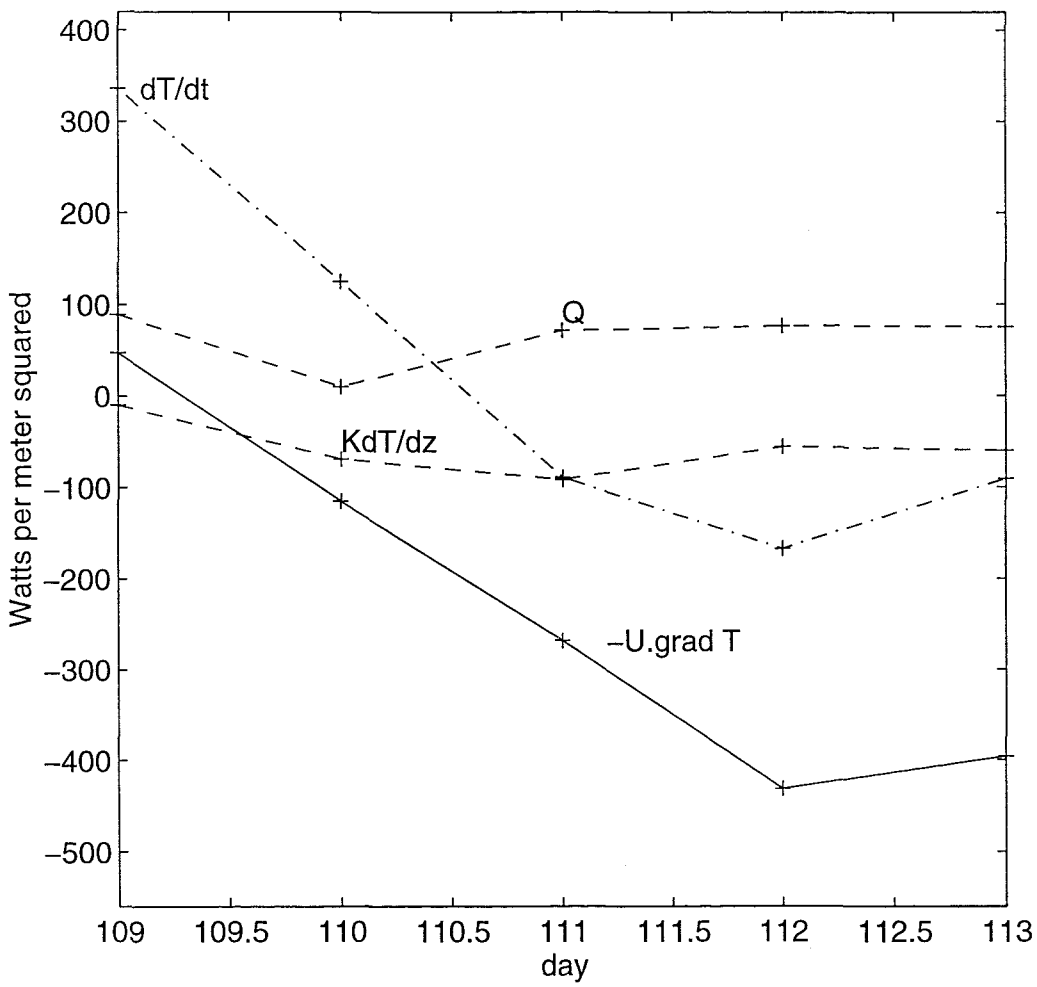

Figure 3.13: Components of the heat budget averaged over 0–50 m as a function of time.

Chapter 4

1D Mixing Models

One dimensional vertical mixing models have met with a fair amount of success in describing the ocean surface boundary layer. Large (1994) gives the most recent review. Observations of the diurnal cycle in mixing described in Chapters 3 and 2 provide a strong stimulus to investigate the possibility of using such models to describe the dominant physical processes in the upper-most layers of the Pacific warm pool. Simple models can then be used to determine the sensitivity of upper ocean properties to fluctuations in surface fluxes, factors responsible for major changes in surface properties identified, and process studies made where insufficient observational information exists to adequately describe a physical process.

Usually such models are used in areas where horizontal advection is known to be small, or they are used in Lagrangian experiments, when vertical shear is known to be small.

Vertical shear can be large in the upper 100 m of the western equatorial Pacific. The heat budget of Section 3.4 has shown that there are times when horizontal advection dominates the heat budget. Thus it is far from clear that a one dimensional mixing model will be appropriate in such a regime. However the heat budget of the TOGA COARE period (Section 2.4) showed that there are periods when the region behaves one dimensionally, at least in terms of heat. This observation encourages the investigation of one dimensional modelling of the WEP.

This chapter first describes the physics of one dimensional mixing models of the upper ocean, reviewing the various approaches taken. The two models used in this dissertation are looked at in more detail. Work published to date using 1D models on the equator is reviewed. The sensitivity of two models in an idealised western equatorial Pacific regime is then presented. A discussion concludes the chapter.

4.1 Model Philosophy and Physics

The upper few tens to hundreds of metres of the ocean are almost continually in a state of turbulence. Active turbulence is maintained mainly by wind and waves and surface cooling (including freezing and brine rejection in high latitudes). Mechanisms which induce turbulence in the ocean interior include shear instabilities, internal wave breaking, and Langmuir circulations.

With the vertical shear in horizontal velocities and large vertical density gradients it is likely that the first two internal mechanisms in addition to surface forcing will be important in equatorial regions.

Turbulent mixing leads to a vertically quasi–uniform distribution of temperature, salinity and often momentum and other conservative properties to a boundary layer depth, h, which is the limit boundary layer eddies can penetrate in the vertical.

Beneath this approximately homogeneous layer there is a rapid increase in density with depth. In much of the world ocean this density gradient is attributable to temperature changes, but in equatorial (and polar) regions salinity stratification can play on important role. It is an observed fact that bulk temperatures or salinities tend to vary more on a vertical scale of hundreds of meters than along a horizontal scale of hundreds of kilometres. Thus forcing by the surface fluxes dominates the advective effects over much of the worlds ocean. The concept of modelling the ocean planetary boundary layer (OPBL) in only the vertical thus appears attractive. Such models strive to represent faithfully the mixing due to turbulent vertical velocities of unresolved eddies.

4.1.1 General Formulation of the Mixed Layer Problem

The problem described so far can be written down in terms of a one dimensional form of the Navier-Stokes equation(see eg (Hinze 1957)). With the addition of an equation of state and conservation equations for dynamically active variables such as temperature and salinity, and a continuity equation this set of equations is closed and exact (for a Newtonian fluid) for all time and space scales of fluid motion. However these equations cannot be solved presently for practical computing reasons. There is a dynamic range in space and time of 12 decades for say global climatic changes. Hence the concept of a separation of scales must, of necessity, be introduced. In this approach, first used by Reynolds, the instantaneous velocity, temperature (density) etc. are separated into statistical mean and

fluctuating quantities. For a property Q then, $Q = q + q'$, where q is the mean part and q' the fluctuating part. Implicit in this procedure is the assumption that there is a spectral gap between q and q' temporal variations and that there exists a time scale over which q can be considered constant and the average of q', $\overline{q'}$, is zero. The aim of this approach is to calculate the distribution of the mean quantities over the region of interest by way of the averaged equations. Since the mean quantities vary much slower in space and time than the instantaneous quantities, much less computer power is needed to solve the averaged equations. The problem now is that the averaging procedure has introduced unknown correlations between various fluctuating quantities into the equations (see (Hinze 1957) or (Tennekes and Lumley 1972) for a full derivation).

Physically these correlations express the transport of momentum, heat and mass by the turbulent (fluctuating) motion. In order to obtain a closed set of equations, so-called closure approximations must be made with the aid of empirical input.

The time evolution of a mean property, q, due to OPBL eddies can be expressed as the vertical divergence of these kinematic turbulent fluxes.

$$\frac{\partial q}{\partial t} = -\frac{\partial \overline{w'q'}}{\partial z} \tag{4.1}$$

where t and z are time and upward vertical coordinates respectively and w' the fluctuating component of the vertical velocity. The overbar denotes a time average. Finding expressions for the $\overline{w'q'}$ terms is the starting point for most geophysical numerical modelling and the starting point for the two mixed layer models used in this study.

4.2 Classes of 1D Model

In the literature four different classes of one dimensional upper ocean model have been reported. Although nomenclature differs from author to author the classifications of Kraus (1988) are used here. The four categories are discussed in Sections 4.2.1 to 4.2.4.

The "order" of turbulence closure is defined here to be equal to the highest prognostic moment. For example if a time evolution equation for a second moment is solved, such as $\frac{\partial \overline{w'q'}}{\partial t}$, then the closure is second order.

4.2.1 Direct Solution

The direct solution of the primitive equations, a so-called deterministic approach (Kraus 1977), used by Deardorff (1970) is too cpu time consuming for all practical applications, as has been noted. For practical application to the WEP such modelling will not be considered any further.

4.2.2 Transilient Models

A class of models which do not start explicitly from the averaged Navier-Stokes equations, although they clearly must satisfy them, are the transilient models. These models, introduced by Fiedler (Fiedler 1984) and Stull (Stull 1984; Stull 1986), involve the parameterisation of a spectrum of turbulent eddies, which can transport properties across a range of distances. A one dimensional transilient model would consist of a fluid column composed of N discrete cells, the quantity of a conservative property S, say temperature or U-momentum, in box j at time $n+1$ is given by

$$S_1, \ldots, S_N(t + \Delta t) = C_{ij} \cdot S_1, \ldots, S_N(t) \tag{4.2}$$

where

$$C_{ij} = \begin{pmatrix} c_{11} & \ldots & c_{1N} \\ \vdots & \vdots & \vdots \\ c_{N1} & \ldots & c_{NN} \end{pmatrix} \tag{4.3}$$

The dimensionless transilient coefficients C_{ij} represents the portion of property S which is mixed into box i from box j in a time Δt. This represents a non-local, first order closure of the turbulent exchange processes. If the off diagonal elements of C_{ij} are zero then the model is equivalent to a linear diffusive model, see Section 4.2.3. In satisfying the conservation requirements it also found that C_{ij} is symmetric. In the original formulation the transilient coefficients were taken to be functions of the bulk Richardson number (in common with many diffusive models), although later parameterisations have used available energy (Gaspar 1988).

4.2.3 Diffusive Models

Diffusive models again describe the time evolution of chosen properties on a finite grid, but exchange is limited to between adjacent grid points with the turbulent exchange processes parameterised by a diffusion type concept. Such models are therefore described as "local".

From the standpoint of the time averaged Navier-Stokes equations the problem is to close the set of equations. The most widely used approach is based on the idea of eddy viscosity and eddy diffusivity. These are conceptually to turbulent exchange what molecular viscosity and diffusivity are to kinetic theory. For example, the turbulent vertical U-momentum flux is assumed proportional to the eddy viscosity,K_M, times the vertical gradient in U;

$$\overline{u'w'} = -K_M \frac{\partial U}{\partial z} \tag{4.4}$$

Specification of K_Q (eddy diffusion coefficient for a property Q) throughout the boundary layer, K-theory, includes constant K_Q and a host of other parameterisations (Gaspar et al. 1988). Thus in this simplest case the time averaged equations can be closed. A sophistication of K-theory is mixing length theory, or L-theory, which follows from the proposition that the significant eddy size, or mixing length, L_m is proportional to the standard deviation of the vertical displacement of the fluid particles. In addition K_Q is then expressed as some functional form of L_m and the dynamics of the flow. Blackadar (1962) arrives at,

$$K_Q = L_m^2 \left[\left(\frac{\partial U}{\partial z} \right)^2 + \left(\frac{\partial V}{\partial z} \right)^2 \right]^{1/2} ; L_m = \kappa d/(1 + \kappa d/L_o) \tag{4.5}$$

where L_o is determined empirically. K and L-theory models are restricted to the prediction of the mean variables, thus representing first-order closure.

Predictive equations for the various correlations of the fluctuating quantities can be formally derived (Rodi 1982) introducing triple correlations of fluctuating quantities, which must be parameterised in terms of lower order quantities to close the expanded set of prognostic equations. Mellor and Yamada (1974; 1982) set down a systematic method of simplifying the parameterised second-order prognostic equations into 4 levels depending on their deviation from isotropy.

The level 4 model has prognostic equations for all ten second-order (ie. double correlation) terms with triple correlations parameterised or simplified in various ways (Rodi (1982) gives good treatment). The addition of a further variable, for example salinity, would require the solution of a further five PDEs in the level 4 scheme.

The level 3 model has predictive equations for turbulent kinetic energy (from equating the three velocity variances), and the temperature variance. Here the addition of salinity

would give two more PDEs, one for the mean salinity and one for the variance. The turbulent transports in the level 3 model come from algebraic expressions.

Level 2 and 1 models have predictive equations only for the mean variables, with diagnostic expressions for the stochastic variables. These models are therefore first-order, akin to L-theory models, and can be equivalent depending on the precise parameterisation used. A further model, level 2.5, was added (Mellor and Yamada 1982) for completeness which differs from the level 3 model in that the predictive equation for the temperature variance is replaced by a diagnostic one. This has the distinct advantage over the level 3 model, in that inclusion of additional scalars (eg. salinity or nutrients) increases the number of predictive equations to solve by only one.

4.2.4 Integral Models

Integral models, also known as bulk models, slab models or "Kraus-Turner" models, due to their pioneering work, are based on the *a priori* assumption that there is a single well defined depth, h, to which all the bulk quantities are homogeneously mixed. This depth is called the mixed layer depth. The time averaged Navier-Stokes equation and conservative scalar (temperature or salinity) equations are integrated over this depth. Thus predictive equations for the properties of the mixed layer are obtained. For example, integrating Equation 4.1 over the mixed layer gives

$$h\frac{\partial q_m}{\partial t} + \Delta q\left[\frac{\partial h}{\partial t} + w_h\right] = \overline{w'q'}(h) - \overline{w'q'}(0) \tag{4.6}$$

where q_m is the mean property value within the layer and $\Delta q = q_m - q(h)$. Given the right hand side as boundary conditions and w_h as a bulk vertical velocity with the layer, Equation 4.6 can be integrated forward in time once the evolution of h is specified. In fact what is required is a prediction of the entrainment velocity w_e, which is the change in mixed layer depth with time due to; (i) underlying fluid being mixed or entrained into the mixed layer or, (ii) mixed layer fluid leaving or detraining from the mixed layer. Clearly $\frac{\partial h}{\partial t} = w_e - w_h$. The work of integral mixed layer modelling has gone into parameterisations of w_e. This has been achieved either in terms of the partition of the turbulent kinetic equation (between wind generated turbulence, shear generated turbulence, buoyancy generated turbulence and turbulent dissipation within the mixed layer) or by the relaxation to some stability criteria of the mean variables or by a combination of these methods. Garwood

(1979) reviews five widely used parameterisations (Kraus and Turner 1967; Elsberry et al. 1976; Gill and Turner 1976; Kim 1976; Garwood 1977), finding his own to be the most sophisticated.

4.3 Choice of Models

Two models were used in this study, an integral model with the so-called Price-Weller-Pinkel (PWP) parameterisation (Price and Weller 1986), and a diffusive model with Mellor and Yamada (Mellor and Yamada 1982) level 2 (first-order, L-theory) closure. A transilient model was not chosen due to time and availability considerations.

The rationale behind the choice of models is as follows. Firstly, why two different classes of models? Integral models, although not necessarily straight forward to code, are very fast to compute. It is thus useful to know if such models are accurate in an equatorial setting, with their computational efficiency being a huge asset in any proposed coupled experiments. However it was envisioned that due to the difference in isothermal and isohaline depths frequently seen in the tropical oceans (Sprintall and Tomczak 1992) integral models may be inappropriate and a differential model required. The PWP model includes more physics than other integral models. The inclusion of a gradient Richardson number criterion smooths the otherwise sharp jump in property values at the base of the mixed layer.

For the choice of diffusive model it was decided that the level 3 code would be too time consuming. The level 2.5 model has been widely used in planetary boundary layer simulations over the years with considerable success. This was fuelled, no doubt, by Mellor and Yamada's (Mellor and Yamada 1982) observation that little was to be gained in terms of accurate boundary layer simulation by implementing the full level 3 scheme. In addition to this, Martin (1986) found less than 2% difference between mixed layer depth estimates of a level 2 and a level 2.5 model in a set of idealised forcing experiments. Thus the level 2 scheme was chosen.

4.3.1 PWP Parameterisation

The only artful part to integral models is the method of evolving the mixed layer depth h. The PWP model achieves vertical mixing within the mixed layer by requiring static stability, ie.

$$\frac{\partial \rho}{\partial z} \geq 0 \tag{4.7}$$

and bulk mixed layer stability, ie.

$$R_b = \frac{g\Delta\rho h}{\rho_0(\Delta V)^2} \geq 0.65 \tag{4.8}$$

where Δ is the difference between mixed layer value and the value just beneath. The first criterion, Equation 4.7 simulates free convection, which occurs whenever there is a net heat loss at the surface. The second criterion, Equation 4.8, simulates entrainment/detrainment by evolving h until the bulk Richardson number, R_b relaxes to a sub-critical value. At this point the model is like all integral models in that it assumes the existence of a sharp jump in properties at the base of the mixed layer. This is not borne out by observations, instead there is a smooth (on a scale of metres) transition layer across which the mixed layer properties match those of the fluid below. To simulate this observation the PWP model requires that the fluid below the mixed layer be stable to stratified shear flow instability, ie.

$$R_g = \frac{g\frac{\partial \rho}{\partial z}}{\rho_0(\frac{\partial V}{\partial z})^2} \geq 0.25 \tag{4.9}$$

4.3.2 Mellor Yamada Level 2

As already discussed, closure of the time averaged Navier-Stokes equations in the level 2 diffusive model is achieved by specifying the functional form for the turbulent viscosity, K_M and diffusivity, K_H

$$K_M = lqS_M \tag{4.10}$$

$$K_H = lqS_H \tag{4.11}$$

where l is a turbulent length scale, $q^2/2$ is the Turbulent kinetic energy (TKE) and S_M and S_H are stability functions which depend on the local Richardson number. The form of the stability functions can be found in the original paper (Mellor and Yamada 1982). The TKE, $q^2 = \overline{u'^2} + \overline{v'^2} + \overline{w'^2}$, is given by

$$q^2 = l^2 \left[(\frac{\partial \overline{U}}{\partial z})^2 + (\frac{\partial \overline{V}}{\partial z})^2 \right] [(S_M - RiS_H)/C_1]^{2/3} \tag{4.12}$$

The problem then remains to specify a length scale for the turbulent motions. For a logarithmic boundary layer we clearly require $l(z) \rightarrow kz$ as $z \rightarrow 0$, where k is von Karman's constant. Away from the boundary one might require $l \rightarrow l_o$ as $z \rightarrow \infty$. Various propositions for l_o have appeared in the literature (Mellor and Herring 1973). For want of a better approach, Mellor and Yamada (1982) suggest the adoption of the simplest length scale characteristic of the turbulent field, namely the ratio of the first to the zeroth moment of the profile $q(z)$. Thus,

$$l_o = \alpha \frac{\int_0^\infty zqdz}{\int_0^\infty qdz} \tag{4.13}$$

where α is an empirical constant which is considered not well known at present. Values between 0.1 and 0.2 have been used in the literature. A further simplification has been used, $l = l_o$, which does not produce logarithmic velocity behaviour near the surfaces, but has little impact on mixed layer deepening or temperature for an ocean surface mixed layer (Mellor and Yamada 1982).

Three commonly used length scale formulations, are (i) a simple boundary layer scaling,

$$l = k(z_o - z) \tag{4.14}$$

where z_o is the roughness length and prevents numerical instability as $l \rightarrow 0$, (ii) the simplification mentioned above

$$l = l_o \tag{4.15}$$

and, (iii) the Blackadar formulation (Blackadar 1962) which interpolates between these two limits

$$l = \frac{k(z_o - z)}{1 + \frac{kz}{l_o}} \tag{4.16}$$

These three scalings are compared in Section 4.7.

4.4 Mixed Layer Modelling in the WEP: A Review

To date four studies using mixed layer models to simulate upper ocean processes in the Equatorial Pacific have appeared in the literature. Three of the studies utilise integral models, (Schudlich and Price 1992; Ravier-Hay and Godfrey 1993; Garwood et al. 1989),

and one a diffusive model, (Chen and Rothstein 1991). Only one article, (Schudlich and Price 1992) appears in a refereed journal.

The first article, (Garwood et al. 1989), uses the Garwood mixed layer model, (Garwood 1977), with the addition of a finite thickness entrainment zone beneath the mixed layer. In this zone mixing is achieved by equal mixing of momentum and buoyancy just sufficient to maintain dynamic stability ($Ri_{cr} > 1/4$). This makes the model very similar to the PWP model discussed in Section 4.3. Salinity is not included. The authors prescribe a depth varying zonal pressure gradient integrally balanced by a constant westward windstress, and a depth varying upward vertical velocity in order to place the model on the equator. A diurnally varying heat flux with a mean of 100 W m^{-2} and a maximum of 800 W m^{-2} produces well mixed layer to approximately 20 m with a marginally stable entrainment zone approximately 100 m thick beneath. Turbulent kinetic energy dissipation in the entrainment zone varies from zero three hours after sunrise to just before sunset to a maximum of 2.1×10^{-7} m^2 s^{-3} which penetrates from 20 m at an hour after sunset to 70 m at six hours after sunset. They also found that over the diurnal cycle and the whole entrainment zone the vertical eddy viscosity, K_M, varied by three orders of magnitude whilst the Richardson number varied from just below 0.25 to 0.254. Thus their two main conclusions were; (1) instabilities initiated just below the well mixed surface layer ripple down into the water column and reach their extent only after many hours, causing a phase delay between surface buoyancy flux and turbulent fluxes at depth, and (2) the conclusion of Peters et al. (1988), that earlier parameterisation of K_M as a function of Ri are inadequate on the equator, is correct.

The second article, (Schudlich and Price 1992), uses the PWP one dimensional upper ocean model (Price and Weller 1986). The version used has a prescribed vertical velocity and is placed on the equator by approximately balancing the purely zonal windstress with a vertically varying zonal pressure gradient. Salinity was not included in the model. The study concentrates on explaining the observations made during the 1984 Tropic Heat experiment (Peters et al. 1988) on the equator at 140° W of large diurnal turbulent dissipation rates well below the mixed layer during nighttime convection. They found that a simple model can simulate the observed diurnal cycle of dissipation, provided such a model includes wind forcing, heat fluxes, a reasonable treatment of vertical mixing and importantly an equatorial undercurrent. A principle result is that the nighttime phase of the cycle is strongly affected by the EUC, resulting in deep mixing and large dissipation at

night that reaches nearly to the core of the EUC. The daytime phase for typical conditions at 140° W gave a 10 m thick stably stratified layer with little dissipation, a warming of SST of 0.2–0.5° C and a surface jet of 0.1–0.2m s^{-1} . Other equatorial features such as the zonal pressure gradient and persistent upwelling had little affect on the diurnal cycle.

The third article, (Ravier-Hay and Godfrey 1993) also uses the PWP model, but with salinity included. Their simulations were motivated by a 10 day data set taken during September 1990 at 4° S 149° E. The data set consists of heat fluxes, SST, surface salinity, precipitation and temperature at depths down to 1 m. The model reproduced temperature and salinity variations in the top metre reasonably well. Their main result, however, seems to be observational, showing a relationship, unquantified, between the diurnal variation of SST, solar radiation (cloud cover) and windspeed.

The diffusive model study (Chen and Rothstein 1991) uses a level 2.5 turbulence closure scheme (Mellor and Yamada 1982) to calculate the eddy viscosity and diffusivity. Salinity is included in the model, which is placed on the equator by setting $f = 0$ and balancing a constant zonal windstress with the vertically integrated zonal pressure gradient. They report on the effect of a single rain event of 20 cm day^{-1} lasting 24 hours, followed two days later by a wind burst of 0.25 N m^{-2} lasting 24 hours, followed again two days later by a wind burst of 0.6 N m^{-2} and of similar duration. From this limited experiment they conclude that two basic mixed layer states exist, one in which a locally produced barrier layer exists, and the other in which salt and heat are homogeneous down to approximately 80 m. Finally, since windbursts are less frequent than rain, they propose that this mechanism accounts for the prevalence of the barrier layer state.

4.5 Model Implementation

4.5.1 PWP Model

The PWP code was supplied by J. Price. The model has a uniform grid spacing, generally $\Delta z = 1$ m was used and a time step of 900 s. The code was modified to incorporate a depth dependent zonal pressure gradient, to drive an EUC. A three band short wave absorption model was also incorporated (Woods et al. 1984) as an improvement on the two band model supplied with the Price model. The equation of state used was the non-linear form developed for numerical modelling (Friedrich and Levitus 1972) but without pressure correction.

A no flux condition was imposed on the base of the model (200 m). Surface boundary conditions were heat, evaporation minus precipitation and momentum fluxes and divergent short wave heating. Initial conditions were profiles of T, S, U and V.

4.5.2 Mellor Yamada Level 2

The diffusive model was implemented and coded by the author as follows. The PDEs, for $\overline{U}, \overline{V}, \overline{T}, \overline{S}$ were differenced with a Crank-Nicholson scheme (Noye 1987). This is a semi-implicit forward time centre space scheme. The equations to solve are simple diffusion equations. For a property C,

$$\frac{\partial C}{\partial t} - \frac{\partial K \frac{\partial C}{\partial z}}{\partial z} = 0 \tag{4.17}$$

where K is a function of z. The momentum equations have a Coriolis term on the left hand side for completeness ($f = 0$ for most model runs). The U momentum equation has an additional forcing term corresponding to a zonal pressure gradient. Both terms are written in semi-implicit form. For the diffusion part of Equation 4.17 the differencing scheme looks like,

$$\begin{aligned} \frac{C_j^{n+1} - C_j^n}{\Delta t} &= \frac{1}{2\Delta z}\left(\frac{K_{j+\frac{1}{2}}^{n+1}(C_{j+1}^{n+1} - C_j^{n+1})}{\Delta z} - \frac{K_{j-\frac{1}{2}}^{n+1}(C_j^{n+1} - C_{j-1}^{n+1})}{\Delta z}\right) \\ &+ \frac{1}{2\Delta z}\left(\frac{K_{j+\frac{1}{2}}^{n}(C_{j+1}^{n} - C_j^{n})}{\Delta z} - \frac{K_{j-\frac{1}{2}}^{n}(C_j^{n} - C_{j-1}^{n})}{\Delta z}\right) \end{aligned} \tag{4.18}$$

where n and j are time and space indices respectively. The four equations are solved simultaneously using a standard tridiagonal matrix solver (Press et al. 1986). The implicit part is handled by iteration. The solution was found to converge rapidly such that two iterations were sufficient. The Richardson number, TKE and integral length scale were diagnosed at each iteration on each time step and hence K_M and K_H found. The same solar absorption scheme and equation of state (Friedrich and Levitus 1972) were used as were the various length scale formulations discussed in Section 4.3.2.

The model has a uniform grid spacing, Δz, variable number of grid points, nz, and variable time step, Δt. As with the PWP model most experiments were run with $\Delta z = 1$ m, $nz = 200$. To maintain numerical stability Δt varied from between 5 and 60 s depending on the experiment.

4.5.3 Model Testing

To test that the models had been implemented correctly a number of checks were made. Checking PWP model was straight forward. As given by J. Price the code had default initial and boundary conditions corresponding to day 131 of Price et al. (1986). The model reproduced the results shown in that article.

The diffusive (Mellor/Yamada level 2) model was tested against the idealised forcing experiments of Martin (1986), who compared a number of models including a Mellor/Yamada level 2. Eight experiments for each model configuration were made, three experiments in each of the two categories of wind deepening, surface heating, and two experiments of surface cooling. Results are shown in Table 4.1. The definition for mixed layer depth for the diffusive model was the depth to which $Ri < Ri_c$. All experiments had the same initial conditions, namely zero vertical shear, constant salinity, SST of 24° C, and thermal stratification a uniform 0.05° C m^{-1}. For the heating and cooling experiments the wind stress was kept constant at 0.1 N m^{-2} . It is clear from Table 4.1 that the MLDs (and SSTs, not shown) are quite insensitive to the particular length scale formulation. This is encouraging as there is no unambiguous theoretical basis for it's form. It also appears that the model coded here systematically underestimates the MLDs during the cooling experiments. This is thought to be due to slight differences in the way the models were set up rather than the different numerical schemes. The most likely candidates, which were not given for the reference case (Martin 1986), are different background diffusivities and/or a different critical Richardson number or simply a difference in the definition of mixed layer depth. Therefore it was taken from these experiments that the model had been coded correctly and was functioning as expected.

4.6 A Modelled Diurnal Cycle

Series of experiments were designed to see how the model's surface properties and depth of mixing over a diurnal cycle depend on boundary and initial conditions. Model boundary conditions are windstress, surface heat flux, and surface moisture flux (evaporation and precipitation). Initial conditions are depth and amplitude of EUC (velocity shear), amplitude of zonal pressure gradient, and presence or otherwise of a "barrier layer". The effect of varying the latitude from 0°to 5°was also examined in order to assess the sensitivity to an off equatorial setting, but still within the warm pool. The effect of varying the verti-

Experiment	Martin (1986)	Length Scale 1	Length Scale 2	Length Scale 3
Q=0 W m^{-2} ,τ = 0.1 N m^{-2}	18	18	18	18
Q=0 W m^{-2} ,τ=0.4 N m^{-2}	42	40	36	32
Q=0 W m^{-2} ,τ=1.6 N m^{-2}	78	80	76	74
Q=73 W m^{-2} ,τ = 0.1 N m^{-2}	26	22	20	20
Q=290 W m^{-2} ,τ = 0.1 N m^{-2}	14	14	12	12
Q=2400 W m^{-2} ,τ = 0.1 N m^{-2}	8	8	8	8
$Q = -48$ W m^{-2} ,τ = 0.1 N m^{-2}	72	67	65	66
$Q = -96$ W m^{-2} ,τ = 0.1 N m^{-2}	101	95	92	92

Table 4.1: Mixed layer depths of diffusive model test runs in metres. The cited MLD is at day 5 for wind deepening, at day 2 for heating, and at day 120 for cooling.

cal velocity was investigated for completeness but is not reported here as the conclusions mirror those of Schudlich and Price (1992), namely that the diurnal cycle is insensitive to physically plausible vertical velocities, since the entrainment velocity associated with the diurnal cycle is far greater than any realistic vertical velocity.

The reference case used has heat loss (long wave, latent and sensible heat) , Q_{loss} = 200 W m^{-2} , 150 W m^{-2} of which is latent heat loss, Q_{lat}, zonal windstress $\tau_x = -0.03$ Nm^{-2}, zero meridional windstress and solar insolation $Q_{sw} = -800\cos^2(\pi t/12)$ from 6 am until 6 pm where t is the hour of day. This functional form is closer to the full astronomical form (Horch et al. 1983) than the simple cosine form often used (Schudlich and Price 1992). It has the advantage of having a similar time integral to the observed short wave radiation given the same maximum value, unlike the simple cosine form which either over estimates the integrated flux or under estimates the maximum value by about 20% (since $\int_0^{\pi/2}\cos(t)dt = \pi/4(\int_0^{\pi/2}\cos^2 tdt)$). These boundary conditions are representative of the CD32 observations of the fluxes, but with Q_{lat} increased and Q_{sw} decreased in order that the net heat flux be zero for this reference case. The reference initial conditions are representative profiles of T, S, U and V observed on the equator during CD32, shown in Figure 3.2.

4.6.1 Depth of Mixing

In order to compare directly the two models series of idealised forcing experiments were carried out. Direct comparison of two fundamentally different models is not straightforward. The diffusive model does not prognose a mixed layer depth, diffusivities in the

slab model are effectively infinite at times of static instability and the gradient Richardson number is undefined in the slab mixed layer. What is required here of the models is that they faithfully predict the surface or mixed layer values of prognosed properties and the depth to which they are homogeneous, or more importantly the rate at which these variables change. In comparing the models, property surface values and depth of mixing are shown in tabular form. Time series of SST and depth of mixing are also compared for the reference case.

Depth of mixing is defined as the mixed layer depth for the PWP model. For the diffusive model the depth of mixing is taken to depend on the value of K_M, as this represents mixing in such a model. To avoid numerical instability the diffusive model has a non zero background diffusivity and viscosity, $K_T = K_S = 1.34 \times 10^{-6}$ m^2 s^{-1} and $K_M = 1.34 \times 10^{-5}$ m^2 s^{-1} respectively, ie. Prandtl number of 10. The question to be answered now is what lower limit of K_M can be considered as representative of turbulent mixing. During convective overturning, model values of $K_M = 0.5$ m^2 s^{-1} are attained. Appealing to empirical input, the mean Monin-Obukov Length, L_M, observed during the net heating phases of CD32 was 6.4 m, which would imply a $K_M = ku^* L_M = 0.01$ m^2 s^{-1}, where the friction velocity $u^* = (\tau/\rho)^{1/2}$ and $k = 0.4$ is von Karman's constant. Thus the depth of mixing was taken as the first depth working from the *bottom* of the domain at which $K_M \geq 0.01$ m^2 s^{-1}. This will be taken as the definition of "mixed layer depth" for the diffusive model in all text that follows.

4.6.2 Transition Layer

The PWP model prognoses a so called "transition layer" depth. This is the layer beneath the mixed layer where properties vary smoothly to match those well below the mixed layer by relaxation of the gradient Richardson number to 0.25. Schudlich and Price (1992) successfully relate this transition layer to the region of high turbulent dissipation observed beneath the equatorial mixed layer. The extent of this transition layer is thus of great interest particularly when considering the divergence of momentum in the upper ocean.

It is straightforward to define a transition layer for the diffusive model in a manner which is physically plausible and gives results consistently similar to the PWP transition layer. The transition layer for the diffusive model is defined as the region beneath the mixed layer, defined above, where K_M is greater than the background value. Thus the transition layer is defined as the region 1.34x10^{-5} $\geq K_M \geq$0.01 m^2 s^{-1}. Within the physics

of the model this represents a region in which mixing has been enhanced by surface forcing or imposed shear but in which significant property gradients exist. Figure 4.1 show heat flux profiles, explained in the next Section (Section 4.6.4). Marked on the profiles with an open circle and a star are the mixed layer and transition layer depths respectively.

4.6.3 Δ t and Δ z

The time step, Δt, for the PWP model was set to 450 s for all runs. At $\Delta t = 900$ s the model began to lose heat. Reducing Δt to less then 450 s made no appreciable difference to the model output. The diffusive model had to be run with a substantially shorter Δt of 5 s for the experiments with the largest surface fluxes. In some experiments using the diffusive model it was possible to increase Δt to 60 s without loss of numerical stability. All experiments reported here were run with $\Delta t = 5$ s.

In all experiments the grid spacing, Δz, was set to 1 m and the grid size to 200 points. Reducing Δz to 0.5 m made no appreciable difference to either model.

All prognostic variables were output at all levels every hour. Additionally K_M and K_T were output in the case of the diffusive model.

4.6.4 Thermal Cycle

As noted above, *changes* in near surface temperatures during the diurnal cycle are of interest. It is thus helpful to describe the thermal cycle in terms of heat flux profiles, $F(z)$, which are calculated by integrating changes in temperature upward from some reference depth of no change (200 m here).

$$F(z) = \rho C_p \int_{200}^{z} \frac{\partial T}{\partial t} dz \tag{4.19}$$

Heat flux profiles calculated in this way are shown in Figure 4.1. Superimposed on the profile plots are the mixed layer depth (open circle) and the transition layer depth (cross). For this qualitative description, only results from the integral model are shown.

Warming Throughout

From about 07:30 until 13:00 there is net heating throughout the water column. At levels shallower than the mixed layer depth the heat flux profiles are linear in z, indicating uniform

heating within the homogeneous layer. Beneath the mixed layer depth the heat flux profiles decrease exponentially with z, illustrating the penetration of short wave radiation beneath the mixed layer. The transition layer is thin O(5 m) showing the effect of the monotonic, stabilising buoyancy flux damping turbulence at all levels. The mixed layer is at its shallowest between 11:00 and 12:00, during the period of most intense warming. SST peaks at around 12:00, just before the mixed layer begins to deepen and the surface heat flux decrease.

Surface Cooling, Deep Warming

From 13:00 onward a kink develops in the heat flux profiles which propagates downward throughout the afternoon and evening. This indicates cooling at the surface and heating at a depth z until the kink passes, at which time cooling at that level will commence. Again linear flux profiles above the mixed layer depth indicate uniform cooling of the mixed layer. Cooling at the surface commences whilst there is still net heating due to the action of the wind mixing the heat downward. Thus the asymmetry in the SST cycle, with SST increasing for only about 5 hours per day, is attributable to wind mixing. From 18:00 the mixed layer deepening becomes more rapid as the net surface heat flux changes sign and convective overturning begins. The layer of sub-surface heating is thus caused by wind mixing and convective overturning and corresponds quite closely to the transition layer in the two models. It should be noted that in this reference case the diurnal cycle is not in equilibrium, in the sense that there is a net decrease in SST and a net increase in temperature at depth as a consequence of progressively greater daily maximum mixed layer depth.

Diurnal Jet

A diurnal velocity jet comes about because momentum is mixed in a similar way to heat and salt in the models. With the constant windstress of the reference run, the zonal jet has a maximum velocity between 11:00 and 12:00, when the mixed layer is shallowest. The absence of rotation makes the diurnal velocity jet more straight forward than at mid-latitudes and at the same time it's impact greater. The inertial oscillation of the jet at mid-latitudes turns it upwind by the following morning, and thus it can be nearly erased by the windstress that caused it the previous day. On the equator, however the windstress acts as a body force on the mixed layer. When integrated over the diurnal cycle, with no

retarding force the layer can rapidly accelerate, as has been seen in Section 2.3. Ultimately the retarding force is the ZPG, which responds to changes in east/west sea surface and thermocline slope on time scales of weeks to months. As has been stated, experiments with mixed layer models have shown the diurnal cycle to be insensitive to the nature of the ZPG.

4.7 Sensitivity Tests and Model Comparisons

A comparison of the behaviour of the two models will be made by considering the reference case. Figure 4.2 shows time series of SST and mixed layer depth for the first 150 hours of both models. The solid line is for the PWP models, the dashed line for the diffusive model. The same pattern of differences is seen in all subsequent experiments. The most significant difference between the models occurs during the heating/restratification phase of the diurnal cycle. The diffusive model stratifies completely at midday, with a mixed layer depth of zero at this time. However the transition layer thickness remains non-zero, with a value of 3 m at midday. In contrast the PWP model mixed layer depth is 2 m at midday, whilst the transition layer thickness is zero at this time. These differences may seem somewhat arbitrary considering the ad hoc nature of the mixing depth definitions for the diffusive model. However these differences are confirmed by the SST time series, which show the diffusive model to warm by 0.1° C more than the PWP model. From this it is seems that wind mixing has a greater efficiency in the PWP model, and is in accord with the conclusion of Kantha and Clayson (1994) that there is too little mixing across stabilising density gradients in the Mellor Yamada level 2 model. A somewhat more surprising result is that both models simulate nighttime convection in a very similar manner. Both the rate of deepening and the maximum depth attained match closely, although the initial deepening of the diffusive model is more rapid. The maximum MLD for the diffusive model is slightly deeper at 48 m compared to 43 m, however in compensation the PWP transition layer is thicker at 26 m compared to 19 m. This was unexpected for a number of related reasons. Firstly, the diffusive model is unable to simulate free convection (without shear there is no mixing), as can be seen in the run with $\tau_x = 0$. Secondly, the results of one 120 day cooling experiments with constant windstress (Martin 1986) showed the same diffusive model deepening considerably less than slab models of Garwood and Niiler. In the same vein, Kantha and Clayson (1994) try to ameliorate what they see as a general trait of too

little convective entrainment in the Mellor and Yamada models by enhancing mixing in the transition region below the mixed layer.

In parallel to the greater surface trapping of buoyancy in the diffusive model, momentum is also surface trapped during strong surface heating (the model has a turbulent Prandtl number $Pr = 0.7$ averaged over a diurnal cycle). The diurnal jet thus has a greater surface value of $U = 16$ cm s^{-1} in the diffusive model compared with $U = 9$ cm s^{-1} in the PWP model. However the transport integrated across the boundary layer, the Ekman transport, is of course the same for both models. It is this large shear built up in the diffusive model which assists the rapid deepening observed as surface heat flux begins to decrease.

Both models are qualitatively able to reproduce a diurnal cycle in the ocean planetary boundary layer. Chapter 5 presents direct simulation of both CD32 data and TOGA COARE data. Before discussing direct simulations of the observations, the sensitivity of the models to changes in boundary conditions, initial conditions and some internal parameters needs to be considered.

4.7.1 Sensitivity Tests

Sensitivity experiments were run for six days with all conditions as for the reference case except for the parameter under examination. Except for the transition layer thickness, values shown in Tables 4.2 to 4.7 are averages over the last five days of daily values of the variables. The transition layer thickness is the difference between the average maximum transition layer depth and average maximum mixed layer depth. All results are given in Tables 4.2 to 4.7.

Integral Length Scale

The relatively shallow boundary layers of the diurnal cycle might be affected by the choice of length scale. The reference experiment employs the simplest length scale formulation, $l = l_o$, where l_o is defined in Equation 4.13. Boundary layer scaling, Equation 4.14, should result in lower values of K_M and K_T in shallow boundary layers. However applying the boundary layer scaling or the Blackadar length scale, Equation 4.16, which tends to the same limit near the surface makes negligible difference (Table 4.5). Thus all experiments with the diffusive model use the simplest scaling, $l = l_o$.

Parameter	MLD (m)		Δ SST	Transition	Δ U
	min	max	°C	layer (m)	cms^{-1}
Reference	2	43	0.22	26	9
$\tau_x = 0\ N\ m^{-2}$	1	48	0.87	12	0
$\tau_x = -0.01\ N\ m^{-2}$	1	45	0.4	18	7
$\tau_x = -0.05\ N\ m^{-2}$	2	47	0.19	30	12
$\tau_x = -0.1\ N\ m^{-2}$	4	56	0.16	37	15
$\tau_x = -0.3\ N\ m^{-2}$	10	81	0.08	60	22
$Q_{sw} = 0\ W\ m^{-2}$	52	54	0.07	26	1
$Q_{sw} = 500\ W\ m^{-2}$	4	47	0.09	27	5
$Q_{sw} = 750\ W\ m^{-2}$	2	44	0.21	27	9
$Q_{sw} = 1000\ W\ m^{-2}$	2	41	0.36	24	12
$Q_{sw} = 1250\ W\ m^{-2}$	2	34	0.6	23	15
$Q_{lat} = 0\ W\ m^{-2}$	1	32	0.5	10	27
$Q_{lat} = 160\ W\ m^{-2}$	2	43	0.21	27	10
$Q_{lat} = 200\ W\ m^{-2}$	2	50	0.21	26	6
$Q_{lat} = 240\ W\ m^{-2}$	3	49	0.16	27	7
$Q_{lat} = 300\ W\ m^{-2}$	4	54	0.14	26	5

Table 4.2: PWP model response to variations in boundary conditions

Wind Stress Dependence

Tables 4.2 and 4.3 show wind stress sensitivity for the PWP and diffusive models respectively. As already pointed out, the Mellor/Yamada level 2 diffusive model is unable to simulate free convection. As the windstress is increased in the diffusive model both transition layer thickness and maximum MLD increase. ΔSST decreases as the same heat is mixed over successively greater depths. ΔU is less sensitive to τ_x as the effects of more momentum and a greater depth of mixing compensate each other to some degree. The response of the PWP model to increasing windstress is less straightforward as both static and Richardson number instability need be considered. With no shear mixing the diurnal cycle is more symmetric and the daily mean SST is constant, ie. there is no entrainment of cooler fluid from below the mixed layer. The thermal stratification generated during the day is completely eroded at night. The maximum MLD is less than that with which the model was initialised only by the mixing performed in the transition layer to smooth the otherwise sharp property jump at the base of the mixed layer. The transition layer is only non-zero when the mixed layer is at its deepest. At other times there is no shear and thus no transition layer beneath the mixed layer.

When wind (shear) mixing is present within the mixed layer, a velocity step is generated at the base of the mixed layer. This is stabilised by diabatic heating during peak heating, after which a non-zero transition layer is formed. Thus the water the mixed layer is mixing into as it deepens is cooler by an amount dependant on the transition layer thickness. Consequently the reduction in maximum MLD as τ_x is increased from 0 to 0.03 N m^{-2} is a function of the thermal stratification beneath the mixed layer.

In these experiments a diurnal cycle is quite pronounced even with a windstress as high as 0.3 N m^{-2} . It should be noted, however, that without some form of atmospheric feedback, whereby, for example increased windspeed may be accompanied by reduced shortwave flux, these results need to be treated with some caution. The four fold increase of ΔSST as τ_x is reduced from the climatological value of 0.03 N m^{-2} to 0 N m^{-2} is worth noting.

Parameter	MLD (m)		Δ SST	Transition	Δ U
	min	max	°C	layer (m)	cms^{-1}
Reference	0	48	0.32	19	16
$\tau_x = 0$ N m^{-2}	0	0	2.22	0	0
$\tau_x = -0.01$ N m^{-2}	0	46	0.60	15	12
$\tau_x = -0.05$ N m^{-2}	0	52	0.24	21	18
$\tau_x = -0.1$ N m^{-2}	0	61	0.19	26	21
$\tau_x = -0.3$ N m^{-2}	50	99	0.16	66	18
$Q_{sw} = 0$ W m^{-2}	54	56	0.07	22	1
$Q_{sw} = 500$ W m^{-2}	0	50	0.11	21	9
$Q_{sw} = 750$ W m^{-2}	0	51	0.28	17	15
$Q_{sw} = 1000$ W m^{-2}	0	44	0.53	18	19
$Q_{sw} = 1250$ W m^{-2}	0	37	0.8	18	23
$Q_{lat} = 0$ W m^{-2}	0	6	0.6	34	22
$Q_{lat} = 160$ W m^{-2}	0	49	0.31	19	15
$Q_{lat} = 200$ W m^{-2}	0	54	0.27	20	11
$Q_{lat} = 240$ W m^{-2}	0	54	0.21	20	12
$Q_{lat} = 300$ W m^{-2}	0	58	0.16	20	9

Table 4.3: Diffusive model response to variations in boundary conditions

Heat Flux Dependence

Sensitivities to short wave radiation and latent heat flux are shown in Tables 4.2 and 4.3. Both models show monotonic increase in ΔSST and ΔU and decreasing minimum and maximum MLD and transition layer thickness with increasing Q_{sw}. In both models the

change in transition layer thickness is not great (4 m). In the PWP model a 25% change in Q_{sw} around 1000 W m^{-2} results in a change in ΔSST of about 0.2°C. The diffusive model is fractionally more sensitive with a change in ΔSST of 0.25°C. This is a reflection of greater suppression of turbulence by diabatic buoyancy forcing in the diffusive model, also seen in the greater sensitivity of the MLD excursion.

With $Q_{lat} = 0$ there is still a heat loss of 50 W m^{-2} due to the sensible and long wave heat fluxes, although the destabilising effect of evaporation is absent. It appears that the PWP model mixes much deeper (MLD=32 m compared with 6 m for the diffusive model) under conditions of very small heat loss, however examination of the MLD time series for the PWP model shows that depths in excess of 15 m are attained for only one or two hours at a time and not on every night. In addition, the maximum depth of influence of surface forcing (mixed layer depth plus transition layer thickness), or transition layer *depth*, is approximately 40 m for both models. With non-zero Q_{lat} both models show increasing maximum MLD with increasing Q_{lat}, while the transition layer thickness is unaffected and ΔSST decreases. It is interesting to note that a 20% change in Q_{lat} (a typical error on any such measurement) can lead to a change in ΔSST of 0.1° C.

ZPG and Latitude Dependence

Variations in the ZPG have little, if any, impact on the diurnal cycle. The value of z_o in Tables 4.4 and 4.5 is the length scale of the vertical guassian form used for the ZPG, namely,

$$ZPGF(z) = ZP_o \exp -(z/z_o)^2 \tag{4.20}$$

where $ZPGF$ is the zonal pressure gradient force applied to the U-momentum equation, and ZP_o is specified by balancing with the windstress, ie.

$$\tau_x = \int_{z=200}^{z=0} ZP_o \exp -(z/z_o)^2 dz \tag{4.21}$$

Thus, even with z_o=100 m, insufficient vertical shear is generated to effect mixing.

Changes in latitude, however, have a very interesting impact on the diurnal response. There is a dramatic reduction in the transition layer thickness as latitude increases. Additionally there is a greater trapping of momentum within the mixed layer. At a latitude of 10° the Ekman Layer e-folding scale, $L_E = (2K_M/f)^{1/2}$, is O(100 m) for $K_M = 0.2$ m^2

s^{-1} , a typical value within the mixed layer of the diffusive model. However within the transition layer, where $K_M \approx 0.005\ m^2\ s^{-1}$, L_E is O(10 m). Thus one might expect rotation to constrain the transition layer thickness in the manner predicted by the models.

Parameter	MLD (m)		Δ SST	Transition	Δ U	Δ V
	min	max	°C	layer (m)	cms^{-1}	cms^{-1}
Reference	2	43	0.22	26	9	0
$\theta = 2.5°$	2	45	0.22	21	11	12
$\theta = 5.0°$	2	51	0.22	11	15	23
$\theta = 10.0°$	2	51	0.22	10	31	35
$z_o = 100m$	2	44	0.22	28	10	0
$z_o = 150m$	2	43	0.22	28	10	0
$z_o = 200m$	2	43	0.22	27	10	0

Table 4.4: PWP model response to variations in latitude (θ) and ZPG

Parameter	MLD (m)		Δ SST	Transition	Δ U	Δ V
	min	max	°C	layer (m)	cms^{-1}	cms^{-1}
Reference	0	48	0.32	19	16	0
$\theta = 2.5°$	0	47	0.32	19	21	5
$\theta = 5.0°$	0	51	0.32	8	21	23
$\theta = 10.0°$	0	51	0.32	8	33	34
$z_o = 100m$	0	49	0.32	20	16	0
$z_o = 150m$	0	47	0.32	20	16	0
$z_o = 200m$	0	48	0.33	20	16	0
Boundary Layer Scaling	0	47	0.35	19	17	0
Blackadar Scaling	0	47	0.35	19	17	0

Table 4.5: Diffusive model response to variations in latitude, ZPG and Integral length scale

Vertical Shear

Tables 4.6 and 4.7 show the sensitivity of the models to imposed vertical shear and, more as a prelude to Section 5.3, the effect on the diurnal cycle of an imposed barrier layer. In the western equatorial Pacific vertical shear can be changed by a change in intensity of the SEC or EUC and/or by a vertical displacement of the EUC. The reference case corresponds to $\frac{\partial U}{\partial z} = -0.5\ s^{-1}$. The range of the sensitivity study is from no imposed vertical shear to

1.5 m s^{-1} over 100 m. This could correspond to an SEC of 50 cms^{-1} overlying an EUC of 100 cm s^{-1} with it's core at 100 m. Both models exhibit the same trend. As the ambient shear is increased from zero to 0.015 s^{-1} the maximum MLD increases by 7 m for the diffusive model and by 19 m for the PWP model. One might expect this increase to be accompanied by a decrease in the diurnal range in SST and U. However mixing in the models in not effected by depth-independent accelerations. In the heating phase of the diurnal cycle the mixed layer depth shallows rapidly to depths O(5 m). The vertical shear, though possibly large, has a depth scale O(100 m) and thus appears depth-independent to the heating phase of the diurnal cycle.

The most dramatic effect of increasing the ambient shear is on the thickness of the transition layer. In the diffusive model it increases from 11 m to 57 m, and in the PWP model from 14 m to 72 m. If one associates this region with potentially high dissipation rates, then one can see penetration of surface information to depths in excess of twice the mixed layer depth under conditions of strong vertical shear.

Parameter	MLD (m)		Δ SST	Transition	Δ U
	min	max	°C	layer (m)	cms^{-1}
Reference	2	43	0.22	26	9
U_z = 0 s^{-1}	2	47	0.22	14	9
U_z = -0.75 s^{-1}	2	43	0.22	34	9
U_z = -1.0 s^{-1}	2	43	0.23	43	9
U_z = -1.25 s^{-1}	2	45	0.22	56	9
U_z = -1.5 s^{-1}	2	62	0.22	72	9
BL = 10 m	2	36	0.22	21	9
BL = 20 m	2	30	0.22	23	9
BL = 30 m	2	27	0.21	21	10

Table 4.6: PWP model response to variations in initial conditions

4.8 Discussion

Both models used seem able to simulate a diurnal cycle typical of the western equatorial Pacific. The diurnal variation in SST of a few tenths of a degree Celsius is in accord with the TOGA COARE observations (Section 2.5) as is the diurnal excursion of the mixed layer depth of around 40 m. Observational evidence for a diurnal velocity jet is difficult to find in the present data sets due to aliasing with tidal currents. Surface drifter observations

Parameter	MLD (m)		Δ SST	Transition	Δ U
	min	max	°C	layer (m)	cms^{-1}
Reference	0	48	0.32	19	16
U_z = 0 s^{-1}	0	48	0.32	11	16
U_z = -0.75 s^{-1}	0	47	0.32	26	16
U_z = -1.0 s^{-1}	0	49	0.32	33	16
U_z = -1.25 s^{-1}	0	52	0.33	41	16
U_z = -1.5 s^{-1}	0	55	0.33	57	16
BL = 10 m	0	37	0.32	16	18
BL = 20 m	0	30	0.32	16	19
BL = 30 m	0	25	0.32	20	16

Table 4.7: Diffusive model response to variations in initial conditions

near the equator quoted by Schudlich and Price (1992) did show a diurnal cycle of 13 cm s^{-1} .

The transition layer defined for the Mellor/Yamada level 2 model gives an indication of the depth of influence of surface forcing beneath the mixed layer. The modelled diurnal cycle is insensitive to the three integral length scale forms tried. However, in agreement with other investigators, there is found to be too little mixing in the model, resulting in a zero thickness midday mixed layer depth with a wind stress of 0.1 N m^{-2} . These findings in combination with a run time two orders of magnitude longer than the PWP model suggest there is nothing to be gained in using this type of diffusive model in equatorial simulations. In the following chapter only the PWP model is used for the 70 day experiments.

Summarising the results of the sensitivity studies: Vertical shear, zonal pressure gradient and the value of f have a negligible effect on the diurnal thermal cycle. Vertical shear and latitude both effect the momentum cycle. Doubling the shear from 0.75 s^{-1} increases the mixed layer depth by 50% and doubles the transition layer thickness. The effects of rotation are seen in reducing the transition layer thickness as the latitude is increased. Variations in wind stress impact both on the thermal and momentum cycles. In light wind conditions the diurnal SST range reaches approximately 1°C. In reality this figure is likely to be higher with increased short wave radiation usually associated with light winds. Large wind stress reduces the amplitude of the diurnal SST cycle and increases both minimum and maximum mixed layer depth and the thickness of the transition layer. Thus large ambient vertical shear and strong winds on the equator provide a situation in which wind stress can penetrate well below the apparent mixed layer. Peak solar insolation can affect

both the SST range and maximum mixing depth by a few tenths of a degree and about 5 m when varied over a realistic range of 800 to 1100 W m^{-2} . heat loss over a reasonable range of 160 to 240 W m^{-2} has a slightly smaller effect on the diurnal SST range of about 0.1°C.

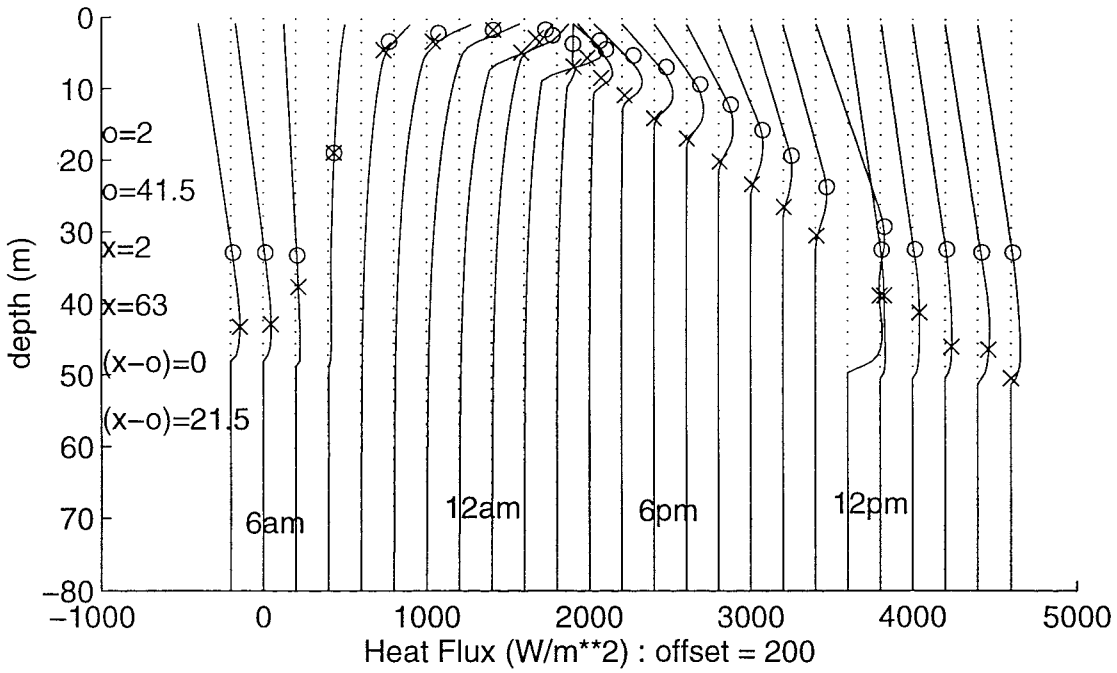

Figure 4.1: Heatflux profiles for the integral model. Profiles are at hourly intervals, starting at 5 am. Profiles are offset by 200 W m^{-2} . Dotted line is the zero heat flux line for each profile: If the solid line is to the left (right) of the dotted line, there is cooling (warming) at that level and at that time. Open circles indicate the mixed layer depth, crosses indicate the base of the transition layer. The numbers on the left hand side are (from top to bottom): minimum mixed layer depth, maximum mixed layer depth, minimum transition layer depth, maximum transition layer depth, minimum transition layer thickness and maximum transition layer thickness.

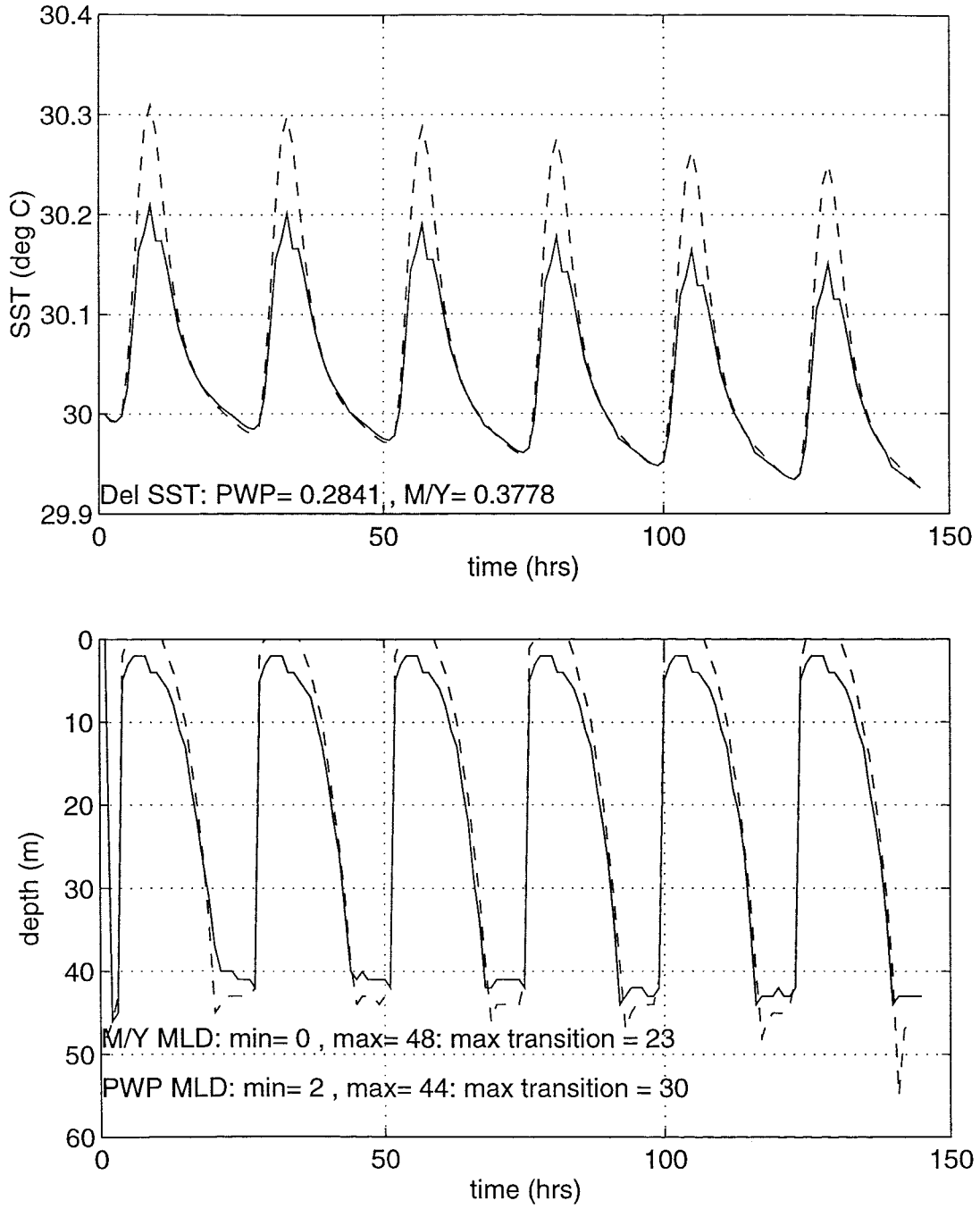

Figure 4.2: Time series of SST (upper panel) and mixed layer depth (lower panel). Dashed line is for the diffusive model, solid line for the PWP model. Mean diurnal ranges of SST for both models are given in the upper panel. Minimum and maximum mixed layer depths and maximum transition layer thickness for both models are also given.

Chapter 5

Simulation of Observed Diurnal Variability

In the last chapter it was seen that one dimensional mixing models are qualitatively able to simulate the diurnal cycle of heating and mixing in an equatorial setting. Both the CD32 and TOGA COARE data sets provide a combination of measurements of surface fluxes, hydrography, and upper ocean currents. Using these observations it is possible to carry out one dimensional simulations of the upper ocean during the survey periods. This exercise serves two purposes. Firstly, it gives some insight into the ability of the models to simulate the *observed* diurnal cycle. Secondly, it allows the physical processes responsible for variability in the observed diurnal cycle to be determined.

Both the PWP and the diffusive models were used in the simulations of the CD32 observations. Only the PWP model was used on the TOGA COARE simulation due to cpu time considerations.

5.1 CD32 Simulation

5.1.1 Boundary and Initial Conditions

Both models were initialised with profiles of T, S, U and V observed on jday 108.0 (1988), shown in Figure 3.2. The models were then forced with the observed fluxes of heat, moisture and momentum for seven days starting on day 108.0. The heat fluxes are shown in Figure 3.7. A note on the moisture flux is in order here. The evaporative moisture flux was calculated directly from the latent heat flux, using a constant latent heat of evaporation. The fresh water flux was taken from the rain gauge measurements, made every 3 hours. The five rain events are listed Table 5.1. All events were of less than 3 hour duration. Rain

events 1 and 3 were omitted from the forcing fluxes as both occurred on the western side of the survey area at times the ship was moving eastward. The 50 cm s^{-1} westward surface current made it unlikely that the water effected by these rain events would be resampled at any point.

Event Number	Local time (jday)	Latitude (degrees)	Longitude (degrees)	rainfall (mm)
1	108.33	−0.038	164.38	46
2	109.08	0.025	164.69	7
3	110.08	0.123	164.49	13
4	111.08	0.130	164.73	67
5	113.08	0.021	164.75	30

Table 5.1: Rain events during CD32, 1988 on the equator at 165°E.

Sensitivity of the simulations to the turbidity of the water is examined, given the poor simulation of near surface temperatures. Following this series of experiments were made to examine the effect on the diurnal cycle of the variability of the components of the boundary conditions and of the nature of the initial conditions.

Results are presented variously as time series of MLD, temperature at 4 m and 15 m, and salinity at 4 m. The 4 m depth of the TSG water intake was the shallowest temperature record made during the cruise.

5.1.2 Direct Simulation of CD32 Observations

The observed diurnal response of the upper ocean during CD32 was discussed in Section 3.3. It was noted there that horizontal temperature gradients across the survey region gave rise to temperature signals in the data of the same order of magnitude as the diurnal cycle, but despite this the oceanic response to the atmospheric forcing was uniform over the survey region. Figure 5.1 shows the spar buoy 15 m temperature record, (blue line), the 15 m temperature extracted from the Seasoar record, (black line) and the 15 m temperature simulation from both models, (PWP in red, diffusive model in green). The observational records have been filtered with a 6 hour low pass filter. This figure shows the problems of spatial aliasing of the Seasoar data and difficulties thus caused in making comparison between model output and Seasoar data. It is ambiguous as to which changes in the Seasoar record are of local atmospheric origin and which are due to horizontal gradients. Comparison of PWP model output with the spar buoy temperature record shows agreement to

within 0.05°C for the first 24 hours of simulation. Thereafter the diurnal signal within the observations becomes less clear. The diurnal signal in the Seasoar data continues beyond this time, but given the spar buoy record it is likely to be a product of the 12 and 48 hour periods in the sampling strategy. It is also fair to say that given the accuracy of the PWP simulation in particular over the first 24 hours and the continuing clear diurnal signal in the model simulation that the loss of diurnal signal in the spar buoy temperature record is due predominantly to advective effects. As one might have predicted from the sensitivity studies the two models behave in a very similar manner, with the 15 m temperatures being within 0.05° C throughout the simulations.

Bearing in mind the spatial aliasing of the Seasoar data there is little to be gained from comparisons of modelled and observed temperature profiles, but by way of comparison with the recently published results of Kantha and Clayson (1994) it is worthwhile to consider the sea surface temperature. Figure 5.2 shows the TSG temperature record with the models 4 m temperatures superimposed. The observed diurnal temperature range at 4 m is up to a factor of 5 greater than the modelled range. However the observed horizontal temperature gradient over the survey area was 4×10^{-6} °C m^{-1}, (see Section 3.4). This could give rise to an increased diurnal range of up to 0.5°C given the sampling strategy. Thus it is not possible to say how accurately the models predicted the diurnal range of 4 m temperature. However, it is fair to say that the modelled range is not greater than that observed. An attempt to remove this sampling bias by assuming a stationary field with a horizontal gradient similar to that observed proved unfruitful. This is more likely to be a result of spatial inhomogeneity rather than the assumption of a stationary field, since $U\frac{\partial T}{\partial x} \times 12$ hours $\approx 0.1°$ C, for a current speed of 50 cm s^{-1} .

What is apparent is that both models systematically underestimate the 4 m temperature since at no point does the model temperature exceed the TSG temperature. Given the horizontal temperature gradients one would expect the TSG record to fall below an accurate simulation of the temperature in a similar manner to that seen in the 15 m records. This is contrary to the findings of Kantha and Clayson (1994) who find the PWP model to underestimate the MLD and thus overestimate the SST in a simulation of the TOGA Pilot study at 156° E. However recourse to the MLD record does not help here. Figures 5.3 and 5.4 show a fairly accurate prediction of the MLD by the PWP model and an underestimation by the diffusive model. Both models show some degree of reduced nighttime mixing on day 113 but both underestimate the extent of the reduction.

Errors in the heat flux estimates are unlikely to cause a discrepancy between our results and those of Kantha and Clayson. A 20% reduction in latent heat loss would increase the diurnal SST range by only 0.05° C on the basis of the sensitivity experiments.

Another possibility is that the optical properties of the water column are inadequately represented in the models. Figure 5.5 shows the PWP model output with Jerlov water types IA, IB, II. From this figure it is apparent that increasing the water turbidity in fact decreases the modelled temperature at this depth and by only a small amount O(0.05°C).

Another possibility is associated with errors in the wind speed measurements. No account was taken of the relative wind direction. For anemometer siting on the forward mast of *RSS Charles Darwin,* relative wind directions greater than ± 30°have been shown to lead to an over estimation in wind speed measurements by as much as 10% (Taylor et al. 1994). This would certainly lead to an under estimation of modelled SST due to elevated wind mixing and latent heat loss.

The discussion of errors in the CD32 simulation does not help explain the difference between simulations here and those of Kantha and Clayson (1994). One possible explanation is that different physical processes are dominating deep nighttime mixing in the two experiments and that the models lack the physics dominant during the TOGA Pilot study. Certainly the experiments occurred during opposite ENSO phases, CD32 during La Niña and the TOGA Pilot during the 1991-93 El Niño . Deeper nighttime mixing was observed during the TOGA Pilot study, 80 m compared to 40 m during CD32. It is the failure of the models to reproduce the deep mixed layers observed during the TOGA Pilot study which results in the over estimation of the SST. This is somewhat conjectural, but without more information it is not possible to say more.

An interesting point to note here is that both these sets of observations disagree somewhat with the longer time averaged observations of Sprintall and McPhaden (1994). They suggest from long term mooring data that deeper mixed layers and negligible influence of salinity stratification on vertical mixing characterise the 1988-89 La Niña , whilst shallower mixed layers and a 30 m thick barrier layer characterise the 1991-93 El Niño . This demonstrates the variability of the system and the dangers of looking at either long term data or short term, high resolution data in isolation. This is discussed more fully in Section 5.5.

5.2 Day to Day Variability

To what extent the diurnal cycle rides passively and non-interactively on top of the ambient oceanic variability is a matter of importance. The interaction between thermocline processes and the diurnal cycle is key to the concept of remote ocean/atmosphere feedback mechanisms. Unfortunately it is difficult with the CD32 data set to discriminate between atmospherically induced variability and thermocline interaction. The upper 60 m advects through the survey area at 50 cm s^{-1} and thus the time history of the water is unknown. In 7 days the water would have travelled 300 km, a scale over which the lower atmosphere could easily be heterogeneous, especially with regard to precipitation and cloud cover. It is however possible to use the models to say something about the observed day to day variability of the diurnal cycle and use the unanswered questions as impetus for further modelling experiments.

5.2.1 Influence of Underlying Stratification

The observations suggest that the depth of nighttime mixing is limited by a sub-surface salinity maximum until day 113, discussed in Section 3.3. The maximum depth of nighttime mixing in the model depends on both the boundary and initial conditions. A simple experiment of initialising the PWP model with no density stratification, Figure 5.6, shows that only when the nighttime mixing penetrates deeper than the previous night's maximum does the underlying stratification exert an influence. There is no surprise in this. However it shows that simply changing the initial salinity stratification and observing the effects on the modelled MLD will not answer the question of whether the salt stratification limits the MLD on a day to day basis. This is due to the large observed spatial/temporal variability of the halocline depth (Figure 3.10). A better method is to model each day separately, starting at midday, initialising the models with T, U and V profiles observed at that time but with salinity stratification observed at the time of maximum MLD on that day. The salinity stratification can then be modified and the effect on the daily maximum MLD examined in subsequent experiments. Figure 5.7 shows an ensemble of the mixed layer depth from such experiments using the PWP model. The dashed and solid curves correspond to the experiments with the salinity profiles linearly translated upward or downward respectively by 10 m. It would not make sense to try a similar procedure with the temperature profiles as the model deepens far too rapidly without the presence of the daytime temperature

stratification to erode. What the figure shows is that for days 109 and 110 the modelled MLD is being limited in it's nighttime maximum by salt stratification beneath the mixed layer. On day 111 the nighttime overturning reaches the halocline and appears to be only partially limited by it given the closer proximity of the red and blue curves. On days 112, 113 and 114 the modelled MLD is not sensitive to the salinity stratification beneath the ML. These modelling results add to the statements made earlier concerning Figure 3.10. From the time series of diurnal and halocline depths it was not clear to what extent the convective overturning was being limited by salinity stratification. The approach taken with the model does depend on continuous CTD observations being available to illustrate the effect on the maximum MLD of the variable halocline depth.

5.2.2 Influence of Surface Flux Variability

One question raised in Section 3.5 was what caused the reduced mixing on days 113 and 114: was it a change in surface forcing or a non-local change in the underlying thermal stratification? Figures 3.5 and 3.6 show the temperature and salinity fields. It is clear from Figure 3.5 and 3.6 that a change in the temperature and the salinity structure of the upper 100 m did occur after day 111. The intermediate thermocline becomes much weaker whilst the temperature stratification shallower than 40 m increases bringing cooler water into the upper 40 m. At the same time salinity becomes almost homogeneous over the top 85 m. This situation could not have arisen from surface-forced one dimensional mixed layer dynamics, but whether this advected structure effects the diurnal cycle is another matter.

The improved MLD simulation of the ensemble experiment discussed above suggests that this advective change in temperature and salinity structure does exert an influence on the diurnal response. However there are also changes in the surface fluxes which could account for reduced nighttime mixing and increased SST. On days 112 to 113 the windstress was reduced by approximately 30% with a consequent reduction in latent heat flux of about 5% compared with preceding days. In addition to this 9 mm of rainfall was recorded over 3 hours centred on day 113.1.

Figure 5.8 shows the results of a 7 day simulation of the PWP model with the rain event on day 113.1 removed from the forcing field. The maximum depth of nighttime mixing is increased from 36 to 40 m, remaining at that depth for an extended period of three hours. The dramatic reduction in MLD from 20 m to 1 m on day 113.1 in the reference experiment can be seen to be as a result of the buoyancy flux due to the rain. A similar effect is also

apparent on day 111.1 in the reference experiment. The effects of rain events on the mixed layer are considered further in more detail in the following section.

Figure 5.9 shows the results of a PWP model simulation with the windstress and latent heat flux set at constant values equal to the average of each variable over the 7 day integration period. This experiment was run to see the effect of the observed reduction in windstress and latent heat flux around day 113. The experiment shows an increased depth of nighttime mixing to 44 m on day 113, especially in the period before the rain event. Again the rain caps the model with a buoyant layer, reducing the mixed layer depth to 2 m, even with the increased latent heat loss and windstress of this experiment.

Thus both the rain event and the decreased windstress and latent heat flux have the potential to cause the reduced nighttime mixing of day 113. However, as mentioned above it is equally possible that the advected stratification is also sufficient to cause this reduction. The results of an experiment in which the windstress and latent heat flux are held constant at their average values and the rain events omitted are show in Figure 5.10. The experiment was run from day 112.5 but with initial conditions corresponding to the T and S profiles observed on day 113.1. As was seen above the salinity profiles had a negligible effect on the depth of mixing at this time, and the day 113.1 rain event is not evident in the Seasoar salinity record. Thus using the salinity profile from day 113.1 does not implicitly include the effects of the rain event, which is as required. In this figure two effects of the advected stratification are evident. Firstly the maximum depth of mixing is reduced to 23 m, this is still deeper than the observed maximum MLD of 13 m but shallower than the reference maximum of 37 m. Secondly, the timing of the modelled deepening is later than in the reference case by about 2 hours and in closer agreement with the observed timing. These two points suggest that the observed diurnal response on day 112-113 is in part effected by the increased temperature stratification advected into the survey region.

Thus it appears that both local (atmospheric) and non-local processes (advected stratification) play their part in limiting the depth of nighttime convective overturning on day 113.

5.3 Effects of Precipitation on the Upper Ocean

In both observational studies the effect on the upper ocean of precipitation was seen. The effect of the positive buoyancy flux on vertical mixing was noted as was the immediate

reduction of SST. The possible mechanism of local formation of a barrier layer by precipitation was discussed and the consequent possible increase in SST on longer time scales (O(weeks)). The key question about precipitation in the western equatorial Pacific is, does precipitation significantly effect the SST on a regional scale? Significant in regard to coupled ocean/atmosphere fluctuations is likely to be a few tenths of a degree celsius (Palmer and Mansfield 1986).

It is impossible from the observations to describe a time history (O(days)) of the ocean response to a rain event, as such a description would require rainfall to occur during a Lagragian type ocean experiment. Measurements of this nature were made by *RV Franklin* during TOGA COARE, but the results have not been published yet.

In this section the PWP model is used to study the effect of precipitation on diurnal mixing and SST.

5.3.1 Precipitation Rate and Timing

Given the strong diurnal temperature and mixing cycle in the upper 50 m it is likely that the timing of rain events exhibits a diurnal signal and that the phase is important to the oceanic response and feedback mechanisms. The precipitation data from *Le Noroit* show two maxima in hourly rainfall volume, one mid to late afternoon and another between 1 am and 4 am. The IMET mooring data show a similar phenomenon, as does TAO array data (McPhaden, personal communication). This observation has been explained in terms of the time evolution of "typical" cloud patterns over the western equatorial Pacific. In essence, the convective cloud, formed when the SST is greatest, evolves over a period of approximately 12 hours into more stratiform cloud, which precipitates a greater volume than the convective cumulus cloud. The two daily maxima in precipitation are responsible for the two surface salinity minima discussed in Section 2.3.4. This bias in the timing of precipitation may have a rectifying effect on the oceanic diurnal cycle. This is investigated.

Table 5.2 shows some basic statistics on the rain gauge record from *Le Noroit*. Three categories are described: events with peak rainfall rates up to 5 mm hr^{-1}, between 5 and 10 mm hr^{-1}, and greater than 10 mm hr^{-1}. An event is defined as a period with consecutive non-zero hourly rainfall rates. It is interesting to note that although the lightest category falls most frequently (75% of events), 85% of the total volume comes from the heaviest events, due in part to the longer duration of the heaviest events. It is also worth noting the large variance in event duration and rainfall rate which illustrates the dangers of trying to

define a "typical" rain event.

Peak rate (mm hr^{-1})	0–5	5–10	>10
Total volume (mm)	50.0	67.0	661.7
no. of events	197	28	37
Mean duration (hrs)	0.2	0.6	1.8
st. dev.	0.4	0.9	2.5
mean rate (mm hr^{-1})	0.6	2.7	9.7
st. dev.	0.7	1.2	7.9

Table 5.2: Rain event statistics from *Le Noroit*, December 1992–February 1993 on 156°E.

The temperature of the rain at the IMET buoy was found to be close to the wet bulb temperature. Over the 70 days of the IMET buoy deployment the mean difference between SST and wet bulb temperature was 5.6° C with a standard deviation of 0.9° C. Thus in all experiments the heat loss associated with the rain was estimated as the heat required to change the temperature of the mass of rain by 5° C.

5.3.2 Timing Experiments

The first set of experiments looks at the influence on the diurnal cycle in the ocean of precipitation alone, ignoring for the time being any associated variations in heat and momentum fluxes.

Three series of twelve experiments were run with the PWP model using the same analytic boundary conditions described in Section 4.6. After five days integration a single rain event was imposed at a different time throughout day 5 for each experiment in the series.

Three series of experiments were run with different rain events: (i) 2 hour event of 10 mm hr^{-1}, (ii) 2 hour event of 20 mm hr^{-1} and, (iii) 4 hour event of 20 mm hr^{-1}. These all represent rainfall rates greater than climatology. The first experiment represents a rate similar to that observed from mid December 1992 to 5 January 1993. The second two series represent heavier events, the heaviest marking an upper bound on the rainfall observed during TOGA COARE.

Results are expressed as anomalies of SST, SSS and MLD between experiment and control (no precipitation). Discussion concentrates on the period up to 48 hours after the rain. SST anomalies are all less than -0.1 ° C after this time. Figures 5.11, 5.12 and 5.13

show the results for experiments (i), (ii) and, (iii) respectively. Anomalies are plotted at 1, 3, 7, 20, and 48 hours after the rain ceased, coloured red, green, light blue, dark blue and black respectively. The approximately even spacing of the anomaly curves plotted at these intervals illustrates the near exponential return of the upper ocean to its unperturbed state.

MLD Anomaly

The MLD anomaly plots qualitatively exhibit the same features. Precipitation reduces the mixed layer depth of the model to 1 m in all cases. After one cycle of mixing there is a slight tendency for day time precipitation to produce a greater anomaly. This is a result of the fresh layer being initially warmed, increasing its density anomaly, rather than cooled. After two nighttime mixing cycles this effect is less evident, and becomes less so with more cycles. After 48 hours the MLD anomaly for the heaviest event is approximately 10 m, for the lightest event approximately 3 m.

Salinity Anomaly

Maximum salinity anomalies of nearly 1 psu immediately following the heaviest rain event are interesting to note in regard to observations in Section 2.5, where surface salinity reductions of this magnitude were noted. After two days the heaviest rain salinity anomaly is about 0.2 psu, suggesting an upper time limit on the 6% statistic of rain reduced SST of 2 days (Section 2.3.5). There is a general tendency for day time rain to produce a greater salinity anomaly, commensurate with the larger MLD anomaly.

SST Anomaly

There are two factors effecting the SST anomalies. Firstly, the greatly reduced depth of mixing confines the surface fluxes to a shallower layer, resulting in greater SST changes. Secondly, the effective heat loss associated with the cool rain directly depresses the SST. Although the climatological mean heat flux due to precipitation is small, O(3 W m^{-2}), instantaneous values can be high. For example, 20 mm hr^{-1} represents a heat loss of 111 W m^{-2} assuming a SST/rain temperature difference of 5° C. In all experiments rain produces a positive SST anomaly at some time between 09:00 and 16:00. The maximum SST anomaly is approximately 0.1° C in all three series of experiments. Heavier rain events do produce slightly shallower mixed layers between hours 10:00 and 15:00. In this set of experiments

the solar heating of progressively shallower layers for the increasingly heavy rain events is entirely offset, in terms of SST anomaly, by the increased heat loss due to a greater volume of cool rain. Likewise the negative SST anomaly due in part to nighttime heat loss from a shallower mixed layer is increased by the direct thermal effect of the rain. This, in addition to the asymmetry of the diurnal heating cycle alluded to in Section 4.6, gives rise to the observed preponderance of cool fresh layers over warm fresh layers. Although the SST anomalies are initially as large as -0.3 °C, after 2 days all anomaly magnitudes are less than 0.1 °C.

5.4 Direct Simulation of the TOGA COARE Domain

The preceding section gave a short time scale description of the effect of a single rain event on upper ocean properties. However, fluxes other than precipitation were held constant. The possibility of *increased* SST due to rain comes from the scenario observed in the western equatorial Pacific of a windy and rainy period followed by a period of reduced wind and rain, and net positive heat flux (due in part to reduced wind stress and in part to reduced cloud modulation of solar radiation). The argument then goes that the mixed layer depth is determined by salinity stratification and is shallower than it would have been were it not for precipitation. Thus the water below the mixed layer is initially the same temperature as the mixed layer. In the presence of a net heat gain by the ocean, this shallower mixed layer will heat up and the zone beneath will again become both salt and temperature stratified. The SST will therefore be greater than had it not rained.

On a time scale of months, the net buoyancy gain due to precipitation may be important in balancing the wind deepening of the mixed layer. In the presence of a net zero heat flux and non-zero wind stress the mixed layer would deepen indefinitely on the equator (in the absence of dissipation). It is quite possible that precipitation is important in balancing this and thus helps maintain the apparent decoupling of the warm pool from water beneath.

It is not possible to test all these hypotheses with the present data set. In this section fluxes from the IMET buoy and rain measurements from *Le Noroit* are used to assess the impact of precipitation on SST during TOGA COARE in a one dimensional sense. I gratefully acknowledge Robert Weller for the IMET fluxes and SST at 2° S, and Bill Smyth for the profiles of T, S, U and V from the *Moana Wave* at 2° S.

Four experiments are presented here, all are compared with a control experiment,

which in each case is the same but with no precipitation. All experiments are with the PWP model as described previously. Integrations run from 19 December 1992 until 16 February 1993. All were initialised with *Moana Wave* profiles. The first experiment was bounded with the IMET fluxes. The second experiment used IMET fluxes but with *Le Noroit* rain measurements. The third experiment used the analytic forcing described in Section 4.6 but with IMET rain measurements, and the fourth experiment used analytic fluxes but with *Le Noroit* rain measurements. The results are summarised in Table 5.3 as mean anomalies over the 60 days of SST, surface salinity and MLD. Figure 5.14 shows time series of SST anomaly and surface salinity anomaly for the first experiment. Figure 5.15[a] shows the modelled SST (blue line) and [b] the SST observed at the IMET buoy (pink line), and modelled temperature at 5 m (blue) and 5 m temperature from the Seasoar data at 2° S (pink).

The latter figure (Figure 5.15) shows that the PWP model is able to simulate the diurnal cycle and the longer term trends remarkably well during the TOGA COARE period, with a small underestimation of the SST. The predominantly one-dimensionality of the region has already been seen in the heat budget results of Section 2.4. The ability of the PWP model to simulate the diurnal variation in SST so well with this high accuracy flux data set (within ± 10 W m^{-2}) is encouraging from both the modelling and flux measurement point of view.

Experiment	Mean SST Anomaly (°C)	Mean Salinity Anomaly (psu)	Mean MLD Anomaly (m)
1	0.01	-0.3	-5
2	0.01	-0.3	-5
3	0.005	-0.3	-4
4	0.02	-0.3	-3
5	-0.0004	-0.002	0.3
6	-0.07	-0.008	3

Table 5.3: TOGA COARE simulation with PWP model

What seems immediately clear from these results is that in a one dimensional sense the SST is not sensitive to the precipitation in the mean over the 60 days of TOGA COARE. However examination of the time series for the first experiment (Figure 5.14) shows SST anomalies of up to $-0.2°$ C lasting for ten days and positive anomalies of 0.05° C from 17 January onward. Such fluctuations may be important in atmosphere/ocean feedback mechanisms, but they represent relatively small components of the total fluctuations in

SST observed throughout this period.

5.4.1 Daily Averaged Fluxes

In the preceding section it was seen that whilst precipitation had significant impact on the surface salinity during TOGA COARE, the effect on SST was small (O(0.1°C)). Section 5.3.2 suggested that although the diurnal cycle observed in the precipitation pattern is important particularly to SST over a time scale of days, on longer times scales (O(10s days)) the diurnal pattern may be unimportant. In this section the question as to whether it is necessary to resolve the diurnal cycle in precipitation and in heat and momentum in terms of diagnosing the average SST during TOGA COARE is addressed.

Two experiments were run using the PWP model. One with the hourly IMET fluxes but with daily mean precipitation rates, and a second with daily means for all the fluxes. The mean anomalies for these two experiments, daily mean precipitation only and daily means of all fluxes, are given as experiments 5 and 6 respectively in Table 5.3. From this it is clear that the timing of the precipitation during the diurnal cycle has a negligible effect on the mean mixed layer properties, and indeed the time series (not shown) are flat at zero with spikes of only a few hours duration maximum. Temperature time series from experiment 6 are shown in Figure 5.16. As the mean anomaly figures suggest the SST trends are well simulated with daily averaged fluxes. However the diurnal peaks in SST with amplitudes as great as 1.5° C are absent. Such peaks are an integral part of the diurnal convective activity in the atmosphere, which in turn modulate the fluxes. Coupled ocean/atmosphere models are needed to examine if and how such diurnal feedback mechanisms could be parameterised. All that this experiment tells us is that if daily averaged fluxes are *measured* then the daily mean SST can be simulated.

5.5 Discussion

The modelling results from this chapter have shown that, independently, both observed mixed layer depth and SST diurnal variability can be simulated. It is unfortunate that the CD32 data set did not allow both SST and MLD to be determined simultaneously without encountering problems of spatial aliasing. When the full IMET Buoy data set becomes available it will be possible to determine a mixed layer time series for the TOGA COARE period at 2° S.

The sub-surface salinity maximum water was found to be important in limiting the depth of nighttime convective overturning. In the case of the 1988 data set, salinity stratification limited the diurnal thermocline to a depth of around 40 m. This increases the thermal decoupling of the upper 40 m from the ocean interior by reducing the potential for entrainment cooling of the upper layer. This was the case for the first half of the CD32 survey.

During the second half of the survey a different regime is apparent. Both surface flux variation and advective changes in sub-surface density structure are shown to exert a significant influence on the MLD and SST. This demonstrates that periods exist when interior processes, such as wave motions, can modulate the diurnal response of the upper ocean and effect the SST.

Precipitation was shown to have a dramatic short term, O(days), effect on SST, salinity and MLD. On this time scale the timing of the rain over the diurnal cycle determines whether the induced SST anomaly will be negative or positive. The temperature of the rain skews the distribution such that an "average" rain event will only produce a positive SST anomaly if it falls between 9 am and 4 pm. This period is reduced for heavier rainfall. SST reduction for rainfall equivalent to the heaviest events observed during TOGA COARE was 0.3°C. These experiments explain the preponderance of cool fresh pools over warm fresh pools in the observations.

The TOGA COARE model runs showed a very accurate simulation of the SST. Predominantly the model underestimated the SST by a few tenths of a degree at most. During the period 23 December 1992 to 5 January 1993 the model SST was about 0.2°C above that observed. This was the period of strongest winds and deepest mixed layer. Such conditions were also prevalent during the TOGA Pilot study when Knatha and Clayson (1994) likewise found the PWP model to underestimate the MLD and thus overestimate the SST. This could be a result of inadequate model physics under these forcing conditions or advective heat fluxes dominating SST changes.

Experiments with observed precipitation patterns suggest that over longer time scales, O(weeks), the diurnal variability in the rainfall does not effect SST or MLD. The experiments also show that if the warm pool can be treated as a one dimensional system then rain has a net effect of increasing the SST, albeit by a relatively small amount, O(0.1° C), by the process of local barrier layer formation.

æ

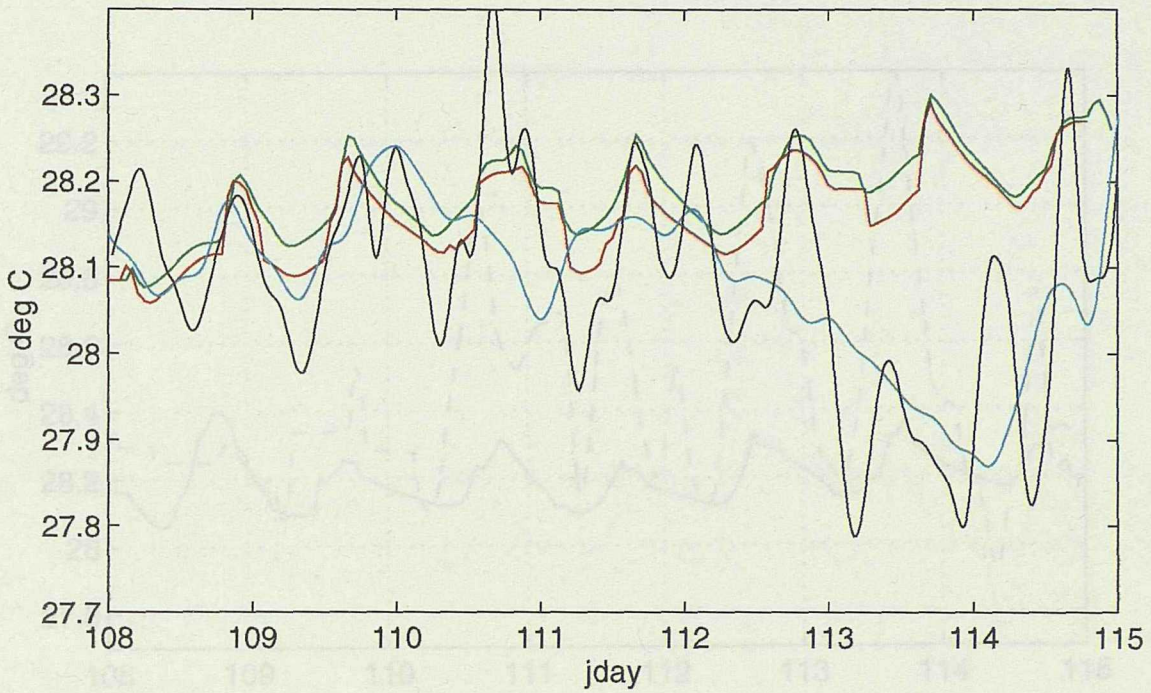

Figure 5.1: Temperature at 15 m from spar buoy (blue line), Seasoar (black line), PWP model (red line) and diffusive model (green line). Both observational records have been 6 hour low pass filtered.

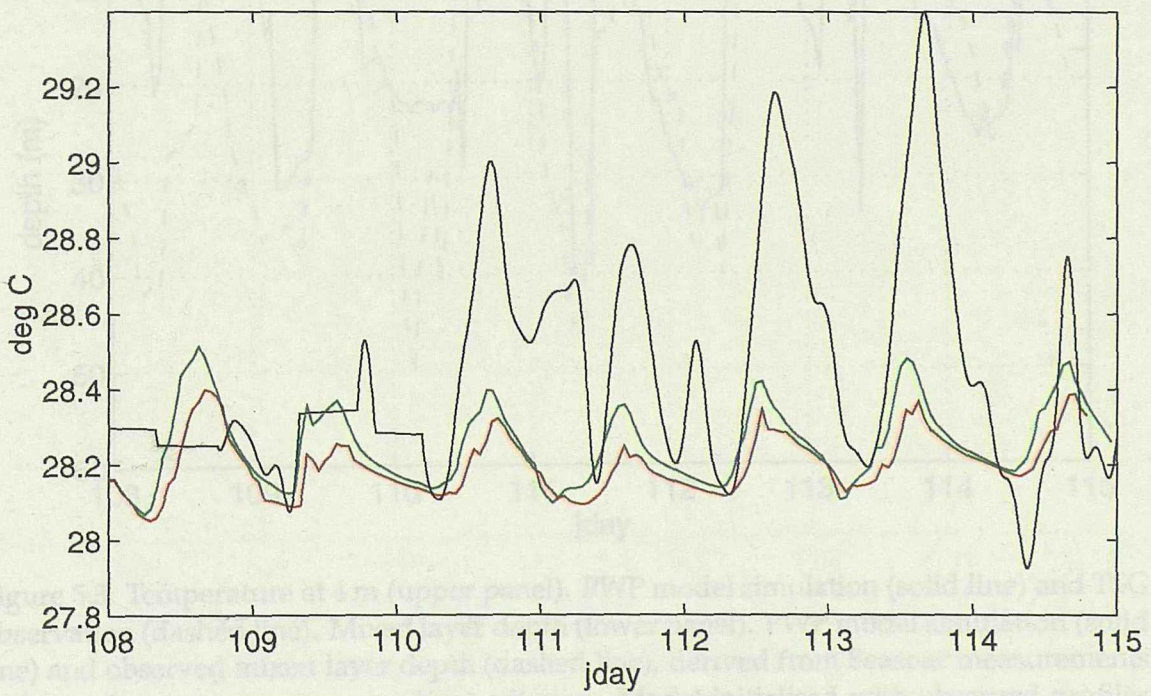

Figure 5.2: Temperature at 4 m from thermosalinograph (black line), PWP model (red line) and diffusive model (green line). TSG record has been 6 hour low pass filtered.

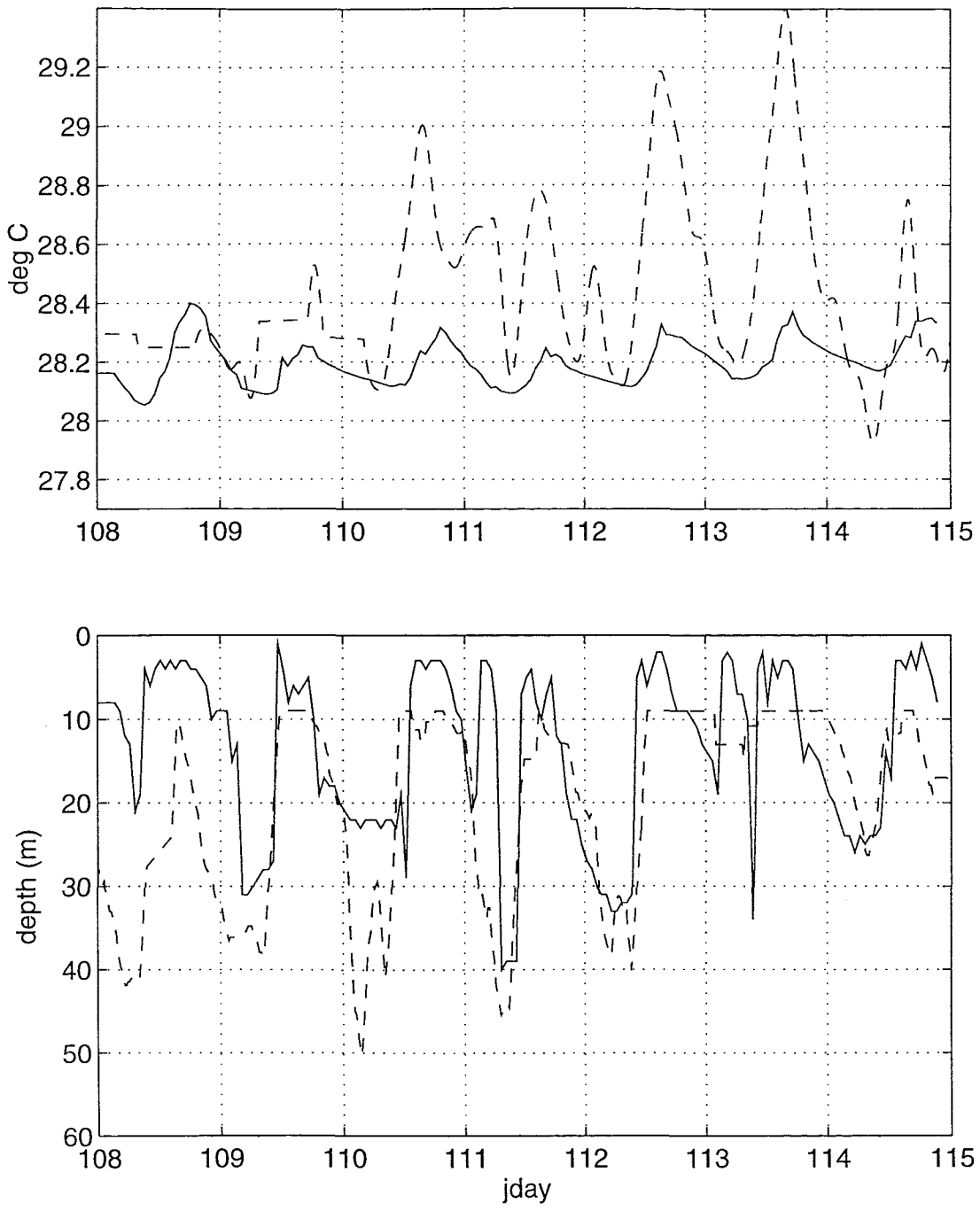

Figure 5.3: Temperature at 4 m (upper panel). PWP model simulation (solid line) and TSG observation (dashed line). Mixed layer depth (lower panel). PWP model simulation (solid line) and observed mixed layer depth (dashed line), derived from Seasoar measurements and based on a temperature gradient criterion. Model initialised with observed profiles and forced with observed fluxes.

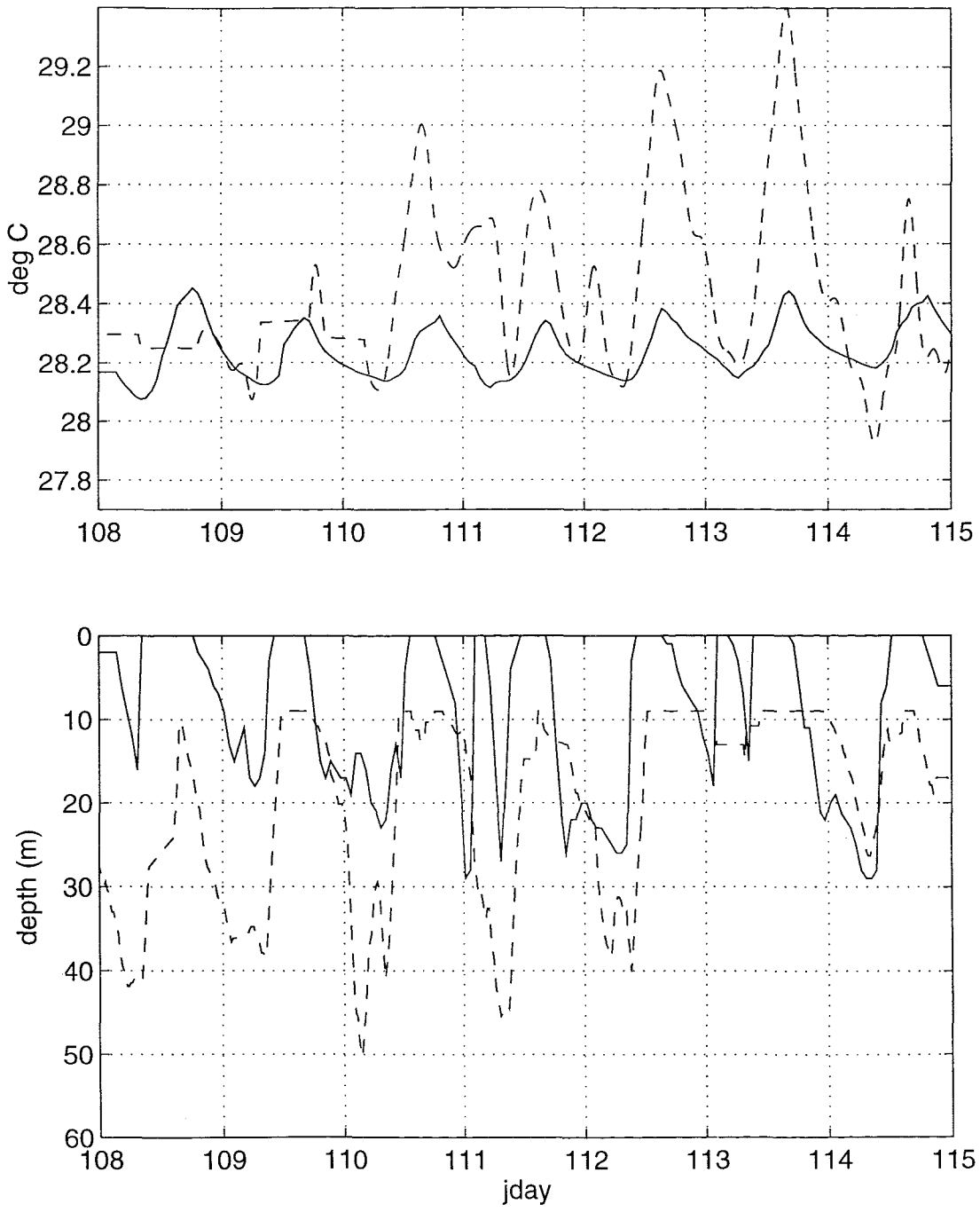

Figure 5.4: Same as Figure 5.3 but for diffusive model.

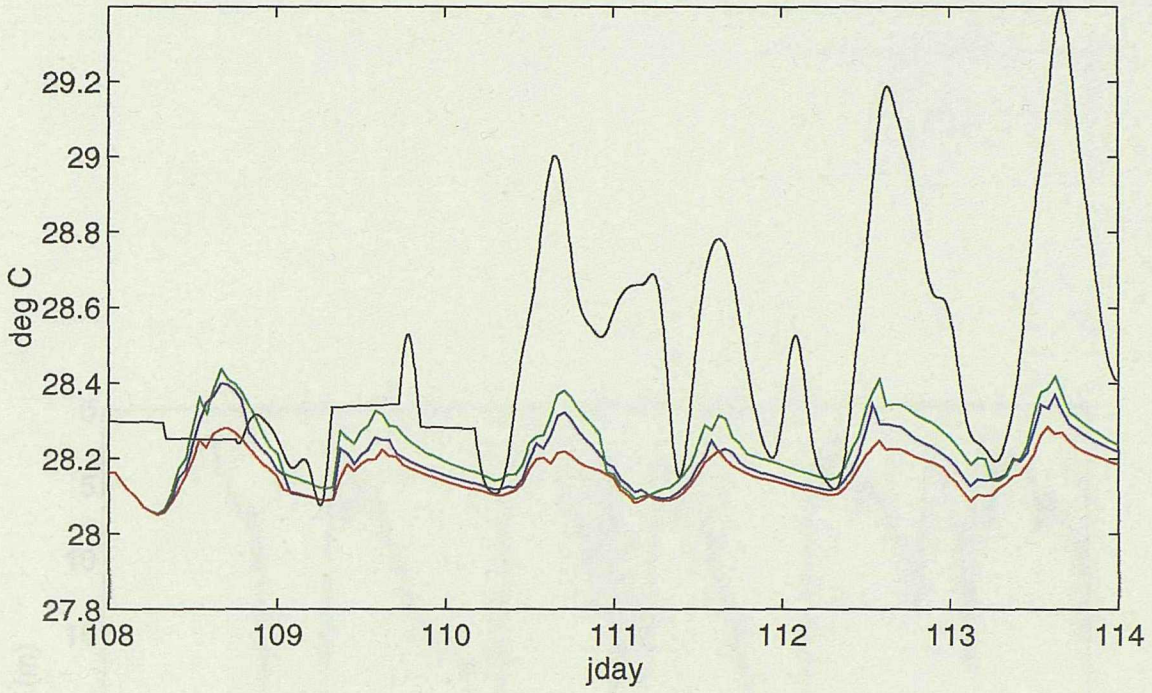

Figure 5.5: Temperature at 4 m. TSG observation (black line) and PWP model simulation. Simulations for 3 water types are shown. Jerlov water types IA (green line), IB (blue line) and II (red line).

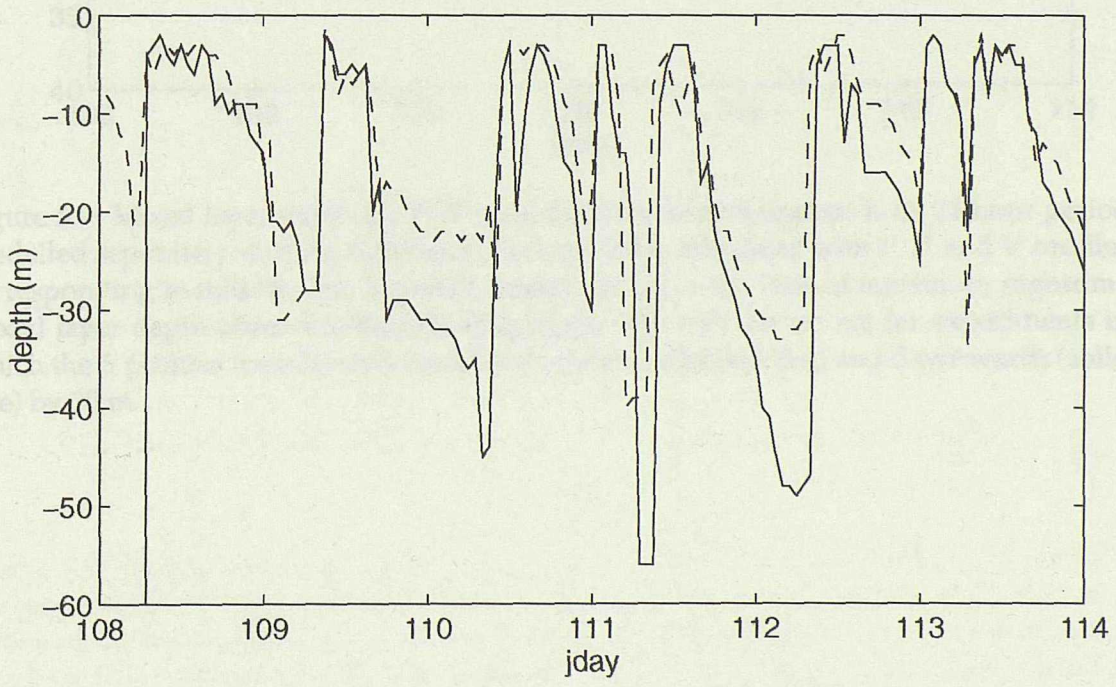

Figure 5.6: Mixed layer depth. PWP model simulation (solid line) and observed (dashed line). Model initialised with zero temperature and salinity stratification.

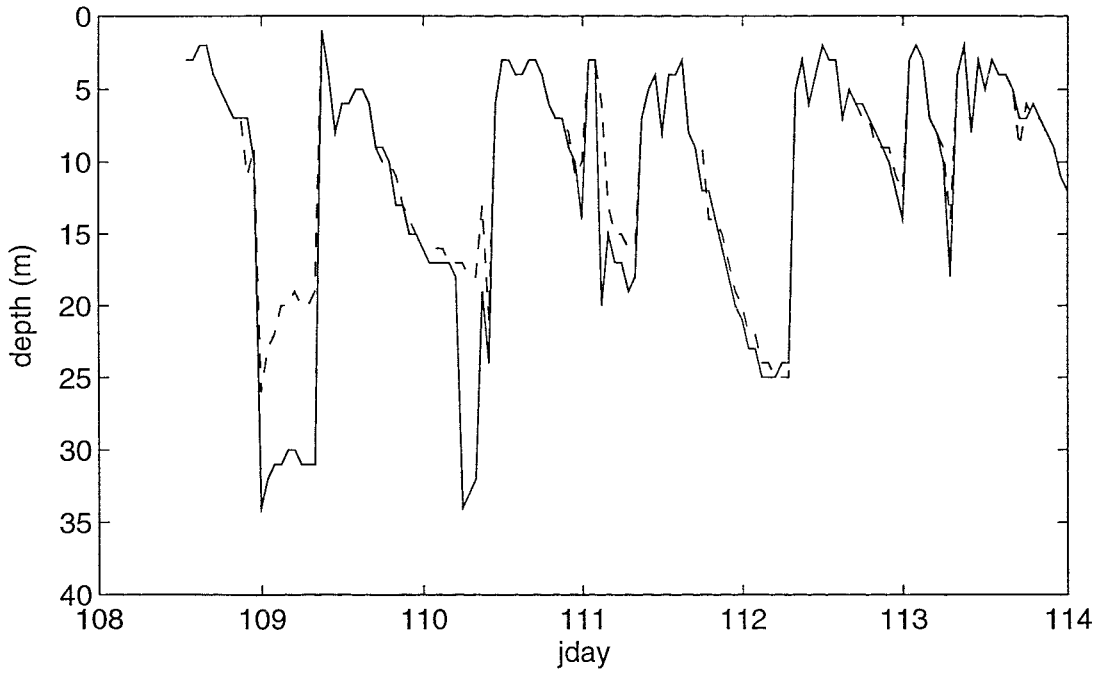

Figure 5.7: Mixed layer depth for PWP model ensemble experiment: Each 24 hour period modelled separately starting at midday. Each period is initialised with T, U and V profiles corresponding to midday and S profile corresponding to the time of maximum nighttime mixed layer depth observed the following night. The two curves are for experiments in which the S profiles were linearly translated upwards (dashed line) and downwards (solid line) by 10 m.

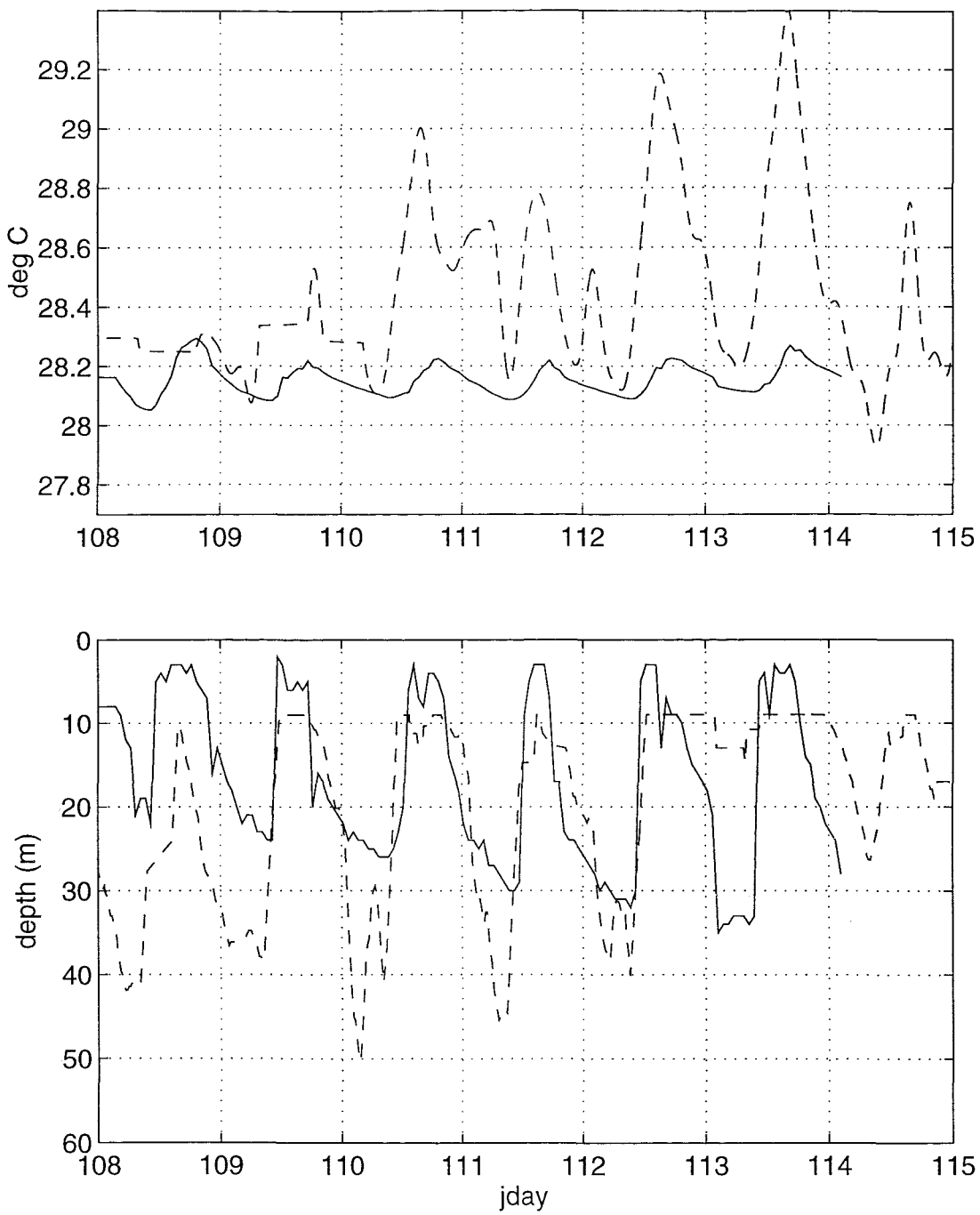

Figure 5.8: Temperature at 4 m (upper panel). PWP model simulation (solid line) and TSG observation (dashed line). Mixed layer depth (lower panel). PWP model simulation (solid line) and observed mixed layer depth (dashed line), derived from Seasoar measurements and based on a temperature gradient criterion. Model initialised with observed profiles and forced with observed fluxes but with precipitation set to zero.

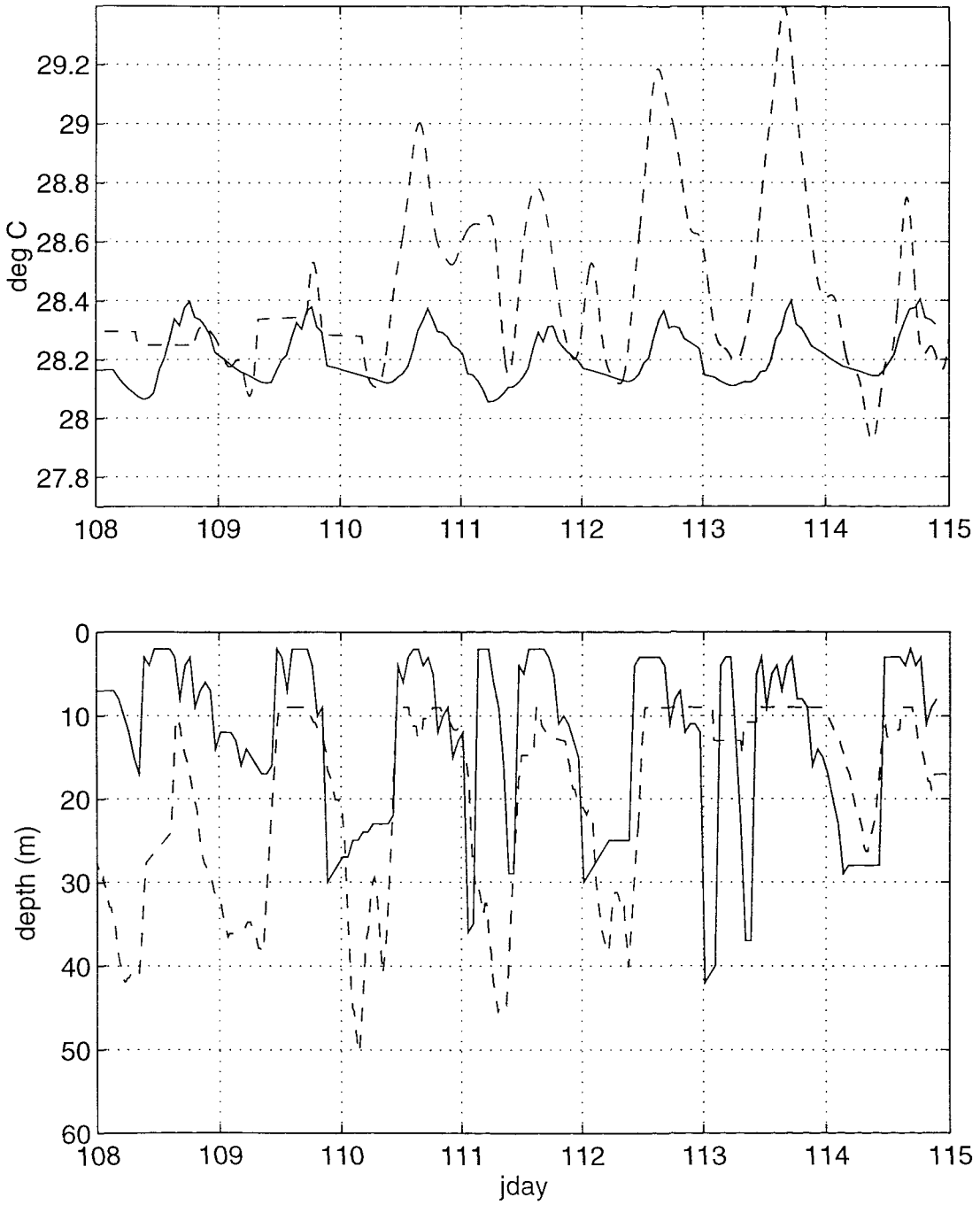

Figure 5.9: Temperature at 4 m (upper panel). PWP model simulation (solid line) and TSG observation (dashed line). Mixed layer depth (lower panel). PWP model simulation (solid line) and observed mixed layer depth (dashed line), derived from Seasoar measurements and based on a temperature gradient criterion. Model initialised with observed profiles and forced with observed fluxes except for windstress and latent heat flux which are held constant at their average observed values.

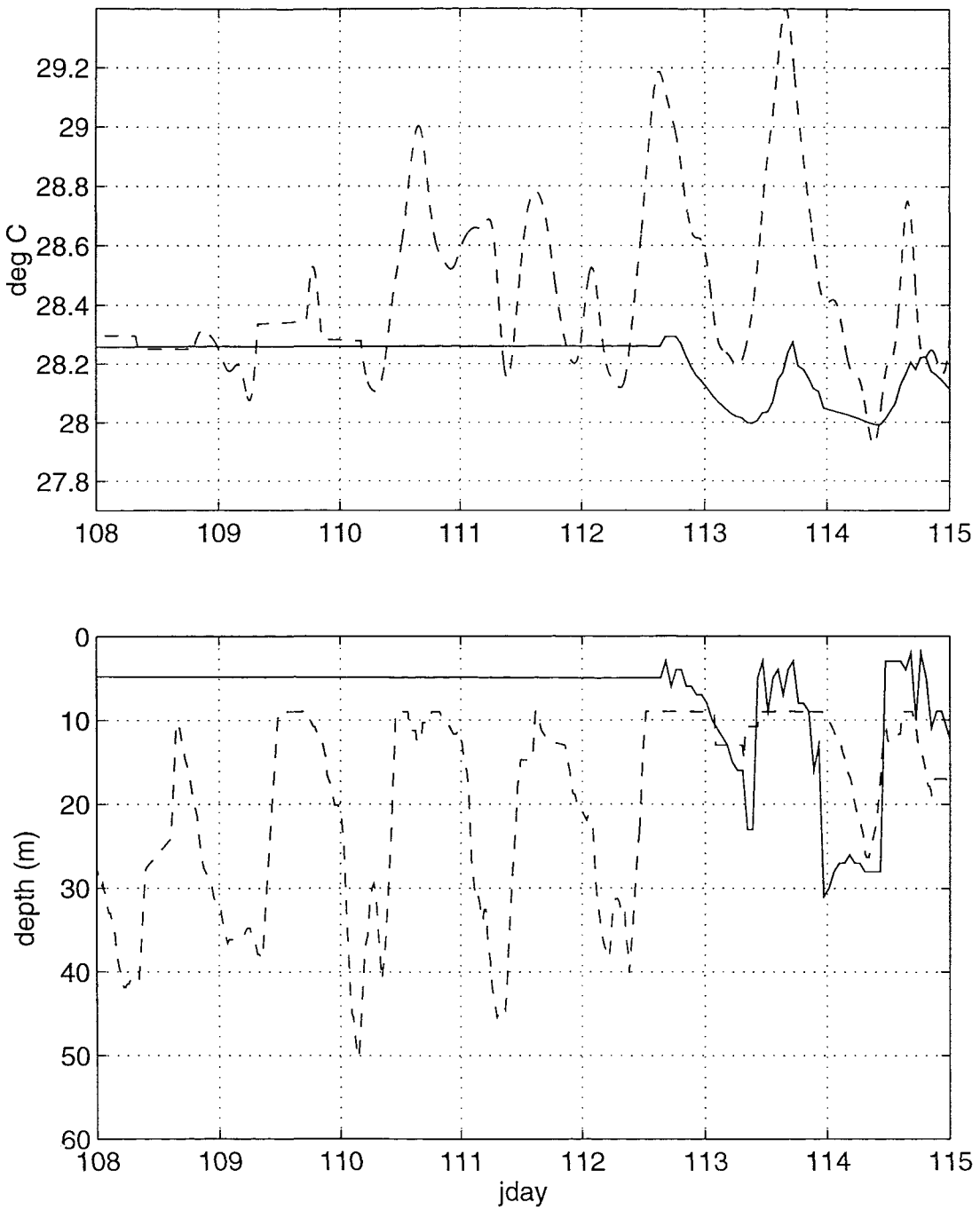

Figure 5.10: Temperature at 4 m (upper panel). PWP model simulation (solid line) and TSG observation (dashed line). Mixed layer depth (lower panel). PWP model simulation (solid line) and observed mixed layer depth (dashed line), derived from Seasoar measurements and based on a temperature gradient criterion. Model initialised with profiles on day 113.1 and forced with observed fluxes from day 113.1, but with precipitation set to zero and windstress and latent heat loss held constant at their average observed values.

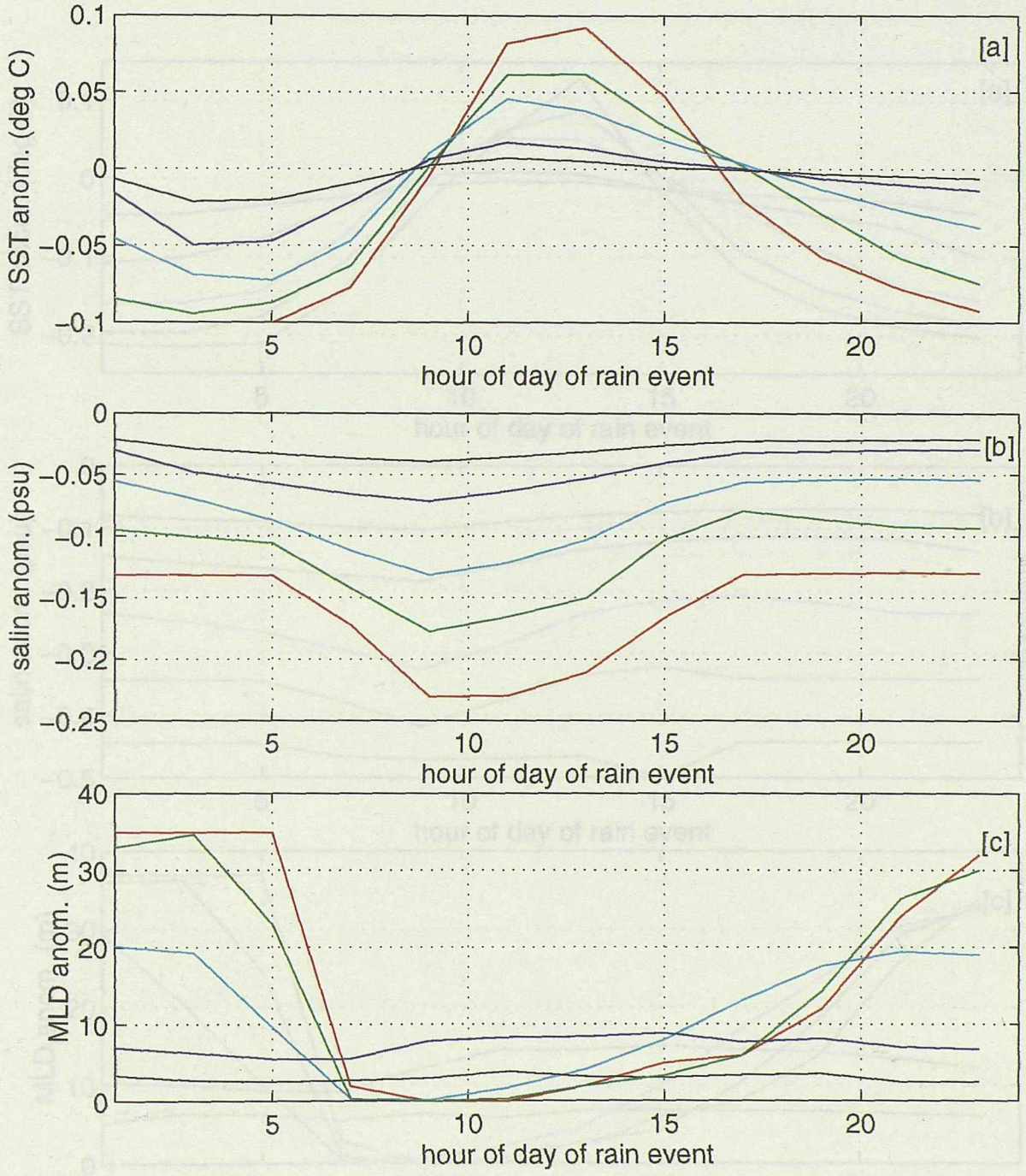

Figure 5.11: [a] SST anomalies (upper panel), [b] salinity anomalies (middle panel) and [c] mixed layer depth anomalies (lower panel) after single rain event: 2 hours of 10 mm hr^{-1}. Horizontal axis is the time of day of the imposed rain event. Anomalies are plotted 1, 3, 7, 20, and 48 hours after the rain ceased, coloured red, green, light blue, dark blue and black respectively.

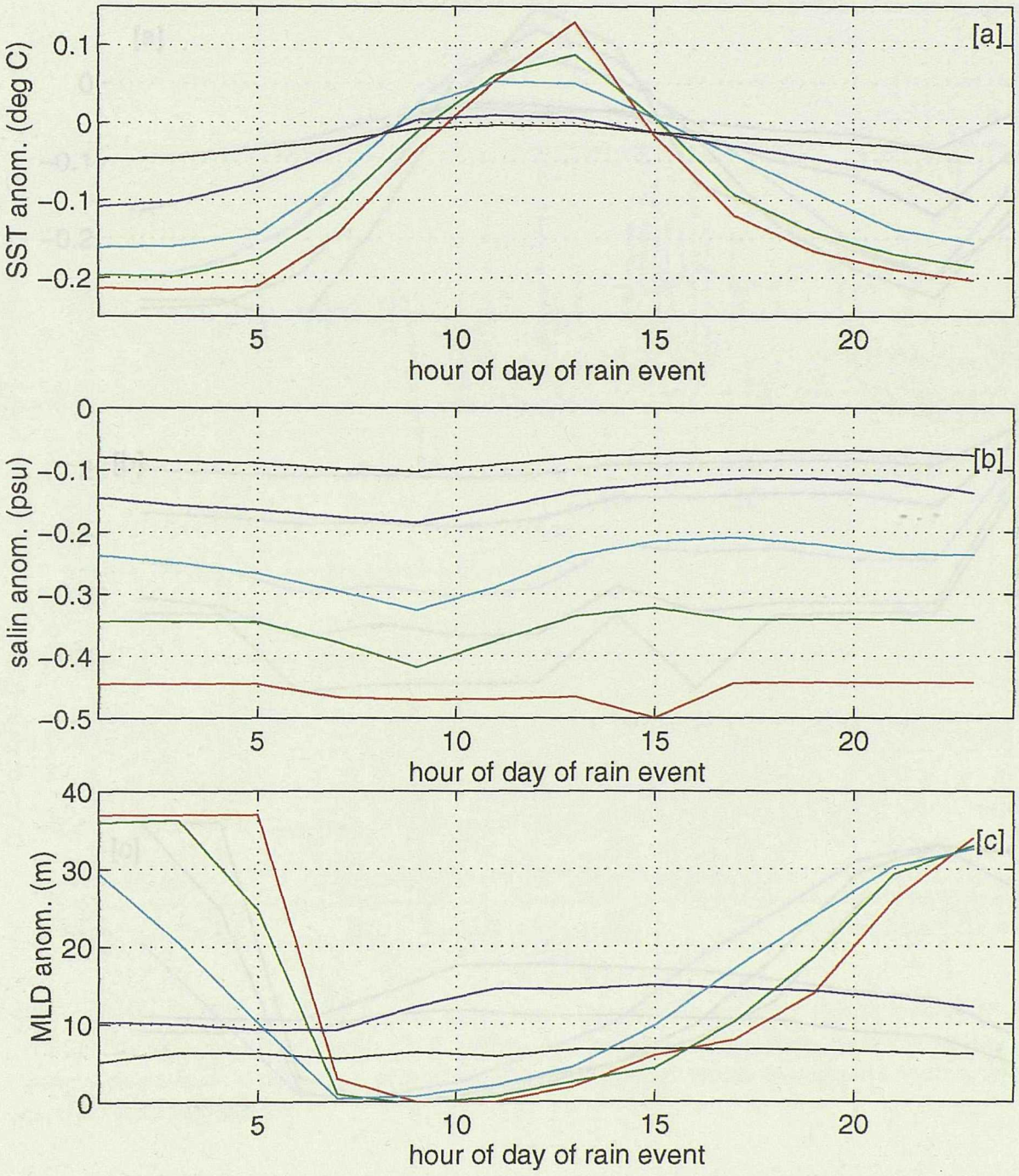

Figure 5.12: Same as Figure 5.11 but for a single rain event: 2 hours of 20 mm hr^{-1}.

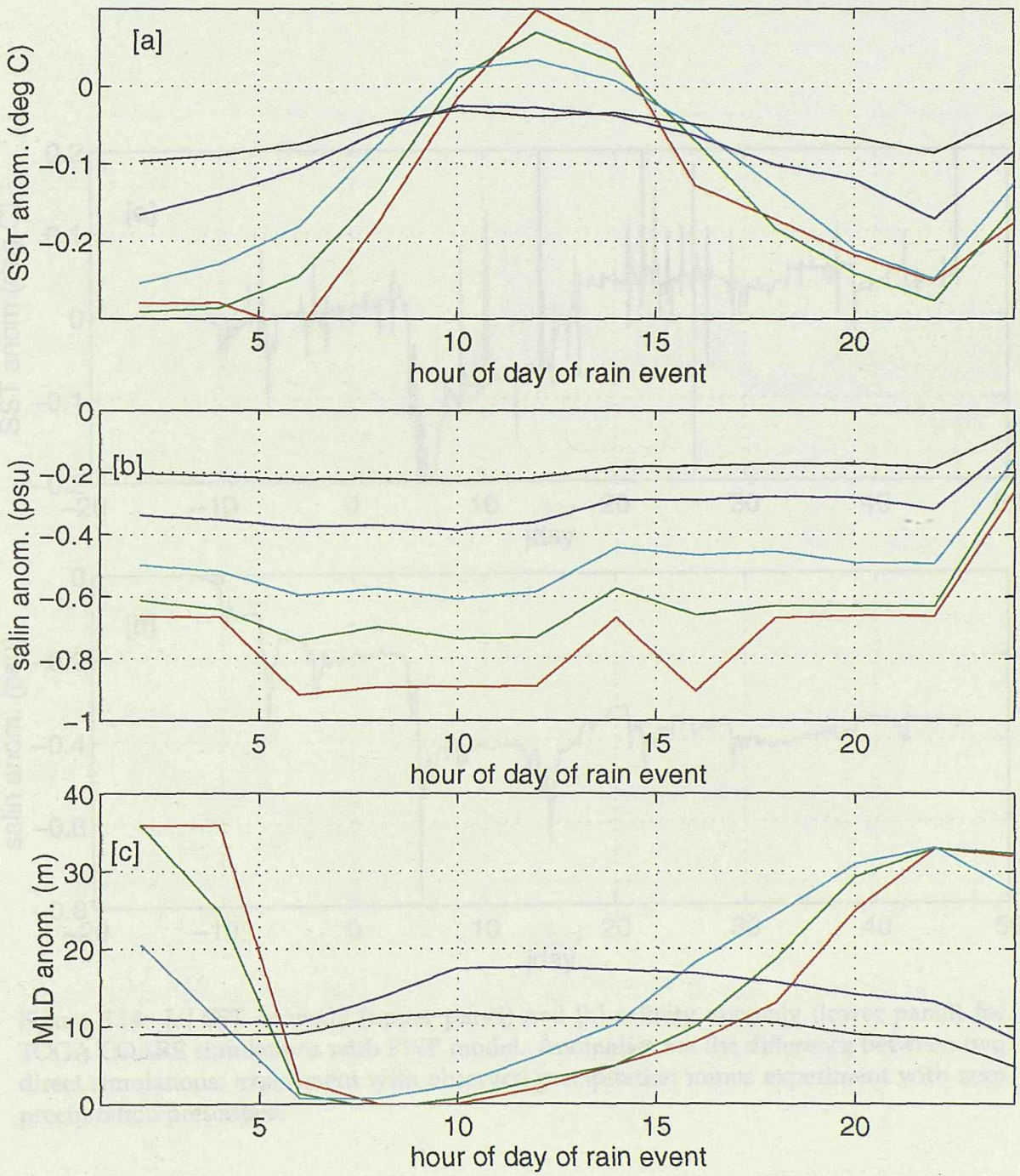

Figure 5.13: Same as Figure 5.11 but for a single rain event: 4 hours of 20 mm hr^{-1}.

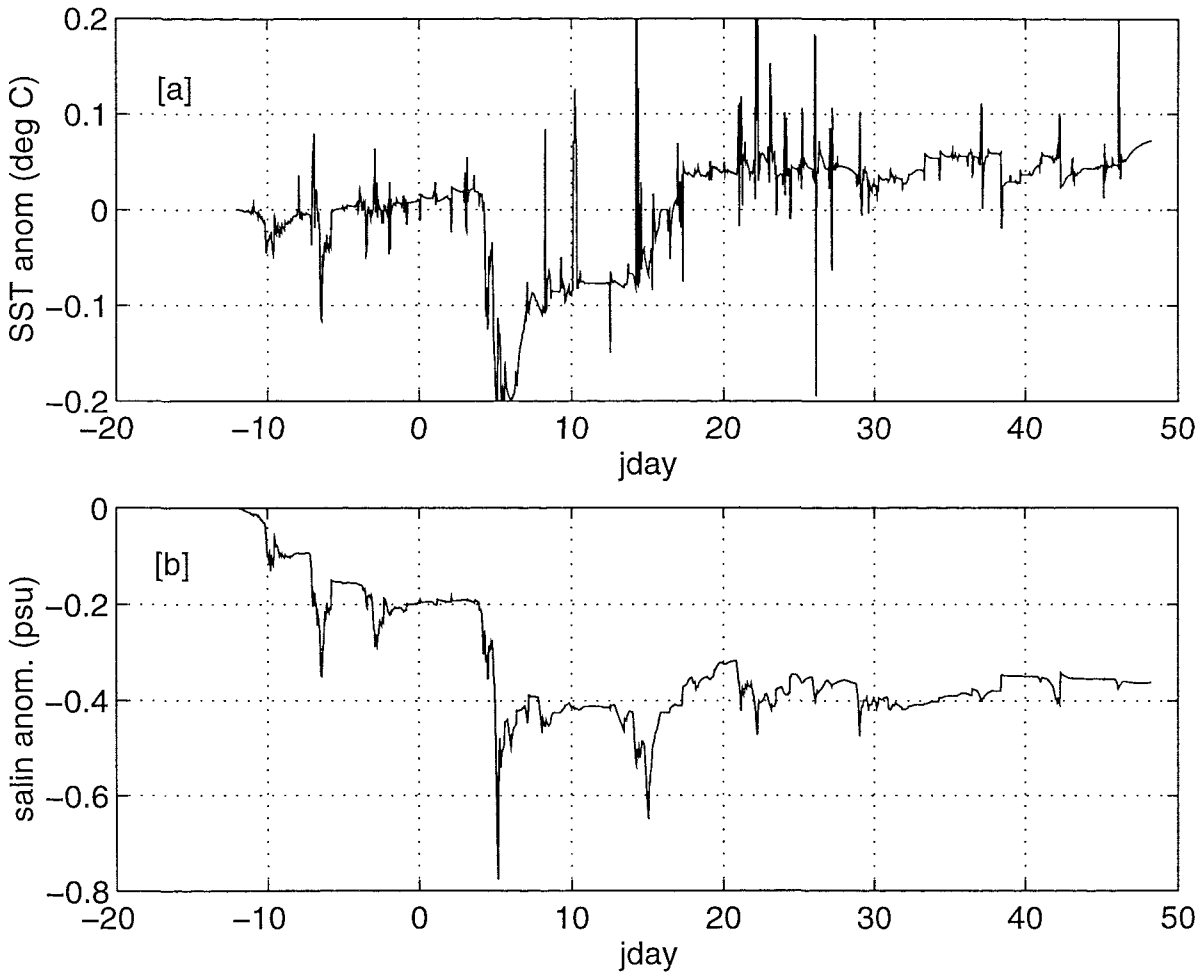

Figure 5.14: [a] SST anomaly (upper panel) and [b] salinity anomaly (lower panel) for TOGA COARE simulations with PWP model. Anomalies are the difference between two direct simulations; experiment with observed precipitation minus experiment with zero precipitation prescribed.

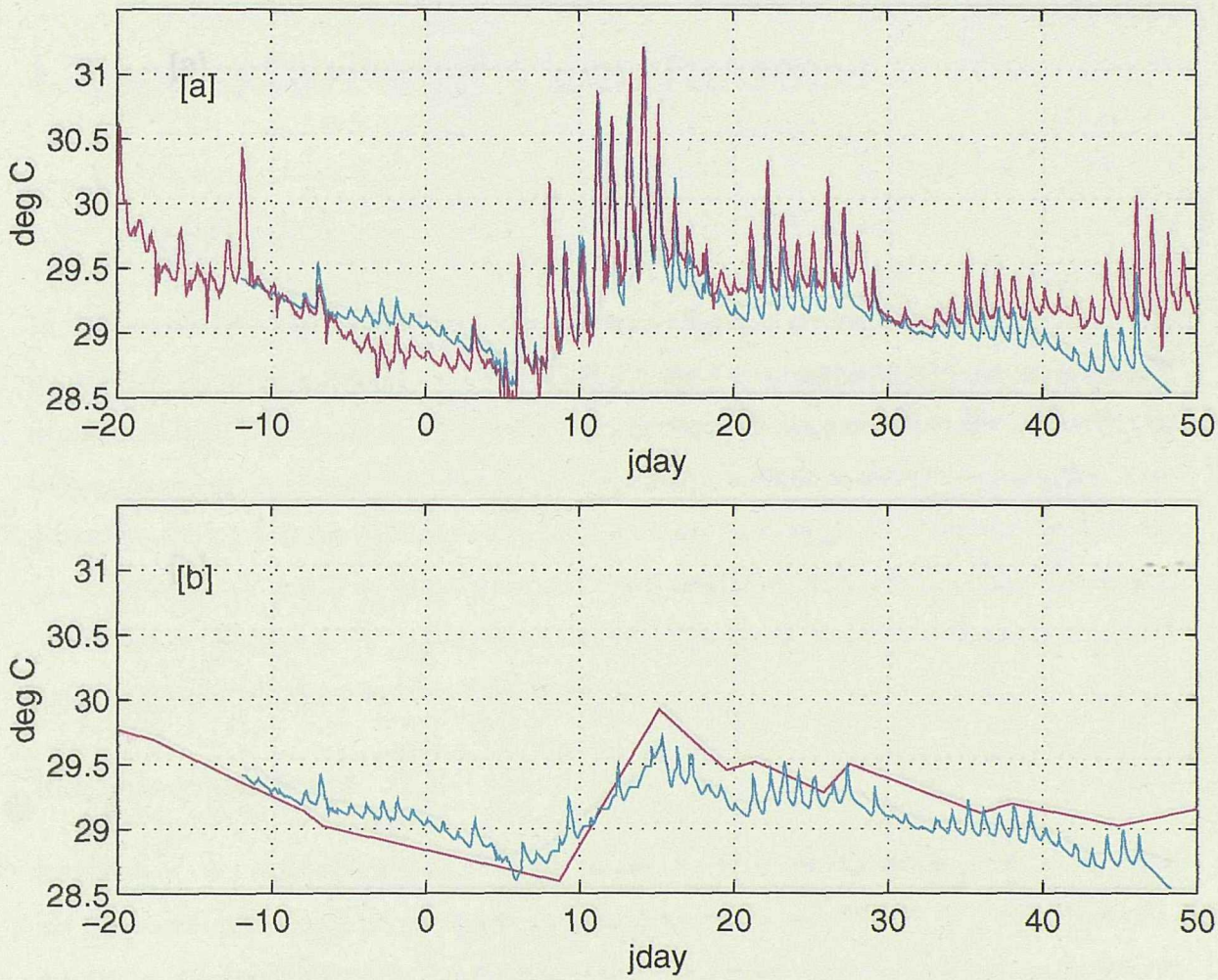

Figure 5.15: Temperature time series for TOGA COARE domain at 2°S. [a] Modelled SST (upper panel, blue line) and observed SST (upper panel, pink line). [b] Modelled temperature at 5 m (lower panel, blue line) and Seasoar 5 m temperature observations (lower panel, pink line). PWP model used, initialised with observed profiles and forced with observed fluxes.

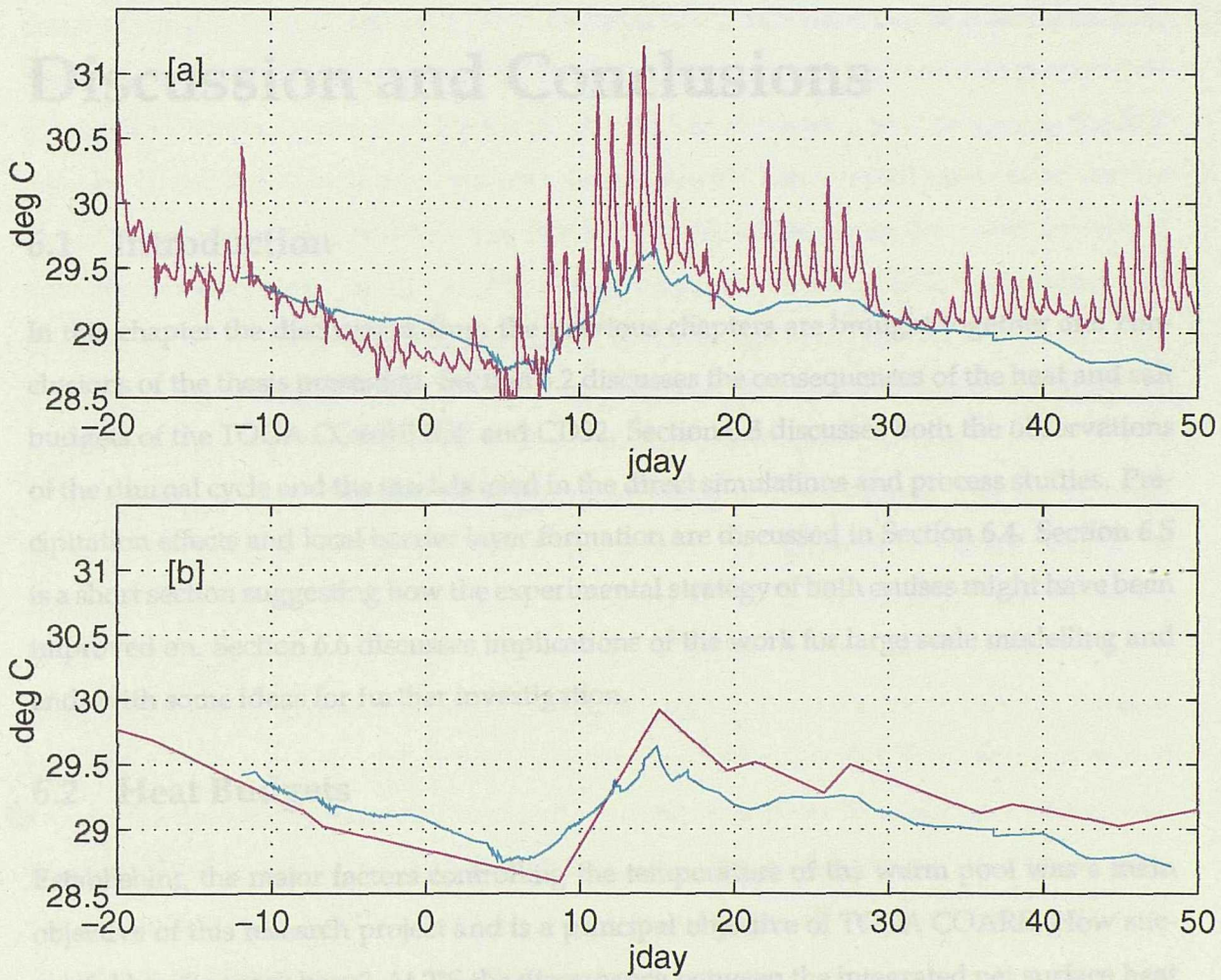

Figure 5.16: Temperature time series for TOGA COARE domain at 2°S. [a] Modelled SST (upper panel, blue line) and observed SST (upper panel, pink line). [b] Modelled temperature at 5 m (lower panel, blue line) and Seasoar 5 m temperature observations (lower panel, pink line). PWP model used, initialised with observed profiles and forced with daily averaged observed fluxes.

Chapter 6

Discussion and Conclusions

6.1 Introduction

In this chapter the discussions from the previous chapters are brought together and conclusions of the thesis presented. Section 6.2 discusses the consequences of the heat and salt budgets of the TOGA COARE IOP and CD32. Section 6.3 discusses both the observations of the diurnal cycle and the models used in the direct simulations and process studies. Precipitation effects and local barrier layer formation are discussed in Section 6.4. Section 6.5 is a short section suggesting how the experimental strategy of both cruises might have been improved on. Section 6.6 discusses implications of the work for large scale modelling and ends with some ideas for further investigation.

6.2 Heat Budgets

Establishing the major factors controlling the temperature of the warm pool was a main objective of this research project and is a principal objective of TOGA COARE. How successful has the work been? At 2°S the discrepancy between the integrated net surface heat flux (divided by $C_p \times \rho \times 40$ m) and the change in temperature of the top 40 m over 70 days was 0.3°C. This is equivalent to a heat flux of 8 W m^{-2} out of the 0–40 m layer for 70 days. Discrepancies between net surface heat flux and heat content change which account for this difference are short period (O(days)) high amplitude events (100–150W m^{-2}). For the majority of the 70 day record the two curves in Figure 2.16[a] (surface heat flux and heat content change) show remarkable agreement.

From the analysis presented here it impossible to identify the cause of the short period discrepancies. It may turn out that surface flux measurements at 2°S are not representative of the 3.4°latitude band of the heat content average. If the surface flux measurements *are*

found to be coherent over this latitude band, horizontal oceanic heat advection is the most likely cause of the deviation from a one dimensional balance.

Although taken in the opposite ENSO state and 10° further east, results of the heat budget of Chapter 3 provide an example of horizontal heat advection dominating the *in situ* temperature change over a period of 7 days. It was speculated that the large horizontal temperature gradients which gave rise to the large horizontal advective heat flux may have been due the uplifting of density surfaces by planetary waves. One could also speculate that such a process was responsible for the deviations from a local heat balance in the IOP data set. There is no evidence to support this at present. However an experiment similar to CD32 was carried out at 2°S during TOGA COARE. Results from that experiment will quantify the advective heat flux at 2°S. Comparison between the CD32 heat budget and the long term TAO mooring data analysis of Sprintall and McPhaden (1994) leads to the conclusion that changes in the temperature structure on these short time scales can be significantly greater than longer term wind induced or advective changes.

Returning to the COARE IOP heat content analysis; It was found that the changes in heat content with an approximate 10 day period were generally coherent over 10°of latitude, with the phase shift of one event attributable to a latitudinal phase difference in the wind stress pattern. This leads to the conclusion that the TOGA TAO Array of fixed ocean moorings *does* have sufficient spatial resolution to monitor changes in the heat content of the warm pool. What is not clear is how well the TOGA TAO Array is able to sample the dynamic response of the ocean. The response of the 20°isotherm was confined predominantly to within $\pm 1°$latitude of the equator. Thus there is reason to doubt that the TAO Array can fully describe the dynamic response of the WEP to wind events. A method to test this hypothesis is suggested in Section 6.6.

Finally, a few speculative remarks: Although there are no surface heat flux measurements from other latitudes during TOGA COARE, the TAO winds allow an estimate of the wind stress as a function of time to be made. The TAO winds have been averaged over the 3 latitude bands. The correlation between the TAO and IMET wind stress estimates is very strong (correlation coefficient, $r = 0.94$) and there is a strong correlation between the wind stress and surface heat flux ($r = -0.65$), principally through the latent heat flux. Assuming that this correlation holds over all latitudes one can compare the ocean heat content change with the wind stress. Centred on 2°S the correlation coefficient between TAO wind stress and ocean heat content change is $r = -0.62$. The correlation coefficient drops to $r = -0.4$

for both the northerly and southerly latitude bands. This is not surprising since the wind stress has a large latitudinal variation.

This result suggests that the change in ocean heat content is more coherent across the 10 degrees of latitude than the windstress, and presumably the heat flux. An implication of this could be that meridional advection of heat is playing a role on these time scales. In this regard examination of the meridional coherency of the ECMWF fluxes is needed. Estimation of the horizontal heat advection during the times of latitudinally coherent heat content change, using the Reynolds SST maps (Reynolds and Smith 1994), is also needed.

6.3 Diurnal Cycle: Observed and Modelled

All the main chapters have talked about the diurnal thermal cycle in the western equatorial Pacific. Both data sets, taken during opposite phases of ENSO, show a diurnal range in near surface temperature of a few tenths of a degree and a range in thermocline depth of 30–40 m. This magnitude of signal was apparent at all latitudes from 5°N to 5° S in the TOGA COARE data. These observations are similar to previous observations in the central equatorial Pacific (eg. Schudlich and Price (1992)). However the observations here appear to be the first such reported for the warm pool region.

An important question is; does the diurnal cycle matter in the warm pool? Or put another way, does a coupled atmosphere/ocean model need to resolve/parameterise the diurnal cycle in order to faithfully predict the evolution of the system?

A diurnal feedback mechanism between atmosphere and ocean is evident in the diurnal modulation of precipitation, But the timing of precipitation through the diurnal cycle has been shown to be unimportant after a period of two days. The TOGA COARE domain model simulation with daily averaged fluxes suggested that the SST could be faithfully predicted without resolving the diurnal cycle. However this experiment prescribed the surface fluxes. The diurnal cycle in SST has been shown to be asymmetric. Under the assumption of a linear relationship between heat flux and SST, this might imply that coupled models which predict fluxes need not resolve or parameterise the diurnal cycle provided the correct mean is used. The story is not as straight forward as that however. Studies suggest that when SST $>$ 27°C the latent heat flux *decreases* with increasing SST (Zhang and McPhaden 1994). Additionally the negative feedback mechanism of high SST causing greater atmospheric convection and cloud, hence reducing incoming short wave

radiation must be considered. It would seem that in a coupled model which predicts fluxes, the asymmetric diurnal SST variation and the non-linear relationship between SST and heat flux require that the diurnal thermal cycle must be adequately resolved or parameterised. It is also evident that accurate treatment of clouds in coupled models is essential. The sensitivity studies showed SST to be effected by a few tenths of a degree when incoming short wave radiation is varied 300W m^{-2} on a day to day basis.

Turning now to the diurnal momentum cycle. Most of the conclusions here come from the model sensitivity studies and hinge on the assertion of Schudlich and Price (1992) that the transition layer in the PWP model corresponds to the observed regions of high turbulent dissipation beneath the mixed layer. One objection to this is that the relaxation of the gradient Richardson number in the transition layer may represent a parameterisation of Kelvin-Helmholtz instabilities but it includes no non-local physics such as internal wave breaking remote from the source of generation. The importance of non-local dissipation is still an unknown. With this caveat in mind, one can conclude from the model studies that the diurnal mixing cycle is essential in mixing momentum into the ocean interior, ie. beneath the mixed layer. The transition layer is thickest during the deep nighttime phase of the diurnal cycle. Additionally, the maximum depth of nighttime mixing and the transition layer thickness are sensitive to the ambient shear. It was also found that within the latitude band of the warm pool, the transition layer is significantly rotationally constrained, with the maximum thickness found obviously on the equator.

6.4 Precipitation and Barrier layers

The excess of precipitation over evaporation is undoubtedly key to the formation of barrier layers in the western equatorial Pacific. Barrier layers have been shown here to be formed in one dimensional mixing models. In the TOGA COARE data set non-zero barrier layers, low sea surface salinity anomalies and precipitation all show strong coincidence.

Whether the maintenance of such layers requires the subduction below the warm pool of more saline waters from the east is the subject of a recent paper by Shinoda and Lukas (1995). In comparison between Lagrangian and Eulerian mixed layer model experiments their most important result appears to be that subduction is important in balancing the continual freshening effect of the precipitation, though not necessarily in the formation or maintenance of barrier layers.

Discussion of barrier layers is meaningless unless the effects of such a phenonemon are quantified. Lukas's definition (thermocline minus pycnocline depth), (Lukas and Lindstrom 1991), says nothing of how great the reduction of entrainment cooling is in the presence of a barrier layer. The definition proposed here (thermocline minus halocline depth) has the advantage of describing situations when entrainment cooling will be zero, although it fails to identify situations when entrainment cooling *may* be reduced. It is noted that the value of R_ρ provides the only quantitative measure of salinity versus temperature stratification.

An interesting finding of Shinoda and Lukas (1995) was that the arrival of an upwelling Rossby wave in the western Pacific prevented the formation of a barrier layer. There investigation was confined to latitudes greater than 5°S. This adds strength to the finding of Chapter 5 that changes in advected sub-surface structure (possible due to planetary waves) contributed to SST and MLD variation during CD32.

The main objective of this research project was to identify and quantify processes effecting the heat content and SST of the warm pool region. Does precipitation significantly effect the SST? On time scales of days, the answer is certainly yes. SST is depressed by up to 0.5°C in the days directly following rain events. On longer time scales one dimensional simulations of TOGA COARE showed SST to be greater after a 70 day integration which included precipitation. Although the increase was only by a small amount (0.05°C) the accuracy of the fresh water flux is unknown and the sensitivity to variations in the flux was not examined. Intuitively one would expect increased SST due to precipitation via a barrier layer effect, but the quantitative evidence for this is not strong at present.

6.5 Experimental Design

6.5.1 CD32 Experiment

Two elements would have improved the CD32 experiment. A thermistor chain on the spar buoy would have allowed better estimation of the horizontal temperature gradients. Such a chain was in fact deployed, but malfunctioned. The chain would also have given an independent description of the diurnal thermal cycle, and one less effected by horizontal temperature gradients. Drouging of the spar buoy to follow the upper 50 m current would have also improved the experiment. Such a lagrangian experiment would have reduced the spatial aliasing problems of the experiment, and additionally might have provided a

description of the time evolution of a rain produced fresh-water pool.

Given that the four sub-boxes of the survey where not used, due to too low a sample rate (once every 48 hours), and only the central cross used, a more efficient experimental strategy could be designed. A "butterfly" survey consisting of a cross with two diagonals across opposite tips would allow the central cross to be occupied at least twice as frequently as the four sub-box design. This would decrease the error in the estimate of the heat flux due to horizontal advection, which was the largest error in the heat budget estimate. In fact, such surveys were implemented during TOGA COARE.

6.5.2 TOGA COARE POI Experiment

The two major drawbacks of the *Le Noroit* POI data set are the lack of surface flux information, and the lack of information on the zonal structure of the upper ocean. The first would have been easy to remedy with an operational meteorological sensor suite. It is unfortunate that no priority was given to maintenance of the system on board. The best solution to the second problem, that of zonal information, would have been to have a second ship run a parallel Seasoar track a degree or so further west. A less satisfactory, but more economical solution would have been to have *Le Noroit* run consecutive sections on alternating meridians of 156°E and, say 154°E.

6.6 Implications and Future Directions

6.6.1 Implications for GCMs

An important aspect of small time and space scale studies concerns the implications for larger time and space scale simulations. A current area of much interest in Ocean General Circulation Models (OGCMs) is in the explicit inclusion of surface mixed layers with the sort of physical processes found, for example, in the two 1D mixing models used in this study.

As has already been said, Coupled GCMs (CGCMs) need to parameterise the diurnal thermal cycle to be able to accurately predict evolution of SST (Section 6.3). To quantify the effect of resolving or using some parameterisation of the diurnal cycle, GCM experimentation is needed.

The relative strengths of the EUC and SEC are important for the vertical transport of momentum in the 1D mixing models, and this transport is highly modulated by the diurnal

mixing cycle. It would seem that to get the upper equatorial ocean current structure right in GCMs, this diurnally modulated penetration of momentum beneath the mixed layer must be parameterised or resolved.

Another argument for the inclusion of realistic mixed layer physics in GCMs is the result from the CD32 data set in which it was seen that horizontally advected sub-surface structure interacted with the mixed layer to effect the SST. It also seems increasingly likely that salinity must be included in any successful GCM. Although the role of precipitation in effecting the SST was not shown conclusively to increase the SST, the observations certainly showed salinity stratification to play a role in limiting mixed layer deepening.

As a final remark on the models used: the conclusions that the Mellor/Yamada Level 2 closure scheme extinguishes turbulence too rapidly under the influence of large solar heating has been noted in CGCMs (Neelin et al. 1992). Neelin comments that such deficiencies, significant in CGCMs due to positive ocean/atmosphere feedback mechanisms, do not necessarily produce problems with uncoupled model tests. This comment is pertinent to the recent paper of Halpern et al (1995) who compare uncoupled GCM experiments including two different Richardson number dependent mixing schemes with observations and suggests their good agreement with observations might not hold with such mixing schemes in a CGCM.

6.6.2 Future Work

There are several very specific lines of investigation which work presented here suggests merit further investigation. Most avenues involve the TOGA COARE data sets, which are of international interest now, and will remain so for the next decade.

IOP Surface Fluxes

The ECMWF surface flux field will greatly enhance the analysis of the data set gathered on board *Le Noroit* . The accuracy of the ECMWF model fields will first need to be assessed by comparison with the IMET fluxes. This may well have already been undertaken. The spatial coherency of the fluxes across the 10° latitude band would then allow the spatial extent of the heating at 2°S around 15 December 1992 to be determined. Comparisons made between surface flux and heat content change could then be made at 5°north and south.

Forcing a one dimensional mixing model at all latitudes will allow the relative contributions of Ekman dynamics and local wind mixing in changing the pycnocline depth to be determined. The ECMWF precipitation field will allow meaningful studies to be made of the sensitivity of the SST to realistic variations in precipitation.

Dynamic Response

In Section 6.2 it was suggested that the TOGA TAO Array may have insufficient spatial resolution to describe fully the dynamic response of the upper ocean to wind bursts, or of the formation of frontal features. Comparisons of TAO Array data with the data set collected on board *Le Noroit*, which spans the spatial and temporal gap between the mooring data and the IFA data, should help clarify this. An important, as yet unanswered question is why some westerly wind bursts excite Kelvin waves whilst other do not. The answer may lie in a smaller space scale response than the TAO Array is able to resolve. An observation from the TAO array is that the December 1992/January 1993 WWB excited an equatorial Kelvin wave whilst the February WWB did not.

A statistical approach could be adopted to see how well upper ocean properties are correlated with increasing distance from the moorings. Such a study would quantify deficiencies in the spatial coverage of the TAO Array. To assess how important these deficiencies are a diagnostic modelling technique could be applied. The theory developed by Colin de Verdiere and Schopp (1994), whereby the zonal velocity is obtained by an inversion technique involving integration of density along lines of constant planetary rotation, could be applied to both data sets (TAO Array and Seasoar). Differences in the diagnosed velocity field would illustrate to what extent the TAO array captures the meridional response. Such a piece of research would quantitatively assess how well the TAO array describes the dynamic response of the western equatorial Pacific to westerly wind forcing.

6.6.3 Different Ocean States

Will TOGA COARE IOP provide enough information to fully describe the dynamics and thermodynamics of the western equatorial Pacific? A criticism sometimes aimed at the IOP is that it concentrated on too small an area. This may not prove to be too great a problem if the insights gained into atmospheric and upper ocean processes facilitate big improvements in coupled ocean atmosphere modelling of regional scale variability. What may prove to

be a greater problem is lack of observational information of the system during La Niña conditions. The deeper thermocline in the WEP during La Niña years, the increased vertical shear and the larger zonal temperature gradients may indicate predominance of different physical processes in the upper ocean of the WEP. Some evidence for this already exists in the poor simulation of SSTs by the PWP model during the TOGA Pilot study (Kantha and Clayson 1994). Time will tell how great a problem this is. One thing TOGA COARE has provided in this regard is the framework for studying atmosphere/ocean interaction, which could again be applied in future experiments.

Appendix A

COARE IOP Data Collection, Processing and Calibration

A.1 Data Collection

The start and end times, the southern and northern extends and the length in distance run of good data for the 12 Seasoar sections are given in Table A.1 in Section A.5. On the whole the Seasoar behaved well as did the processing system. There was very little data lost and most of the 12 sections are complete. This is pleasing given tight cruise schedule which allowed little time for instrument failure. It is also pleasing considering that this was one of the longest Seasoar surveys ever undertaken by UK scientists. The data gaps which did occur were due either to a failure of the Seasoar hydraulic system or the CTD. At no time did we have to recover the Seasoar because of the termination failing, typically a common cause for Seasoar recovery. On one occasion data was lost due to a processing system failure, see Section A.2. The full schedule meant that the ship had to continue steaming during some of the repairs, during these few times full depth CTD casts were made a 0.5°C intervals.

During the first half of the seasoar sections (sections 6 to 12) a maximum depth of 300 m was attained. At the beginning of section 13 it was noticed that one strand of the Seasoar cable had broken. This limited operations to a maximum depth of 200 m on sections 12 to 17, this may cause some problems in subsequent analysis but does not adversely effect the work reported here.

In addition to the Seasoaring, full depth CTD casts were made at every crossing of 2°S and occasionally at 5°S and 5°N.

A.1.1 Data Logging

The Seasoar data stream from the CTD deck unit was logged on a PC running the EC&G software **CTDACQ**, which is supplied for use with Neil Brown CTD instruments. Every 4 hours data files were transferred via an Ethernet link to a Sun IPC SPARCstation. This necessitated a break in the data acquisition of 3 minutes. By coinciding the start of the data transfer with the time when the Seasoar was at its maximum depth, only the bottom part of an up profile was lost (the Seasoar was cycling approximately every 10 minutes, surfacing every 2.5 km). Data were backed up on a tape streamer at the end of a section or during a CTD station, involving no interruption to data acquisition.

The variable "time" was a problem as the **CTDACQ** software did not generate time as a variable. This is because it would be unwise to rely on the PC clock. This problem is not encountered on UK NERC vessels as the time variable is provided by the RVS Level A software/hardware. To overcome the problem a file mark was placed in the data file by simulating a bottle fire at the beginning of each file and at hourly intervals and noting the time of each "fire". This worked well with the time being accurate generally to within 1 second (the accuracy of the time mark) over the 4 hour period.

The system was totally reliant on the PC working, which it did for most of the time. However on a few occasions the PC crashed either because of overheating when the air conditioning was down or an apparent incompatibility between the **CTDACQ** software and MS–Dos version 5 operating system. On most occasions few data were lost except on one occasion when the only solution was to reformat the hard disc. On this occasion the previous 4 hours of data were lost.

With a more reliable PC and software this method of data logging is a useful expedient when working on non-UK vessels. It would have been preferable to have logged the data directly on the Sun workstation together with GMT. However it is uncertain whether a single Workstation could have coped with both the data logging and data processing.

A.2 Data Processing

The processing of Seasoar data followed roughly that set out in (Cunningham et al. 1992). The major difference was in the reading in of data to the Pstar data processing system. *Le Noroit* did not have the RVS ABC system which automatically generates data files in the Pstar format. There were differences also in the way the salinity was calibrated.

For most of the cruise a CTD with 2 conductivity cells was used. One of the cells was labelled as the primary cell and used as the primary cell for calculating salinity. The second cell was used to check the calibration of the first and where necessary replacing the data from the first when the primary cell was fouled. This proved very effective. During a short period a single cell CTD was used whilst repairs were being carried out on the twin cell instrument.

A.2.1 Four-hour Processing

Every four hours a data file was transferred from the PC to the Workstation. The following programs and execs were then run to unpack the data, add time to the file, create a Pstar file and edit the data. The software in stages (1) and (2) below were purpose written in Fortran 77, C and Unix C–Shell scripts by the author. The other software was written by staff of the James Rennel Centre for Ocean Circulation (JRC) and the Institute of Oceanographic Sciences Deacon Laboratory (IOSDL) and were modified by the author. The program names are included for ease of cross–referencing to Cunningham et al. (1992) and Richards et al. (1993).

- **Step 1** – (Program: **bottle.f**)
  This program creates an input file to **ssexec0** of the times of bottle firings. Asks for timings from the user.

- **Step 2** – (Program: **ssexec0** (unix script))
  Programs called by this script are:

- **mk3unpack.c** – unpacks the binary raw file to an ascii file (written by S.G. Alderson, JRC).

- **mk3levela.f** – performs the equivalent of the RVS level A software for a Neil Browm Mk3 CTD, i.e. groups the data into 1 second "windows", removes data spikes, calculates the gradient of temperature (for use with the salinity calculation), performs a further median despike, then averages the final good values to give a 1 second average for each variable (Cormack 1992).

- **mk3time.f** – adds a time variable to the ascii file by locating the first bottle fire mark and incrementing time. Subsequent bottle file marks are used as a check for missing sections of data.

- **pascin** – creates a Pstar file and adds a header.

- **Step 3** – (Program: **ssexec1** (unix script)
  Performs simple editing and applies instrument calibrations. These are given in (Richards et al. 1993).

- **Step 4** – (Program: **ssexec2** (unix script)

  Hardcopy plots on an HP Paintjet XL were produced of temperature versus salinity and salinity versus pressure and on occasion temperature versus pressure to aid the editing process and for future reference.

- **Step 5** – (Programs: **plpred, finctd, prepl** (Pstar programs))

  The data were edited for remaining salinity spikes and shifts. On the whole the data were relatively clean with few spikes and fewer shifts (although there were some bad patches). The second conductivity cell proved to be very useful in checking for shifts of the primary cell and drifts in calibration (Section A.3).

Due to the slower response time of the thermistor compared with the conductivity cell, hysteresis occurs between up and down casts in the presence of temperature gradients. A time constant deltaT is applied to the temperature signal in Step 3 above. This was varied within a range 0.14 to 0.18 seconds on each four hour file such that the hysteresis appeared by eye to be a minimum.

The period of the cruise spanned the end and beginning of a year. The variables **time**, given in seconds, and **jday** are referenced to the beginning of the particular year in which the data were taken. This was to avoid excessively large values of **time** had all data been referenced with respect to 1992. A little over 1 days worth of data was collected in 1992. In this thesis negative julian days appear, these are days for 1992 counting backwards from **jday** 1 of 1993.

The software developed for the processing described above has since been used to good affect by scientists from the JRC whilst on board an American research vessel *RV Melville*.

A.2.2 Twentyfour-hour Processing

The cleaned four hour files were appended and merged with the navigation data to form between 3 and 4 files for each section (about 24 hours worth of data in each file). The GPS navigation data were obtained from the TSG file created by a PC logging the TSG in 5 minute averages. Occasionally the TSG file was corrupted. Then the navigation data were obtained from the ADCP data file logged on a different PC but again in 5 minute averages. The following programs and execs were run. Steps 1, 2 and 3 were written by K. Richards and the author, steps 4 & 5 by JRC and IOSDL staff.

- **Step 1** – (Program: **navinput.f**)
  Strips out the navigation data from the TSG file.

- **Step 2** – (Program: **navexec0** (unix script))
  This exec creates a Pstar file of navigation information.

- **Step 3** – (Program navexec1: (unix script)) This exec averages and filters the ship velocity in the navigation file.

- **Step 4** – (Program: **ss12exec1** (unix script))
  This exec subtracts 125 seconds from time to allow for the distance of the Seasoar behind the ship, merges navigation data with Seasoar data on time variable and calculates potential density from pressure, temperature and salinity.

  The start and end times of the 41 final calibrated **sa** files together with the start and stop latitude are given in Table A.1.

- **Step 5** – (Program: **ss12exec2** (unix script))

  The **sa** files were gridded on distance run and pressure and distance run and density using the Pstar program **pgrids**. The data were gridded onto 4 m x 4 km bins for pressure and 0.1 kg m^{-3} $\times$ 4 km bins for density.

A.3 Salinity Calibration

The calibration of the Seasoar CTD during the cruise was accomplished by reference to the SeaBird thermosalinograph (TSG). The upper waters of the region are characterised by

a surface layer of fresh water, with even fresher pools of water in places. This limits the range of salinities over which both the TSG and the Seasoar were calibrated. Calibrated deeper CTD data were not available during the cruise. The Seasoar CTD salinity and the CTD data have been compared post cruise showing agreement to within the accuracy of the two calibrations.

A.3.1 TSG Calibration

The TSG data were logged on a PC. The sampling rate was rather low, instantaneous measurements being taken every 15 secs. A 5 minute average had to be taken to obtain a sufficiently large sample. Attempts to increase the sampling rate were unsuccessful. The PC was unable to cope with the increased load (the PC was also logging meteorological data). However this low data rate does not appear to have been too detrimental.

Water samples from the supply to the TSG were taken every 2 hours and subsequently analysed on a Guideline Salinometer. The mean difference in the TSG and bottle samples (after discarding outliers) together with the standard deviation and error are given in Table A.2. The standard deviation and the error are encouragingly small even with the low sampling rate. During period B the conductivity cell malfunctioned (a period of 5 days) and was replaced. The new cell maintained the same calibration during periods C and D. Period D covers the whole of the 4 sections during leg 3. One set of samples was discarded as the salinometer gave much higher values than the TSG (a period of 2 days worth of data). This was due probably to a failure of the air conditioning resulting in increased temperatures in the room of the salinometer.

A.3.2 Seasoar CTD Calibration

Because of the low sampling rate of the TSG the TSG data were merged onto the Seasoar data. This produced many more data points (O(2000)). The presence of very shallow (less than 5 m depth) fresh water pools when the TSG salinity could be significantly lower than the Seasoar salinity meant that the estimate of the calibration constant had to be limited to periods outside of these times. Also surface heating on occasion produced sharp temperature gradients close to the surface. Again these periods were avoided.

The primary cell on the Seasoar CTD underwent a number of shifts in calibration. These occurred mainly between recovery and redeployment of the Seasoar. The secondary cell maintained its calibration throughout the cruise with only a small drift downwards of a few

thousands of a psu over the whole cruise (however the data from this cell was somewhat noisier than the primary cell). During the time covered by files **saPOI018–022** there was no useful TSG data. The primary cell was then calibrated using the secondary cell with a constant offset of 0.011. The single cell CTD was used during **saPOI028**. Calibration data for all the **sa** files are given in Tables A.3 and A.4.

The programs and execs used in the calibration procedure are detailed below. All unix scripts were written by K. Richards.

- **Step 1** – (Program: **tsgmake**)unix script))

  Creates a pstar file of TSG data and applies calibration to the salinity.

- **Step 2** – (Program: **tsgexec1** (unix script))
  This exec calibrates the Seasoar CTD salinity against the calibrated TSG salinity. The following programs are called by this exec

- **datpik** – picks out variables within specified limits close to the surface. The minimum and maximum depths were set at 2 and 5 m respectively, the inlet to the TSG being at 3.5 m.

- **pmerg2** – merges the TSG data onto the surface Seasoar data.

- **parith** – finds the difference between the TSG and Seasoar temperature and salinity.

- **phisto** – calculates the mean and standard deviation of the differences.

- **Step 3** – (Program: **tsgplot** (unix exec))
  An exec which uses **plxyed** to identify those periods to be used for the calibration.

- **Step 4** – (program: **tsgexec2** (unix script))
  This exec calculates the mean and standard deviation over a limited number of data cycles.

- **Step 5** (Program: **salcalexec12** (unix script))

  Applies the calibration constant to the Seasoar salinity.

A.3.3 Sections

The calibrated **sa** files making up a complete 5°N to 5°S section were appended. The data was then regridded on latitude and pressure (0.1°lat x 4 m) and latitude and density (0.1°lat x 0.1 kg m^{-3}).

A.4 Additional Data

A.4.1 ADCP

Data from the hull mounted ADCP was logged on a PC and processed using CODAS3 software. Gridded files were transferred to Pstar files **POIsecn.adcp**, the data being gridded on 0.25°lat x 8 m bins. The data did exhibit some bias with the heading of the ship but have been finally calibrated by ORSTOM removing this bias.

A.4.2 Meteorological Data

Meteorological measurements of air temperature, relative humidity, rain fall, wind speed, wind direction and hull sea surface temperature were made at 15 second intervals. Five minute averages were logged on a PC with GPS position and GMT time added to each observation. The meteorological instruments were mounted on the mast head at 15 m above sea level. The rain gauge was a Scientific Technology Inc. ORG-100 Optical Precipitation Sensor with a quoted accuracy of 10% over a range of $0.5 - 1600$ $mmhr^{-1}$. No radiation measurements were made. Unfortunately it became apparent after the cruise that the only reliable meteorological measurements were those of wind speed and precipitation.

In addition to these measurements an abbreviated version of the standard three hourly WMO bridge observations was made. The variables stored were: GMT time, GPS position, total cloud cover in octants, dry bulb temperature, wet bulb temperature, sea surface temperature, atmospheric pressure.

A full data set of heat, moisture and momentum fluxes from the Woods Hole Oceanographic Institute IMET mooring at 2°S have been obtained. The data are used here, I acknowledge Bob Weller of WHOI for the use of the data.

A.5 IOP Seasoar Start and Stop Times

file	section	start time jday	end time jday	start lat.	end lat.	dist. run start	dist. run end
saPOI001	1	365.835	366.667	4.949N	2.312N	304	632
saPOI002	1	366.671	366.999	2.299N	1.243N	633	762
saPOI003	1	1.002	1.996	1.237N	1.744S	762	1121
saPOI004	1	1.998	3.236	1.751S	4.999S	1122	1542
saPOI005	2	3.238	4.192	5.026S	2.011S	1542	1903
saPOI006	2	4.641	5.664	2.009S	1.223N	2006	2402
saPOI007	2	5.666	6.676	1.229N	4.500N	2402	2788
saPOI009	3	6.689	6.667	4.501N	1.397N	2800	3168
saPOI010	3	7.669	8.665	1.393N	1.998S	3169	3572
saPOI011	3	8.767	9.719	2.063S	5.016S	3586	3938
saPOI012	4	14.256	15.146	4.906S	2.003S	4561	4882
saPOI013	4	15.280	16.334	1.884S	1.556N	4896	5277
saPOI014	4	16.336	17.315	1.573N	4.995N	5278	5657
saPOI015	5	17.327	18.334	5.001N	1.797N	5662	6048
saPOI016	5	18.336	19.490	1.789N	2.024S	6049	6511
saPOI017	5	19.583	20.419	1.991S	5.002S	6528	6891
saPOI018	6	20.425	21.293	5.022S	2.006S	6894	7263
saPOI019	6	21.445	22.923	1.975S	3.014N	7283	7882
saPOI020	6	22.925	23.532	3.021N	5.002N	7882	8119
saPOI021	7	23.550	23.884	4.984N	3.859N	8132	8257
saPOI022	7	23.985	25.042	3.853N	0.598N	8266	8631

Table A.1: List of **sa** files, with section numbers, start and end times and distance run.

file	section	start time jday	end time jday	start lat.	end lat.	dist. run start	dist. run end
saPOI023	7	25.044	25.857	0.592N	2.007S	8632	8920
saPOI024	7	26.236	26.720	2.922S	4.497S	9030	9204
saPOI025	8	26.732	27.523	4.510S	2.002S	9209	9487
saPOI026	8	27.792	28.129	1.442S	0.523S	9557	9660
saPOI027	8	28.127	29.125	0.518S	2.755N	9661	10023
saPOI028	9	33.833	34.708	4.667N	1.750N	11358	11707
saPOI029	9	35.396	35.947	0.127S	1.995S	11939	12150
saPOI030	9	36.023	36.939	2.032S	5.012S	12161	12512
saPOI031	10	36.944	38.058	5.026S	2.001S	12514	12881
saPOI032	10	38.141	38.781	1.965S	0.032N	12894	13132
saPOI033	10	39.076	39.897	0.023N	2.726N	13172	13500
saPOI034	10	39.989	40.659	2.830N	4.993N	13520	13780
saPOI035	11	40.707	41.321	4.986N	3.017N	13784	14019
saPOI036	11	41.435	42.290	2.927N	0.268N	14039	14354
saPOI037	11	42.292	43.017	0.264N	1.994S	14355	14627
saPOI038	11	43.092	43.941	2.017S	4.859S	14634	14976
saPOI039	12	43.941	44.877	4.859S	2.004S	14976	15317
saPOI040	12	44.934	45.420	1.984S	0.429S	15323	15514
saPOI041	12	45.422	46.136	0.424S	1.974N	15514	15796
saPOI042	12	46.208	47.089	2.068N	4.983N	15810	16158

Table A.1: (continued) List of **sa** files, with section numbers, start and end times and distance run.

A.6 IOP Seasoar Calibration Data

Period	start time	end time	S_{tsg} - S_{bottle} mean	S_{tsg} - S_{bottle} std. dev.	std. error
A	30/12 16:50	20/1 04:00	0.032	0.011	0.0009
B	20/1 06:00	25/1 02:33	0.125	0.09	0.013
C	25/1 04:50	29/1 21:38	-0.003	0.005	0.0009
D	2/2 17:00	12/2 00:00	-0.003	0.005	0.0005

Table A.2: Calibration data of the Seabird thermosalinograph.

file	S_{ss} - S_{tsg} mean	S_{ss} - S_{tsg} s.d.	$S1_{cal}$ - S2 mean
saPOI001	0.185	0.005	0.012
saPOI002	0.189	0.004	0.011
saPOI003	0.197	0.006	0.016
saPOI004	0.199	0.006	0.009
saPOI005	0.198	0.003	0.011
saPOI006	0.196	0.005	0.008
saPOI007	0.195	0.003	0.008
saPOI009	0.196	0.007	0.009
saPOI010	0.196	0.003	0.012
saPOI011	0.199	0.018	0.010
saPOI012	0.213	0.006	0.010
saPOI013	0.213	0.006	0.010
saPOI014	0.214	0.007	0.008
saPOI015	0.218	0.007	0.009
saPOI016	0.227	0.005	0.010
saPOI017	0.228	0.011	0.008
saPOI018	0.277*	–	0.011
saPOI019	0.261*	–	0.011
saPOI020	0.250*	–	0.011

Table A.3: Calibration data for Seasoar CTD salinity. S_{ss} is the Seasoar salinity, S_{tsg} TSG salinity, $S1_{cal}$ the calibrated Seasoar salinity and S2 the salinity of the second CTD cell; * indicates no tsg data; [1] the "old" single cell CTD.

file	S_{ss} - S_{tsg} mean	S_{ss} - S_{tsg} s.d.	$S1_{cal}$ - S2 mean
saPOI021	0.249*	–	0.011
saPOI022	0.208*	–	0.011
saPOI023	0.210	0.003	0.011
saPOI024	0.206	0.009	0.012
saPOI025	0.207	0.006	0.013
saPOI026	0.217	0.004	0.011
saPOI027	0.208	0.012	0.007
saPOI028	-0.669[1]	0.005	–
saPOI029	0.192	0.004	0.010
saPOI030	0.197	0.005	0.012
saPOI031	0.195	0.005	0.015
saPOI032	0.193	0.017	0.017
saPOI033	0.193	–	0.015
saPOI034	0.194	0.012	0.012
saPOI035	0.189	0.006	0.015
saPOI036	0.212	0.003	0.013
saPOI037	0.212	0.007	0.017
saPOI038	0.209	0.005	0.013
saPOI039	0.207	0.006	0.016
saPOI040	0.255	0.006	0.019
saPOI041	0.255	0.004	0.014
saPOI042	0.212	0.005	0.015

Table A.4: Calibration data for Seasoar CTD salinity. S_{ss} is the Seasoar salinity, S_{tsg} TSG salinity, $S1_{cal}$ the calibrated Seasoar salinity and S2 the salinity of the second CTD cell; * indicates no tsg data; [1] the "old" single cell CTD.

References

Albright, M. D., E. E. Recker, R. J. Reed and R. Dang, 1985: The diurnal variation of deep convection and infrared precipitation in the central tropical pacific during january-februrary 1979, *Monthly Weather Review*, **113**, 1663–1680.

Barber, R. T., and F. P. Chavez, 1993: Biological consequences of el niño, *Science*, **222**, 1203–1210.

Baumgartner, A., and E. Reichel, 1975: *The World Water Balance*, p. 179, Elsevier.

Bearman, G. (ed.), 1989: *Ocean Circulation*, pp. 90–92, Pergamon Press.

Berg, W., 1993: Rainfall variability over the tropical pacific inferred from satellite estimates, Ph.D. thesis, University of Colarado.

Bjerknes, J., 1969: Atmospheric teleconnections from the equatorial pacific, *Monthly Weather Review*, **97**, 163–172.

Blackadar, A. K., 1962: The vertical distribution of wind and turbulent exchange in a neutral atmosphere, *Journal of Geophysical Research*, **67**, 3095–3102.

Bond, G., and D. Alexander, 1994: Toga coare meteorological atlas, *TCIPO Publication, UCAR, Boulder, CO June*, Bureau of Meteorology, Australia.

Bradley, E. F., J. S. Godfrey, P. A. Coppin and J. A. Butt, 1993: Observations of net heat flux into the surface mixed layer of the western equatorial pacific ocean, *Journal of Geophysical Research*, **98**, 22521–22532.

Brady, E. C., and H. L. Bryden, 1987: Estimating vertical velocities on the equator, *Oceanologica Acta*, **33**, 33–37.

Bryden, H. L., and E. C. Brady, 1985: Dianostic model of the three-dimensional circulation in the upper equatorial pacific ocean, *Journal of Physical Oceanography*, **15**, 1255–1273.

Bryden, H. L., and E. C. Brady, 1989: Eddy momentum and heat fluxes and their effects on the circulation of the equatorial pacific ocean, *Journal of Marine Research*, **47**, 55–79.

Chen, D., and L. M. Rothstein, 1991: Modeling the surface mixed layer structure in the western equatorial pacific, *Toga Notes*, **2**, 13–16.

Cormack, A., 1992: Mark 2 level a support for ctd applications, *Tech. Rep. 11/4/4.sp.001.1.1*, Research Vessel Services, Barry, UK.

Crawford, W. R., and T. R. Osborn, 1981: Control of equatorial ocean currents by turbulent dissipation, *Science*, **212**, 539–540.

Cunningham, S. A., R. T. Pollard, M. J. Griffiths, S. G. Alderson and R. Lowry, 1992: Seasoar data processing and calibration, *Tech. Rep. Internal Document No. 5*, James Rennell Centre for Ocean Circulation, Chilworth Research Park, Southampton, England.

de Verdiere, A. C., and R. Schopp, 1994: A. and r. schopp, 1994. flows in a rotating spherical shell: The equatorial case., *Journal of Fluid Mechanics*, **276**, 233–260.

Deardorff, J. W., 1970: T, *Geophysical Fluid Dynamics*, **1**, 377–410.

Delcriox, T., et al., 1993: Campagne coare–poi a bord du n. o. le noroit 1er decembre 1992–2 mars 1993, *Tech. Rep. 10*, ORSTOM, Noumea, New Caladonia.

Delcroix, T., et al., 1992: Variation of the western equatorial pacific ocean 1986-1988, *Journal of Geophysical Research*, **C4**, 5423.

Dillon, T. M., et al., 1989: Zonal momentum balance at the equator, *jpo*, **19**, 561.

Dorman, C. E., and R. H. Bourke, 1979: Precipitation over the pacific ocean 30 s to 60 n, *Monthly Weather Review*, **107**, 896,910.

Eldin, G., T. Delcroix, C. Henin, K. J. Richards, Y. du Penhoat, J. Picaut and P. Rual, 1994: Large-scale current and thermohaline structures along 156°e during the coare iop, submitted to Geophysical Research Letters.

Elliot, W. P., and R. K. Reed, 1984: A climatological estimate of precipitation for the world ocean, *Journal of Climate and Applied Meteorology*, **23**, 434,439.

Elsberry, R. L., T. S. Fraim and R. N. Trapnell, 1976: A mixed layer model of the oceanic thermal response to hurricanes, *Journal of Geophysical Research*, **81**, 1153.

Enfield, D. B., 1986: Zonal and seasonal variations of the near-surface heat balance of the equatorial pacific ocean, *Journal of Physical Oceanography*, **16**, 1038–1054.

Eriksen, C. C., 1985: The tropic heat program: An overview, *EOS*, **66**, 50–52.

Esbensen, S. K., and Y. Kushnir, 1981: The heat budget of the global ocean: An atlas based on estimates from surface marine observations, *Tech. Rep. 29*, Climate Research Institute, Oregon State University, Corvallis, Oregon.

Fiedler, B. H., 1984: An integral closure model for the vertical turbulent flux of a scalar in a mixed layer, *Journal of Atmospheric Sciences*, **41**, 674–680.

Friedrich, H., and S. Levitus, 1972: An approximation to the equation of state for sea water, suitable for numerical ocean models, *Journal of Physical Oceanography*, **2**, 514.

Garwood, R. W., 1977: An oceanic mixed layer model capable of simulating cyclic states, *Journal of Physical Oceanography*, **7**, 455–468.

Garwood, R. W., 1979: Air-sea interaction and the dynamics of the surface mixed layer, *Journal of Physical Oceanography*, **17**, 1507–1524.

Garwood, R. W., P. C. Chu, P. Muller and N. Schneider, 1989: Equatorial entrainment zone: the diurnal cycle, in *Western Pacific international meeting and workshop on TOGA COARE*, edited by J. Picaut, R. Lukas, and T. Delcroix, Noumea, New Caledonia.

Gaspar, P., 1988: Modelling the seasonal cycle of the upper ocean, *Journal of Physical Oceanography*, **18**, 161.

Gaspar, P., Y. Gregoris, R. Stull and C. Boissier, 1988: Long-term simulations of upper ocean vertical mixing using models of different types, in *Small scale turbulence and mixing in the ocean*, edited by J. Nihoul, and B. Jamart, pp. 169–184, Elsevier, Amsterdam.

Gent, P., 1991: The heat budget of the toga coare domain in an ocean model, *Journal of Geophysical Research*, **96**, 3323–3330.

Gill, A. E., and E. Rasmusson, 1983: The 1982-1983 climate anomaly in the equatorial pacific, *Nature*, **306**, 229–234.

Gill, A. E., and J. S. Turner, 1976: A comparison of seasonal thermocline models with observations, *Deep-Sea Research*, **23**, 391–401.

Godfrey, J. S., E. F. Bradley, P. A. Coppin and E. J. Lindstrom, 1991: On the net surface heat flux into the western equatorial pacific, *Journal of Geophysical Research*, **96**, 3391–3400.

Godfrey, S., and E. Lindstrom, 1989: Heat budget of the western equatorial pacific surface mixed layer, *Journal of Geophysical Research*, **94**, 8007.

Gordon, C., and R. A. Corry, 1991: A model simulation of the seasonal cycle in the tropical pacific ocean using climatological and modelled forcing, *Journal of Geophysical Research*, **96**, 847–864.

Gregg, M. C., H. Peters, J. C. Wesson, N. S. Oakey and T. J. Shay, 1985: Intensive measurements of turbulence and shear in the equatorial undercurrent, *Nature*, **318**, 140–144.

Halpern, D., Y. Chao, C. Ma and C. R. Mechoso, 1995: Comparison of tropical pacific temperature and current simulations with two vertical mixing schemes embedded in an ocean general circulation model and reference to observations, *Journal of Geophysical Research*, **100**, 2515–2521.

Halpern, D., et al., 1988: Observations of 20 day period meridional current oscillations in the upper ocean along the pacific equator, *Journal of Physical Oceanography*, **18**, 1514–1534.

Hansen, D. V., M. S. Svenson and M. C. Pazos, 1994: The drifter data assembly center, *International WOCE Newsletter*, **15**, 27–30.

Herbert, D., J. N. Moum, C. A. Paulson and D. R. Caldwell, 1992: Turbulence and internal waves at the equator, part 2 : Details of a single event, *Journal of Physical Oceanography*, **22**, 1346–1356.

Herbert, D., J. N. Moum, C. A. Paulson, D. R. Caldwell, T. K. Chereskin and M. J. McPhaden, 1991: The role of turbulent stress divergence in the equatorial pacific zonal momentum balance, *Journal of Geophysical Research*, **96**, 7127–7136.

Hinze, J. O., 1957: *Turbulence*, p. 770, McGraw-Hill, London.

Holyer, J. Y., T. J. Jones, M. G. Priestly and N. C. Williams, 1987: The effect of vertical temperature and salinity gradients on double diffusive interleaving, *Deep-Sea Research*, **34A**, 517–530.

Horch, A., W. Barkmann and J. D. Woods, 1983: Die erwarmung des ozeans hervorgerufen durch solare strahlungsenergie, *Tech. Rep. 120*, Institut fur Meereskunde, University of Kiel, Germany.

Hsiung, J., 1985: Estimates of global meridional heat transport, *Journal of Physical Oceanography*, **15**, 1405–1413.

Johnson, E. S., L. A. Regier and R. A. Knox, 1988: A sutdy of geostrophy in the tropical pacific ocean during the norpax tahiti shuttle using a shipboard acoustic current profiler, *Journal of Physical*

Oceanography, **18**, 708–723.
Kantha, L. H., and C. A. Clayson, 1994: An improved mixed layer model for geophysical applications, *Journal of Geophysical Research*, **99**, 25235–25266.
Kim, J. W., 1976: A generalised bulk model of the oceanic mixed layer, *Journal of Physical Oceanography*, **6**, 686–695.
Knox, R. A., and D. Halpern, 1982: Long–range kelvin wave propogation of transport variations in pacific ocean equatorial currents, *Journal of Marine Research*, **40 (suppl.)**, 329–339.
Kraus, E. B. (ed.), 1977: *Modelling and Prediction of the Upper Layers of the Ocean*, p. 325, Pergamon Press.
Kraus, E. B., 1987: The torque and flux balance in the upper equatorial ocean, *Journal of Geophysical Research*, **92**, 14242.
Kraus, E. B., 1988: *Small-Scale Turbulence and MIxing in the Ocean. Ed Nihoul*, pp. 37–50, Elsevier.
Kraus, E. B., and J. S. Turner, 1967: A one-dimensional model of the seasonal thermocline. II The general theory and its consequences, *Tellus*, **19**, 98–106.
Large, W. G., J. C. McWilliams and S. C. Doney, 1994: Oceanic vertical mixing: a review and model with a nonlocal boundary layer parameterisation, *Reviews of Geophysics*, **32**, 363–403.
Large, W. S., and S. Pond, 1981: Open ocean momentum flux measurements in moderate to strong winds, *Journal of Physical Oceanography*, **11**, 324–336.
Lemasson, L., and B. Piton, 1968: Anomalie dynamique de la surface de la mer le long de l'equator dans i'ocean pacifique, *Tech. Rep. Ser Oceanogr. 6*, Orstom, Noumea, New Caledonia.
Lindstrom, E., et al., 1987: The western equatorial pacific ocean circulation study, *Nature*, **330**, 533–537.
Lockyer, N., and W. J. S. Lockyer, 1904: Short-period atmospheric pressure variation, *Proceedings of the Royal Society of London*, **73**, 457–470.
Lukas, R., and E. Lindstrom, 1991: The mixed layer of the western equatorial pacific ocean, *Journal of Geophysical Research*, **96S**, 3343–3359.
Madden, R. A., and P. R. Julian, 1972: Description of global-scale circulation cells in the tropics with a 40-50 day period, *Journal of Atmospheric Sciences*, **29**, 1109–1123.
Mangum, L. J., S. P. Hayes, J. M. Toole, Z. Wang, S. Pu and D. Hu, 1990: Thermohaline structure and zonal pressure gradient in the western equatorial pacific, *Journal of Geophysical Research*, **95**, 7279–7288.
Martin, P. J., 1986: Simulation of the mixed layer at ows november and papa with several models, *Journal of Geophysical Research*, **90**, 903–916.
McPhaden, M. J., 1984: On the dynamics of equatorial subsurface counter currents, *Journal of Physical Oceanography*, **14**, 1216–1225.
McPhaden, M. J., 1993: Toga-tao and the 1991-93 el nino-southern oscillation event, *Oceanography*, **6**, 36–44.
McPhaden, M. J., et al., 1992: The response of the western equatorial pacific ocean to westerly wind bursts during november 1989 to january 1990, *Journal of Geophysical Research*, **97**, 14289–14303.
McPhaden, M. J., S. P. Hayes and L. J. Mangum, 1990: Variability in the western equatorial pacific ocean during the 1986–1987 El Niño /southern oscillation event, *Journal of Physical Oceanography*, **20**, 190–208.
McPhaden, M. J., and H. Peters, 1992: On the diurnal cycle of internal wave variability in the equatorial pacific ocean: Results from moored observations, *Journal of Physical Oceanography*, **22**, 1317–1329.
Mellor, G. L., and H. J. Herring, 1973: A survey of the mean turbulent field closure models, *AIAA J*, **11**, 590–599.
Mellor, G. L., and T. Yamada, 1974: A hierarchy of turbulence closure models for planetary boundary layers, *Journal of Atmospheric Sciences*, **31**, 1791–1806.
Mellor, G. L., and T. Yamada, 1982: Development of a turbulence closure model for geophysical fluid problems, *Reviews of Geophysics and Space Physics*, **20**, 851–875.
Moum, J. N., T. K. Chereskin, M. M. Park and L. A. Regier, 1987: Monitoring geostrophic currents at the equator, *Deep-Sea Research*, **34(7)**, 1149–1161.
Moum, J. N., M. J. McPhaden, D. Herbert, H. Peters, C. A. Paulson and D. R. Caldwell, 1992: Internal

waves, dynamic instabilities and turbulence in the equatorial thermocline: An introduction to 3 papers in this issue, *Journal of Physical Oceanography*, **22**, 1357–1359.
Neelin, J. D., et al., 1992: Tropical air-sea interaction in general circulation models, *Climate Dynamics*, **7**, 73–104.
Niiler, P., 1982: Tropic heat: A study of the tropical pacific upper ocean heat, mass, and momentum budgets, *Tech. rep.*, Oregon State University.
Niiler, P. P., and J. W. Stevenson, 1982: The heat budget of tropical ocean warm water pools, *Journal of Marine Research*, **40**, 465–480.
Noye, B. J., 1987: *Numerical Simulations of Fluid Motion*, p. 112, North Holland, Amsterdam.
Palmer, T. N., and D. A. Mansfield, 1986: A study of wintertime circulation anomalies during past El Niño events using a high resolution general circulation model. ii. variability of the seasonal mean response, *Quarterly Journal of the Royal Meteorological Society*, **112**, 639–660.
Pedlosky, J., 1987: An inertial theory of the equatorial undercurrent, *Journal of Physical Oceanography*, **17**, 1978–1990.
Pedlosky, J., 1991: The link between western boundary currents and equatorial undercurrents, *Journal of Physical Oceanography*, **21**, 1553–1558.
Peters, H., M. C. Gregg and T. B. Sanford, 1994: The diurnal cycle of the upper equatorial ocean: Turbulence, fine-scale shear, and mean shear, *Journal of Geophysical Research*, **99**, 7707–7723.
Peters, H., M. C. Gregg and J. M. Toole, 1988: On the parameterisation of equatorial turbulence, *Journal of Geophysical Research*, **93**, 1199–1218.
Picaut, J., S. P. Hayes and M. J. McPhaden, 1989: Use of the geostrophic approximation to estimate time-verying zonal currents at the equator, *Journal of Geophysical Research*, **94C3**, 3228–3236.
Pollard, R. T., and K. Thomas, 1989: Vertical circulation revealed by diurnal heating of the upper ocean in late winter. part 1 - observations, *Journal of Physical Oceanography*, **19**, 269.
Press, W. H., B. P. Flannery, S. A. Teuolsky and W. T. Vetterling, 1986: *Numerical Recipes*, p. 820, Cambridge University Press.
Price, J. F., and R. A. Weller, 1986: Diurnal cycling: observations and models of the upper ocean response to diurnal heating, cooling and wind mixing, *Journal of Geophysical Research*, **91**, 8411–8427.
Rasmusson, E. M., and T. H. Carpenter, 1982: Variations in tropical sea surface temperature and surface wind fields associated with the southern oscillation/el niño, *Monthly Weather Review*, **110**, 354–384.
Ravier-Hay, P., and J. S. Godfrey, 1993: A model of diurnal changes in sea surface temperature for the western equatorial pacific ocean, *Toga Notes*, **6**, 5–7.
Read, J. F., S. G. Alderson and R. T. Pollard, 1989: Pstar data processing programs, *Tech. Rep. 9-89*, Institute of Oceanographic Sciences, Deacon Laboratory, Wormley, Surrey, England.
Reed, P. K., 1985: An estimate of the climatological heat fluxes over the tropical pacific ocean, *Journal of Climate and Applied Meteorology*, **24**, 833–840.
Reynolds, R. W., and T. M. Smith, 1994: Improved global sea surface temperature analyses using optimum interpolation, *Journal of Climate*, **7**, 929–948.
Richards, K. J., 1991: Double-diffusive interleaving at the equator, *Journal of Physical Oceanography*, **21**, 933–938.
Richards, K. J., et al., 1988: Rrs charles darwin cruise 32, 3 april - 2 may 1988. a study of the upper density and current structure of the western equatorial pacific, *Tech. rep.*, Southampton University, Department of Oceanography.
Richards, K. J., M. E. Inall and S. Keene, 1993: Coare–poi cruise report: Seasoar data collection, processing and calibration, *Tech. rep.*, University of Southampton, The University, Highfield, Southampton, UK.
Richards, K. J., M. E. Inall and N. C. Wells, 1995: Observations of the upper ocean in the western equatorial pacific ocean, Journal of Geophysical Research, in press.
Richards, K. J., and R. T. Pollard, 1991: Structure of the upper ocean in the western equatorial paific, *Nature*, **350**, 48.
Rodi, W., 1982: *Turbulent Buoyant Jets and Plumes*, p. 183, Pergamon Press.
Schneider, N., and P. Müller, 1990: The meridional and seasonal structures of the mixed-layer depth

and its diurnal amplitude observed during the hawii–to–tahiti shuttle experiment, *Journal of Physical Oceanography*, **20(9)**, 1395–1404.
Schudlich, R., and J. F. Price, 1992: Diurnal cycles of current, temperature and turbulent dissipation in a model of the equatorial upper ocean, *Journal of Geophysical Research*, **97C4**, 5409.
Shinoda, T., and R. Lukas, 1995: Lagrangian mixed layer modeling of the western equatorial pacific, *Journal of Geophysical Research*, **100**, 2523–2541.
Smith, S. D., 1989: Water vapour flux at the sea surface, *Boundary-Layer Meteorology*, **47**, 277–293.
Sprintall, J., and M. J. McPhaden, 1994: Surface layer variations observed in multiyear time series measurements from the western equatorial pacific, *Journal of Geophysical Research*, **99**, 963–979.
Sprintall, J., and M. Tomczak, 1992: Evidence of the barrier layer in the surface layer of the tropics, *Journal of Geophysical Research*, **97C5**, 7305.
Stull, R. B., 1984: Transilient turbulence theory, part 1: The concept of eddy mixing across finite distances, *Journal of Atmospheric Sciences*, **41**, 3352–3367.
Stull, R. B., 1986: Transilient turbulence theory, part 3: Bulk dispersion rate and numerical stability, *Journal of Atmospheric Sciences*, **43**, 50–57.
Taylor, P. K., M. H. Smith, I. E. Consterdine and M. J. Yelland, 1994: The use of the inertial dissipation technique for shipboard wind stress determination, *Journal of Atmospheric and Oceanic Technology*, **11**, 1093–1108.
TCIPO, 1992: *TOGA COARE operations plan: working version*, UCAR, Boulder CO 80307.
TCIPO, 1993: Toga coare intensive observing period operations summary, *Tech. rep.*, University Corporation for Atmospheric Research TOGA COARE International Project Office.
TCIPO, 1994: Toga coare data management plan: Version 2.0, *Tech. rep.*, University Corporation for Atmospheric Research TOGA COARE International Project Office.
Tennekes, M., and J. L. Lumley, 1972: *A First Course in Turbulence*, p. 512, MIT Press.
Tsuchiya, M., R. Lukas, R. A. Fine, E. Firing and E. Linsdtrom, 1989: Source waters of the pacific equatorial undercurrent, *Progress in Oceanography*, **23**, 101–147.
Walker, G. T., and E. W. Bliss, 1930: World weather. iv, *Mem. R. Meteorol. Soc.*, **3**, 81–95.
WCRP, 1990: Scientific plan for the coupled ocean-atmosphere response experiment, *WCRP Publication Series 3*, World Meteorological Organisation.
Weare, B. C., P. T. Strub and M. D. Samuel, 1980: *Marine Climate Altas of the Tropical Pacific Ocean*, p. 147, University of California.
Weickmann, K. M., 1991: El niño/southern oscillation and madden-julian (30–60 day) oscillations during 1981–1982, *Journal of Geophysical Research*, **96**, 3187–3197.
Woods, J. D., W. Barkmann and A. Horch, 1984: Solar heating of the oceans-diurnal, seasonal and meridional variation, *Quarterly Journal of the Royal Meteorological Society*, **110**, 633–655.
Wyrtki, K., E. Firing, D. Halpern, R. Knox, G. J. McNally, E. D. Patzert, E. D. Stroup, B. A. Taft and R. Williams, 1981: The hawii to tahiti shuttle experiment, *Science*, **211**, 22–28.
Zhang, G. J., and M. J. McPhaden, 1994: On the relationship between sea surface temperature and latent heat flux in the equatorial pacific, submitted to Journal of Climate.